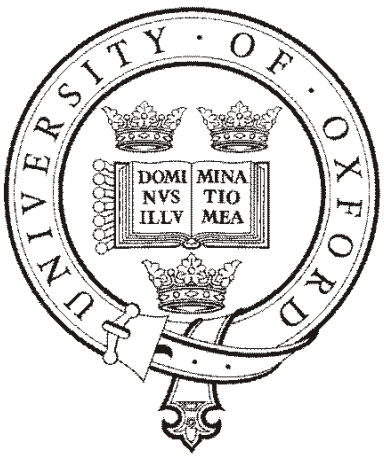
Soaring and Gust Response in the Steppe Eagle

KATE VICTORIA REYNOLDS

A thesis submitted in partial fulfilment of
the requirements for the degree of
Doctor of Philosophy at the University of Oxford



New College
University of Oxford
2015

Soaring and Gust Response in the Steppe Eagle

Kate Reynolds, New College.
(Department of Zoology)

Thesis submitted for the degree of Doctor of Philosophy
at the University of Oxford, 2015.

Abstract

This thesis explores how onboard instrumentation can be used to study how birds interact with the atmosphere, in particular to understand their soaring strategies and gust response mechanisms. The instrumentation unit consists of integrated sensors, including a GPS, IMU (inertial measurement unit) and pressure transducer, which provide accurate, high frequency measurements of the aerodynamics and kinematics of a free flying bird. The equipment development and derivation of parameters are initially presented. The data recorded from multiple flights of a steppe eagle (*Aquila nipalensis*) are then used to analyse the different aspects of its soaring flight throughout the rest of the thesis.

First, the occurrence and mechanism of the wing tuck manoeuvre is investigated and found to be a gust response, precipitated by a drop in aerodynamic loading. It is suggested that this reduction in loading results in a moment imbalance on the wings, and that ultimately the wings are pulled down by an internal musculoskeletal moment. The bird's slope soaring behaviour is then studied by using CFD analysis to model the local updrafts for comparison with the bird's performance. The analysis shows that the bird predominantly flew in the regions of strongest updraft along the ridge but did not attempt to maximise gravitational potential energy. This leads to gliding flight and a review of the theoretical derivation of the classic glide polar. A sensitivity analysis of the polar to different drag coefficients highlights the need for more research into the selection of suitable values. The development of a new 'soaring optimisation' chart to include the effect of wind conditions on the selection of best glide speed is presented. This is then compared with experimental glide data from the bird and used to determine the optimal drag coefficients for the polar model. Finally, a technique is developed for automatically identifying sections of thermalling flight and for removing the wind drift component to allow us to test thermalling behaviour. This exploratory analysis highlights the complexity of the flow structure within the thermal and the distinctly unsteady circling of the bird.

Statement of Authorship

This thesis is structured as a series of papers, each with a self-contained introduction and discussion. Chapter 3 has been published as a paper in *J. R. Soc. Interface* (Reynolds et al. 2014a), and is presented in its published form with a few minor alterations to correct typographical errors. I am first author and the text was written together with co-authors Graham Taylor and Adrian Thomas. I developed the equipment and performed the field tests for collecting all of the steppe eagle flight data used in the thesis, with the exception of a small subsection of GPS data in Chapter 4, which was originally recorded by James Gillies (2010) in 2008 and 2009. In the same chapter, the CFD model used to analyse the air flow over a ridge at one of our field sites was generated as part of a Master's thesis by Benjamin Boisserie (2012). I summarised this model in Section 4.2.1 and used the results to analyse the flight of our bird when ridge soaring. Except where otherwise indicated above, the text of this thesis is entirely my own.

This *D.Phil* was funded through a Biotechnology and Biological Sciences Research Council (BBSRC) CASE studentship with Blue Bear Systems Research Ltd. The research leading to these results has received funding from the European Research Council under the European Community's Seventh Framework Programme (FP7/2007-2013)/ERC grant agreement no. 204513.

Word count 57,245

Acknowledgements

My sincere thanks go to my supervisors, Graham Taylor and Adrian Thomas for their guidance and support throughout the project and for their optimism and consistent belief in me. I have thoroughly enjoyed working with them both. I am extremely grateful to Graham who first invited me to do this project and patiently introduced me to research. His infectious enthusiasm, knowledge and love of biology are inspirational. Adrian's insight and in depth flying knowledge have been invaluable, helping me to tie different aspects of the project together and putting it into context. Thank you to all the past and present members of the Animal Flight Group who have provided constant encouragement and friendship over the last four years; from conferences to late nights in the office/pub and through hours of sitting on chilly hill tops, watching birds! I am grateful to both BBSRC and Blue Bear for funding this project and for the opportunity to be involved in the applied engineering side of this research. Many people have helped me over the last four years, both in the office and elsewhere; friends, family and colleagues. It has been an amazing experience and I would like to thank everyone who has encouraged and supported me along the way. Finally, I would like to thank Dr. Robin Wootton, who originally introduced me to the Oxford Animal Flight group which resulted in this *D.Phil*, and my grandfather, Dr. Robert Bugler, who sparked everything off by introducing me to Robin.

"If bird's can glide for long periods of time,
then... why can't I?"

– Orville Wright

Contents

1 Introduction **3**

2 Instrumentation and data analysis **12**
2.1 Introduction . . . 12
2.2 Experiments . . . 13
2.3 Instrumentation . . . 15
2.4 Data post-processing and sensor performance . . . 22
2.4.1 GPS . . . 22
2.4.2 Barometric Pressure . . . 26
2.4.3 Temperature . . . 29
2.4.4 Dynamic Pressure . . . 30
2.4.5 Energy . . . 33
2.4.6 IMU data . . . 34
2.5 Derived quantities . . . 42
2.5.1 Data fusion for state estimation . . . 43
2.5.2 Load factor . . . 44
2.5.3 SC_L . . . 44
2.5.4 Wind velocity . . . 45
2.6 Discussion . . . 46

3 Wing tucks are a response to atmospheric turbulence in the soaring flight of the Steppe Eagle *Aquila nipalensis* **49**
3.1 Introduction . . . 51
3.2 Materials and Methods . . . 53
3.2.1 Experiments . . . 53
3.2.2 Instrumentation . . . 56
3.2.3 Data processing . . . 58

3.2.4 Automatic tuck identification 60
3.2.5 Environmental predictors of atmospheric turbulence 62
3.3 Results 64
3.3.1 Mechanics of wing tucking 64
3.3.2 Environmental predictors of wing tucking 68
3.4 Discussion 71
3.4.1 Wing tucks as a form of gust response 71
3.4.2 Mechanics of wing tucking 75
3.4.3 Conclusions 78
3.5 Acknowledgements 79

4 Modelling updrafts for slope soaring 80
4.1 Introduction 80
4.2 Materials and Methods 82
4.2.1 CFD model 82
4.2.2 Steppe eagle experiments 84
4.3 Results 85
4.3.1 CFD analysis 85
4.3.2 Steppe eagle flights 93
4.3.3 Comparison of CFD and bird data 93
4.4 Discussion 101

5 Theory of gliding flight 104
5.1 Introduction 104
5.2 The glide polar model 105
5.2.1 Induced drag coefficient 107
5.2.2 Parasite drag coefficient 108
5.2.3 Profile drag coefficient 110
5.2.4 Fixed-wingspan polar model 112
5.2.5 Variable-wingspan polar model 112
5.2.6 Performance area 115
5.3 Theoretical glide polar for the steppe eagle 116
5.3.1 Sensitivity of fixed-wingspan model to drag coefficients 117
5.3.2 Effect of variable wingspan 119
5.3.3 Estimated performance area 124
5.4 Discussion 125

6 Glide polar: experimental data and optimisation 132
6.1 Introduction . . . 132
6.2 Methods . . . 133
6.2.1 Data collection . . . 133
6.2.2 Glide identification . . . 134
6.3 Experimental results and analysis . . . 135
6.3.1 Comparison of experimental and theoretical performance area 138
6.3.2 Wind effect . . . 140
6.3.3 Soaring optimisation . . . 142
6.4 Discussion . . . 152

7 Thermalling characteristics 155
7.1 Introduction . . . 155
7.2 Methods . . . 157
7.2.1 Thermal identification . . . 157
7.2.2 Drift elimination . . . 159
7.3 Results . . . 168
7.3.1 Thermal characteristics . . . 172
7.3.2 Thermal comparison . . . 174
7.3.3 Time series and spatial analysis of thermalling behaviour . . . 176
7.4 Discussion . . . 180

8 Discussion 181

Appendix A Flight sites 186

Appendix B AHRS algorithm 198

Appendix C Thermal identification 207

List of symbols

α	Acceleration at centre of mass of rigid body
α	Glide angle
AR	Aspect ratio
$\bar{V}$	Mean MIDAS wind speed*
$\bar{v}$	Mean anemometer wind speed
β	Span coefficient
$\mathbf{b}$	Magnetic field vector (in IMU axes pre-calibration)
$\mathbf{v_t}$	Velocity vector at time t
$\boldsymbol{\beta}$	Magnetic field vector (in Cartesian coordinates post calibration)
$\boldsymbol{\delta}$	Magnetometer bias error vector
$\boldsymbol{\epsilon}$	Magnetometer noise vector
$\boldsymbol{\gamma}$	Residuals vector for accelerometer CoM dispacement
$\boldsymbol{\lambda}$	Magnetometer scale factor error vector
Δp	Dynamic pressure
Δ_i	AIC difference
$\dot{E}_t$	Total energy rate of change
ϵ	AIC estimated residuals
η	Linear span-coefficient slope
γ	Linear span-coefficient constant
μ	Dynamic viscosity
ω	Angular rate of rotation
ϕ	Roll/Bank angle
ψ	Yaw angle
ρ	Density
τ	Circling period
θ	Pitch angle
$\tilde{v}$	Standard deviation of anemometer wind speed
ξ	Angle between velocity vectors
A	Altitude above sea level*
a	Acceleration
b	Wingspan
C	Calibration constant airspeed
c_1, c_2	Polar constants
C_D	Drag coefficient
C_L	Lift coefficient
$C_{D,i}$	Induced drag coefficient
$C_{D,par}$	Parasite drag coefficient
$C_{D,pro}$	Profile drag coefficient
C_{L_w}	Mean wing section lift coefficient
D	Drag force
d_1, d_2	Distance
d_x, d_y, d_z	Displacement of board from bird's centre of mass
E_k	Kinetic energy
E_p	Potential energy
E_t	Total energy
F	Total aerodynamic force

f	Frequency
g	Gravitational acceleration
h	Altitude
k	AIC number of estimated parameters
k	Induced drag factor
k	Ratio of specific heat
L	Lapse rate
L	Lift force
M	Moment
m	Mass
m_b	Body mass
M_m	Musculoskeletal moment
m_w	Wing mass
n	Sample size
N_t	Total load factor
p	Static pressure
p, q, r	Angular rate of rotation*
p_t	Stagnation pressure
R	The gas constant
r	Pearson correlation coefficient
r	Radius
r	Ridge height*
Re	Reynolds number
S	Wing area
s	Length of arc
S_b	Body frontal area
S_w	Wing area
S_{fp}	Equivalent flat plate area
T	Temperature
t	Time
T_p	Phugoid period
U	Airspeed*
V, V_a	Airspeed
V, V_a, V_e	Equivalent airspeed
V_*	Best glide speed
V_c	Calibrated airspeed
V_d	Vertical inertial velocity
V_g	Ground (inertial) velocity
V_i	Indicated airspeed
V_s	Sink rate
V_t	True airspeed
V_w	Wind velocity
V_{min}	Airspeed at minimum sink rate
$V_{s,min}$	Minimum sink rate
V_{stall}	Stall speed
W	Weight
w_i	Akaike weight
W_z	Vertical wind speed component
W_{xy}	Horizontal wind speed component
x, y, z	Displacement of board from bird's centre mass*

** The notation for Chapter 3 is the same as in the original published paper but is different to the rest of the thesis.*

Chapter 1

Introduction

Whether flapping or effortlessly soaring, avian flight has fascinated mankind for centuries. With their flexible, morphing structures, rapid response times, impressive endurance and extreme gust tolerance, birds are able to explore the skies with enviable freedom. As a result, they have inspired designers throughout the history of both conventional aircraft and un-powered glider development (Kahveci et al. 2007; Videler 2005).

Bird flight can roughly be divided into phases of flapping, gliding descent or soaring ascent (Spaar 1997). An optimal flight strategy requires a bird to sense and interact efficiently with the atmosphere. Not only must each phase of its flight be optimised, but also the combined strategy (i.e. appropriate choice of flight mode); this will vary between species. Despite soaring's prominent role in flight, particularly for larger species, the complex strategies and mechanisms that birds employ when soaring are perhaps the least understood. Soaring exploits energy from natural updrafts, or lift sources, in the atmosphere to offset an animal or aircraft's inherent sink rate (Edwards and Silberberg 2010). It generally constitutes circling in thermals or straight line soaring in ridge lift (Andersson et al. 2009; Hunter 1984) as these are the most abundant lift sources in the boundary layer (see Figure 1.1). The turbulent

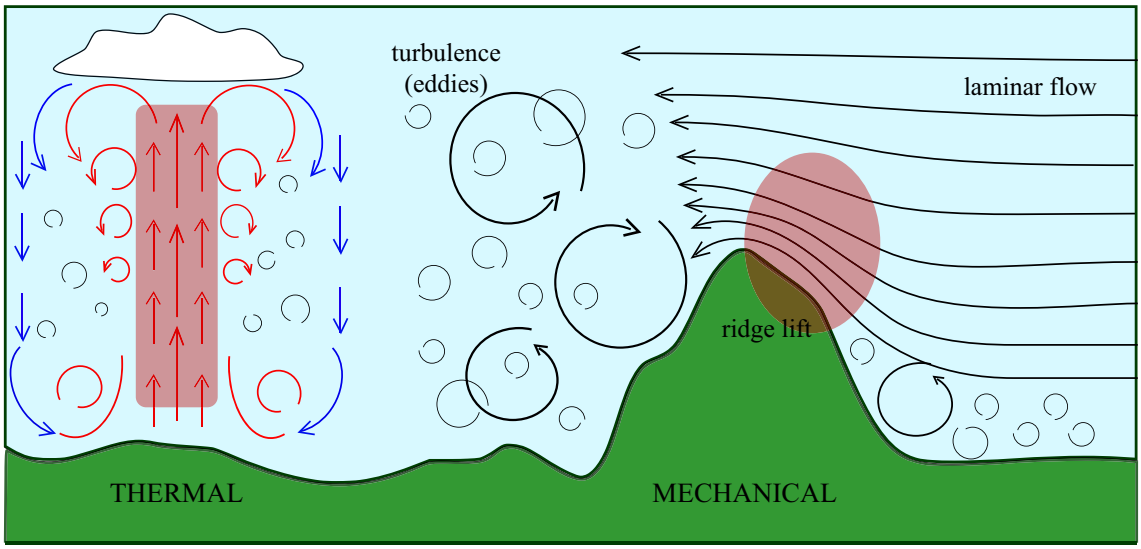


Figure 1.1: Illustration of the thermal and mechanical processes which are prominent within the boundary layer of the atmosphere. Ultimately all air movement is powered by solar heating. Lift sources originate from either terrain topography or thermal flows and have long been used by birds and glider pilots to travel huge distances with minimal energy cost. Thermals are columns (red arrows) or bubbles of rising warm air that has been heated by the ground (Andersson et al. 2009). The strongest lift is in the thermal core and is generally surrounded by regions of sink (blue arrows) as the air recirculates, but the internal structure can be extremely complex and variable. Although a good source of energy, thermals are notoriously sporadic and hard to locate, though cues such as building cumulus clouds can be a good indication of their presence. Ridge lift on the other hand is fixed to topographical features as it is formed by the deflection of airflow over obstructions (from mountains and ridges to walls or even hedgerows). The strongest lift is generated at the crest of the hill where the flow is accelerated (Reichmann 1993). Wind gradients (shear layers), microlift and small scale gusts are also able to provide lift if used efficiently (Hunter 1984; Reichmann 1993). Intrinsically related to the generation of lift is turbulence (black arrows), which consists of rotating vortices (or eddies) of variable size (Jacobson 2005; Rohli and Vega 2011). The resulting unpredictable, gusty conditions can be difficult to negotiate. Numerous hypotheses and theories exist on how to best exploit the available lift sources (Reichmann 1993).

conditions of the atmosphere mean that soaring is by necessity very opportunistic and requires agile, rapid manoeuvring (Kahveci et al. 2007). Recently this behaviour has been of particular interest for the design of unmanned air vehicles (UAVs) and their control algorithms (McGowan et al. 2003).

The extensive research exploring each aspect of flight has until now been focused on performance, morphological differences, energetics, choice of flight mode and the influence of weather conditions. This has been studied through mathematical and mechanical modelling, specialised wind tunnel experiments, ground based

observations and tests where researchers have flown alongside birds in small aircraft to collect data on flight conditions (Videler 2005). However, such methods do not allow accurate recording of the bird's instantaneous response to atmospheric stimuli in free-flight, for example, the subtle kinematic response to encountering a gust. This requires high frequency sampling, ideally of both the bird's response and the atmospheric perturbation at the bird's position.

In the last couple of decades, the use of onboard instrumentation units to study the behaviour and kinematics of animals has become increasingly common (Gillies et al. 2011; Grünewälder et al. 2012; Ropert-Coudert and Wilson 2005; Ropert-Coudert et al. 2009; Taylor et al. 2008; Watanabe et al. 2005; Wilson et al. 2013; Yoda et al. 1999). With the development of inertial measurement units (IMUs) and global positioning systems (GPS) small and light enough to mount on a bird, an abundance of information can now be obtained on free-flight performance.

Given the strict payload limitation for birds, the majority of studies have primarily used GPS units for tracking flight paths (Ákos et al. 2008; Biro et al. 2004; Bohrer et al. 2012; Guilford et al. 2009; Mellone et al. 2011; Sachs et al. 2013). Others have combined GPS data with *in vivo* heart rate measurements (Mandel et al. 2008; Sapir et al. 2010) or made use of accelerometers to quantify behaviour through estimates of body movements and posture (Bouten et al. 2013; Nathan et al. 2012; Portugal et al. 2014; Shamoun-Baranes et al. 2012; Shepard et al. 2008). Often these loggers are used for long-range tracking and are therefore limited to extremely low sampling rates, or have incorporated machine learning techniques to selectively sample at high rates for short periods.

With additional sensors such as an IMU (which integrates accelerometer data with gyros and magnetometers), a pressure transducer to estimate airspeed, or a barometer for altitude, many of the errors associated with using GPS or raw accelerometer data can be improved to provide more accurate parameter estimates. Such integrated sensors have rarely been used on birds (Gillies et al. 2008; Gillies et al. 2011) as the design of equipment for onboard flight analysis is technically

challenging. The sensors must not only be robust to operate in harsh conditions on the bird's back, but size and weight must also be minimised to prevent interference to its flight.

This thesis aims to build on the work by Gillies (2010), using an updated instrumentation unit. Using the example of a steppe eagle (*Aquila nipalensis*), we explore how the instrumentation can be used to extract the aerodynamics, kinematics and mechanisms for the different aspects of the bird's flight. Specifically, we aim to study the bird's soaring strategies in terms of how the bird responds to different atmospheric conditions, whether it is turbulence mechanisms or the effect of wind velocity on glide performance. Steppe eagles are natural soarers; they are well adapted to preserve energy and rarely resort to flapping flight. They exploit both ridge lift and thermals when travelling on their yearly migration from sub-Saharan Africa across the Gulf of Suez to breeding grounds that stretch from Russia (north of the Caspian Sea) as far as the Altain Mountains in western Mongolia (Spaar and Bruderer 1996).

Initially, in Chapter 2, we review the equipment design, using similar sensors to those found on a UAV or glider. The different sensors are discussed in detail, highlighting the limitations that should be carefully considered when analysing results. We also derive a wide range of parameters to illustrate the extent to which the data can be interpreted, and develop a suitable framework for similar studies in the future. The experimental design to record data from our steppe eagle's flight, which is used throughout this thesis, is also presented. The subsequent chapters go on to use this onboard flight data to explore some of the characteristic aspects of our specific bird's flight, but draw no conclusions about the species population.

It is well known that the energy cost associated with soaring is much less than for flapping flight, a relationship which becomes more pronounced in larger birds; as bird's body mass (m) increases, powered flight (flapping) becomes increasingly energetically demanding given that mechanical power is proportional to $m^{7/6}$ (Duerr et al. 2012; Hedenström 1993; Rayner 1982; Sachs 2015). Many large birds almost

exclusively use soaring strategies, only resorting to flapping when no lift source is present or during take-off and landing. However, energy cost is not the only optimisation criterion; otherwise almost all birds would soar. Hedenstrom (1993) showed that birds also aim to minimise travel time, partly explaining why flapping is often favoured by smaller birds. Many migrating species, such as vultures, eagles and other raptors, use ridge and thermal lift to travel thousands of kilometers, whilst some marine birds with extreme wing loadings, like the albatross, are able to use dynamic soaring to exploit wind gradients (Ákos et al. 2010; Sachs et al. 2013). Of course, even soaring is not entirely cost free; in addition to the energy loss from the bird's inherent sink rate, in gliding or soaring the bird must also exert energy to hold its wings in position and counteract the lift force acting on them (Baier et al. 2007; Gray 1968; Kuroda 1961; Pennycuick 1972; Pennycuick 1982). A possible consequence of this required musculoskeletal force is discussed in Chapter 3, where we explore the occurrence and mechanism of the wing tuck manoeuvre and show that wing tucks represent a gust response, precipitated by a transient drop in aerodynamic loading that is not immediately compensated by a corresponding reduction in the musculoskeletal force (Reynolds et al. 2014a). A method for automatic identification of flapping and wing tucks from the onboard accelerometer data is also described, allowing us to eliminate these sections from the flight data in other chapters where necessary.

The most common way to describe the performance of a wing or bird is the glide polar—a plot of the vertical versus horizontal speed during gliding (Pennycuick 1998)—as direct measurements of a bird's energy consumption during flight are extremely difficult. Even with careful monitoring of respiration, aerodynamic power and mass loss, limited useful data can be determined (Rayner 1982). The glide polar can be calculated theoretically using suitable drag coefficients (Pennycuick 1989a; Taylor and Thomas 2014; Tucker 1987). However the choice of drag coefficients can vary significantly as experimental results of polars from both wind tunnel tests and free-flight observations can be extremely variable. This subsequently causes variations in the estimates of minimum sink rates and optimum glide speeds derived

from the polar (Parrott 1970; Pennycuick 1982; Rosén and Hedenström 2001; Spaar and Bruderer 1996). An accurate estimate of the glide polar is therefore important for both species comparisons and determining optimal flight strategies, but results in the literature often contradict one another. We discuss this in detail in Chapter 5, presenting the general theory of gliding flight and the different wingspan models. We also demonstrate the sensitivity of the polar to the choice of coefficients using the case study of our steppe eagle, as well as the effect of horizontal and vertical wind components on the bird's predicted performance. In Chapter 6 we attempt to extract the glide polar of our bird from the experimental data, automatically identifying phases of gliding flight. However, as in many studies, our data bears little resemblance to the theoretical glide polar. This is unsurprising given that the data is an amalgamation of a family of polars that the bird can switch between by changing its wing morphology. In addition, effects from the atmosphere can significantly shift the position of the data on the polar axes. This leads us to explore, theoretically, how the glide data is affected by the bird optimising its flight speed for different wind conditions, or according to different flight objectives. Finally an optimisation chart which illustrates this theory is constructed and compared with our experimental glide data.

Research into the behaviour of birds exploiting lift sources has often looked at the effect of meteorological conditions on their large scale movements and how the choice of flight strategy can influence migration routes. Whilst ridge lift is fairly constant (for a given wind direction), there are peak times in the day and year when thermals are more frequent and/or stronger. This was accurately reflected in studies where the flight modes and times of different species were correlated with parameters such as the time of day, year, weather, topography and temperature (Careau et al. 2006; Spaar and Bruderer 1996). A comparison of turkey vultures (*Cathartes aura*) and golden eagles (*Aquila chrysaetos*) during migration revealed that, despite their anatomical similarity, the vultures nearly exclusively used thermals whereas the eagles mainly exploited ridge lift (Bohrer et al. 2012). It concluded that this dictated their choice of migration path along the east coast of America, each favouring routes

optimal for thermal or ridge lift respectively. Conversely, it may be that that their choice of lift source was dependent on their selection of migration route. Using GPS devices, Mellone (2011) found that to reduce transport cost, short-toed eagles (*Circaetus gallicus*) would detour over a thousand kilometers during migration from Europe to Africa to avoiding crossing large bodies of water where no lift sources are available. Duerr (2012) meanwhile compared cross-country speeds of golden eagles and found that slope soaring in ridge lift was slower as birds were diverted more from their migration paths whilst they were able to glide faster after a thermal.

The behaviour of birds on a smaller spatial scale (i.e. whilst exploiting a specific lift source) has been relatively unexplored, specifically strategies for slope soaring. This is perhaps because ridge lift is fixed to geographic features and so is fairly predictable (when compared to sporadic thermals) provided the wind direction is approximately perpendicular to the ridge. As wind direction and speed tend to change slowly, ridge lift often lasts many hours (Bower et al. 2010). The potential altitude gain varies with wind strength and direction but typically the region of lift extends around two or three times the height of the obstruction (Andersson et al. 2009; Reichmann 1993), enabling migrating raptors to soar for hundreds of kilometers, for example along the ridges of the Appalachian Mountains (Bohrer et al. 2012). Due to acceleration of the flow, the maximum updraft is generated at the peak of the hill. Downwind of the peak there are often areas of turbulence and sinking air which should be avoided. In Chapter 4 we use a computational fluid dynamics (CFD) model of one of our field sites to simulate the generation of ridge lift and compare this with the recorded flight of our bird. Understanding the formation and structure of lift is key to any soaring strategy (Andersson et al. 2009), and without a suitable way of modelling or directly measuring the atmosphere, we cannot test the bird's success at finding the best lift and avoiding downdrafts. Chapter 4 is therefore a feasibility study using a relatively simple landscape to determine whether similar methods could be used for more complex terrain—perhaps an urban environment. We show that on average the bird flew close to the point of maximum lift along the ridge, as predicted by the CFD analysis.

Compared to slope soaring, there has been much more interest in understanding thermalling strategies, both in biology and engineering. For autonomous UAV soaring, numerous algorithms have been designed which aim to find and maintain position in the strong thermal core (Allen 2005; Andersson et al. 2010; Cowling et al. 2009; Wharington and Herszberg 1998), however, very few have gone beyond simulations to implementation in vehicles for real flight tests (Allen and Lin 2007; Edwards and Silberberg 2010). According to Wharrington (1998), "the objective of thermal centring is to find the path that terminates in a circling manoeuvre about the thermal centre and which maximises the net lift over the course". Thermal centring is by necessity a continuous process as the core is easily lost on account of the wind drift effect. Despite the abundance of theories on the topic, it is still unknown how birds achieve this. The majority of bird thermalling studies are generally descriptive observations of thermalling flight with little analysis of subtle manoeuvring within the thermal which can only be obtained from instantaneous data (Ákos et al. 2008; Ákos et al. 2010; Cone 1962; Pennycuick 1971b; Pennycuick 1972; Pennycuick 1983; Pennycuick 1998; Shamoun-Baranes et al. 2003; Spaar 1997; Spaar and Bruderer 1996). This illustrates the value of onboard instrumentation able to measure a wide range of parameters at high sampling rates. In Chapter 7 we present a descriptive analysis of the soaring flight of our eagle using instantaneous measures of parameters which are compared with similar studies using traditional methods. We finally discuss the potential for using our data to determine what specific strategy the bird might be using to thermal successfully, and whether it is possible to detect any atmospheric cues sensed by the bird.

This thesis is structured as a set of papers, each with a self-contained introduction and discussion, though the derivation of most parameters is presented in Chapter 2 to avoid repetition. The project scope is to learn more about flight physics (with a focus on understanding soaring and gust response mechanisms), in addition to exploring the use of onboard instrumentation for analysing flight. Although the conceptual advances presented in this thesis are motivated by measurements taken from a single individual, their basis in theory gives them considerable generality. Further testing is

required before any conclusions can be extended beyond the individual steppe eagle. However, the range of behaviours studied are present in many soaring species and I hypothesise that our theoretical models—such as the physical model of wing tucking and the concept of the soaring optimisation chart for the prediction of airspeed—will be widely applicable.

Chapter 2

Instrumentation and data analysis

2.1 Introduction

The use of instrumentation units mounted on board free-flying birds has become a popular technique for biological studies of flight dynamics and behaviour (Ákos et al. 2008; Bohrer et al. 2012; Gillies et al. 2008; Gillies et al. 2011; Portugal et al. 2014; Sachs et al. 2012; Taylor et al. 2008). By using sensors similar to those found in many aviation applications and on small UAVs to record the characteristics of bird flight, analogous analysis techniques and performance measures can be applied. This has become possible due to the development of more compact and accurate instrumentation; however it is essential that the output of these sensors is understood and used appropriately.

This chapter presents the instrumentation and experimental methods used in this thesis for studying a free-flying steppe eagle (*Aquila nipalensis*), specifically with the aim of understanding the bird's response to atmospheric conditions such as turbulence and updrafts. We explore the range of parameters that can be obtained from a standard off-the-shelf instrumentation unit and highlight key limitations and

errors associated with such sensors. Off-the-shelf systems provide relatively cheap and accessible solutions but may not meet experimental requirements therefore verification of their performance is necessary.

2.2 Experiments

We flew a trained, captive, male steppe eagle for 45 separate flight tests (see Table 2.1 for morphological measurements). The bird's body mass was measured daily during the field season; other morphological measurements were made using ImageJ (National Institutes of Health, Bethesda, Maryland, USA) from a digital photograph of the bird's planform in flight with the wings outstretched in a typical soaring configuration (Figure 2.1a). The image was scaled against measurements of wing chord from a previous study using multi-station photogrammetry (Carruthers et al. 2010).

The bird was flown at several sites in the Black Mountains region of South Wales, UK during the summer of 2012. Sites were selected for suitable ridge lines running perpendicular to the wind direction on a given day (see Table 2.2 and Appendix A for the locations of each site). The bird was flown under a wide range of atmospheric conditions, but not in rain, or in winds exceeding 8ms^{-1}. The flights, which lasted between 10 and 50 minutes (in total $>$ 20 hours), all involved ridge soaring or thermalling behaviour. The bird was filmed with a Sony HDR-SR1 high-definition digital video camera. A WindMaster Pro 3-axis Ultrasonic anemometer (Gill Instruments Ltd, Hampshire, UK) was used to obtain measurements of local wind velocity. The anemometer was positioned at the top of the ridge, approximately 2m above the ground, and measured 3-axis velocities at 10Hz.

An onboard instrumentation package was mounted dorsally on the bird prior to each flight using a removable harness with Teflon ribbon straps (Marshall Direct Ltd, Lancashire, UK). The harness was worn in a rucksack-like arrangement over the back and chest, with the instrumentation positioned as close to the centre of gravity as possible (Figure 2.1b). The experimental protocol was approved by the United

States Air Force, Surgeon General's Human and Animal Research Panel and by the Oxford University, Department of Zoology, Local Ethical Review Committee, and was considered not to pose any significant risk of causing pain, suffering, damage or lasting harm to the animal involved.

measurement	
body mass	2.25–2.40 kg
aspect ratio	6.7
wing area	0.54 m^2
wing span	1.9 m

Table 2.1: Morphological measurements of the steppe eagle used in this study. Body mass was measured daily, and its range reflects the range of variation over the course of the study. Wing area, wing span, and aspect ratio are given for a typical soaring flight configuration with the wings fully outstretched. Measurements were made using IMAGEJ from a digital photograph (Figure 2.1a) of the bird's planform.

site	coordinates (dd.dd)		no. flights	wind
Hay Bluff	52.020322 N	-3.107739 W	6	W-NW
Merthyr Common	51.725977 N	-3.332133 W	14	SSW-W
Llanddewi Rhydderch	51.813242 N	-2.960578 W	10	S-WSW
Blorenge	51.803840 N	-3.061836 W	2	WNW-SE
Llangorse	51.947011 N	-3.222856 W	3	W
Great Llwgy Farm	51.946478 N	-3.222592 W	3	S or NW
Blaenavon	51.781715 N	-3.146225 W	2	NNE-ENE
Abertysswg	51.747380 N	-3.244051 W	2	W-NW
Skirrid	51.857886 N	-2.983035 W	1	W
Bryncaws	51.715363 N	-3.783703 W	2	ESE

Table 2.2: Summary of field sites where the bird was flown; latitude and longitude coordinates in decimal degrees, number of flights recorded at each site and the required wind directions for ridge soaring.

2.3 Instrumentation

Basic parameters required to observe flight performance in aviation include airspeed, attitude of vehicle and 3D position. Ideally we would like to extract a similar set of parameters from our bird. The greatest limitation for an instrumentation unit is its physical size and weight: it must weigh less than 5% of the bird's body mass and be sufficiently small and streamlined to have minimal impact on the bird's flight performance. The unit must also have sufficient logging capability to record large volumes of data at high sampling frequencies for the duration of a flight.

There are numerous instrumentation units which meet these requirements and the technology is continuously improving. With a unit built in-house, the designer has more control over the settings and any data processing, whilst off-the-shelf models are often more compact, cheaper, and are quick to implement with easy access to both the source code and logs. After reviewing the different options, we opted to use the ArduPilot Mega 2.0 (APM2) (3D Robotics, San Diego, CA).

The APM2 unit was originally designed as an autopilot for use by hobbyists in small remote controlled and autonomous aircraft. It is comprised of an Invensense 6DoF MPU-6000 inertial measurement unit (IMU), MediaTek MT3329 global positioning system (GPS), Honeywell HMC5883L 3-axis magnetometer and a MEAS (Switzerland) MS5011 variometer module (for sensor specifications see Table 2.4). All sensors are fully integrated onto the board which is run by an ATmega2650 processor. The processor uses a 12 bit analogue to digital converter (ADC) with a 5V range and logs the data to a 16MB DataFlash memory. An additional airspeed sensor consisting of a Freescale MPXV7002 pressure sensor and pitot tube is also integrated into the system. The board requires a 5V power supply for which we used a Hyperflight 240mAh SmartLiPo battery which is regulated to 5V and features a buzzer to alert the user when the battery is on, or running low. The unit was covered in HeatShrink tubing to protect it from adverse weather and damage. Combined, the board, battery and airspeed sensor are 100×45×25mm and weigh <0.075kg; this represents less than half the range of natural variation in body mass

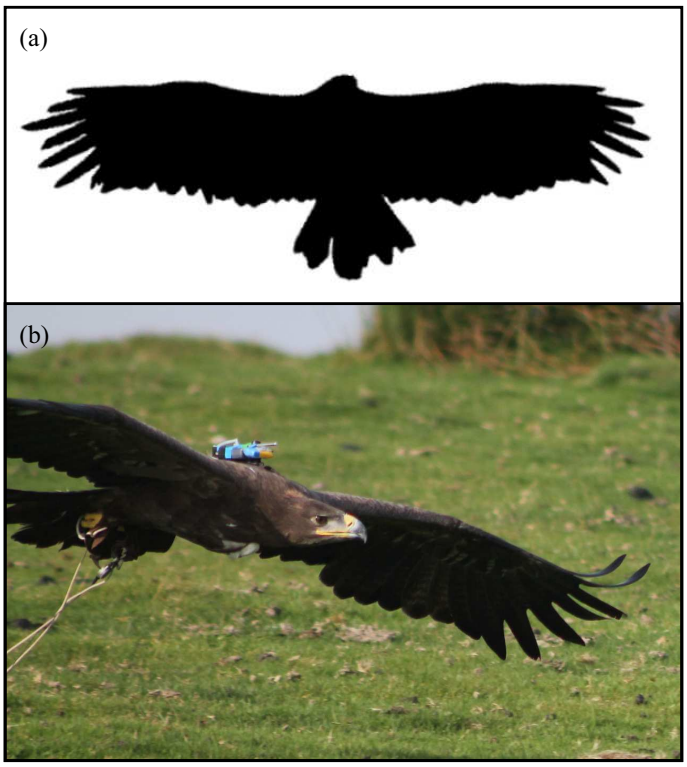


Figure 2.1: (a) Intensity thresholded digital photograph of the bird's planform taken from directly below when the bird was gliding in a typical soaring posture with its wings fully outstretched (wing span = 1.9m, from tip to tip). The irregular outline of the wings and tail reflects the state of the feathers, some of which were recently moulted. (b) Photograph showing instrumentation mounted dorsally on steppe eagle with Velcro harness

of the steppe eagle, and was always <3.3% of body mass. Observations of flights with and without onboard instrumentation indicate that the bird adapted easily to the additional loading, which made no noticeable difference to flight performance. A Marshall radio telemetry transmitter, commonly used in falconry, was attached to enable recovery of the unit if it detached from the bird during a flight. Although not the most compact of boards available, it meets all the animal welfare requirements and provides a greater range of information at a higher sampling rate than smaller models.

Another advantage of this system is that the ArduPlane firmware (version 2.28) installed on the board is open access and therefore well documented. The firmware can be customised in Arduino and C++ whilst the log files are saved as comma delimited text files which can be imported into MATLAB for data calibration, post

processing and analysis.

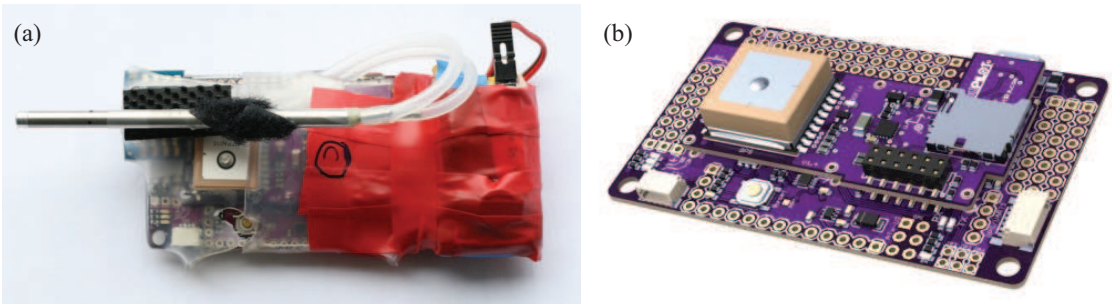


Figure 2.2: (a) Complete onboard instrumentation unit with APM2 board, pitot tube and battery pack; 100×45×25mm and weighs <0.075kg. (b) APM2 board.

Modifications to Arduino code

To log data at the high rate and accuracy required for detecting the subtle movements that characterise avian flight, modifications were made to the Arduino code. These changes were largely aimed at maximising the logging time of the board and selecting the raw data and sampling rates to log.

The majority of the original APM2 onboard processing was dedicated to running the autopilot system used for controlling an aircraft. This code was therefore redundant in a logging system and could simply be deleted.

To prevent unknown filtering and calibration of the recorded variables, where possible the raw signal was logged directly from the sensors and at the highest available sampling frequency. The final log (summarized in Table 2.3) contained raw 3-axis acceleration and angular rate data from the IMU sampled at 50Hz, 3-axis Earth magnetic field strength data from the magnetometer also at 50Hz, dynamic pressure from the airspeed sensor, barometric pressure and temperature from the variometer and GPS measurements of UTC time, latitude, longitude, altitude, satellite fix and ground speed, all logged at 10Hz.

Estimates of the board attitude in the form of roll pitch and yaw angles were

not included in the log, instead attitude was estimated using a customised extended Kalman filter based optimisation algorithm during data post processing. This reduced the amount of data recorded to the memory card and also allowed fine tuning of the Kalman filter that could not have been performed in real time.

To prevent any loss of data an overwrite function in the code was disabled. Unfortunately, given the range of parameters recorded and the high sampling frequencies required, the 16MB of memory available on the flash micro SD card limited the logging time to under 10mins; too short to record whole flights which could last up to an hour. It was not possible to simply replace the specialised memory card which was customised for recording data at high sampling rates. Instead the code was altered to store the majority of the data as short integers instead of floats or long integers, which is essentially a lossless form of data compression. In some cases this meant the variable itself had to be altered, and these changes are detailed here.

Initially we eliminated unnecessary labels in the log files by removing the parameter units and reducing the line identifiers to single letters: G for GPS data, A for pressure and temperature data and R for the raw IMU data. These line identifiers were used in MATLAB post processing to distinguish between variables.

From the GPS data, satellite fix and ground speed are < 4 significant figures and can simply be saved as short integers. However, latitude and longitude coordinates are recorded in units of decimal degrees (dd.dddd) which require long integers and at the high sampling rate of 10Hz, this consumes much of the available memory space. In Arduino programming, when variables exceed the maximum capacity of the unsigned integer, the integer "rolls over" back to its minimum capacity. As the bird is flown within a relatively small region, the coordinates can therefore be saved as unsigned short integers whilst maintaining the same resolution. Reverting the logged positional data back to conventional coordinates can be easily achieved by "unwrapping" the integer (described in Data Post-Processing). The same approach was applied to GPS altitude. UTC time, which counts in milliseconds from the start of the day, was kept as a long integer.

The original settings on the APM2 allowed direct logging of airspeed data which was calculated from raw dynamic pressure data using a calibration set by the manufacturers. This was subsequently filtered and saved as a long integer. To both save memory and ensure none of the original airspeed data was lost through over filtering, the code was altered to instead record the raw voltage signal directly from the pressure sensor as a short integer. This was then converted to airspeed during post-processing.

The temperature from the variometer is measured in degrees Centigrade, with an offset of 20°C. This is small enough to be saved as a small integer whilst the barometric pressure, measured in Pa, required a long integer.

Accelerometer and gyro logging was also modified to record the raw voltage output from the sensors prior to conversion into accelerations and angular rates. This again ensured no filtering effect was applied to the data and as the IMU signal is passed through a 12 bit ADC, short (16 bit) integers were more than sufficient to log the voltage readings.

These changes to the code resulted in an increase of logging time up to 52 minutes. This was generally sufficient given that the bird's average flight was approximately 30 minutes. For longer flights, the bird was recalled and the board switched for an empty one.

sensor	logged parameters	original settings		customised settings		
		units	size	units	size	sampling frequency
IMU	x, y, z acceleration	ms^{-2}	int 32	volts	int 16	50Hz
	x, y, z rate of angular rotation	$^{\circ}s^{-1}$	int 32	volts	int 16	50Hz
magnetometer	x, y, z magnetic field strength	mGauss	int 32	mGauss	int 16	50Hz
GPS	position	decimal	int 32	decimal	int 16	10Hz
	altitude	m	int 32	m	int 16	10Hz
	UTC time	ms	int 32	ms	int 32	10Hz
	satellite fix	0/1	byte	0/1	byte	10Hz
	ground speed	cms^{-1}	int 32	cms^{-1}	int 16	10Hz
variometer	temperature	°C	int 32	°C	int 16	10Hz
	barometric pressure	Pa	int 32	Pa	int 32	10Hz
pressure sensor	dynamic pressure	Pa	float	volts	int 16	10Hz

Table 2.3: Summary of modifications made to the logging of the sensor measurements used in this study.

sensor	sampling	units	resolution	noise	noise characteristic
accelerations	50 Hz	ms^{-2}	2.4×10^{-3}	3.9×10^{-3} / $\sqrt{Hz}$	spectral density (at 10 Hz)
angular rates	50 Hz	$^{\circ}s^{-1}$	6.1×10^{-2}	5.0×10^{-3} / $\sqrt{Hz}$	spectral density (at 10 Hz)
Earth magnetic field strength	50 Hz	gauss	1×10^{-3}	2.0×10^{-3} / $\sqrt{Hz}$	spectral density (at 10 Hz)
GPS position	10 Hz	$^{\circ}$	1×10^{-7}	$<$ 1m RMS	static test 3000 samples
GPS altitude	10 Hz	m	1×10^{-2}	$>$ 3m RMS	static test 3000 samples
dynamic pressure	10 Hz	kPa	4.9×10^{-3}	< 7.9 % RMS	full bandwidth (at 0.03 kPa)
barometeric pressure	10 Hz	mbar	1×10^{-2}	$< 2.4 \times 10^{-2}$% RMS	at 1.0213 bar
barometeric altitude	10 Hz	m	8.9×10^{-2}	$< 3.1 \times 10^{-1}$% RMS	at 67 m above MSL

Table 2.4: Specifications of the sensors used in this study. Noise characteristics are given according to the manufacturers' specifications for accelerations, angular rates and Earth magnetic field strength. The pressure transducer (dynamic pressure) we characterised ourselves in a low-turbulence wind tunnel (0.03kPa $\equiv$ 7.0ms^{-1}), and the GPS and barometer were characterised using a static test, as described in the text.

2.4 Data post-processing and sensor performance

Logged data was downloaded from the APM2 using the Mission Planner interface (3D Robotics 2012). The text files were then read into MATLAB for post processing and analysis. In this section we analyse the output from each sensor and discuss the calculation and quality of the resulting parameter estimates.

2.4.1 GPS

Post-processing

To convert the truncated GPS 3D position data, which was logged by the unit as a 16 bit integer, back into conventional coordinates, the number of times the integer "rolled over" (n) must be found. The size of an unsigned 16 bit integer is 65536; using the known starting position of the GPS unit as a reference, the precise value of n is calculated as $n = \textit{start position}/65536$. This initial reference position of the APM2 was obtained from a ground based GeoVision GPS receiver unit; small discrepancies between the receivers do not affect the accuracy of n. For flights where the bird ranged far enough such that n changed, the 'unwrap' function in MATLAB (used to correct radian phase angles when jumps between consecutive values are greater than π) was applied to the position data, after temporarily converting to radians. The data compression used to log the GPS was therefore entirely lossless, with no reduction in precision or quantisation error.

GPS tracks can be conveniently viewed in mapping software packages by creating kml files from the positional data, generated using a simple text file template with altitude entered in meters and longitude and latitude data in decimal degrees. This also provides quick verification of the above conversion to conventional coordinates.

In some analyses, the metric distance between sampled points is required. The equivalent distance of a degree in meters changes depending on the latitude. The length of a degree of latitude at our flight sites was approximately 111262.03m

whilst for longitude, it is approximately 69102.60m (CGS network 2011). These scale factors were used to convert the position data from degree minutes to metric units.

Resolution of the logged GPS latitude and longitude coordinates was 1×10^{-7} decimal degrees; when converted to metric units this corresponds to 0.069m and 0.11m respectively. This is the quantization error of the GPS position estimates.

Sensor performance

GPS error can be caused by a combination of factors including inaccurate time keeping which affects the synchronisation of satellites, and distortion of signals from atmospheric disturbances. Reflections of the satellite signals from buildings and large objects, or interference from other signals, can also reduce accuracy or in extreme cases, cause a loss of satellite fix altogether (Beard and McLain 2012; DoD Positioning, Navigation, and Timing Executive Committe 2008). The number of satellites used, receiver sensitivity and reacquisition time of the GPS unit are therefore important considerations. For this study where the bird was flying in the Welsh mountains, these error effects were considered minimal. However, because the GPS patch antenna can only detect satellites within roughly a 60° cone, the GPS error will be greatest when the bird changes bank angle as this will rapidly affect which, and how many, satellites the GPS uses to get an accurate fix. There is therefore a dilution of GPS position precision as the bird banks.

According to the manufacturer's specifications, the time required for the GPS receiver to achieve a navigation fix from a cold start is 35 seconds. Although in practise this time varies, under an open sky it was never found to be longer than two minutes. A useful feature of the APM2 board is a LED which indicates to the user when the GPS was fixed, minimising the chance of losing data at the start of a flight.

It is important to characterise the noise associated with GPS position so that realistic uncertainties can be assigned to the estimated parameters. Although abso-

lute accuracy of the location fix with respect to the actual location (static navigation accuracy) is beneficial when comparing GPS tracks with physical characteristics of the landscape, this is less important than the relative accuracy of the location fix between consecutive points which will have a large effect on parameters derived from the GPS track data, such as velocity.

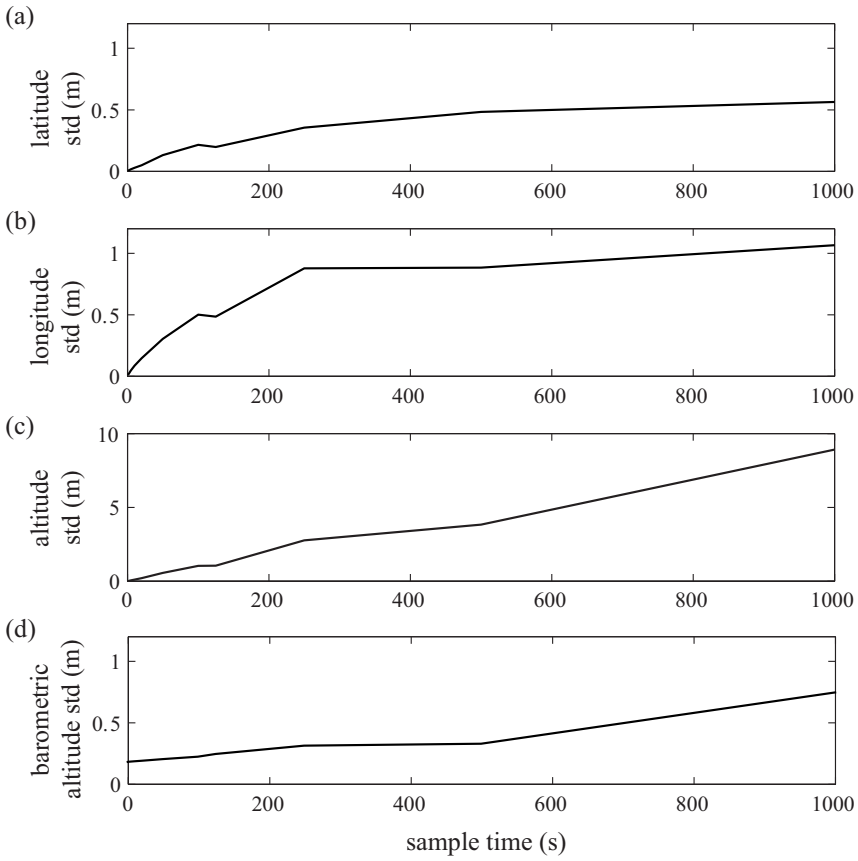


Figure 2.3: Static GPS position error analysis showing the standard deviation of (a) latitude, (b) longitude, and (c) altitude in meters against length of sample block in seconds. (d) shows the same analysis carried out for the barometer estimate of altitude. The GPS altitude (c) records an unacceptably large error and is therefore excluded from our analyses.

Static test: A static navigation test was carried out on the GPS unit to verify the accuracy of the location fix reported by the manufacturers. The instrumentation unit was positioned under open sky, away from possible sources of interference such

as buildings or pylons, and allowed to record for 20 minutes after achieving a location fix. The logged longitude, latitude and altitude data were extracted and converted into Cartesian coordinates. To characterise the error associated with GPS position for different sampling periods, the recorded data was separated into sample blocks and the mean of the standard deviations of the relative position for each block was calculated. This was repeated using a range of block sizes which varied from 1s to 1000s. The results of this static test, plotted in Figure 2.3, show that the error associated with latitude and longitude position data converges for sample sizes after 300s and is <1m for longitude and <0.5m for latitude. However the altitude error clearly continues to increase and reports a much larger standard deviation of almost 10m: although this may not mean that the altitude accuracy is poor throughout the recording, this is an unacceptably large error. The GPS altitude data is therefore discounted from the majority of our analyses, unless no barometric altitude data is available.

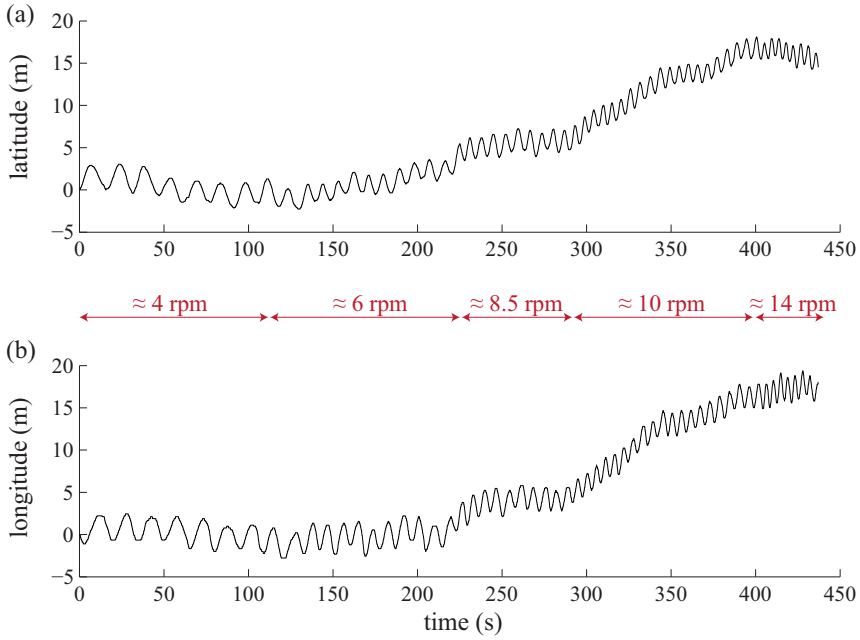


Figure 2.4: Dynamic GPS error test. Change in GPS (a) latitude and (b) longitude with time as board is rotated at increasing velocity through a fixed, circular path of radius 1.5m. As velocity increases, relative accuracy decreases. Approximate rpm velocity is shown.

Dynamic test: Although the 2D GPS data was shown to have sufficient absolute accuracy during a static test, this does not necessarily hold for dynamic performance (Stombaugh et al. 2002). We therefore used a fixture testing approach to dynamically test the accuracy of our GPS receiver. This involves attaching the instrumentation unit to a mechanical fixture that can move through a predefined path (Stombaugh et al. 2002). In this test a roundabout in a children's playground was used to rotate the unit through a known, and repeatable, circular path with radius 1.5m. The unit was rotated at increasing speed from approximately 4rpm up to 14rpm The recorded position is shown in Figure 2.4.

It is evident from Figure 2.4 that the dynamic relative accuracy is worse than the static accuracy, and that the error increases at higher speeds as the relative position drifts. The amplitude of the position varies throughout. Although it is not possible to remove this dynamic error from the data collected, during circling sections of flight where the bird is maintaining its position in a thermal, the positional accuracy of the bird relative to the air mass can be improved by eliminating both GPS drift and wind drift from the track. This method is described in full in Chapter 7. In addition to this, the circling flight of our bird occurs at both a lower frequency and larger turn radius, so the error is expected to minimal, though will be influenced by bank angle.

There is little that can be done to correct for either the static or dynamic error in this GPS position data, though it is possible to achieve better accuracy with more sophisticated arrangements such as differential global positioning systems (DGPS) which require a ground reference. Over the bird's flights however, the recorded GPS data appears reasonable and we see no unexpected jumps in the measurements from loss of satellite fix.

2.4.2 Barometric Pressure

A static sensor test was performed to characterise the pressure data measured by the onboard variometer; the sensor resolution was 1Pa and the data contained high

frequency noise with a standard deviation of 2.4Pa at a mean of 102134.68Pa (see Table 2.4).

The primary source of error in the pressure readings is due to temperature changes of the board which heats up during the flight, causing the pressure to drift. The bird's airspeed causes an opposing effect as at higher speeds, the board is cooled down by the airflow. As the board is relatively open to the atmosphere, changes in the bird's attitude can also influence the pressure readings.

Altitude

Given the GPS altitude data is unreliable, an alternative measure of the bird's altitude can be obtained from the barometric pressure following the method described in Vinh (1993).

Two basic equations govern the change of density (ρ) with altitude (h). The first is the equation of state which relates density to static pressure (p) and temperature (T):

$$p = \rho RT \tag{2.1}$$

where R is the gas constant. The second equation states that the rate of change of pressure with altitude must equal the weight of the atmosphere supported, assuming hydrostatic equilibrium (Vinh 1993):

$$dp = -\rho g dh \tag{2.2}$$

where g is gravitational acceleration. Temperature also changes with altitude, however within the troposphere the rate of change of temperature with altitude, known as Lapse rate ($L = dT/dh$), is assumed to be constant. Therefore the temperature at an altitude h above sea level can be predicted by:

$$T = T_0 + Lh \tag{2.3}$$

where T_0 is the temperature at sea level. From Equations 2.1-2.3 we can derive the relationship (Vinh 1993):

$$\frac{d\rho}{\rho} = -\Big(\frac{g}{R(T_0 + Lh)} + \frac{L}{T_0 + Lh}\Big)dh \tag{2.4}$$

Integrating Equation 2.4 from the condition at sea level gives us:

$$\rho = \rho_0\Big(1 + \frac{L}{T_0}h\Big)^{-\frac{1}{L}(\frac{g}{R} + L)} \tag{2.5}$$

where ρ_0 is density at sea level. When we substitute into Equation 2.5 the constants for the standard atmosphere $R = 287.05$, $g = 9.81\text{ms}^{-2}$ and $L = -0.06°\text{m}^{-1}$, the relationship between density and altitude becomes:

$$\frac{\rho}{\rho_0} = \Big(1 + \frac{L}{T_0}h\Big)^{4.2558774} \tag{2.6}$$

From the equation of state (Equation 2.1) this can be rewritten in terms of pressure as:

$$\Big(\frac{p}{p_0}\Big)^{0.1902632} = 1 + \frac{Lh}{T_0} \tag{2.7}$$

where p_0 is pressure at sea level. If the atmospheric conditions at sea level are known, it is then very simple to estimate the altitude from our barometric pressure data. From the MIDAS weather data (MetOffice 2012) recorded at a nearby station we can obtain a measure of MSL pressure but unfortunately only temperature at the location of the weather station, and not MSL temperature, is recorded. Given we know both the temperature at the station (T_1) and the station altitude (h_1), we can instead use the relationship in Equation 2.3 to estimate T_0:

$$T_0 = T_1 - Lh_1 \tag{2.8}$$

This is substituted back into Equation 2.7 and rearranging for h, we get the

following relationship between altitude and barometric pressure:

$$h = \left[1 - \left(\frac{p}{p_0}\right)^{0.190263}\right]\left\{\frac{T_1}{L} + h_1\right\} \tag{2.9}$$

The resulting altitude calculated from our variometer therefore has a resolution of 0.089m. The same static test used for the GPS data was performed and shows that the error associated with the barometric altitude data converges for sample sizes after 300s and is <0.5m (Figure 2.3).

Climb rate

Climb rate is the bird's rate of change of altitude. This provides an important measure of the bird's performance in updrafts. Altitude was calculated from the onboard variometer using the relationship in Equation 2.9. However, because these measurements suffer from high frequency noise, climb rate was calculated by differencing the altitude over a 1 second period rather than between consecutively sampled points, effectively performing a moving average filter.

2.4.3 Temperature

Temperature was logged from the variometer but provided little useful information as the measurement was dominated by the circuit board heating up and the cooling effect of the bird flying at high speeds, both of which mask the subtler changes in the actual atmospheric temperature at different altitudes. We had hoped to extract information on lapse rate and hence atmospheric stability from the temperature recording, but this proved unfeasible as we found no correlation between temperature and barometric altitude. The temperature measure was therefore not used in any of the data analysis.

2.4.4 Dynamic Pressure

Dynamic pressure (Δp), which represents the kinetic energy of a moving fluid, is measured by the deflection of a diaphragm in the onboard pressure transducer. One side of the diaphragm is connected to the stagnation pressure (p_t) port on the pitot tube which points directly into the on-coming airflow; this is the pressure exerted by the airflow as it is brought to rest. The other side is fed by a static pressure port (p), positioned at 90° to the stagnation port. The difference between the pressures causes the diaphragm to deflect ($\Delta p = p_t - p$). The dynamic pressure from the pressure transducer is then passed though the onboard 12 bit ADC.

To convert the logged output from the ADC back to a voltage in post processing, it must be multiplied by the system voltage (in this case 4V) and divided by the resolution of the ADC (a 12 bit ADC has 2^{12} discrete analog levels). To account for diurnal fluctuations in pressure, the initial voltage offset which was measured in zero airflow at the start of each flight, was then subtracted from the data before conversion to conventional pressure units of Pascals. The pressure transducer sensitivity is 1V/kPa; therefore the voltage is multiplied by 1×10^3 to convert to Pascals. The resulting dynamic pressure has a resolution of 4.9×10^{-3} kPa.

Airspeed

The relative speed (V_t) of a body with respect to the surrounding atmosphere is referred to as the true airspeed, which is an important parameter for studying the aerodynamic forces acting on a body. Likewise, for all practical purposes, the inertial forces experienced by the bird are dependent on velocities and accelerations relative to the earth fixed frame (Beard and McLain 2012). The vector relationship between true airspeed and the speed with respect to the inertial frame, ground speed (V_g), is:

$$V_t = V_g – V_w \tag{2.10}$$

where V_w is the wind velocity vector relative to the inertial frame (Beard and McLain 2012). We can calculate airspeed from the dynamic pressure measured by the pitot tube and pressure transducer using the compressible form of Bernoulli's equation and assuming isentropic conditions at subsonic speeds. V_t is therefore a function of air density (ρ), static and stagnation pressure (Vinh 1993):

$$V_t^2 = \frac{2kp}{(k-1)\rho}\left[\left(\frac{\Delta p}{p}+1\right)^{\frac{k-1}{k}} - 1\right] \tag{2.11}$$

where k is the ratio of specific heat ($k = 1.4$ for air). However, for our system we can assume incompressible flow, so Equation 2.11 simply becomes a linear relationship between V_t^2 and Δp (Beard and McLain 2012; Vinh 1993):

$$V_t^2 = \frac{2\Delta p}{\rho} \tag{2.12}$$

As the air density, or static temperature, cannot be obtained from the pitot tube, by convention the standard value for air density at sea level ($\rho_0 = 1.01325 \times 10^5 \mathrm{Nm}^{-2}$) is used instead. The resulting airspeed is known as the indicated airspeed V_i which is the speed of an aircraft as recorded by the onboard airspeed instrumentation, calibrated to reflect standard atmospheric conditions at sea level.

$$V_i^2 = \frac{2\Delta p}{\rho_0} \tag{2.13}$$

The indicated airspeed in Equation 2.13 includes instrumentation errors such as scale factor error; these can be corrected for by calibrating the sensor. The calibrated airspeed (V_c) for our data is therefore:

$$V_c = \sqrt{C\Delta p} \tag{2.14}$$

where C is a calibration constant that combines both a correction constant for the scale factor error and the proportionality constant $2/\rho_0$.

For any airspeed comparison, the convention is to use equivalent airspeed (V_e), which is V_c calibrated for a particular altitude and therefore takes into account variation of density and temperature. V_e is a function of incompressible dynamic pressure and is calculated by correcting V_c for compressible flow. However at low speeds when the incompressible flow assumption holds (Mach<0.3), the equivalent airspeed is assumed to be the same as the calibrated airspeed ($V_e = V_c$) (Pennycuick 2001; Vinh 1993). It is possible to compute the true airspeed from equivalent airspeed if the relative air density (ρ/ρ_0) is known (Vinh 1993):

$$V_t = \frac{V_e}{\sqrt{\rho/\rho_0}} \tag{2.15}$$

A bench calibration was performed on our instrumentation unit to calculate the calibration constant in Equation 2.14 and thereby correct for any instrumentation errors. For low speeds, the APM2 instrumentation was place in a wind tunnel with the pitot tube aligned with the direction of air flow. The wind tunnel was then run at a range of speeds from 0ms^{-1} to a maximum of $\approx$ 8ms^{-1}, and at each speed the dynamic pressure was recorded for two minutes whilst a 3-axis Ultrasonic anemometer was used to provide a reference airspeed. A high speed calibration was also carried out in a similar way using a car to reach speeds of approximately 22ms^{-1}. The calibration constant was calculated from the slope of the linear regression between the APM2 dynamic pressure and the square of the anemometer airspeed readings. As the calibration constant was not calculated at standard sea level atmospheric conditions a final correction was applied; the air density for the day and location at which the calibration was performed ($\rho_c = 1.228$kgm^{-3}) was obtained from MIDAS weather station recordings and used to correct the calibration constant for standard sea level air density ρ_0. This resulted in approximately a 0.1% correction for a recorded airspeed of 10ms^{-1}.

The resolution of the airspeed data improves as the airspeed increases according to the square root relationship between dynamic pressure and airspeed. At very low speeds ($<$ 5ms^{-1}), the resolution is consequently insufficient for reliable measure-

ments and is excluded from the data set. This has little impact on our analysis as the bird rarely flew at airspeeds less than 8ms^{-1} and was in fact not considered to be flying for speeds $< 5\text{ms}^{-1}$.

An important consideration when using a pitot tube is that it must be aligned with the airflow in order to obtain an accurate reading. We tested the effect of changing the angle of incidence of the airflow on the measurement using the wind tunnel. We found that for angles of up to 15° deviation there was no significant effect on airspeed measurements, beyond this however, the airspeed started to drop off increasingly rapidly. We were unable to test this effect at higher airspeeds ($> 8\text{ms}^{-1}$). This should therefore be a consideration when analysing the data.

The mean airspeed of 14.5ms^{-1} that we recorded during field testing was close to the mean airspeed of $15.6\pm0.32\text{ms}^{-1}$ (mean $\pm$ standard error) measured in a previous radar tracking study of $n = 52$ migrating steppe eagles (Spaar and Bruderer 1996). At 14.5ms^{-1}, the resolution of the airspeed data is $\approx 0.32\ \text{ms}^{-1}$. Therefore, although our pressure transducer provides an fair estimate of airspeed, the poor resolution and noise is a significant limitation.

2.4.5 Energy

During soaring flight, birds extract energy from updrafts in the atmosphere. By definition, soaring requires an increase in the 'total energy' of the bird—simply gaining altitude by converting kinetic energy to potential energy, for example by performing a pull up manoeuvre, is not soaring (Pennycuick 2002). Total energy, or rate of change of energy, is therefore an important measure for quantifying the performance of bird flight. Conversion between kinetic and potential energy is never perfect in reality as some energy is always lost due to drag.

Total energy (E_t) is the sum of both kinetic energy (E_k) and potential energy

(E_p) which are defined as:

$$E_k = \tfrac{1}{2}mV^2 \tag{2.16}$$

$$E_p = mgh \tag{2.17}$$

where m is mass of the bird, V is equivalent airspeed, g is gravitational acceleration and h is the altitude. Note it is essential that airspeed and not ground speed is used in the above equation as only when speed is relative to the air mass is kinetic energy exchangeable with potential energy (Pennycuick 2002). Similar to the previous calculation of climb rate, to calculate the rate of change of total energy ($\dot{E}_t$), total energy was differenced over 1s to mitigate some of the high frequency noise from both the altitude and airspeed data.

2.4.6 IMU data

Before the IMU data was calibrated or analysed, an initial transformation was applied to the 3-axis accelerometer, magnetometer and gyro data to convert the measurements to a conventional right-handed axis system in the body frame of reference with the x-axis aligned approximately with the longitudinal axis of the bird's body and the z-axis pointing ventrally (Figure 2.5).

Magnetic field strength

The 3-axis digital compass, or magnetometer, uses Anisotropic Magnetoresistive (AMR) technology to record the strength and direction of the Earth's magnetic field vector by measuring the change in resistance of the AMR elements which is proportional to the angle of incidence of the magnetic field (Renaudin et al. 2010). Although the continual development of inexpensive and small magnetometers has enabled their use in increasingly diverse applications, including our avian backpack, the sensors suffer from reduced accuracy due to both instrumentation errors and

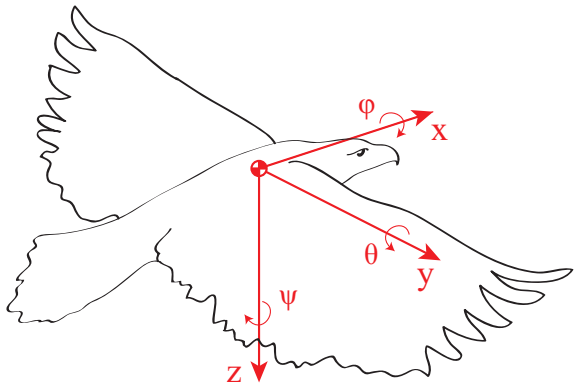


Figure 2.5: Conventional right-handed axis system in the bird's body frame of reference. Directions of roll (ϕ), pitch (θ) and yaw (ψ) rotations respectively about the x, y & z-axes are also shown. The measurements recorded by the IMU in the IMU fixed reference frame are transferred to the body frame by 2 rotations.

errors from magnetic perturbations. Calibration of the sensors is therefore essential in order to achieve reliable heading measurements.

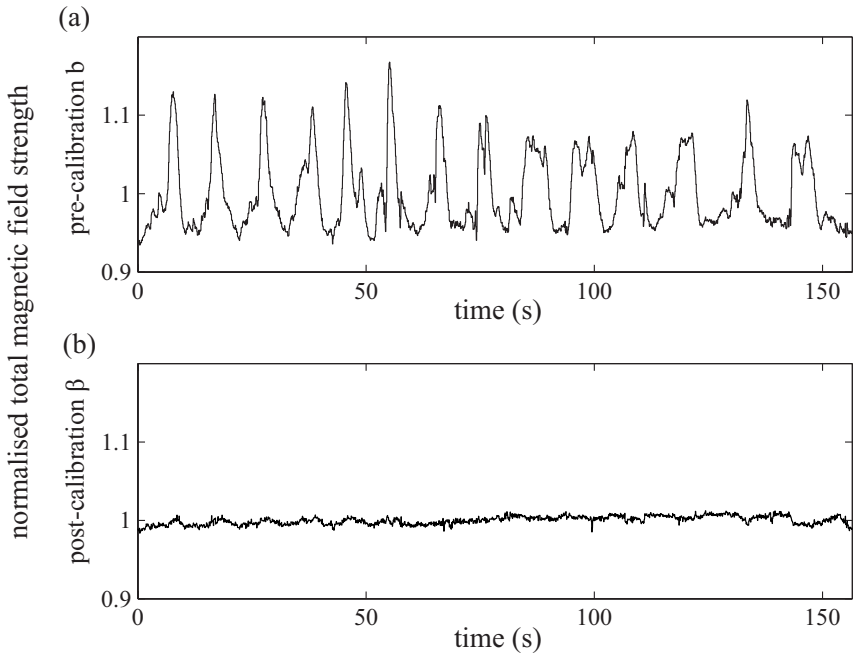


Figure 2.6: Total magnetic field strength for a section of the bird's flight when circling in a thermal, normalised by mean magnetic field strength. (a) Pre-calibration b: The plot shows clear periodicity in the magnitude of the magnetic field as the birds heading changes, highlighting the need for calibration of the magnetometer data. (b) Post-calibration β: The magnetic field strength is approximately constant within expected noise tolerances

In the ideal case, the magnitude of the measured Earth magnetic field vector should be constant in all sensor orientations. The locus of the readings from the three axes should therefore describe a perfect sphere, with radius equal to the Earth's magnetic field strength (Renaudin et al. 2010). However, in reality the measurements are corrupted by various errors which distort the sphere, principally by either adding a sensor bias to the data which shifts the centre of the sphere from the origin, or a scale factor error. Although it is possible for the HMC5883L unit to perform some onboard calibration, inspection of the flight data shows large fluctuations (up to approximately 20%) in the magnitude of the Earth magnetic field vector, see Figure 2.6. There is therefore a clear need for further calibration to be applied during post processing.

Sensor bias errors are time invariant offsets (δ) along each axis which are caused by a combination of small errors in the fabrication of the AMR elements and by hard iron distortions from permanent magnetic fields generated by other ferromagnetic materials on the instrumentation unit (Gebre-Egziabher et al. 2001; Renaudin et al. 2010).

Sources of scale factor errors are sensitivity non linearities of the AMR elements across the measurement range and soft iron distortions. Soft iron distortions are due to materials on the instrumentation unit which generate magnetic fields depending on their alignment within the Earth magnetic field lines, consequently the effect of these distortions changes with the orientation of the sensor. Effectively, the result of scale factor errors is to apply a gain constant (λ) to each axis of the sensor which distorts the ideally spherical locus of measurement points to an ellipsoidal shape.

In addition to these main sources of error, magnetometers may also suffer from misalignment error due to non orthogonality which results in cross coupling of the magnetic field axes, however, in most applications the sensor alignment is assumed to be perfect (Gebre-Egziabher et al. 2001) and we will not include a correction for it here. We also do not account for the temperature dependence of the sensors.

Based on the errors discussed above, a suitable mathematical model which forms

the foundation of many magnetometer calibration algorithms is:

$$\boldsymbol{\beta} = (\boldsymbol{\lambda}\mathbf{b} - \boldsymbol{\delta}) - \boldsymbol{\epsilon} \tag{2.18}$$

where $\boldsymbol{\beta}$ is the true, error free, magnetic field vector in Cartesian coordinates $[\beta_x, \beta_y, \beta_z]$, $\mathbf{b}$ is the measured magnetic field vector in the IMU axes $[b_x, b_y, b_z]$, $\boldsymbol{\lambda}$ is the scale factor error correction which is a diagonal matrix $[\lambda_x, \lambda_y, \lambda_z]$, $\boldsymbol{\delta}$ represents the sensor bias error vector $[\delta_x, \delta_y, \delta_z]$, and $\boldsymbol{\epsilon}$ is the sensor measurement noise vector $[\epsilon_x, \epsilon_y, \epsilon_z]$ which is assumed to be white Gaussian.

By normalising the magnetic field vector relative to the mean field strength, the radius (r) of the magnetometer vector locus sphere will be one, in the ideal case where the Earth's magnetic field strength is constant. Radius is calculated by:

$$(\lambda_x b_x - \delta_x)^2 + (\lambda_y b_y - \delta_y)^2 + (\lambda_z b_z - \delta_z)^2 = r \tag{2.19}$$

It is therefore possible to find values of parameters $\boldsymbol{\lambda}$ and $\boldsymbol{\delta}$ that satisfy Equation 2.19 where $r = 1$. This is achieved using a non-linear least squares optimisation process to determine the optimal parameter values such that the error sum of squares of the difference between the estimated locus radius (r_{est}) and the ideal radius of 1, was minimised. For the optimisation process to converge on the global optimum, and not on a local minimum, initial parameter estimates were carefully selected. We used initial values of 0 for the bias error ($\boldsymbol{\delta}$) and mean magnetic field strength (approx. 300milli-Gauss) for the scale factor error ($\boldsymbol{\lambda}$). Due to variation in the Earth's magnetic field strength between days and at different locations, calibration values of scale factor and bias were re-calculated for each flight.

Numerous approaches to magnetometer calibration have been trialled, both for in-flight and post processing applications. The most traditional technique is the swinging calibration where the sensor is rotated between known headings to estimate the scale factor and bias errors (Renaudin et al. 2010; Wahdan et al. 2013). However this method is limited to 2-axis systems and requires both that the plat-

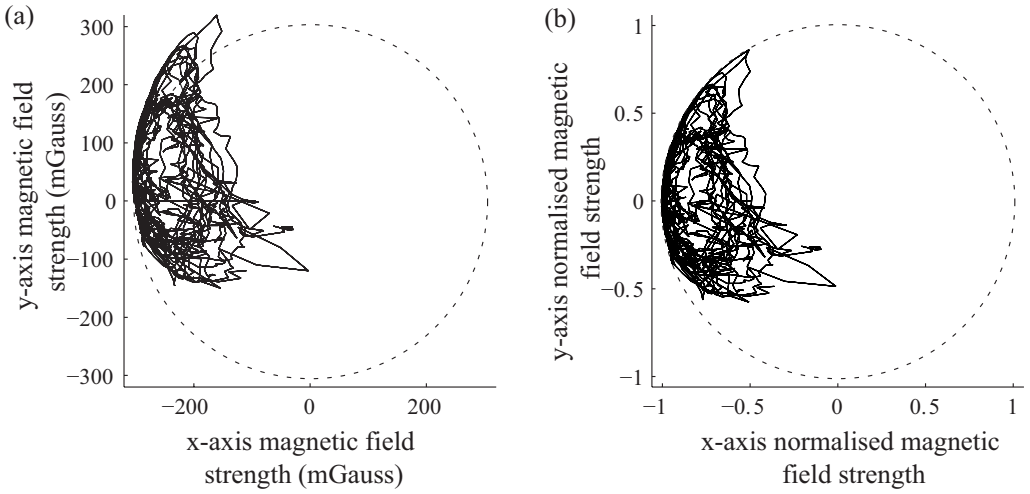


Figure 2.7: (a) Raw 2D magnetic field strength plotted for a 160s section of thermalling flight. Dotted lines represent a sphere with radius equal to mean magnetic field strength. (b) Normalised 2D magnetometer data for same section of flight after calibration. Dotted lines represent a sphere with radius of 1.

form is held level during calibration and that the user rotates through pre-defined external measures of heading which limits its use for some applications. Alternatively, there has been some development of real-time algorithms which require no user involvement, however these depend on knowledge of the device attitude from the accelerometers and gyros (Wahdan et al. 2013). Recently, the more common approach is to use ellipsoidal fitting, a variation of which we have described above, which is based on the error-free magnetic field locus being spherical. Although this is location dependant and requires a fairly large sample of data covering a range of headings, it is suitable for use in post processing applications and requires no external heading reference. The results of this calibration method are shown in Figures 2.6 & 2.7, which illustrate the reduction in both scale factor and bias error after calibration for a section of the bird's circling flight.

Angular rates

The three orthogonal rate gyros measure the angular rate of rotation of the instrumentation unit in the body reference frame $(\omega_x, \omega_y, \omega_z)$. The gyros sample at 50Hz, with a full scale range of $\pm 2000^{\circ}\text{s}^{-1}$. The analogue voltage signal is run through

a 12 bit ADC before being logged to the dataflash memory as a 16bit integer. The recorded voltage is converted to conventional units during post processing in MATLAB using the sensitivity factor of 16.4LSB/($^\circ s^{-1}$) specified in the data sheet (InvenSense 2011). This results in an angular rate resolution of 0.06$^\circ s^{-1}$.

Calibration of the gyro sensors is essential to correct for systematic bias which can cause cumulative errors. Gyros, particularly MEMS designs, typically suffer from both random noise and systematic bias errors such as angular white noise, angular random walk, scale factor and misalignment errors (Looney 2010; Quan et al. 2015).

Gyro bias was initially calculated from a static test where the board was held stationary and the mean value recorded along each axis calculated; theoretically the gyros should report 0$^\circ s^{-1}$ in this situation. This bias calibration was repeated at the beginning of each flight when the instrumentation unit was left stationary during the time required for the GPS unit to acquire satellite fix. The 3-axis gyro offsets (ranging from -1.54 to 3.89 $^\circ s^{-1}$) were calculated for each board used and subtracted from the final data set, however, it should be noted that the gyro zero bias also drifts over time with temperature and motion so although the data is improved, it is not error free and further correction is often required for calculating values such as attitude.

To ensure there were no scale factor error effects, the gyro data was verified using a rotary stage (Aerotech ABRT) which spun the gyro around its 3 axes over a range of speeds. The recorded angular rates were compared with recordings from the rotary stage. It was found that for all boards and all axes, gyro error was $<0.7\%$ of the recorded angular rate (maximum regression slope = 1.007 at 1000$^\circ s^{-1}$).

Accelerations

As with the gyros, the signals from the IMU accelerometers are fed through the 12 bit ADC and logged on the dataflash. Accelerations are sampled at 50Hz with full

scale range ±8g (78.5ms^{-1}) and corresponding sensitivity and resolution 4096LSB/g and 2.4×10^{-3}ms^{-1} respectively.

Calibration of the accelerometers is also required to correct for scale factor and offset errors. The same method was used as outlined previously for the magnetometer data, where the radius of the locus sphere described by the three accelerometer axes should be equal to gravitational acceleration (g=9.81ms^{-2}).

Although the inertial instrumentation was positioned as close as possible to the average position of the centre of mass of the bird, it could not have coincided exactly, because the centre of mass falls inside the bird's body. It follows that the accelerations sensed by the accelerometers during rigid body motion would have included additional contributions due to the angular velocity and angular acceleration of the body, proportional to the displacement of the accelerometers from the centre of mass. In the absence of measurement error, the accelerations $[a_x, a_y, a_z]$ sensed at an arbitrary point on a rigid body are given by the equations:

$$\begin{aligned} a_x &= \alpha_x + (-\omega_z^2 - \omega_y^2)d_x + (-\dot{\omega}_z + \omega_x\omega_y)d_y + (\dot{\omega}_y + \omega_x\omega_z)d_z \\ a_y &= \alpha_y + (\dot{\omega}_z + \omega_x\omega_y)d_x + (-\omega_z^2 - \omega_x^2)d_y + (-\dot{\omega}_x + \omega_y\omega_z)d_z \\ a_z &= \alpha_z + (-\dot{\omega}_y + \omega_x\omega_z)d_x + (\dot{\omega}_x + \omega_y\omega_z)d_y + (-\omega_x^2 - \omega_y^2)d_z \end{aligned} \tag{2.20}$$

where $[\alpha_x, \alpha_y, \alpha_z]$ is the acceleration at the centre of mass, $[\omega_x, \omega_y, \omega_z]$ is the angular velocity, $[\dot{\omega}_x, \dot{\omega}_y, \dot{\omega}_z]$ is the angular acceleration, and $[d_x, d_y, d_z]$ is the displacement of the IMU from the centre of mass (Stengel 2004). These equations are linear in $[d_x, d_y, d_z]$, and it is therefore possible to estimate the mean displacement $[\bar{d}_x, \bar{d}_y, \bar{d}_z]$ over all $i \in 1...n$ samples for a given flight as the least squares solution to the matrix

equation (Gillies et al. 2011; Reynolds et al. 2014a):

$$\begin{bmatrix} a_{x,1} \\ a_{y,1} \\ a_{z,1} \\ \vdots \\ a_{x,n} \\ a_{y,n} \\ a_{z,n} \end{bmatrix} = \begin{bmatrix} 1 & 0 & 0 & (-\omega_{z,1}^2 - \omega_{y,1}^2) & (-\dot{\omega}_{z,1} + \omega_{x,1}\omega_{y,1}) & (\dot{\omega}_{y,1} + \omega_{x,1}\omega_{z,1}) \\ 0 & 1 & 0 & (\dot{\omega}_{z,1} + \omega_{x,1}\omega_{y,1}) & (-\omega_{z,1}^2 - \omega_{x,1}^2) & (-\dot{\omega}_{x,1} + \omega_{y,1}\omega_{z,1}) \\ 0 & 0 & 1 & (-\dot{\omega}_{y,1} + \omega_{x,1}\omega_{z,1}) & (\dot{\omega}_{x,1} + \omega_{y,1}\omega_{z,1}) & (-\omega_{x,1}^2 - \omega_{y,1}^2) \\ \vdots & \vdots & \vdots & \vdots & \vdots & \vdots \\ 1 & 0 & 0 & (-\omega_{z,n}^2 - \omega_{y,n}^2) & (-\dot{\omega}_{z,n} + \omega_{x,n}\omega_{y,n}) & (\dot{\omega}_{y,n} + \omega_{x,n}\omega_{z,n}) \\ 0 & 1 & 0 & (\dot{\omega}_{z,n} + \omega_{x,n}\omega_{y,n}) & (-\omega_{z,n}^2 - \omega_{x,n}^2) & (-\dot{\omega}_{x,n} + \omega_{y,n}\omega_{z,n}) \\ 0 & 0 & 1 & (-\dot{\omega}_{y,n} + \omega_{x,n}\omega_{z,n}) & (\dot{\omega}_{x,n} + \omega_{y,n}\omega_{z,n}) & (-\omega_{x,n}^2 - \omega_{y,n}^2) \end{bmatrix} \begin{bmatrix} \bar{\alpha}_x \\ \bar{\alpha}_y \\ \bar{\alpha}_z \\ \bar{d}_x \\ \bar{d}_y \\ \bar{d}_z \end{bmatrix} + \begin{bmatrix} \gamma_{x,1} \\ \gamma_{y,1} \\ \gamma_{z,1} \\ \vdots \\ \gamma_{x,n} \\ \gamma_{y,n} \\ \gamma_{z,n} \end{bmatrix} \tag{2.21}$$

where $[\gamma_{x,1}, \gamma_{y,1}, \gamma_{z,1}, ..., \gamma_{z,n}]^T$ is a vector of residuals whose sum of squares is minimized by the solution $[\bar{\alpha_x}, \bar{\alpha_y}, \bar{\alpha_z}, \bar{x}, \bar{y}, \bar{z}]^T$, with T as the matrix transpose.

We solved this matrix equation separately for each flight, using the instantaneous acceleration and instantaneous angular velocity sensed by the IMU as $[a_{x,i}, a_{y,i}, a_{z,i}]$ and $[\omega_{x,i}, \omega_{y,i}, \omega_{z,i}]$, respectively, and using central differencing to estimate the instantaneous angular acceleration $[\dot{\omega}_{x,i}, \dot{\omega}_{y,i}, \dot{\omega}_{z,i}]$ from the instantaneous angular velocity. The fitted parameters $[\bar{\alpha_x}, \bar{\alpha_y}, \bar{\alpha_z}]$ estimate the mean acceleration at the centre of mass over the whole flight, and can be interpreted as regression intercepts. The fitted parameters $[\bar{d}_x, \bar{d}_y, \bar{d}_z]$ estimate the mean displacement of the IMU from the centre of mass, and can be interpreted as regression slopes. In effect, then, we are regressing the acceleration sensed by the IMU on those combinations of angular velocity and angular acceleration that are expected to be linearly related to the sensed acceleration by virtue of the IMU's unknown—but still possible to estimate—displacement from the centre of mass.

It can be seen by comparing this matrix equation with the preceding set of simultaneous equations that the instantaneous acceleration at the centre of mass $[\alpha_{x,i}, \alpha_{y,i}, \alpha_{z,i}]$ is estimated as:

$$\begin{bmatrix} \alpha_{x,i} \\ \alpha_{y,i} \\ \alpha_{z,i} \end{bmatrix} = \begin{bmatrix} a_{x,i} \\ a_{y,i} \\ a_{z,i} \end{bmatrix} - \begin{bmatrix} (-\omega_{z,i}^2 - \omega_{y,i}^2) & (-\dot{\omega}_{z,i} + \omega_{x,i}\omega_{y,i}) & (\dot{\omega}_{y,i} + \omega_{x,i}\omega_{z,i}) \\ (\dot{\omega}_{z,i} + \omega_{x,i}\omega_{y,i}) & (-\omega_{z,i}^2 - \omega_{x,i}^2) & (-\dot{\omega}_{x,i} + \omega_{y,i}\omega_{z,i}) \\ (-\dot{\omega}_{y,i} + \omega_{x,i}\omega_{z,i}) & (\dot{\omega}_{x,i} + \omega_{y,i}\omega_{z,i}) & (-\omega_{x,i}^2 - \omega_{y,i}^2) \end{bmatrix} \begin{bmatrix} \bar{d}_x \\ \bar{d}_y \\ \bar{d}_z \end{bmatrix} \tag{2.22}$$

This will tend to underestimate the required correction for the sensed accelerations, because the estimates of the mean displacement of the IMU from the origin of the bird's axis system are effectively regression slopes, so will be asymptotically biased towards zero in the presence of any error in the measurements of angular velocity and angular acceleration that were used to form the predictor variables. In fact, the IMU was estimated to be ≤ 29 mm from the centre of mass in the x- and y-directions, and ≤ 37 mm above the centre of mass in the z-direction. These estimates seems reasonable, if a little on the low side perhaps. Nevertheless, the effect of making this correction will be to reduce a known source of systematic error in our measurements of the bird's acceleration, and for this reason alone, the correction is worthwhile. The same correction should also serve to reduce measurement errors associated with rotation of the IMU with respect to the bird's axis system, as occur, for example, during flapping (i.e. to correct for accelerations sensed by the IMU as a result of the bird's non-rigid body motion).

2.5 Derived quantities

In the previous section the parameters that can be directly extracted from the raw, onboard instrumentation measurements were discussed, all of which are commonly used in aeronautics from commercial aircraft to gliders or UAV's. A number of additional quantities which are extremely useful for exploring the mechanisms and strategies of bird flight, can also be obtained from the data set and are derived here.

2.5.1 Data fusion for state estimation

Individually, sensors inherently suffer from a range of errors, as discussed above. However, it is possible to improve parameter estimates by combining the data from multiple sensors, thereby reducing the error. This is an extremely widely used technique in many fields, particularly for autonomous vehicle control. The type of data fusion typically used in autopilots for real time kinematic state estimation (Barton 2012a) of autonomous vehicles is often known as an attitude and heading reference system (AHRS) which can range from basic proportional controls to complex non-linear estimators.

For this study we chose to implement an open source, extended Kalman filter (EKF) based state estimation algorithm which was originally designed for use on small UAV's (Barton 2012a) and consequently makes use of similar sensors and dynamic models as our bird mounted instrumentation unit. The SUAS algorithm written by Barton, provides a basic 7-state estimation of vehicle attitude (in terms of four quaternions which can be simply converted to Euler angles—roll, pitch and yaw) and three gyro biases. We customised the code for our data set and included a correction for magnetic inclination. A possible future development of the code would be to include additional states such as wind velocity or altitude.

The underlying theory of the AHRS and the implementation of the algorithm is described in Appendix B. For more detail refer to Barton (2012a) or the original SUAS code (Barton 2012b).

Examining the results of the AHRS algorithm, the Euler angles appear to generate a realistic estimate of the bird's attitude whilst flying. A simple simulation of the bird was created which provided a reality check, ensuring that the Euler angles did not drift, resulting in situations such as the bird flying backwards or upside down. These animations were also qualitatively compared with the video footage recorded during flights and showed good similarity. However, we expect the accuracy of our state estimates, which are dependent on the sensor performance, to change depending on the system dynamics—i.e. rapid manoeuvres may not be recorded as

accurately as smooth gliding flight. The results from an example flight are shown in Figure 2.8.

2.5.2 Load factor

The instantaneous total load factor (N_t, colloquially the 'g-load') experienced by the bird is defined as the total acceleration at the centre of mass divided by the gravitational acceleration ($g = 9.81\text{ms}^{-2}$):

$$N_t = \frac{1}{g}\sqrt{\alpha_x^2 + \alpha_y^2 + \alpha_z^2} \tag{2.23}$$

The load factor is a standard quantity in aeronautics and has the useful property that $N_t = 1$ at equilibrium, when the total aerodynamic force vector is equal and opposite to the weight of the bird (i.e. directed vertically) (Reynolds et al. 2014a).

2.5.3 $\mathbf{SC}_L$

At shallow glide angles, the lift vector (i.e. the component of the total aerodynamic force vector that is perpendicular to the relative airflow) is itself close to the vertical. In this case, the load factor is approximately equal to the instantaneous lift of the bird (L) divided by its body weight (W). We may therefore make use of the approximation $L \approx N_t W$ to rewrite the standard lift equation:

$$L = \frac{1}{2}\rho V^2 S C_L \tag{2.24}$$

as:

$$SC_L \approx \frac{2N_t W}{\rho V^2} \tag{2.25}$$

where ρ is the air density, V is the airspeed, S is the total lifting surface area, and C_L is the mean section lift coefficient. The quantity SC_L is a function of flight morphology and angle of attack, and so measures the net effect of the bird's

instantaneous flight configuration on the lift that it produces. Hence, although we are unable to use our measurements of SC_L to separate the effects of changing wing and tail area from the effects of changing wing and tail angle of attack, we are able to use our measurements of SC_L to identify the net effect of these control inputs upon the bird's flight. It should be noted, however, that the approximation in Equation 2.25 breaks down if the bird is not in a shallow glide (Reynolds et al. 2014a).

2.5.4 Wind velocity

An approximation of the bird's instantaneous wind velocity (V_w) can be made from the simple vector relationship between wind velocity, ground velocity (V_g) and the bird's velocity relative to the air (airspeed, V_a):

$$V_w = V_g - V_a \tag{2.26}$$

We use the bird's track angle, calculated from the GPS position data, to estimate the direction of V_g. The corresponding magnitude is simply the GPS ground speed measurement. Similarly, V_a is formed from the pitot tube airspeed measurement and the estimate of yaw angle calculated using the AHRS algorithm.

For our set of flights, there is a strong correlation between the mean estimated wind velocity and the mean anemometer wind measurements (N= 32, $p < 0.0005$, $R^2 = 0.39$). Errors are introduced to our instantaneous wind velocity estimate primarily from the airspeed sensor which is affected by the angle of the on-coming airflow. We note that only the simple 2D case using just the horizontal velocity components is considered here.

2.6 Discussion

From our onboard instrumentation unit, which was used to record over 20 hours of free-flight from our steppe eagle, we have extracted a set of parameters which are used throughout this thesis to characterise the bird's flight and explore the mechanisms it uses. The accuracy and reliability of the data from each sensor has been discussed with the aim of highlighting common considerations for any instrumentation unit, such as the importance of sensor calibration, centre of mass corrections and understanding the limitations of the recorded data.

A sample section of the bird's flight (flight 8 in Appendix C and Figure 2.9) is shown in Figure 2.8 to illustrate a typical set of results obtained from the unit. Some key features which are explored in the following chapters are highlighted. At point 1 we see the bird take off. Both between points 2 & 3 and 5 & 6, the bird is clearly climbing up the ridge, circling most likely in a thermal (see Chapter 7). This is matched by the bank and yaw angle estimates and SC_L is consistently high, suggesting wing area is near its maximum as we would expect during slow circling to maximise the lift generated. Airspeed remains relatively consistent in comparison to ground speed which oscillates as the bird circles and changes from flying in a head to tail wind. Between points 3 & 4 the bird is generally slope soaring and gaining altitude or gliding (see Chapters 4, 5 & 6) along the ridge line with sections of flapping and the occasional tuck which is identified from spikes in the load factor and from the transient drops in SC_L as wing area decreases (see Chapter 3). On average the bird's airspeed is higher than when circling which is consistent with the generally lower values of SC_L. Finally, at point 6 the bird performs a steep dive before landing. This is characterised by the rapid reduction in altitude combined with high ground and airspeeds, a drop in SC_L and large pitch angles.

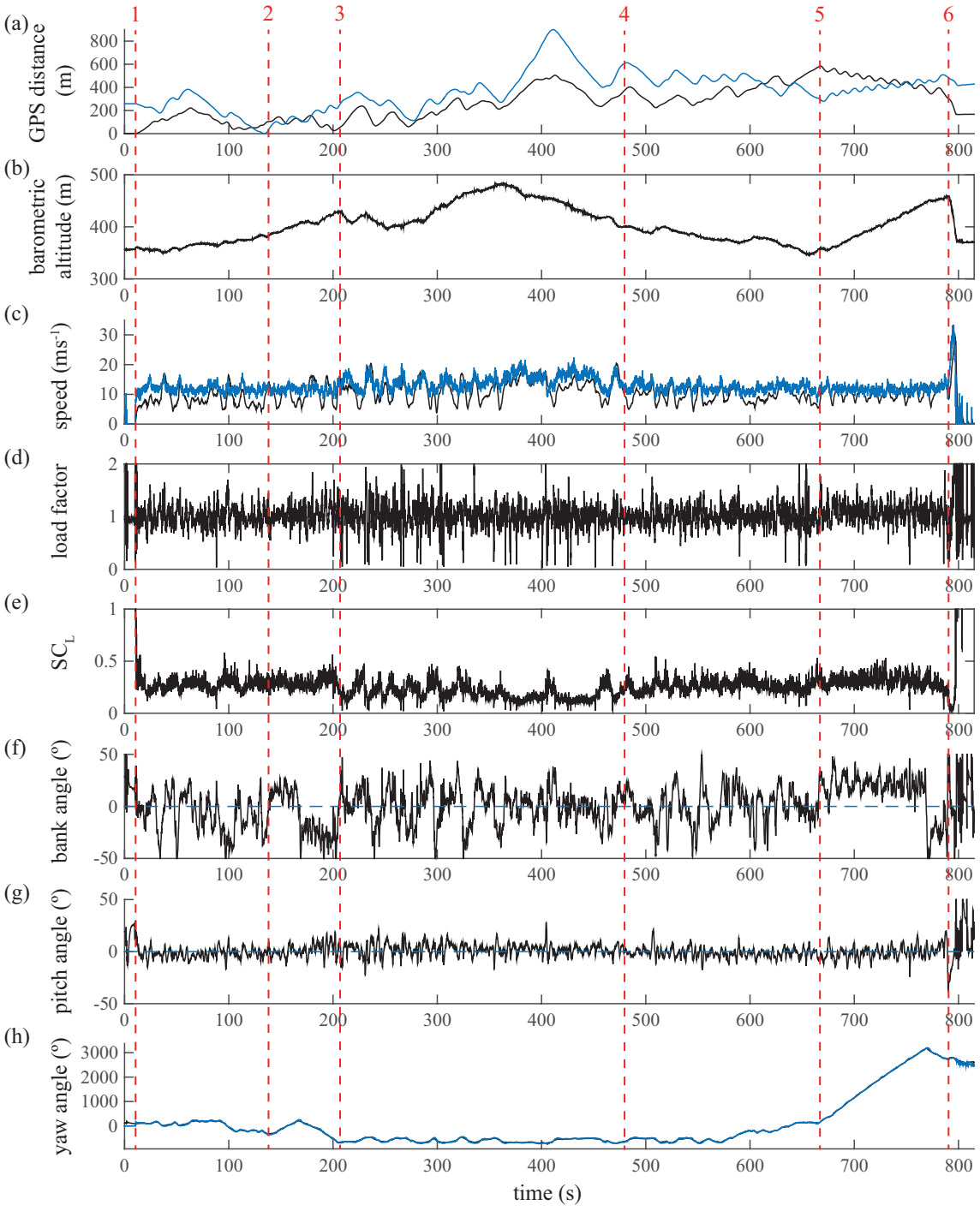


Figure 2.8: Example set of data for the 13 minute flight in Figure 2.9. (a) GPS distance after position data converted to meters and minimum value subtracted. Black: x-distance and Blue: y-distance. (b) Barometric altitude. (c) Black: GPS ground speed. Blue: airspeed. (d) Load factor (e) SC_L. (f) Bank angle. (g) Pitch angle. (h) Blue: yaw angle. Black: heading calculated from GPS position data. See text for description of points 1-6 (red-dashed lines) which highlight key characteristics of the bird's flight

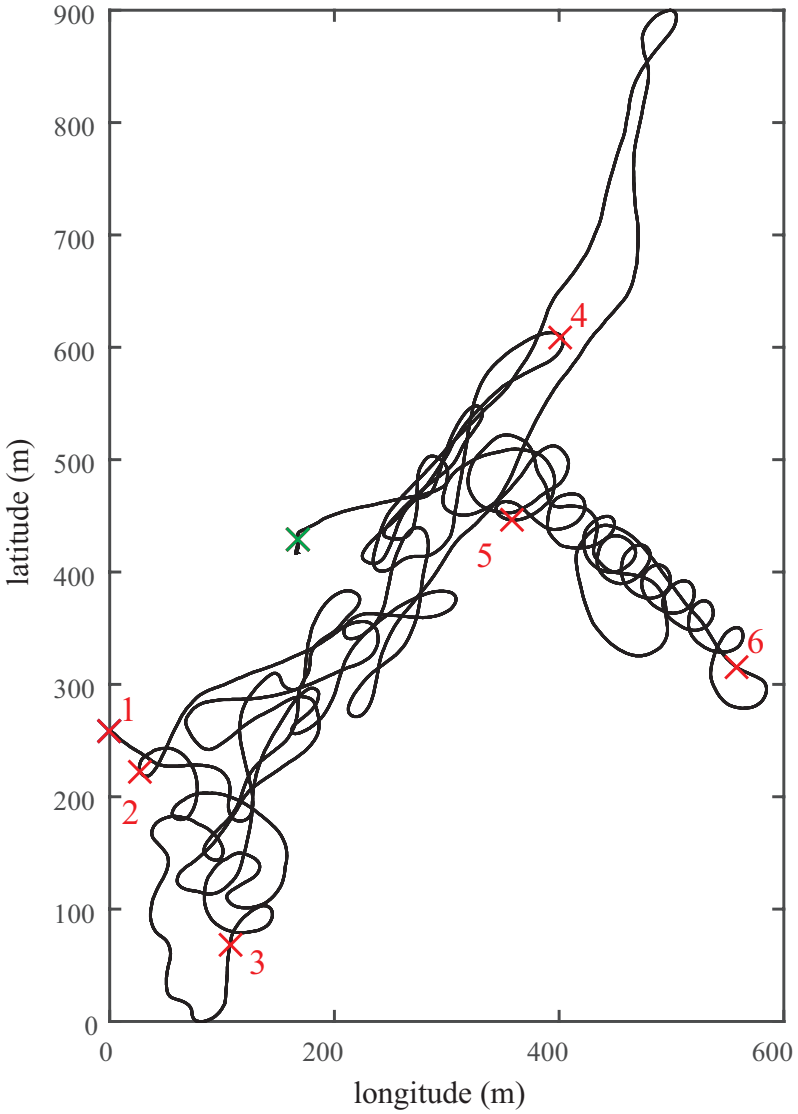


Figure 2.9: Example GPS position data for the section of flight results shown in Figure 2.8 with corresponding labels. Flight consists of both ridge soaring and thermalling. Point 1: start of flight. Green-cross: end of flight.

Chapter 3

Wing tucks are a response to atmospheric turbulence in the soaring flight of the Steppe Eagle *Aquila nipalensis*

Originally published as:

Reynolds, K. V., Thomas, A. L. R. & Taylor, G. K. (2014). Wing tucks are a response to atmospheric turbulence in the soaring flight of the Steppe Eagle *Aquila nipalensis*. *J. R. Soc. Interface.* 11. DOI: 10.1098/rsif.2014.0645

Revised 9^{th} July 2015

Abstract

Turbulent atmospheric conditions represent a challenge to stable flight in soaring birds, which are often seen to drop their wings in a transient motion that we call a tuck. Here we investigate the mechanics, occurrence, and causation of wing tucking in a captive Steppe Eagle (*Aquila nipalensis*), using ground-based video and onboard inertial instrumentation. Statistical analysis of 2594 tucks, identified automatically from 45 flights, reveals that wing tucks occur more frequently under conditions of higher atmospheric turbulence. Furthermore, wing tucks are usually preceded by transient increases in airspeed, load factor and pitch rate, consistent with the bird encountering a headwind gust. The tuck itself immediately follows a rapid drop in angle of attack, caused by a downdraft or nose-down pitch motion, which produces a rapid drop in load factor. Positive aerodynamic loading tends to elevate the wings, and the resulting aerodynamic moment must therefore be balanced in soaring by an opposing musculoskeletal moment. Wing tucking presumably occurs when the reduction in the aerodynamic moment caused by a drop in load factor is not met by an equivalent reduction in the applied musculoskeletal moment. We conclude that wing tucks represent a gust response precipitated by a transient drop in aerodynamic loading.

3.1 Introduction

One of the most impressive features of birds is their ability to fly in atmospheric conditions that would keep a light aircraft grounded. Most recent research on avian flight stability has treated the airframe as fixed (Sachs 2005a; Sachs 2005b; Sachs 2007; Sachs 2009; Sachs and Moelyadi 2010; Taylor and Thomas 2002; Thomas and Taylor 2001), but birds differ fundamentally from fixed-wing aircraft in the way in which their flexible, neuromuscularly controlled airframe responds to atmospheric turbulence. As Wilbur Wright first observed, a bird pitched up by a gust "immediately lowers its wings much below its body" (Wright 1900). We call this type of motion a wing tuck (Gillies et al. 2011), which we define as a manoeuvre in which a soaring bird rapidly pulls its wings down beneath the level of the body, before spreading them back up into a gliding configuration (Figure 3.1a; Supplementary Video 1 (Reynolds et al. 2014b)). This motion is distinct from a wingbeat (Figure 3.1b; Supplementary Video 2 (Reynolds et al. 2014b)), because at no point are the wings are raised above the level of the body. Furthermore, the extent to which the wings are pulled down beneath the body varies considerably between tucks. Wing tucks are a common and phylogenetically widespread behaviour among large soaring birds, having been described in New World vultures (*Cathartidae*) (Wright 1900), Old World vultures, kites and eagles (*Accipitridae*) (Gillies et al. 2011; Hankin 1913), and storks (*Ciconiidae*) (Hankin 1913). Indeed, wing tucks are a sufficiently common behaviour in certain soaring species, notably the New World vultures, that they are used as a taxon-specific identification character in some ornithological handbooks (Sibley 2003).

Birds fly predominantly in the surface boundary layer of the atmosphere, where turbulence is strongly influenced by surface conditions, including terrain and temperature (Rohli and Vega 2011). There are two main sources of atmospheric turbulence: mechanical and thermal. Mechanical turbulence is caused by friction as air flows over the surface of the Earth. Wind speeds decrease nearer the surface as the effects of surface friction increase, which creates wind shear (Rohli and Vega 2011).

This shear produces rotating air motions, or eddies, on a large scale: other things being equal, the greater the wind speed, the greater the mechanical turbulence that is generated. Other factors influencing mechanical turbulence include the surface roughness, and the height of obstructions which deflect and mix the airflow (Jacobson 2005). In contrast, thermal turbulence is caused by buoyancy effects (Jacobson 2005). Under unstable atmospheric conditions, uneven heating of the Earth's surface generates large circulation systems called thermals, where rising warm air is replaced by colder air drawn in at the bottom of the thermal column. Thermal turbulence increases with the intensity of surface heating and the degree of atmospheric instability, which is related to temperature lapse rate (Forest encyclopedia 2008). In addition, thermals actually magnify the vertical mixing caused by mechanical turbulence (Jacobson 2005). These two distinct sources of atmospheric turbulence present obvious challenges to flight stability and control, but they also provide the opportunity and energy source for soaring flight. It follows that soaring birds have to be able to cope with turbulence in order to soar, and we hypothesise that their wing tucks represent a response to this.

Wing tucks have previously been interpreted as a deliberate mechanism for restoring pitch equilibrium following a gust perturbation (Wright 1900), as an active mechanism for gaining airspeed prior to a flat glide or dive (Hankin 1913), and as an active mechanism for alleviating gust loads (Gillies 2010; Gillies et al. 2011). However, none of these hypotheses has yet been tested conclusively. Here we use ground-based video and onboard inertial instrumentation (Gillies et al. 2011) to analyse the mechanics, occurrence, and causation of wing tucking in the steppe eagle (*Aquila nipalensis*) (Hodgson) — a typical thermal-soaring migrant (Meyburg et al. 2012; Spaar 1997; Spaar and Bruderer 1996). We use these data to detect the occurrence of wing tucks automatically, and to identify the changes in the motion state of the bird that characteristically precede and accompany wing tucks. We then use standard model selection techniques (Burnham and Anderson 2002) to investigate the statistical relationship between the rate of wing tucking and several environmental predictors of atmospheric turbulence. This analysis allows us to identify the

environmental parameters that best predict the rate at which wing tucking occurs in flight. Finally, we analyse the causation of wing tucking, making use of our inertial measurements to do so. Together, these analyses provide strong evidence that wing tucks occur in response to atmospheric turbulence, as well as offering insight into the mechanistic and functional basis of wing tucking.

3.2 Materials and Methods

3.2.1 Experiments

We used the same trained, captive, male Steppe Eagle over 45 separate flight tests (see Table 3.1 for morphological measurements). The bird's body mass was measured daily during the flight season; other morphological measurements were made using ImageJ (National Institutes of Health, Bethesda, Maryland, USA) from a digital photograph of the bird's planform in flight with the wings outstretched in a typical soaring configuration (Figure 3.2). The image was scaled against measurements of arm wing chord made in flight in a previous study using multi-station photogrammetry (Carruthers et al. 2010).

measurement	
body mass	2.25–2.40 kg
aspect ratio	6.7
wing area	0.54 m^2
wing span	1.9 m

Table 3.1: Morphological measurements of the Steppe Eagle used in this study. Body mass was measured daily, and its range reflects the range of variation over the course of the study. Wing area, wing span, and aspect ratio are given for a typical soaring flight configuration with the wings fully outstretched (Figure 3.2).

The bird was flown at several sites in the Black Mountains region of South Wales, UK during the summer of 2012. Sites were selected according to wind direction to

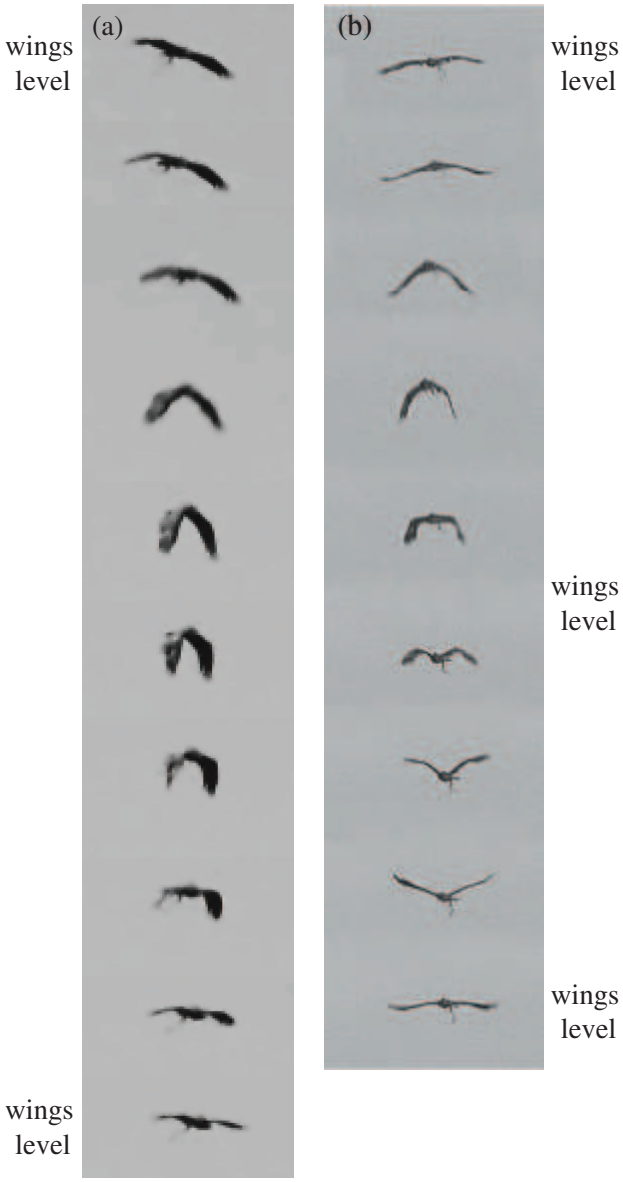


Figure 3.1: (a) Sequence of video frames showing a typical wing tuck. (b) Sequence of video frames showing a typical wingbeat, which is easily distinguishable from a tuck on account of its shorter period, and the fact that the wings are raised above the body before being returned to a level configuration. Time interval between frames: 0.033s. Complete animations of these video sequences are provided as Supplementary Videos 1 and 2 (Reynolds et al. 2014b).

provide a soarable ridge line facing into the wind on the day of the test. The bird was flown under a wide range of atmospheric conditions, but was not flown in rain, or in winds exceeding 8ms^{-1}. The flights, which lasted between 10 and 50 minutes, all involved ridge soaring or thermalling behaviour. The bird was filmed with a

Sony HDR-SR1 high-definition digital video camera. A WindMaster Pro 3-axis Ultrasonic anemometer (Gill Instruments Ltd, Hampshire, UK) was used to obtain measurements of local wind velocity. The anemometer was positioned at the top of the ridge, approximately 2m above the ground, and measured 3-axis velocities at 10Hz.

An onboard instrumentation package was mounted dorsally on the bird prior to each flight using a removable harness with Teflon ribbon straps (Marshall Direct Ltd, Lancashire, UK). The harness was worn in a rucksack-like arrangement over the back and chest, with the instrumentation positioned as close to the centre of gravity as possible. The experimental protocol was approved by the United States Air Force, Surgeon General's Human and Animal Research Panel and by the Oxford University, Department of Zoology, Local Ethical Review Committee, and was considered not to pose any significant risk of causing pain, suffering, damage or lasting harm to the animal involved.

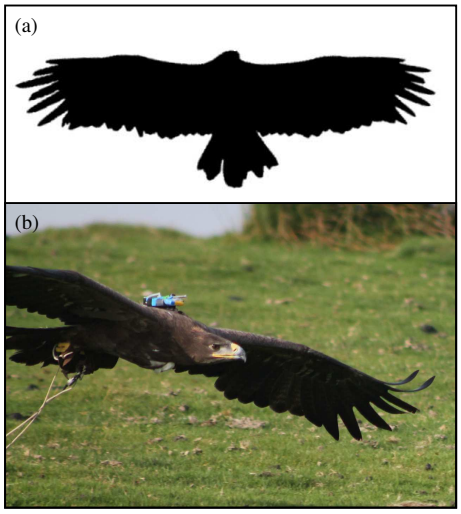


Figure 3.2: (a) Thresholded digital photograph of the bird's planform taken from directly below when the bird was gliding in a typical soaring posture with its wings fully outstretched (wing span = 1.9m, from tip to tip). The irregular outline of the wings and tail reflects the state of the feathers, some of which were recently moulted. (b) Photograph of bird showing instrumentation unit mounted dorsally.

3.2.2 Instrumentation

The onboard instrumentation comprised an ArduPilotMega2 (3D Robotics, San Diego, CA) board running customized software, containing an inertial measurement unit (IMU), global positioning system (GPS), thermometer, barometer, and pitot tube. The equipment gave up to 50 minutes of continuous recording time and weighed <0.075kg with battery. This represents less than half the range of natural variation in body mass, and was always <3.3% of body mass (see Table 3.1). Observations of flights with and without onboard instrumentation indicate that the bird adapted easily to the additional loading, which made no noticeable difference to flight performance—even in turbulent conditions. The IMU logged measurements of 3-axis linear acceleration, angular rotation rate, and Earth magnetic field data at 50Hz, defined in a right-handed axis system fixed with respect to the measurement unit, with the x-axis aligned approximately with the longitudinal axis of the bird's body and the z-axis pointing ventrally. Position, altitude and ground speed were obtained at 10Hz from the GPS. Temperature, barometric pressure, and airspeed were also recorded at 10Hz. Airspeed was calculated from the differential pressure measured by the pitot tube, using a calibration factor that was determined in a wind tunnel prior to field tests. The mean airspeed of 14.5ms^{-1} that we recorded is reassuringly close to the mean airspeed of 15.6±0.32ms^{-1} (mean ± standard error) measured in a previous radar tracking study of n=52 migrating Steppe Eagles (Spaar and Bruderer 1996).

sensor	sampling	units	resolution	noise	noise characteristic
accelerometers	50 Hz	ms^{-2}	2.4×10^{-3}	3.9×10^{-3} / $\sqrt{\mathrm{Hz}}$	spectral density (at 10 Hz)
rate gyros	50 Hz	$^{\circ}\mathrm{s}^{-1}$	6.1×10^{-2}	5.0×10^{-3} / $\sqrt{\mathrm{Hz}}$	spectral density (at 10 Hz)
pitot tube	10 Hz	kPa	3.9×10^{-3}	< 7.9 % RMS	full bandwidth (at 0.03 kPa)
anemometer	10 Hz	ms^{-1}	1.0×10^{-3}	< 1.5 % RMS	full bandwidth (at 12 ms^{-1})

Table 3.2: Specifications of the sensors used in this study. Noise characteristics are given according to the manufacturers' specifications, except for the pitot tube, which we characterised ourselves in a low-turbulence wind tunnel.

The performance specifications of the sensors which we use in this study are given in Table 3.2. During a typical wing tuck, the wings are returned to their initial position within approximately 0.35s of the time at which they begin to drop (Figure 3.1a; Supplementary Video 1). This is 3.5 times the sampling interval of the airspeed measurements, and 17.5 times the sampling interval of the inertial measurements, which demonstrates that the sampling rate of the instrumentation is more than sufficient to characterise even this quickest portion of the tuck manoeuvre. The transient body motions that are associated with wing tucking occur over a much longer period (> 6s), so will obviously be well characterised at this sampling rate.

3.2.3 Data processing

Although the inertial instrumentation was positioned as close as possible to the average position of the centre of mass of the bird, it could not have coincided exactly, because the centre of mass falls inside the bird's body. It follows that the accelerations sensed by the accelerometers during rigid body motion would have included additional contributions due to the angular velocity and angular acceleration of the body, proportional to the displacement of the accelerometers from the centre of mass. The accelerations $\{a_x, a_y, a_z\}$ sensed at an arbitrary point on a rigid body are:

$$a_x = \alpha_x + (-r^2 - q^2)x + (-\dot{r} + pq)y + (\dot{q} + pr)z \tag{3.1}$$

$$a_y = \alpha_y + (\dot{r} + pq)x + (-r^2 - p^2)y + (-\dot{p} + qr)z \tag{3.2}$$

$$a_z = \alpha_z + (-\dot{q} + pr)x + (\dot{p} + qr)y + (-p^2 - q^2)z \tag{3.3}$$

where $\{\alpha_x, \alpha_y, \alpha_z\}$ is the acceleration at the centre of mass, $\{p, q, r\}$ is the angular velocity, $\{\dot{p}, \dot{q}, \dot{r}\}$ is the angular acceleration, and $\{x, y, z\}$ is the displacement of the IMU from the centre of mass (Stengel 2004). These equations are linear in $\{x, y, z\}$, and the IMU's average displacement from the bird's centre of mass was therefore estimated from a least squares solution of these equations using the inertial

measurements themselves (see Chapter 2 (Gillies et al. 2011; Reynolds et al. 2014b)). The resulting parameter estimates were then used to correct the measurements of the sensed acceleration, so as to reduce the effect of any systematic measurement errors introduced by the placement of the IMU.

The instantaneous total load factor (N_t, colloquially the 'g-load' experienced by the bird) was defined as the total acceleration at the centre of mass divided by the gravitational acceleration ($g = 9.81\text{ms}^{-2}$):

$$N_t = \frac{1}{g}\sqrt{\alpha_x^2 + \alpha_y^2 + \alpha_z^2} \tag{3.4}$$

The load factor is a standard quantity in aeronautics and has the useful property that $N_t = 1$ at equilibrium, when the total aerodynamic force vector is equal and opposite to the weight of the bird (i.e. directed vertically).

At shallow glide angles, the lift vector (i.e. the component of the total aerodynamic force vector that is perpendicular to the relative airflow) is itself close to the vertical. In this case, the load factor is approximately equal to the instantaneous lift of the bird (L) divided by its body weight (W). We may therefore make use of the approximation $L \approx N_t W$ to rewrite the standard lift equation:

$$L = \frac{1}{2}\rho U^2 S C_L \tag{3.5}$$

as:

$$SC_L \approx \frac{2N_t W}{\rho U^2} \tag{3.6}$$

where ρ is the air density, U is the airspeed, S is the total lifting surface area, and C_L is the mean section lift coefficient. The quantity SC_L is a function of flight morphology and angle of attack, and so measures the net effect of the bird's instantaneous flight configuration on the lift that it produces. Hence, although we are unable to use our measurements of SC_L to separate the effects of changing wing and tail area from the effects of changing wing and tail angle of attack, we are able to use our measurements of SC_L to identify the net effect of these control

inputs upon the bird's flight. It should be noted, however, that the approximation in Equation 3.6 breaks down if the bird is not in a shallow glide.

3.2.4 Automatic tuck identification

Wing tucks were identified automatically in Matlab from the inertial data that we collected, using a method first developed in (Gillies 2010) but explained fully below. We used the z-acceleration traces (Figure 3.3) as the basis of this identification procedure, because the dorso-ventral acceleration of the bird provides a reliable indicator of whether the wings are open or closed. In the first instance, we manually identified 80 tucks from approximately 20 minutes of video data, sampled over 6 days. The inertial measurements corresponding to these manually-identified tucks were then used to construct a template for the accompanying pattern of changes in the z-acceleration sensed by the IMU (Figure 3.4a). We aligned the z-acceleration traces for each manually identified tuck with respect to the point of peak z-acceleration, taking this reference to define the time $t = 0$s. The mean instantaneous z-acceleration over all of the aligned tucks was then used to form the template.

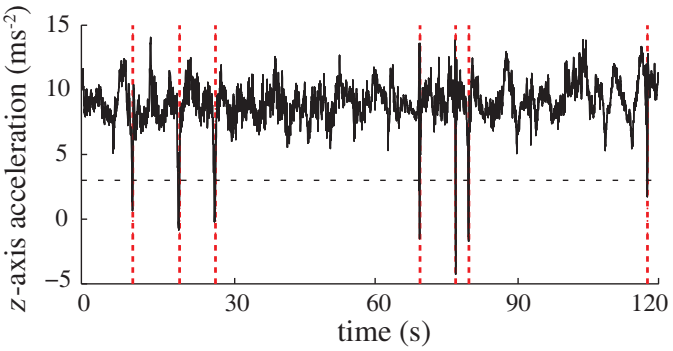


Figure 3.3: Plot of measured z-acceleration against time for one randomly chosen section of flight lasting 2 minutes. The 7 wing tucks (red dashed lines) occurring in this sequence were identified automatically as sections of flight for which the correlation with the tuck template (Figure 3.4) was >0.45, and during which the magnitude of the z-acceleration dropped below 3ms^{-2} (blue dashed line).

Wing tucks were identified automatically by searching the data for peaks in the cross-correlation function between the tuck template and the z-acceleration data sensed by the IMU. Peaks in the cross-correlation function occurring within 0.25s of each other were assumed to represent a single tuck, with the chosen interval corresponding to the width in the template of the spike in the z-acceleration (Figure 3.4). We identified tucks as sections of flight for which the correlation with the tuck template was >0.45, and during which the magnitude of the z-acceleration dropped below $3ms^{-2}$. In arriving at this combination of threshold values, we tested the automatic tuck identification algorithm on the sections of data that we had analysed manually, with the objective of maximizing the number of wing tucks that the algorithm identified whilst keeping the number of false positives zero. Having optimized the algorithm accordingly, our automatic procedure successfully identified >80% of the tucks that we had identified ourselves from the 20 minutes of video data that we analysed manually. Thus, we chose threshold values that gave a sample Type I error rate of 0.8 and a sample Type II error rate of zero in respect of the wing tucks identified automatically during these 20 minutes of video data.

To ensure that occasional wingbeats were not mistaken for wing tucks, a flapping template (Figure 3.4b) was created using the same method, and the results compared. Any ambiguous records were checked manually by exploring the raw inertial data, and were easily distinguished as either a wingbeat or a wing tuck (compare Figures 3.4a and 3.4b). In total, we identified 2594 tucks over the entire dataset, giving an overall identified tuck rate of approximately 2.2 identified tucks per minute. Given that the thresholds that we set for the automatic tuck-identification algorithm resulted in a sample Type I error rate of 0.8 for the manually analysed video data, the true tuck rate is expected to have been closer to 2.7 tucks per minute. In any case, it is clear that wing tucks are a common feature of soaring flight in our Steppe Eagle.

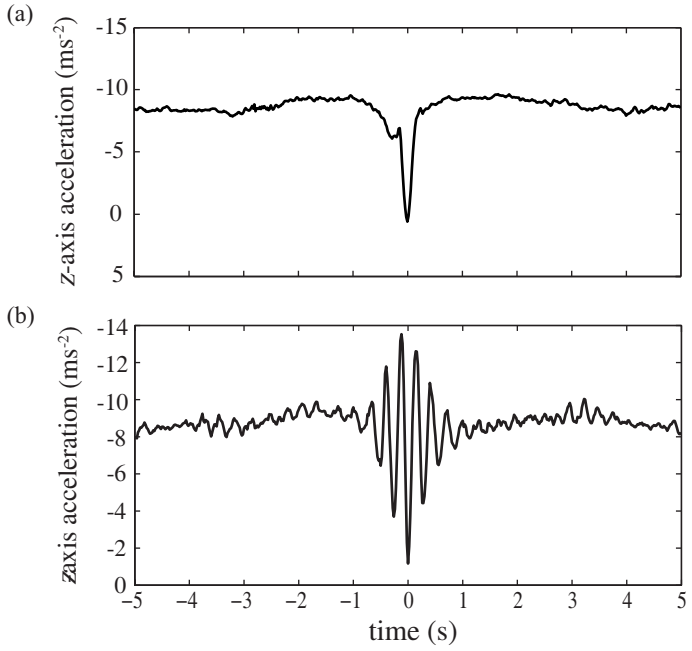


Figure 3.4: (a) Tuck template, defined as the time history of the z-acceleration (α_z), averaged over the 80 tucks which we manually identified from the ground-based video, aligned with respect to the peak in α_z at $t = 0$s. (b) Flapping template, defined as the time history of α_z, averaged over 69 manually identified wingbeats and aligned similarly. Because wingbeats rarely occur singly, the template shows multiple peaks, each representing a single wing beat; the attenuation of the wingbeats to either side of the middle wingbeat is an effect of the averaging method used to construct the template, but has no adverse effect upon wingbeat identification. Wingbeat frequency is approximately 3Hz. Note that, in contrast to the tuck template, the wingbeat template shows approximately symmetric, rather than one-sided, changes in α_z.

3.2.5 Environmental predictors of atmospheric turbulence

In order to test whether the rate of wing tucking was related to atmospheric turbulence, we computed the identified tuck rate for each flight (f) and defined several environmental predictors of atmospheric turbulence that could be measured for each flight. Other things being equal, we would expect the level of mechanical turbulence to increase with increasing mean wind speed, as a result of the greater wind shear strength (see Introduction). Mean wind speed estimates ($\bar{V}$) were obtained from the MetOffice Integrated Data Archive System (MIDAS) land and marine surface station data (MetOffice 2012) for the Credenhill weather station near Hereford. At an altitude of 76m, this weather station is 21.6km from the nearest flying site and

54.0km from the farthest, so the MIDAS measurements only provide a general indication of how windy it was during a given flight. We averaged the three hourly MIDAS recordings closest to the time at which the bird flew, to give an estimate of the mean wind speed for each flight. We also included our anemometer measurements of the mean local wind speed on the ridge ($\bar{v}$) in the analysis. The fluctuating local wind velocity components provide a direct measure of atmospheric turbulence levels at the time of the flight, which were summarized by the standard deviation of the anemometer readings ($\tilde{v}$). The MIDAS measurements of mean wind speed and the anemometer measurements of local wind speed on the ridge merely characterise the wider atmospheric conditions pertinent to a given flight, and should not be interpreted as estimates of the mean wind speed or turbulence at the precise time and location at which the bird was flying.

The mean altitude above sea level ($\bar{A}$) at which the bird flew was computed from the onboard GPS altitude log. Flight altitude is dependent on the height of the terrain, but other things being equal, the bird is expected to have flown higher on days with greater thermal activity, and hence greater buoyant production of turbulence. Furthermore, the structure of mechanical turbulence changes with altitude, as eddy size becomes larger with increasing altitude, and so for both reasons we would expect mean altitude above sea level to be positively correlated with mean atmospheric turbulence levels. The size of the orographic obstruction generating this mechanical turbulence was approximated as the height above sea level (r) of the ridge where the bird was flown, which was taken from Ordnance Survey maps; the larger the obstruction, the greater the wind shear, and hence the higher the expected level of mechanical turbulence. Regional Atmospheric Soaring Prediction (RASP), a forecasting tool designed for glider pilots to evaluate soaring conditions (Scorer 2012), was also used to estimate thermal updraft strength, averaged over the three predictions closest to the time of flight.

3.3 Results

3.3.1 Mechanics of wing tucking

The video sequences in Figure 3.1 show a typical wing tuck (Figure 3.1a; Supplementary Video 1), and a typical wingbeat for comparison (Figure 3.1b; Supplementary Video 2). The bird starts the tuck with its wings outstretched in the gliding position. It then begins to drop its wings down beneath the body by rotating them leading-edge down about the shoulder joint. The wings are held in their dropped position momentarily before the recovery stroke, in which the wings are rotated leading-edge up, brought in and raised back to the level of the body. Thus, whereas the wings are raised above the level of the body during a wingbeat, this does not happen during a wing tuck. Nevertheless, the time taken for the whole tuck is about 50% longer than the time taken to go from wings level to wings level during the equivalent downstroke-upstroke sequence in a normal wingbeat (Figure 3.1). The accompanying changes in total load factor, airspeed, pitch rate, and SC_L are summarized for all 2594 identified tucks in the 2D histogram plots shown in Figure 3.5, which represent the frequency density of the values taken by each variable at each time step over a period of 5s either side of time $t = 0$s (i.e. over a 10s window beginning 5s before the point of peak z-acceleration). Figure 3.6 plots the raw data from 5 randomly selected tucks to provide an indication of how the pattern of variation during a single wing tuck reflects the overall pattern of variation shown in the 2D histograms (Figure 3.5).

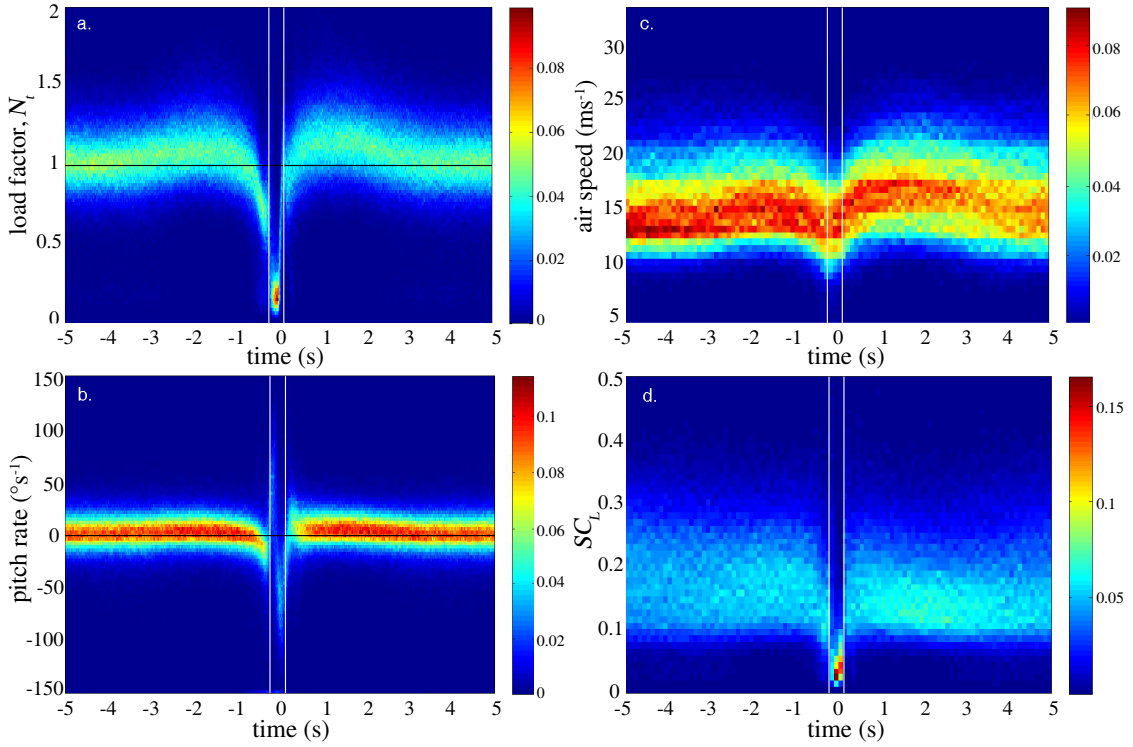


Figure 3.5: Two-dimensional histograms for all 2594 automatically identified tucks showing the temporal variation in the frequency density of (a) instantaneous total load factor, N_t; (b) pitch rate q, signed positive in a nose-up direction, (c) airspeed, U; and (d) SC_L, representing the product of wing area (S) and lift coefficient (C_L). All times are referenced to the point of minimum load factor $N_z = -\alpha_z/g$ for each tuck at $t = 0$s, as calculated from the z-component of acceleration (α_z). The colour bars to the right of each histogram relate the colour of each point on the histogram to the proportion of the sampled tucks at that time to which it corresponds. The data were binned into 100 bins for load factor and pitch rate, which were sampled at 50Hz; 50 bins were used for airspeed and SC_L, which were sampled at a lower rate of 10Hz. The approximate beginning and end of the tucking movement of the wings, inferred from the discontinuities in the distributions for load factor and SC_L, is denoted by the vertical white lines.

In the period leading up to a wing tuck, the bird typically averages close to an equilibrium flight condition, with a mean instantaneous load factor of $N_t \approx 1$ (Figure 3.5a) and a mean instantaneous pitch rate of approximately zero at $t = -5.0$s (Figure 3.5b). The wing tuck itself typically occurs between $t = -0.225$s and $t = 0.125$s, as is obvious from the discontinuity and drop-off in the SC_L plot (Figure 3.5d), and also from the corresponding decline in total load factor at this time (Figure 3.5a). These changes in wing loading are accompanied by a distinct drop in airspeed (Figure 3.5c) and by a sharp nose-down pitching motion (Figure 3.5b). The

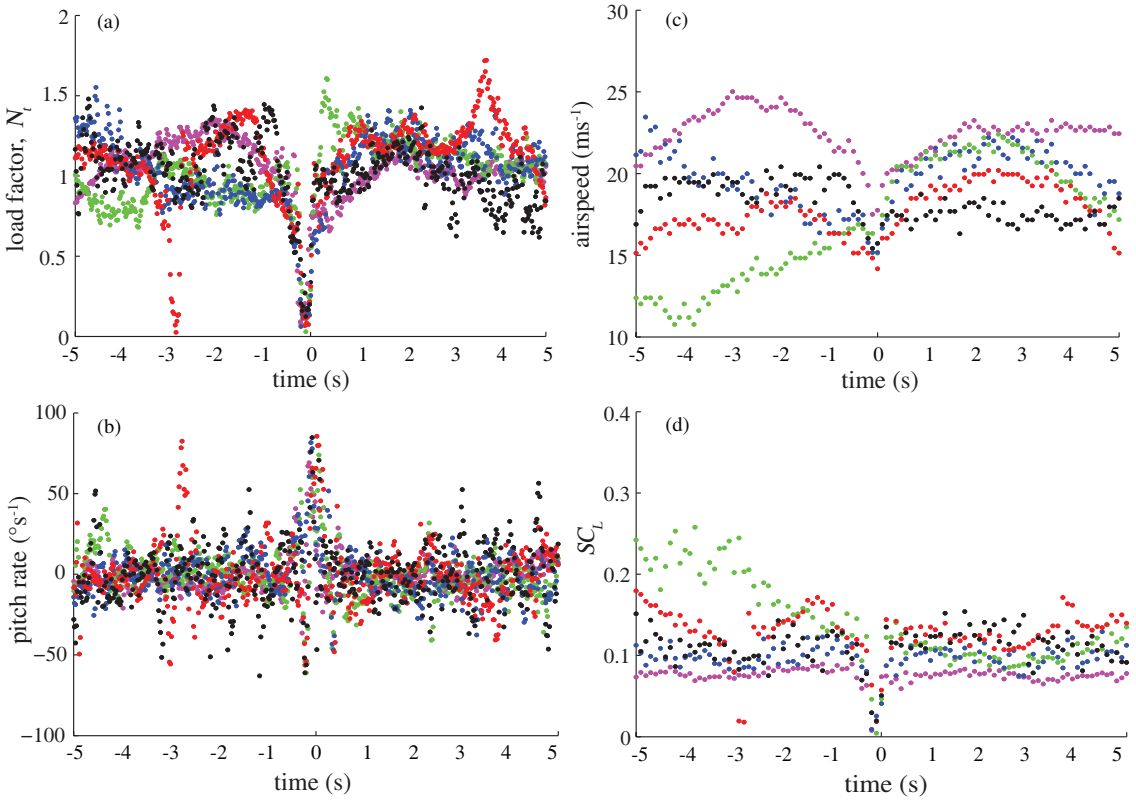


Figure 3.6: Data for 5 individual tucks randomly selected from the 2594 automatically identified tucks, showing (a) instantaneous total load factor, N_t; (b) pitch rate q, signed positive in a nose-up direction, (c) airspeed, U; and (d) SC_L, representing the product of wing area (S) and lift coefficient (C_L).

wings are re-opened shortly after $t = 0$s, whereupon loading is rapidly re-established (Figure 3.5a), airspeed increases (Figure 3.5c) and the bird starts to pitch nose-up again (Figure 3.5b). The 0.35s duration of the tuck estimated from the inertial data (Figure 3.5) closely matches the duration of the wing tucking movement seen in the video sequence in Figure 3.1a. Following the tuck, there is typically a second surge in airspeed (Figure 3.5c) and load factor (Figure 3.5a), which occurs between $t \approx 0.125$s and $t \approx 3$s. By $t = 5s$, the bird has returned to an equilibrium flight condition with $N_t \approx 1$ (Figure 3.5a) and a mean instantaneous pitch rate of approximately zero (Figure 3.5b). On average, SC_L tends to be slightly lower after the tuck than before (Figure 3.5d), which implies that angle of attack and/or wing area are decreased slightly following a tuck. This is associated with the slight gain in airspeed that is apparent in Figure 3.5c.

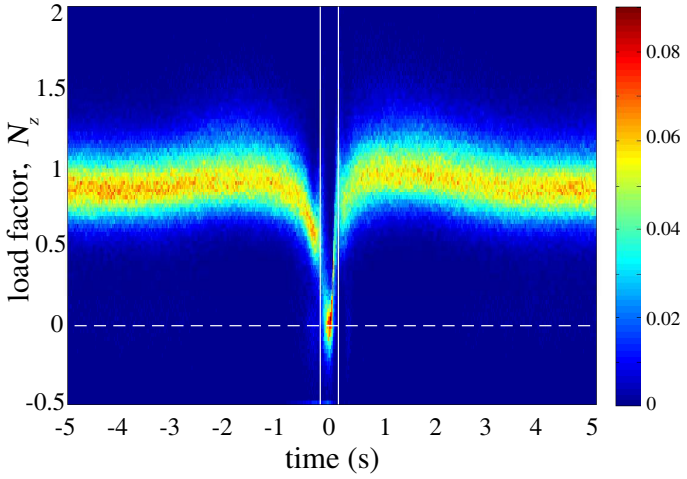


Figure 3.7: Two-dimensional histogram for all 2594 automatically identified tucks, with 100 bins showing the temporal variation in the frequency density of the instantaneous load factor $N_z = -\alpha_z/g$ as calculated from the z-component of acceleration (α_z). All times are referenced to the point of minimum load factor N_z for each tuck at $t = 0$s. The colour bar relates the colour of each point on the histogram to the proportion of the sampled tucks at that time to which it corresponds. The approximate beginning and end of the tucking movement is denoted by the vertical white lines, as in Figure 3.5. The dashed horizontal white line denotes zero load factor.

The total load factor N_t did not usually drop to zero during a wing tuck (Figure 3.5a). However, N_t is calculated from the magnitude of the total acceleration vector, independent of its direction, and is therefore constrained to be non-negative by definition (Equation 3.4). Hence, we cannot tell directly from Figure 3.5a whether the wings actually experienced load reversal at any point during the tuck. We therefore examined the component of the total load factor calculated from the z-acceleration component, $N_z = -\alpha_z/g$ (Figure 3.7). This quantity does not measure the total aerodynamic load experienced by the bird, and indeed its equilibrium value was <1 at $t = -5$s (Figure 3.7), which indicates that the z-axis of the IMU was not quite vertical at equilibrium. Nevertheless, N_z is generally signed positive if the wings are generating a dorsally-directed aerodynamic force, and signed negative if the wings are generating a ventrally-directed aerodynamic force. The minimum value of N_z during a tuck was centred on zero, which suggests that the wings may sometimes have experienced a slight negative aerodynamic loading, and that the bird approached a momentary state of free fall when its wings were dropped.

In order to identify the probable cause of wing tucking, we looked at the IMU data corresponding to the 5s period leading up to the point of peak z-acceleration at $t = 0$. Although the airspeed data are noisy, there was usually a distinct surge in airspeed between $t = -5$s and -1.5s (Figure 3.5c). This was accompanied by an increase in total load factor (Figure 3.5a,b), and by a nose-up pitching motion of approximately 5° amplitude, estimated by integrating the mean measured pitch rate (Figure 3.5b). Airspeed, total load factor, and pitch rate all began to fall off at an increasing rate from $t \approx -1.5$s, and were already in sharp decline by $t \approx -0.7$s, roughly 0.45s before the wings had started to tuck (Figure 3.5). We therefore conclude that these changes in airspeed, total load factor, and pitch angle cannot possibly have been caused by tucking of the wings. Instead, they may very well have been its immediate cause.

We may explore the relationship between total load factor and airspeed further by rearranging Equation 3.6 to yield:

$$N_t \approx \frac{1}{2}\frac{\rho U^2}{W} S C_L \tag{3.7}$$

Because air density (ρ) and body weight (W) are effectively constants, and because SC_L does not increase before the wings begin to tuck (Figure 3.5d), it is clear by inspection of Equation 3.7 that the initial surge in load factor must have been caused by the accompanying surge in airspeed (U). Furthermore, since there is no indication of any consistent change in SC_L before the tuck, this surge in airspeed must have been caused by atmospheric perturbation, rather than by deliberate changes in airspeed on the part of the bird.

3.3.2 Environmental predictors of wing tucking

If wing tucking occurs in response to atmospheric perturbation, we would expect the rate of wing tucking to be positively related to the level of atmospheric turbulence. We used model selection techniques to investigate the statistical relationship between

the square root transform (Sokal and Rohlf 1994) of the rate of wing tucking, $\sqrt{f}$, and several environmental predictors of atmospheric turbulence. A candidate set of 29 ordinary least squares models were created from all possible linear combinations of MIDAS mean wind speed ($\bar{V}$), mean local wind speed on the ridge ($\bar{v}$), standard deviation of the local wind speed on the ridge ($\tilde{v}$), the interaction ($\bar{v} * \tilde{v}$), and either mean flight altitude ($\bar{A}$) or ridge height (r). Average flight altitude ($\bar{A}$) and ridge height (r) were highly correlated with each other (Pearson's correlation coefficient: 0.94), so we did not combine these predictors in any one model, to avoid the problems of multicollinearity that would have resulted from combining them in a single model. RASP thermal predictors explained almost none of the variation in tuck rate (e.g. $R^2 = 0.072$ for the regression of $\sqrt{f}$ on the predicted thermal height), so were not considered further here.

The second-order Akaike information criterion (AIC_c) was used to rank the relative performance of the competing candidate models. This is a standard approach to model selection with a rigorous information theoretic interpretation (Burnham and Anderson 2002), but has been largely overlooked in the biomechanics literature to date. AIC_c was calculated for each model as:

$$\text{AIC}_c = n \log \frac{\sum \hat{\epsilon}_j^2}{n} + 2k + \frac{2k(k+1)}{n-k-1} \tag{3.8}$$

where $\hat{\epsilon}_j$ denotes the estimated residuals, n the sample size, and k the number of estimated parameters. Under this criterion, the best model within the candidate set is the one which minimizes AIC_c. The criterion therefore favours models with higher predictive power, but penalizes this according to the number of parameters that are estimated in fitting the model. The relative performance of the other models is expressed as the difference (Δ_i) between their AIC_c value and that of the best model. This difference can be used to compute the likelihood of each model given the data (Burnham and Anderson 2002), which is proportional to $e^{-\Delta_i/2}$. Thus, the best model has the highest likelihood given the data. The 15 most highly ranked candidate models are shown in Table 3.3. The relative likelihood of each

of the candidate models is summarized by their Akaike weights (w_i) in Table 3.3, calculated by normalizing the likelihoods of the models given the data so that they sum to one (Burnham and Anderson 2002).

model parameters	AIC_c	Δ_i	w_i
$\bar{v},\ \tilde{v},\ \bar{v}*\tilde{v},\ \bar{A}$	-90.556	0.000	0.612
$\bar{V},\ \bar{v},\ \tilde{v},\ \bar{v}*\tilde{v},\ \bar{A}$	-88.242	2.314	0.192
$\bar{v},\ \tilde{v},\ \bar{v}*\tilde{v},\ r$	-87.285	3.271	0.119
$\bar{V},\ \bar{v},\ \tilde{v},\ \bar{v}*\tilde{v},\ r$	-84.460	6.096	0.029
$\bar{v},\ \tilde{v},\ \bar{v}*\tilde{v}$	-83.993	6.563	0.023
$\bar{v},\ \tilde{v},\ \bar{A}$	-81.914	8.642	0.008
$\bar{V},\ \bar{v},\ \tilde{v},\ \bar{v}*\tilde{v}$	-81.315	9.241	0.006
$\bar{V},\ \bar{v},\ \tilde{v},\ \bar{A}$	-79.901	10.655	0.003
$\bar{v},\ \tilde{v},\ r$	-79.648	10.908	0.003
$\bar{v},\ \tilde{v}$	-78.598	11.958	0.002
$\bar{V},\ \tilde{v},\ \bar{A}$	-77.446	13.110	0.001
$\bar{V},\ \bar{v},\ \tilde{v},\ r$	-77.155	13.401	0.001
$\tilde{v},\ \bar{A}$	-77.062	13.494	0.001
$\bar{V},\ \bar{v},\ \tilde{v}$	-76.213	14.343	0.000
$\bar{V},\ \bar{v},\ \bar{A}$	-74.484	16.072	0.000

Table 3.3: Top 15 candidate models predicting the square root transform of the identified tuck rate ($\sqrt{f}$), ranked by their AIC_c values, and rated by their Delta AIC_c values (Δ_i) and Akaike weights (w_i). The 95% confidence set, defined as the smallest set of models whose Akaike weights w_i sum to ≥ 0.95, contains the top 4 models, and is delimited by a horizontal line. $\bar{v}$: mean local wind speed on the ridge; $\tilde{v}$: standard deviation of local wind speed on the ridge; $\bar{v}*\tilde{v}$: interaction between mean and standard deviation of local wind speed on the ridge; $\bar{A}$: mean flight altitude; r: ridge height; $\bar{V}$: mean MIDAS wind speed.

The best approximating model for these data (top row of Table 3.3) includes the mean local wind speed on the ridge ($\bar{v}$), the standard deviation of the local wind speed on the ridge ($\tilde{v}$), their interaction ($\bar{v}*\tilde{v}$), and the mean flight altitude ($\bar{A}$). The estimated regression coefficients for this model, and their associated conditional standard errors are shown in Table 3.4 ($F_{5,34} = 19.59$; $p \ll 0.001$; $R^2 = 0.697$). Several of the other models also perform well, however, and the 95% confidence set,

defined as the smallest set of models whose Akaike weights sum to 0.95, includes 3 other models. The evidence ratios, calculated as the ratios of their Akaike weights to that of the best model, are 3.2, 5.1 and 21.1 respectively, so it is quite likely that the second and third models might become top-ranked if replicate samples of data were available (Burnham and Anderson 2002). In any case, our anemometer measurements of the mean $\bar{v}$ and standard deviation $\tilde{v}$ of the local wind speed on the ridge, and the interaction between them $\bar{v} * \tilde{v}$, appear in all of the models within the 95% confidence set. We therefore infer that local atmospheric conditions are the most important predictors of tuck frequency, which is precisely as expected if wing tucking occurs in response to atmospheric perturbation.

parameter	intercept	$\bar{v}$	$\tilde{v}$	$\bar{v} * \tilde{v}$	$\bar{A}$
regression coefficient	-1.78	0.290	2.16	-0.223	1.04×10^{-3}
standard error	0.513	6.80×10^{-2}	0.485	6.56×10^{-2}	3.42×10^{-4}

Table 3.4: Parameter estimates for the best candidate model predicting the square root transform of the identified tuck rate ($\sqrt{f}$), giving the regression coefficient estimates and associated conditional standard errors for each term.

3.4 Discussion

3.4.1 Wing tucks as a form of gust response

Our two analyses—of the mechanics of wing tucking, and of the environmental predictors of tuck rate—each provide independent support for the hypothesis that wing tucks occur in response to atmospheric turbulence. The former analysis demonstrates that wing tucks occur following a surge in load factor explained by a transient increase in airspeed caused by atmospheric perturbations. The latter analysis shows that the occurrence of wing tucks is positively associated with environmental predictors of atmospheric turbulence (Table 3.4). As a further check, we now show that

the timescale of the transients associated with wing tucking is consistent with our interpretation of the manoeuvre as a response to atmospheric turbulence.

In a fixed-wing air vehicle, changes in airspeed caused for example by horizontal gusts, lead to phugoid oscillations (Etkin and Reid 1996) involving coupled changes in altitude, airspeed, pitch angle, and load factor. These changes occur at an almost constant aerodynamic angle of attack (Etkin and Reid 1996), so the lift coefficient (C_L) remains approximately constant during phugoid oscillation. Although the gust response of a bird is likely to be more complicated than this, we would expect the bird's rigid body response to horizontal gusts to operate on a timescale similar to that of a phugoid oscillation. Lanchester's phugoid approximation (Etkin and Reid 1996) treats the motion as a conservative interchange between kinetic and potential energy, with period T_p given by:

$$T_p = \pi\sqrt{2}\frac{U_0}{g} \tag{3.9}$$

where U_0 is the equilibrium airspeed, and where g is gravitational acceleration. With $U_0 \approx 14.5\text{ms}^{-1}$, as estimated from our airspeed data (see Instrumentation), the predicted phugoid period for our bird is $T_p \approx 6.5$s, which agrees quite closely with the timescales of the transients visible in Figure 3.5. These transients appear to represent one half-period of oscillation before the wing tuck movement, and another half-period of oscillation after—each lasting approximately 3.5s. The predicted timescale of the phugoid is therefore comparable to the timescale of the observed gust response. It is interesting to note that the duration of the wing tuck movement itself (0.35s) is an order of magnitude shorter than the duration of the transients observed before and after, so that there may be expected to be comparatively little interaction between the events occurring on these two distinct timescales.

Although the time series data for an individual tuck do not necessarily display all of the characteristics of a phugoid motion, the onboard data are consistent, in general terms, with an initial phugoid-like response to a headwind encountered between $t \approx -3.5$s and $t \approx -0.7$s. This would explain the initial increase in airspeed

that occurs in the lead up to the tuck (Figure 3.5c) and the consequent increase in load factor (Figure 3.5a), as well as the slow accompanying changes in pitch rate (Figure 3.5b). Immediately prior to the wing tucking movement, however, the load factor starts to drop precipitously (Figure 3.5a). The rate at which this drop in load factor occurs is too high to be explained by the coincident decrease in airspeed (Figure 3.5c), which is manifest in the drop in SC_L that is also visible from $t \approx -0.7$s (Figure 3.5c,d). This initial drop in SC_L occurs well before the bird has begun to close its wings, and must therefore be due primarily to a decrease in lift coefficient rather than in wing area. We now consider two possible explanations of this decrease in lift coefficient in the lead-up to a tuck.

One potential explanation of the drop in lift coefficient at $t \approx -0.7$s is that the wings stall at this time, but in this case we would expect to see an increase in SC_L immediately beforehand, as the lift coefficient approaches its maximum at the point of stall. In fact, SC_L shows no sign of increasing prior to the tuck (Figure 3.5d). Furthermore, as we now show, the numerical value of SC_L at $t \approx -0.7$s is too small ($SC_L < 0.3$) for the stall hypothesis to be credible. Making the reasonable assumption that the tail contributes either positive lift or no net lift in soaring, we know that $S_w C_{L_w} \leq SC_L$, where S_w is the total area of the wings and C_{L_w} is their mean section lift coefficient. Assuming that the wings were held fully outstretched with area $S_w = 0.54\text{m}^2$ prior to tucking (see Table 3.1), we can therefore conclude that they were operating with a mean section lift coefficient of $C_{L_w} < 0.55$. The theoretical mean section lift coefficient of an ideal elliptically-loaded wing is predicted by the higher-order lifting line theory of Van Dyke (1975) as:

$$C_{L_w} = \frac{2\pi\alpha}{1 + 2/\text{Æ} + 16(\log_e(\pi\text{Æ}) - 9/8)/(\pi\text{Æ})^2} \tag{3.10}$$

where Æ is aspect ratio, and where the angle of attack α is in radians (see Taylor and Thomas (2014) for discussion of this asymptotic approximation, which is accurate to within 1% of the exact numerical solution at Æ ≥ 2.55, in the context of soaring birds). Most wings stall at an angle of attack $\alpha \approx 15°$. Hence, given an aspect ratio

of $\text{Æ} = 6.7$ in soaring (see Table 3.1), we would predict a maximum attainable mean section lift coefficient of $C_{L_w} \leq 1.2$. Our estimated value of $C_{L_w} < 0.55$ is therefore less than half that which would be expected if the wings were fully outstretched with all sections operating close to stall. This factor of two difference is much too large to be explained by any error in the assumed wing area, or by deviations from elliptic loading. Specifically, if the wings had been operating at their predicted stall limit of $C_L = 1.2$ then they would need to have been operating at less than half of their maximum area in order to produce the observed value of SC_L, which is completely inconsistent with our ground-based video data (Figure 3.1a; Supplementary Video 1). Hence, although we cannot exclude the possibility that some sections of the wing may have been stalled, our data allow us to demonstrate unequivocally that most of the wing must have been operating far from stall.

A second possible explanation of the drop in lift coefficient at $t \approx -0.7$s is that the angle of attack of the wings decreases at at this time. Setting $C_{L_w} \leq 0.55$ and $\text{Æ} = 6.7$ in Equation 3.10 and solving for α, we estimate that the wings would have been operating at a mean angle of attack $\alpha \leq 7^\circ$ at $t \approx -0.7$s. Hence, given that the load factor halves between $t \approx -0.7$s and the point at which the wings begin to close (Figures 3.5, 3.7), and given that lift coefficient is proportional to angle of attack in Equation 3.10, this drop in load factor could in principle have been caused by a halving of the angle of attack. Thus, a decrease in angle of attack of $< 4^\circ$ would be sufficient to explain the observed drop in load factor. This comparatively small change in angle of attack might in principle have been caused either by the nose-down pitching motion that occurs at $t \approx -0.7$s (Figure 3.5c), or by a hypothetical decrease in the angle of incidence of the wings relative to the body, or by an atmospheric perturbation such as a downdraft. Our data do not allow us to distinguish between these three possibilities, but we can safely conclude in light of the above that the wings begin to tuck after experiencing a sharp loss of lift caused by a comparatively small decrease in angle of attack. Given that this loss of lift follows a transient surge in lift associated with a headwind, it is reasonable to suppose that it is ultimately the result of the same atmospheric perturbation. In

summary, we conclude that wing tucks are a response to atmospheric perturbations comprising a headwind, possibly—but not necessarily—followed by a downdraft.

3.4.2 Mechanics of wing tucking

Wing tucking represents a disturbance from an equilibrium in which the wings are held outstretched, and in order to understand the mechanics of wing tucking it is necessary to understand this equilibrium. The simplest possible model of the problem that nevertheless captures the essential physics involves treating the wings as a pair of rigid elements of mass m_w, connected by a pivot at which the mass of the body m_b is concentrated (see Figure 3.8). The centre of mass of each wing is located at a distance d_1 from the pivot. Each wing is assumed to produce an aerodynamic force $L/2$ equal to half of the total lift, which acts at the centre of pressure, located at a distance d_2 from the pivot. Because inboard portions of a bird's wing are much heavier per unit area than outboard portions of the wing, the centre of pressure will always lie outboard of its centre of mass such that $d_2 > d_1$. For simplicity, we will only consider the equilibrium condition in which the wings are horizontal, so that the lift force can be assumed to act vertically. Considering each wing separately, the net moment (M) acting on the wing at equilibrium, resolved at the wing pivot, can then be expressed as:

$$M = \frac{1}{2}Ld_2 - m_w g d_1 + M_m \tag{3.11}$$

where M_m is a musculoskeletal moment, and where the moments are signed positive in the direction of wing elevation. At equilibrium, the total forces and moments acting on the wing are zero, such that $L - mg = 0$ and $M = 0$, where $m = m_b + 2m_w$ is the total mass of the bird. Substituting these identities into Equation 3.11, the musculoskeletal moment that must be generated by the bird at equilibrium is:

$$M_m = (m_w d_1 - \frac{m}{2}d_2)g \tag{3.12}$$

Given that $d_2 > d_1$ and $m > 2m_w$, it follows that $M_m < 0$ at equilibrium, and hence that there must always be a musculoskeletal moment acting to pull the wing downward in opposition to the lift produced at equilibrium (see also (Baier et al. 2007; Gray 1968; Kuroda 1961; Pennycuick 1972; Pennycuick 1982)).

In principle, this musculoskeletal moment could either be provided by a skeletal locking mechanism, as is known to occur in albatrosses (*Diomedeidae*) (Meyers and Stakebake 2005; Pennycuick 1982), or by tetanic contraction of the flight muscles which act to depress the wing. No skeletal locking mechanism is yet known to occur in raptors (*Accipitriformes*), but the postural muscles of many soaring birds are known to consist of slow tonic and slow twitch muscle fibres, which are specialized for sustained contraction and have a higher fatigue resistance than the fast twitch fibres found in muscles used for flapping (Meyers 1993). Among the main flight muscles, the pectoralis muscle serves to depress the wings, and therefore has the appropriate action to provide the musculoskeletal moment needed to pull the wing downward in opposition to the lift produced at gliding equilibrium (Baier et al. 2007; Kuroda 1961; Pennycuick 1972). Indeed, owing to its short lever arm, the pectoralis muscle has been suggested to sustain a load of at least 6 times body weight at gliding equilibrium (Baier et al. 2007; Gray 1968; Pennycuick 1972). It is therefore noteworthy that slow tonic fibres are present in the deep pectoralis of some birds, but only in those species which soar for extended periods (Meyers 1993). This is consistent with the long-held view that the anatomical subdivision of the pectoralis in soaring birds reflects the adaptation of one of its layers for holding the wings level in gliding flight (Kuroda 1961). In fact, the picture is more complicated than this, because the net musculoskeletal force acting to hold the wing in place in gliding is produced by multiple musculoskeletal elements, with the ventromedial force of the pectoralis balanced laterally by the dorsomedial force of the acrocoracohumeral ligament and a lateral push from the glenoid (Baier et al. 2007).

In light of the fact that wing tucking follows a drop in aerodynamic loading (see Results), it is likely that the wings are pulled down because the musculoskeletal

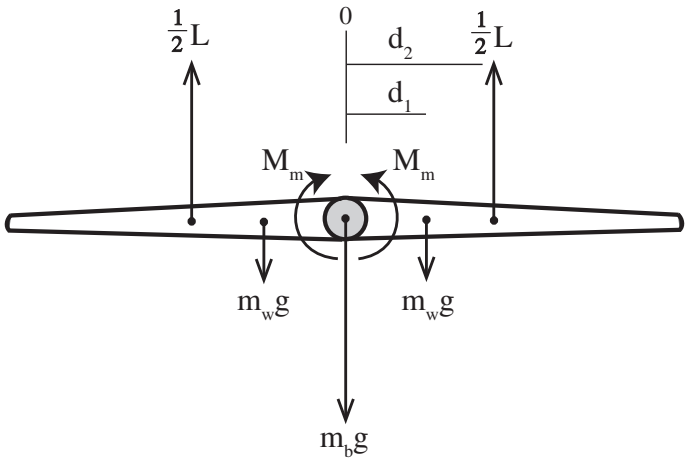


Figure 3.8: Model of the forces and moments acting on the bird's wings and body. Two rigid wings of mass m_w are assumed to be connected to the body at a single pivot point at which the mass of the body m_b is concentrated. Each wing generates half of the total lift L, which acts at the centre of pressure. The lengths d_1 and d_2 measure the distance from the wing's pivot to the wing's centre of mass and to the wing's centre of pressure, respectively. M_m is an applied musculoskeletal moment, signed positive in the direction of wing elevation.

moment produced by the pectoralis and other flight muscles does not decrease as rapidly as the opposing aerodynamic moment. Although we cannot exclude the possibility that the bird might actively tuck its wings, in the sense of issuing a direct motor command to do so, it is perfectly plausible that wing tucks might arise passively. This is because the pectoralis is always under tension when the wings are level—even when the muscle is fully relaxed (Peters and Dobbins 2012). Consequently, there will always be a net musculoskeletal moment acting to pull the wings down, unless the wing elevator muscles are actively commanded to oppose this. It follows that the wings are bound to tuck under a complete loss of aerodynamic loading, unless the bird not only relaxes its wing depressor muscles but also engages its wing elevator muscles. The same must be true of any partial loss of aerodynamic loading where the moment due to the passive tension in the pectoralis exceeds the moment due to the remaining aerodynamic load.

3.4.3 Conclusions

An obvious limitation of our study is that the data pertain to a single captive bird. Although we can draw no conclusions about the wider significance of wing tucking in this species from our data, we note that wing tucking behaviour with qualitatively indistinguishable kinematics can be observed in videos of migrating Steppe Eagles posted in online public video archives (Lind 2010; Lind 2011). We draw attention to this footage principally to show that wing tucking is not in itself an unusual behaviour for this species, so that there is no reason to suppose that the behaviour that we have observed in our captive bird is a stereotypy or other abnormal phenomenon. Moreover, although the details of the muscle actions that are involved are unknown, the underlying physics of this kinematically similar behaviour in wild birds is unlikely to differ greatly from that which we have analysed in detail here for our captive bird. Here, we have shown specifically that the occurrence of wing tucks in our captive steppe eagle is not a deliberate mechanism for gaining airspeed prior to a flat glide or dive (Hankin 1913), nor an active mechanism for restoring pitch equilibrium following a gust perturbation (Wright 1900). Instead, we have provided evidence that this wing tucking behaviour is simply a response to atmospheric turbulence, just as we hypothesised previously in (Gillies 2010). Specifically, our inertial data confirm that the wings only begin their tucking movement *after* experiencing a substantial loss of aerodynamic lift caused by a decrease in aerodynamic angle of attack. Logically, this *must* be because the applied musculoskeletal moment acting to pull the wing down temporarily exceeds that required to balance the aerodynamic moment acting to lift the wing up. Normal wing loading is recovered soon after the wings are reset to their equilibrium position, but it remains unclear whether the fact that the wings do tuck serves to alleviate the gust in any useful way. Nevertheless, given that soaring necessarily involves flying in turbulent conditions, the ability to deal with the adverse effects of turbulence would certainly be an important evolutionary adaptation for soaring birds. We speculate that supporting a jointed wing by using the flight muscles to resist the aerodynamic moments associated with soaring

flight—with all of the energetic costs that this entails—serves to damp atmospheric turbulence, rather like the suspension of a car. It remains an open question whether wing tucking is an intrinsic part of this damping mechanism, or whether it instead represents a bifurcation in the dynamics caused when the system is pushed outside of its normal working range.

3.5 Acknowledgements

The research leading to these results has received funding from the European Research Council under the European Community's Seventh Framework Programme (FP7/2007-2013) / ERC grant agreement no. 204513 to GKT. KR was funded by a Biotechnology and Biological Sciences Research Council CASE studentship with Blue Bear Systems Research Ltd. The authors thank Martin Cray for his assistance as falconer during experiments, and Jo Binns for husbandry of the bird. We thank Joseph Blackham and others for kindly allowing access to land. We thank Paul Scorer for providing atmospheric predictions from the RASP software.

Chapter 4

Modelling updrafts for slope soaring

This work was done in collaboration with Blue Bear Systems Research and Cranfield University. Data collected by James Gillies (2010) is also used.

4.1 Introduction

Large migrating birds use both ridge lift and thermals to reduce the energy cost of flight, often making considerable detours from their migration routes in order to exploit these energy sources (Mellone et al. 2011; Spaar 1997; Spaar and Bruderer 1997). There have been multiple studies exploring how birds' soaring flight strategies, including the choice of route and lift source, are influenced by weather, turbulence, temperature, time of day or year and topography (Careau et al. 2006; Leshem and Yom-Tov 1998; Mandel et al. 2011; McLaren et al. 2012; Sparr et al.

2000). It is also thought that different morphologies may be suited to different types of soaring (Bohrer et al. 2012; Taylor and Thomas 2014). The majority of these studies have examined the large scale movement of wild birds, studying general trends during migration, either from ground based observations or from tagging and analysing GPS data (Bouten et al. 2013). Often this information can be used for applications such as choosing wind farm locations, aircraft flightpath planning or conservation.

However, less is understood about the behaviour and performance of birds on a smaller scale when exploiting the individual lift sources. In comparison to thermals, exploiting slope lift appears relatively simple as it is a more predictable and constant source of lift, fixed to topographical features (Reichmann 1993). However, the lift is greatly influenced by the surrounding upwind terrain and varies considerably with both wind strength and direction, which can generate complex airflows for birds to negotiate. How birds adapt and respond to these different conditions is therefore an important aspect of any soaring strategy. Although the potential altitude gain is less impressive than for thermals, slope soaring can still significantly improve endurance and even very small obstructions, such as hedges or buildings, can generate enough lift for birds to use. This is also of interest for the development of mission planning systems in small unmanned air systems (SUAS) which are required to fly in complex environments. A number of algorithms for optimising flight in ridge lift already exist (Chakrabarty and Langelaan 2011; Langelaan 2007; White et al. 2012).

For effective exploitation of lift sources, it is essential that a bird or vehicle can assess the local airflow. To determine the bird's ability to do this therefore requires accurate sampling of the atmosphere across a large domain, but this is extremely difficult and time intensive (e.g. LIDAR). Only a general estimate of the conditions can be obtained from weather data and, whilst the use of airspeed sensors mounted on board the bird measure at the bird's exact location, without also knowing the movement of the surrounding atmosphere it is not possible to quantify the bird's performance or locate better lift sources. Rather than directly sample

the atmosphere, an alternative option is to use a computational fluid dynamics (CFD) model to estimate the airflow across a large domain for a range of inflow wind conditions. This theoretical model cannot take account of sporadic gusts and thermal turbulence but has been shown to successfully predict ridge lift for UAV applications (Mohamed et al. 2015).

In this chapter we use a CFD simulation of Hay Bluff in Wales to predict the updraft strength along the ridge and surrounding terrain. Onboard instrumentation was used to record 22 flights of our steppe eagle soaring, exploiting both ridge and thermal lift. GPS data from the bird was compared with the CFD simulation as a proof of principle for using CFD techniques to study the performance of the bird whilst ridge soaring.

4.2 Materials and Methods

4.2.1 CFD model

A digital elevation model (DEM) of the Hay Bluff site (location 2 in Appendix A) in the Black Mountains region of South Wales, UK, was provided by Blue Bear Systems Research Limited (a company that specialises in unmanned air systems). The DEM included the terrain upwind of the ridge, extending between latitudes 52.0352N and 52.0028N, and longitudes 3.0653W and 3.1749W, see Figure 4.1. Hay Bluff sits on the edge of the Black Mountains and is frequently used by glider pilots for soaring in winds from West to North-North-West. Vegetation on the ridge is primarily short grass with some small bushes and trees. The resolution of the DEM is 5m which provides sufficient detail to capture features of the terrain that influence the airflow for a CFD analysis on this scale.

The CFD model was generated by Boisserie and Thornber at Cranfield University as a Master's thesis (Boisserie 2012). The chosen RANS turbulence model, meshing strategy, solver, wall and inlet boundary conditions were initially validated

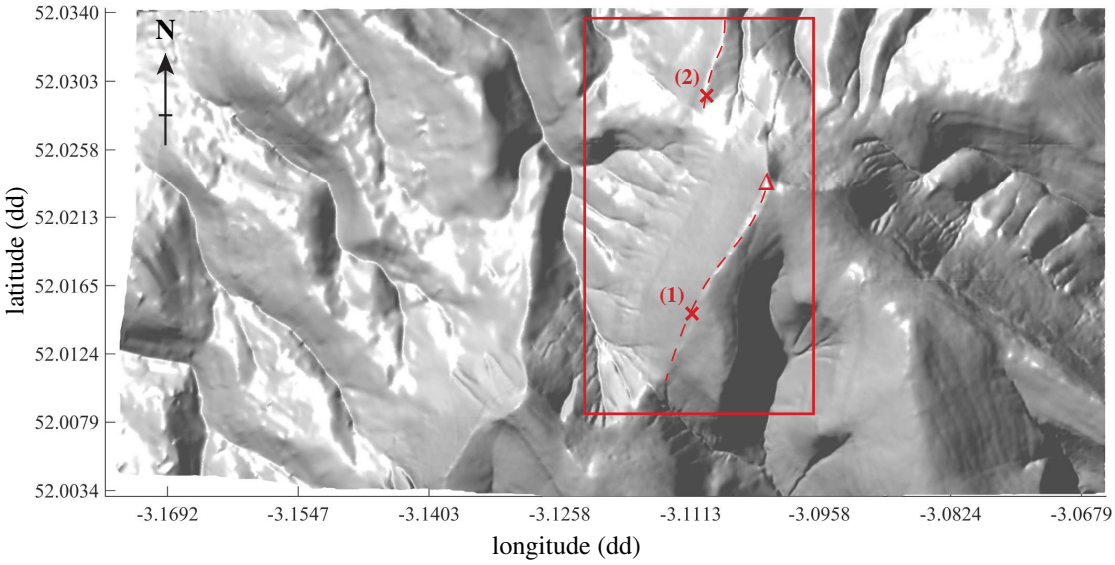


Figure 4.1: Aerial view of the DEM with 5m resolution provided by Blue Bear for the Hay Bluff ridge. CFD analysis was performed on this surface for prevailing wind directions W, WNW, NW & NNW. The red rectangle encompasses the region of terrain over Hay Bluff where the bird was recorded flying, bounded by latitudes 52.0084N and 52.0342N, and longitudes 3.0974W and 3.1232W. Points (1) and (2) indicate the launch sites used for the bird on the upper and lower ridges respectively, which are marked by dashed lines. The main Hay Bluff ridge line runs at an angle approximately 30° from true North and rises over 250m above the upwind terrain, reaching a peak altitude of 677m above sea level at the trig point (Δ). The maximum incline is approximately 36°. The smaller ridge is positioned slightly upwind of the main hill and runs at approximately 20°, with a maximum altitude of around 460m.

on both 2D and 3D test cases. An unstructured, tetrahedral mesh was chosen for the simulation of the full scale geometry. Sizes of elements were controlled by the maximum element size and through the curvature based refinement method. Grid convergence was considered to be reached at 4 million cells. An aerodynamic roughness of $z_0 = 0.05$ was used to approximate the terrain. For simulation of the atmospheric boundary layer flows over complex terrain, a k-ϵ model with modified constants ($C_\mu = 0.033$, $C_{\epsilon 1} = 1.46$, $C_{\epsilon 2} = 1.83$, $\sigma_k = 1.0$ and $\sigma_\epsilon = 2.38$, see Boisserie (2012)) was determined to be the most accurate for predicting the streamwise velocity, though it is still thought to slightly over-predict the turbulent kinetic energy. The CFD analysis was carried out using ANSYS Fluent 12.1. The full details on the CFD can be found in (Boisserie 2012).

The analysis was run for a set of inflow conditions W, WNW, NW & NNW, each

at two reference velocities of $5ms^{-1}$ and $15ms^{-1}$. We are primarily concerned with the predicted updraft (vertical velocity wind component) in this study.

4.2.2 Steppe eagle experiments

Our trained steppe eagle was flown at Hay Bluff over three field seasons on days when the prevailing wind conditions were suitable for ridge soaring (between W and NNW) and under a range of atmospheric conditions, but not in rain or winds exceeding $8ms^{-1}$. Two launch sites were used; one at the south end of the upper ridge, marked by point (1) in Figure 4.1, and the other at point (2) on the lower ridge. Flights lasted between 20 and 140 minutes before the bird returned to the falconer. This resulted in approximately 18.1 hours of data.

Before each flight, an onboard instrumentation package was mounted dorsally on the bird. For the six flights recorded in 2012, we used the customised ArduPilotMega2 described in Chapter 2, which weighed <0.075kg (GPS data was logged at 10Hz). Sixteen additional flights were included in this analysis from a previous study on the same bird in 2008 and 2009 (Gillies 2010). The flights were recorded using an earlier version of the instrumentation unit; a SmartIMU (Innovative Automation Technologies LLC, Gainesville, FL.), which weighed <0.15kg and logged angular velocity and linear acceleration at 25Hz and GPS position and velocity at 4Hz. For a full description of the SmartIMU see (Gillies 2010).

Each flight was filmed from the ground and measurements of the wind conditions for all but five flights were obtained from the Credenhill weather station MIDAS data (MetOffice 2012). This weather station is at an altitude of 76m, 21.6km from Hay Bluff. The three hourly MIDAS recordings were averaged closest to the time at which the bird flew, to give an estimate of the mean wind speed and direction for each flight. For flights in 2012, the WindMaster Pro three-axis ultrasonic anemometer was also used to obtain local wind velocity measurements. The anemometer was positioned at the top of the ridge at the bird's launch site (see Figure 4.1), approximately 2m above the ground, and measured wind velocity at 10Hz.

As no barometric altitude data were available from the SmartIMU, for all flights GPS altitude was used to track the bird's position and estimate climb rate; although we note that there is more error associated with this GPS measure than the equivalent barometric data. The six 2012 flights were down-sampled to match the 4Hz sampling frequency of the SmartIMU recordings. The data for each flight were then manually trimmed to only include periods where the bird was actually flying, eliminating data pre-take-off, when the bird was sat on the ridge or carried by the falconer. Finally the bird's climb rate was calculated from the GPS data by differencing the altitude over 1 second (4 sample points).

4.3 Results

4.3.1 CFD analysis

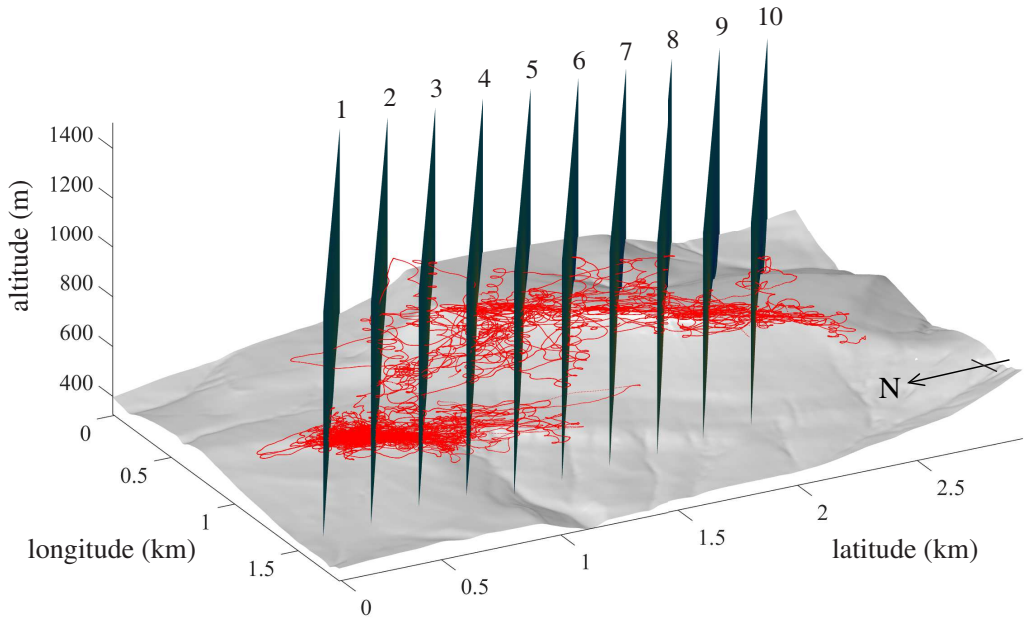


Figure 4.2: Elevation of the terrain where the bird was recorded to fly (the area of the CFD domain depicted by the red rectangle in Figure 4.1). The flight paths of the bird soaring on both the upper and lower ridges for all 22 flights are shown in red, with the occasional circling flight in thermals. The location of the ten slices along the ridge used for visualisation of the CFD flow analysis are also labelled.

Results of the CFD simulation presented in this chapter have been extracted for the subsection of the larger domain in which the bird was recorded to fly. To visualise the CFD results for the different inflow conditions, ten slices were taken perpendicular to the ridge line, regularly spaced at the locations shown in Figure 4.2. Colour maps of the predicted vertical wind velocity were then plotted for each slice for the different inflow wind directions at 5ms^{-1} in Figure 4.3. These were created in MATLAB by interpolating the meshed updraft data for each slice.

The inflow wind condition WNW at the higher speed of 15ms^{-1} is also shown for comparison. Boisserie (2012) determined that at different inflow speeds the flow velocity is self-similar when nondimensionalized for sufficiently high Reynolds numbers; therefore the reference inflow velocity governs the magnitude of the flow predicted across the domain. This consequently allows us to interpolate CFD results at intermediate wind velocities. The vertical velocities for the inflow wind condition of 15ms^{-1} are therefore 3 times larger than for the 5ms^{-1} case, as illustrated in Figure 4.3. The same applies for horizontal wind velocity components.

Theory predicts that the steeper the gradient of the slope and the larger the obstruction, the more the airflow is deflected and consequently accelerated over the ridge (Reichmann 1993). This is demonstrated in Figure 4.3 where the updraft strength increases towards the top of both ridges whilst for slices 1 and 2, far less updraft is generated as the terrain is fairly shallow. Due to the acceleration of the flow, maximum total velocities predicted at the top of the ridge can be over 4 times the inflow reference wind velocity. The airflow is fastest close to the surface of the terrain, (though must be 0ms^{-1} at the surface itself) and decreases with altitude. This is shown by the dimensionless vertical wind velocity profiles in Figure 4.4 for the three locations (a,b & c) marked in red on slice 8, Figure 4.3e.

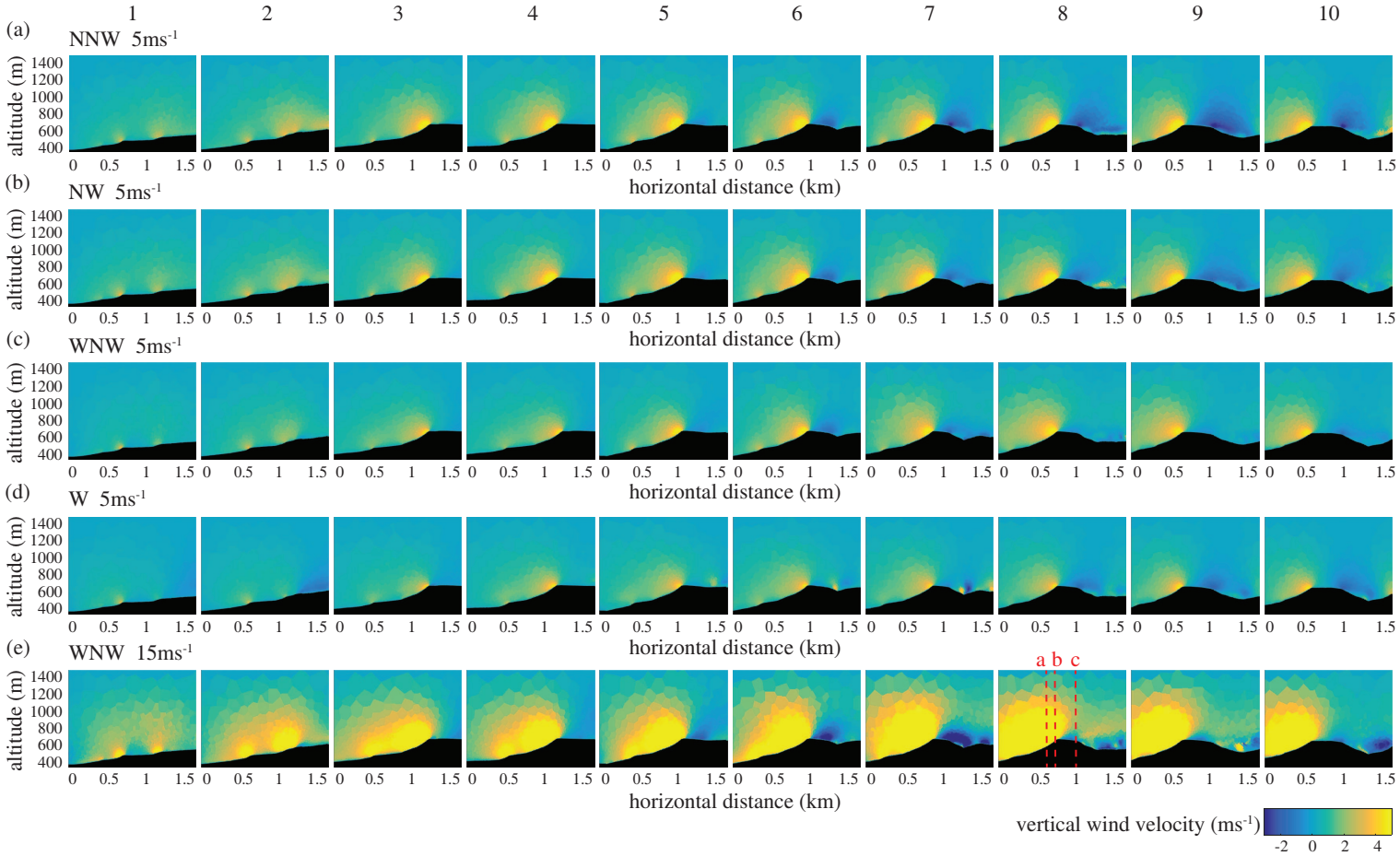


Figure 4.3: Ten slices showing the cross-section of the Hay Bluff ridge at the locations in Figure 4.2, coloured by the CFD predicted vertical wind velocity (updraft positive), for inflow conditions: (a) NNW at 5ms^{-1}, (b) NW at 5ms^{-1}, (c) WNW at 5ms^{-1}, (d) W at 5ms^{-1} and (e) WNW at 15ms^{-1}. There is a clear increase in updraft strength both as the slope of the ridge increases and towards the peak of the ridge. On the leeward side of the upper ridge there is evidence of downdrafts as the flow recirculates, causing turbulence. Updraft strength is proportional to the inflow velocity and the results indicate that the strongest updrafts are generated for the NNW wind condition. Note the polygonal discretisation is due to the structure of the mesh which becomes coarser with altitude.

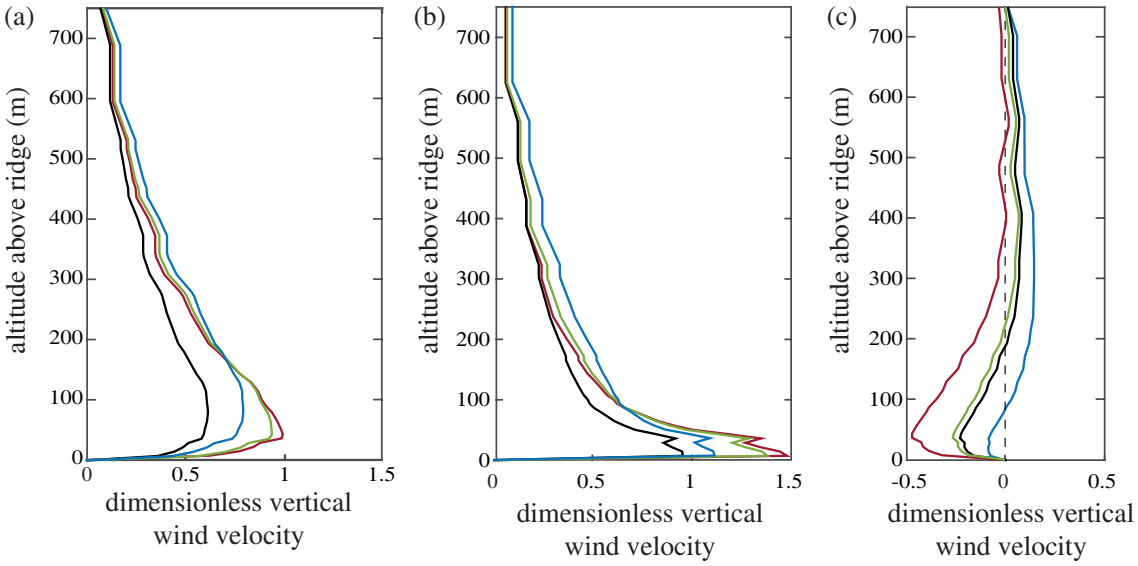


Figure 4.4: Dimensionless vertical wind velocity profile above the ridge for locations (a), (b) and (c) correspondingly in Figure 4.3e. Velocity was nondimensionalised by the inflow velocity (5ms^{-1}). Red: NNW. Green: NW. Blue: WNW. Black: W. The profile for each wind direction varies in magnitude but follows the same trend; by definition, the flow velocity must be zero at the surface, it then rapidly increases to a maximum within about 50m before tailing off to the free stream velocity at altitudes $>$ 700m. For both (a) & (b), the strongest updrafts are generated for the NNW wind condition and decrease as the wind swings round to W. Location (c) is downwind of the ridge and detects turbulent downdrafts near the surface for all wind directions.

Given the upwind terrain on Hay Bluff is relatively smooth, the CFD analysis does not predict significant turbulence or regions of sinking air; the airflow is smoothly deflected up as it flows towards the top of the ridge. However, on the leeward side we do see turbulent downdrafts due to recirculation of the air flow over the crest of the ridge. This is shown in Figure 4.4c where the profile taken downwind of the peak is negative (sinking air). Any bird or aircraft would ideally avoid these turbulent downdraft zones. It was initially thought that we might see a region of downdraft downwind of the lower ridge, much like on the upper ridge, but this is not the case as the terrain leads smoothly up, allowing no room for recirculation.

Theoretically, the greatest updrafts should be generated when the oncoming airflow is perpendicular to the slope. Given the ridge runs at $\approx 30°$, we would therefore expect the WNW condition (which is at 97.5° to the ridge line) to create

the strongest updrafts. However, this contradicts the results in Figure 4.3. Instead, the strongest updrafts are created when the inflow wind condition is NNW. To understand this disparity, in Figure 4.5 we look at the direction of the flow over the terrain for the different inflow cases, taking velocity vectors at 20m above the surface.

It is immediately obvious from Figure 4.5 that the airflow is deflected towards the ridge for WNW, NW & NNW winds. This seems to be a genuine feature of the flow caused by the topography. In particular, a valley slightly upwind of the ridge funnels the air flow so that in each case, it hits the ridge perpendicularly. There is no distinguishable difference between the inflow conditions when examining the flow on the ridge itself. The stronger updrafts in the NNW condition are therefore due to the greater acceleration of the flow, caused by the larger deflection, rather than the angle at which the flow hits the ridge. In the case of a westerly wind in Figure 4.5d, the flow is not deflected and therefore hits the ridge at an angle, producing weaker updrafts. Of course, given the extent to which the flow is influenced by the relatively flat, and small region of terrain we have modelled, if more landscape was included in the CFD model, we might get different results.

It should also be considered that the boundary condition at the model wall might have caused the deflection. Indeed, wall effects are a common problem in CFD studies and given the proximity of the walls to our area of interest, it is likely they will have some influence on the flow behaviour. Although this CFD model is limited by the DEM available, a possible modification would be to extrapolate the terrain beyond the current limits to minimise any such effects.

Figures 4.3 & 4.4 illustrate how the direction of the flow is relatively insensitive to the inflow condition for WNW to NW directions; though the strength of the resulting updraft does change. This also highlights the value of such CFD analyses, as the behaviour of the air flow is not as entirely intuitive—even on a relatively featureless ridge—as we might have predicted. Consequently, modelling sufficient terrain upwind of the ridge is essential for producing an accurate CFD model.

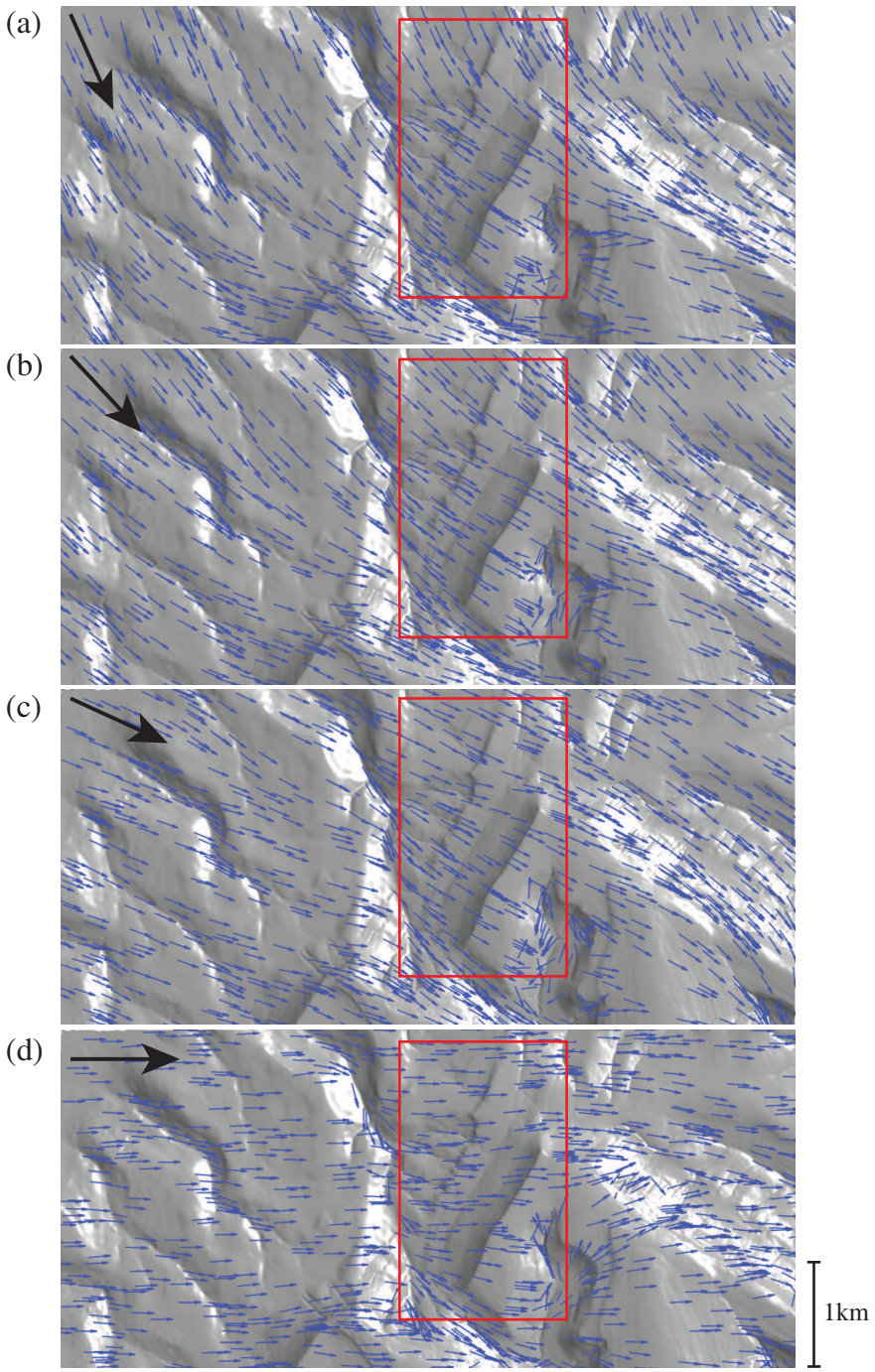


Figure 4.5: Aerial view of the entire Hay Bluff CFD domain (flight region depicted in red) with wind velocity vectors illustrating the behaviour of the flow across the terrain, at 20m above the surface, for inflow wind velocity of 5ms^{-1} and directions (a) NNW, (b) NW, (c) WNW and (d) W, which are shown by the large black arrows. The flow is deflected in (a), (b) & (c) such that it hits the upper ridge at 90°. The flow is deflected most for the NNW condition, causing greater acceleration over the ridge and consequently generating the strongest updrafts (see Figure 4.3).

Inflow conditions

To compare the data collected from flights of our steppe eagle with results of the CFD analysis, inflow conditions for the CFD model should be chosen to match the atmospheric conditions on the day the bird was flown. Wind velocity from the MIDAS weather station data ranged from 1.4 to 10.8ms^{-1}, with nine flights in approximately W winds, six in WNW and two in NW. We use these measurements to select the most suitable CFD inflow conditions to model the updrafts, scaling the results by recorded wind speed. Although this is our best estimate of the wind conditions, these measurements are limited; the weather station is 22km away from Hay Bluff and given the deflection of the flow predicted in the CFD model, it is probable that both the wind speed and direction will be significantly different at the two sites.

The anemometer data recorded on the ridge is even less reliable. Given that, for the majority of cases modelled, the flow is predicted to hit the ridge perpendicularly, we cannot distinguish between the different inflow conditions when taking measurements from the ridge. Another consideration is how close to the surface the recordings are taken; at 2m the wind will be affected by surface turbulence and boundary layer effects. Similarly when trying to estimate the inflow wind velocity, the anemometer readings will record much higher velocities than at the inflow to the domain as the flow is being accelerated up over the ridge.

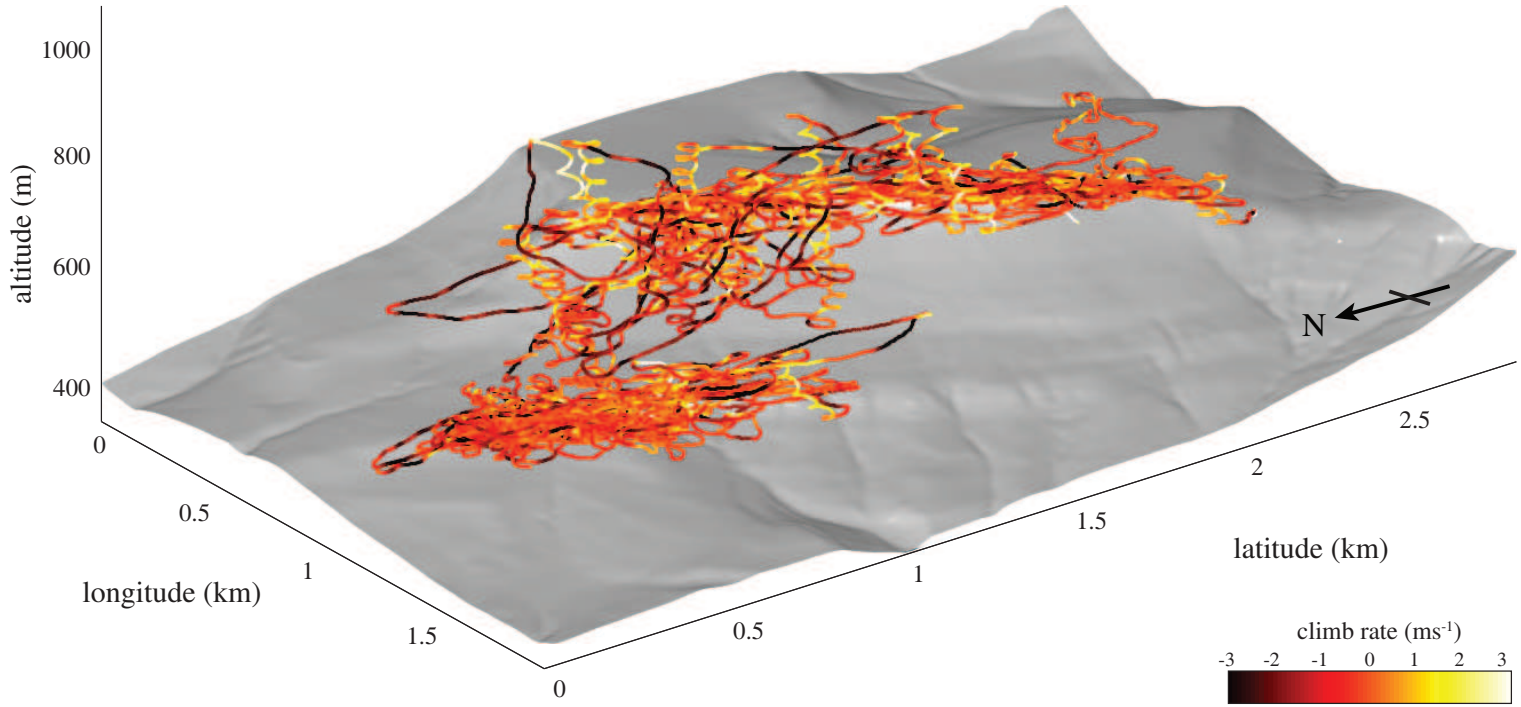


Figure 4.6: GPS tracks of our steppe eagle (a total of 18 hours over 22 days) coloured by the climb rate measured from GPS altitude data (smoothed over 10s). The high climb rates recorded whist circling indicate thermalling flight, this is often followed by straight flight with high sink rates as the bird glides fast. The majority of the flights are spent flying along the upper or lower ridge, slightly windward of the ridge peak.

4.3.2 Steppe eagle flights

The GPS tracks in Figure 4.6 show the trajectory of all flights recorded for our bird, coloured by the measured climb rate. Maximum altitude was 946m and 96% of the climb rates were between -2.02ms^{-1} and 1.70ms^{-1}. The bird spent the majority of the time flying along both the upper and lower ridges, normally staying on the ridge from which he was released (six flights from the upper ridge and sixteen from the lower). On a number of occasions, the bird did climb from the lower to the upper ridge using thermals which are characterised by circling flight and high climb rates. The bird achieved much higher altitudes when using thermals, whilst climb rates when soaring along the ridge were on average approximately zero.

4.3.3 Comparison of CFD and bird data

Position of flights on ridge

To test whether the bird flew in the regions of maximum updraft predicted from the CFD analysis, the GPS position data were coarsely binned into the same ten slices along the ridge as used in Figure 4.3. The binned data are plotted in Figure 4.7, both as (a) individual points coloured by day and (b) as 3D histogram plots showing the frequency density of the bird's position relative to the ridge. These are compared to the CFD results for the NW inflow condition of 5ms^{-1} (arbitrarily chosen as the updraft pattern is comparable for all wind directions). There is a clear similarity between the areas of strong predicted updrafts and where the bird chose to fly most frequently (Figure 4.7b&c); which is slightly upwind of the ridge peak. We also note that the bird avoids flying over the back of the ridge into the areas of predicted sinking air.

On a theoretically ideal, semi-circular ridge line, the updraft generated will be constant at a constant altitude and distance from the ridge. It is therefore possible for the bird to select an airspeed such that its inherent sink rate exactly balances the updraft in which it is flying, resulting in a constant altitude, constant airspeed

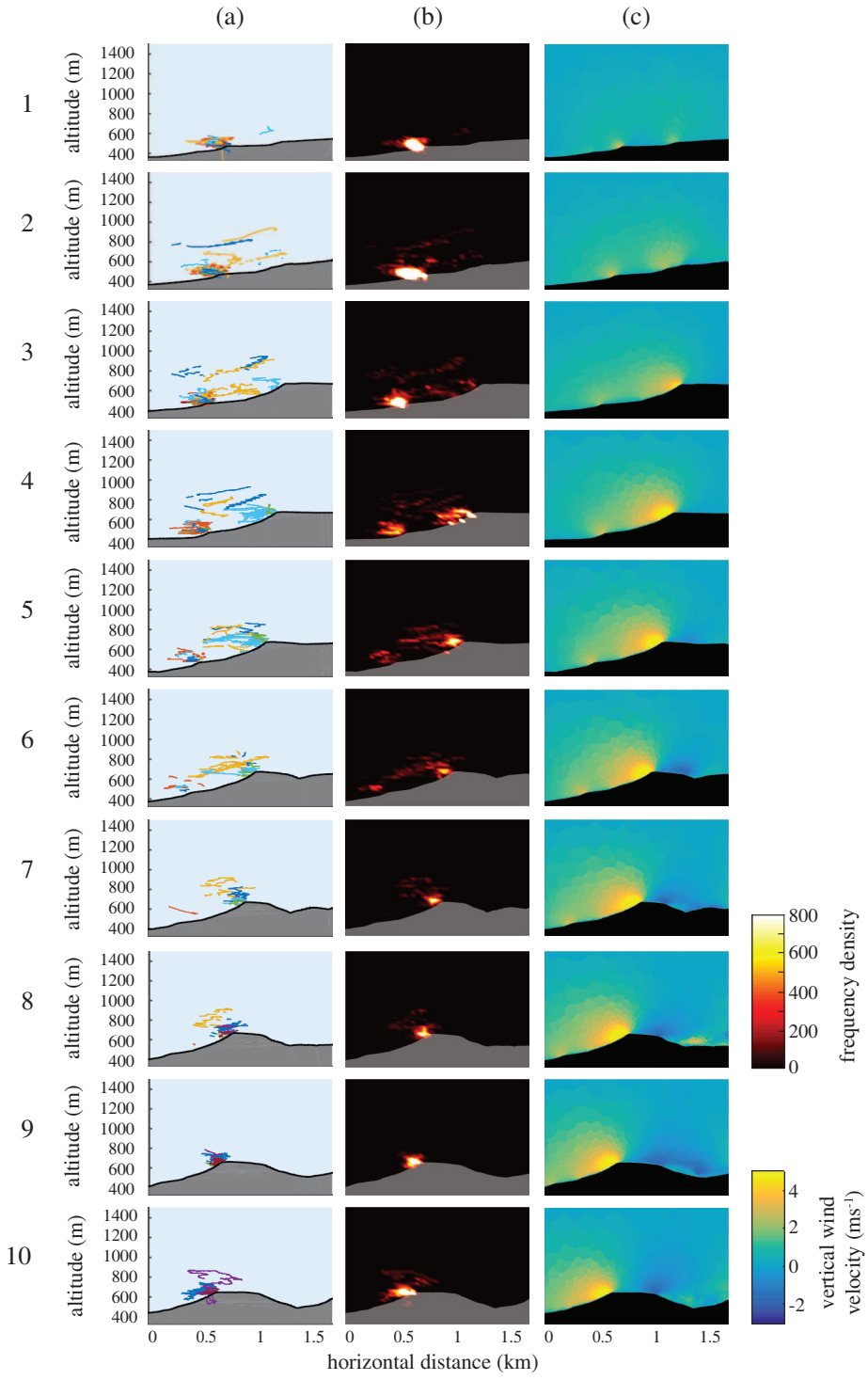


Figure 4.7: Position of GPS flight data along the ridge, binned into the slices shown in Figure 4.2, and compared to the predicted updraft strength. (a) GPS data, coloured by flight number. (b) 3D histogram plots showing the frequency density of the bird's position along the ridge. (c) Predicted updraft for inflow wind condition NW at 5ms^{-1}. From this qualitative comparison it is evident that the majority of the bird's flight is spent in the regions of strongest updraft along the ridge.

strategy (Langelaan 2007). In reality we would not expect this to be so easily achieved as there are likely to be fluctuations in updraft strength along the ridge, requiring adjustments in either altitude or airspeed. If the bird were using a strategy whereby he flew at a specific airspeed regardless of the wind conditions, we would expect that, for days where the wind was stronger (and consequently the updraft along the ridge was stronger), the bird would on average fly at a higher altitude above the terrain—or alternatively further from the point of maximum updraft—as there is more energy available in the atmosphere.

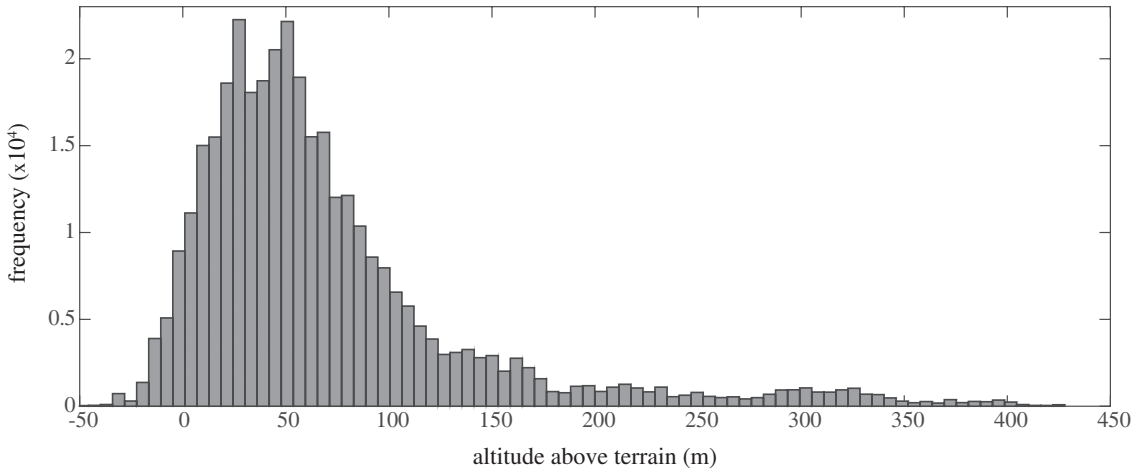


Figure 4.8: Histogram of the bird's altitude above the terrain, calculated as the difference between GPS altitude above sea level and the elevation of the ridge at the corresponding latitude for the binned slice data. Negative values are an artefact of the binning. Altitudes above ≈175m are are primarily from thermalling flight. 82.3% of the bird's flight was spent at an altitude of 100m or less above the ridge.

We can test this from our data set by correlating estimated wind speed with the mean altitude above the ridge (a histogram of the bird's altitude relative to the ridge is shown in Figure 4.8). This is complicated by the fact that at lower wind speeds, the bird spends more time thermalling which increases his average altitude. If the thermalling sections of flight are excluded from the calculation of mean altitude for a given flight day, we find that the regression of wind speed against mean altitude is not significant ($n = 17$, $R^2 = 0.19$, $p = 0.079$). Similarly, testing wind speed

with average distance from point of maximum updraft on the ridge also shows no significance ($n = 17$, $R^2 = 0.15$, $p = 0.128$), see Figure 4.11 for calculation of this. This could be due to the inaccuracy of the wind data or insufficient statistical power to discern the effect, but alternatively suggests that the bird does not fly according to a constant airspeed strategy and instead actively adjusts his flight to fly either at an optimum airspeed and/or at an approximately constant altitude. This hypothesis is explored further in Chapter 6.

Another plausible objective is that the bird might aim to maximise altitude, and consequently its potential energy during a flight. Assuming the bird has a minimum sink rate of -0.54ms^{-1} (calculated using the traditional Pennycuick (1989a) polar model, see Chapter 5), the bird will be able to maintain altitude in regions where the updraft is $\geq$0.54ms^{-1}. From the CFD data, the bird should therefore be able to reach altitudes above the terrain of at least 550m to 600m, regardless of the wind direction but assuming wind speeds of at least 5ms^{-1} (which is less than the average wind speed he was flown in). Nevertheless, at no point during the flights does the bird come close to this altitude whilst ridge soaring; from Figure 4.8, max altitude above the ridge was 428m and this corresponded to thermalling flight. This implies that the bird is not attempting to maximise altitude.

Climb rate and predicted updraft strength

The predicted updraft at the bird's recorded GPS location can be extracted from the CFD model by finding the nearest point in the mesh (using the *scatteredInterpolant* function in MATLAB). Figure 4.9 shows the flight trajectories, each coloured by predicted updraft as estimated from the CFD model with inflow conditions that match the recorded measured wind direction on the day, and scaled for the mean wind speed. The predicted updraft where the bird flies is always positive as he never ventures out beyond the top of the upper ridge into the regions of sink (range is 0 to 9.16ms^{-1}). On days with stronger winds, the estimated updraft will be stronger; however, the accuracy of these results is limited by the accuracy of the wind speed

measurements for the free stream conditions at Hay Bluff.

Qualitatively comparing the predicted updraft strength with the climb rates recorded from on board the bird (Figures 4.6 & 4.9), the climb rate data is considerably noisier and covers a wider range. This is because the bird is not simply gliding at a constant airspeed throughout the flights but performs manoeuvres and changes airspeed which will alter its inherent sink rate according to the glide polar (Pennycuick 1989a). In addition to the bird actively adjusting its flight, small scale gusts and thermals which are not modelled by the CFD analysis will also have an effect. Despite the considerable noise, as expected the average predicted updraft over all flights is higher than the bird's average climb rate. This is due to its natural sink; the mean predicted updraft is 2.56ms^{-1} $\pm 1.76\text{ms}^{-1}$.

We fitted a linear ANOVA, type 1 model to the climb rate data as a function of *flight number*, normalised *predicted updraft* and the interaction between *flight number* and *predicted updraft*, to determine whether there is any correlation between the CFD model and our actual measurements. Due to the uncertainty of the wind velocity estimates, the predicted updraft was calculated only from the NW inflow condition and not scaled by wind speed. Instead, the difference in wind conditions between flights was accounted for by the *flight number* parameter in the model; the interaction between flight day and predicted updraft estimates of the wind conditions. The model was significant overall ($F_{43,333294} = 190.78$, $p < 0.0005$, $\text{R}^2 = 0.024$) but explains very little of the variance, which is likely due to the bird's changing morphology and airspeed. Each parameter in the model was also significant: flight ($F_{21,333294} = 3.71$, $p = 0.001$), predicted updraft ($F_{1,333294} = 3047.08$, $p < 0.0005$) and the interaction between flight and predicted updraft ($F_{21,333294} = 241.84$, $p < 0.0005$).

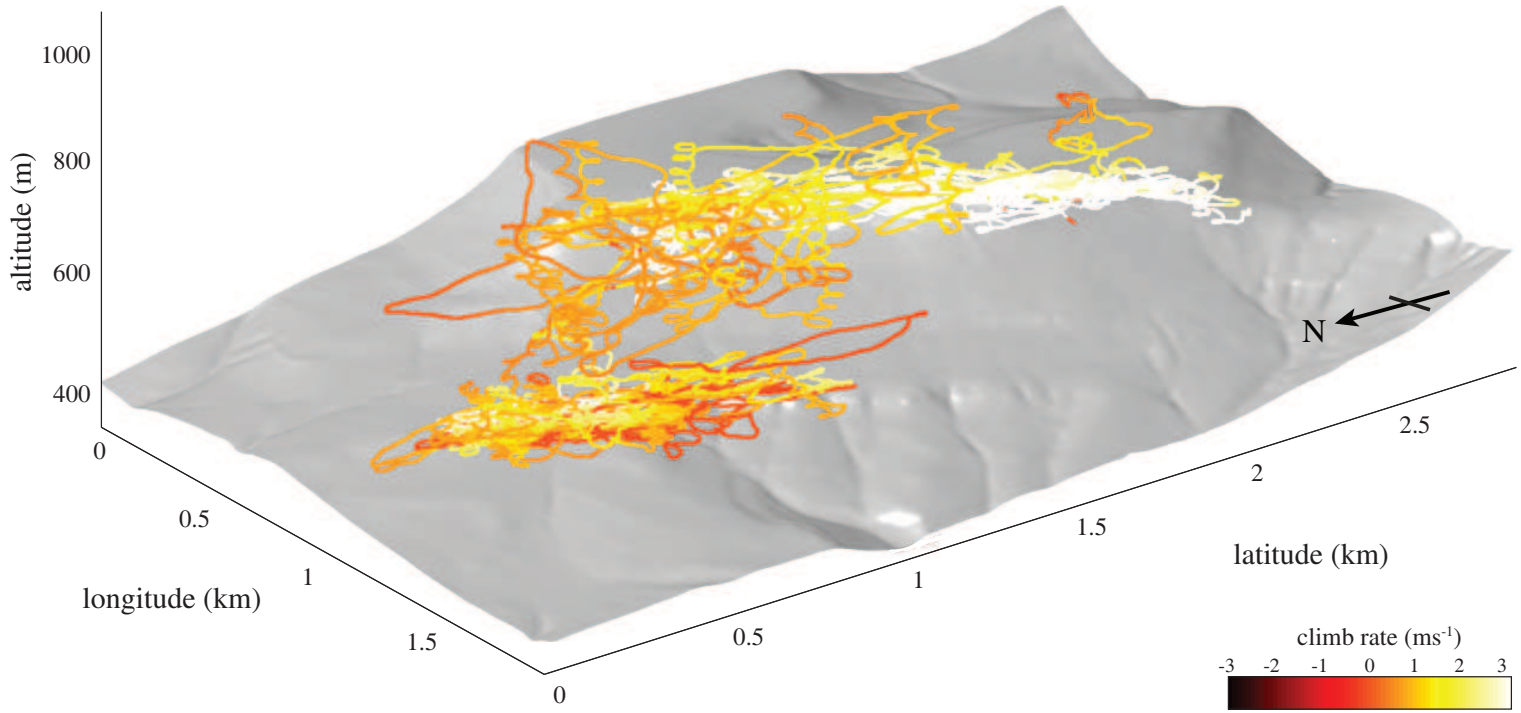


Figure 4.9: GPS tracks of our steppe eagle, coloured by the estimated updraft strength predicted from CFD analysis which was calculated from the approximate inflow condition that matched the wind direction for the flight day and subsequently scaled by wind velocity. The strongest updrafts are predicted when the bird is closest to the crest of the two ridges.

Performance comparison

The comparison between where the bird flew and the predicted updraft in Figure 4.7, strongly suggests that the bird selects optimum updrafts when slope soaring. However, precisely quantifying the bird's performance is difficult as we have no reference with which to compare the performance measures.

One way of testing the bird's performance is to compare the bird's actual trajectory along the ridge with the same flight pattern, but shifted by a constant displacement. In this way we can test, assuming a fixed flightpath, whether the bird is in the optimal position relative to the ridge. As our measure of the performance for each shifted trajectory, we use the predicted updrafts at each sample point (calculated from normalised NW inflow condition data) and take the mean over the entire set of flights. This is a measure of the mean updraft potential experienced by the bird.

Figure 4.10 shows the results of systematically shifting the GPS trajectory in three directions: perpendicular (x) and parallel (y) to the line of the ridge and vertically (z). Parts of the track which were positioned under the terrain after the track was shifted were excluded from the mean.

From Figure 4.10a-c, in each direction the performance decreases the further the track is shifted from the original position (0m displacement). There is obviously a fairly rapid decrease in performance for negative x-displacement and positive z-displacement as the track is moved further from the strongest updrafts, away from the ridge. The performance decrease when the flights are shifted parallel to the ridge (Figure 4.10b) is relatively minor as the variation in the updraft pattern in this direction is minimal.

The same data are shown in Figure 4.10d-f, but are focused on the narrow band around the optimum, between $\pm$15m displacements. For the x and z directions, the optimal position of the data is at 10m and 6m of the original position respectively, and represents a difference in performance of $<$1.5%. This suggests that our bird is on average flying very close to the optimum.

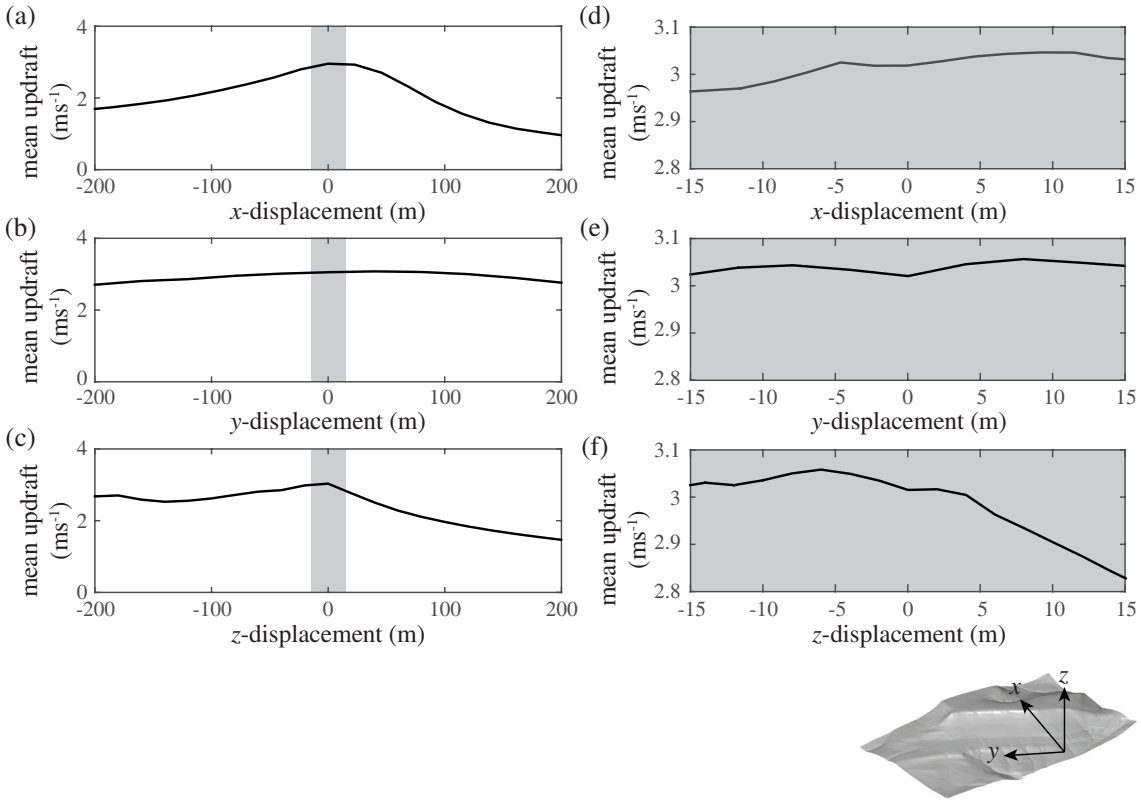


Figure 4.10: Performance of GPS track position calculated as the mean of the potential updraft across all flights (based on the inflow condition NW). (a) GPS track shifted perpendicular to the line of the ridge, where a positive shift moves towards the ridge, (b) GPS track shifted along the ridge line (parallel) where positive is in approximately a north-easterly direction, and (c) GPS track shifted vertically where positive is up. Performance decreases as the track is shifted further away from the original position. Grey strips highlight the narrow range which is examined at a higher resolution in (d), (e) and (f) for each direction. Optimal position is at -4m, -8m and 4m for x, y and z directions respectively, which effectively is a shift towards the hill and closer to the stronger updrafts.

If we consider that for each perpendicular slice through the terrain there is a point of maximum updraft predicted from the CFD analysis at the top of both the upper and lower ridge, from our binned GPS data, it is then simple to calculate the distance of the bird from the maximum updraft point on one or other of the ridges (based on whichever ridge the bird is closest to). This is plotted as histograms in Figure 4.11 for both vertical and horizontal distance. Thermalling sections of flight account for the higher values. We find that 75.4% of the bird's total flight was spent within 100m of the maximum updraft point, on a given ridge but that there is large variation. Given this, the optimal track shift of approximately 11.7m from

Figure 4.10 (10m x-shift and 6m z-shift) is small in comparison.

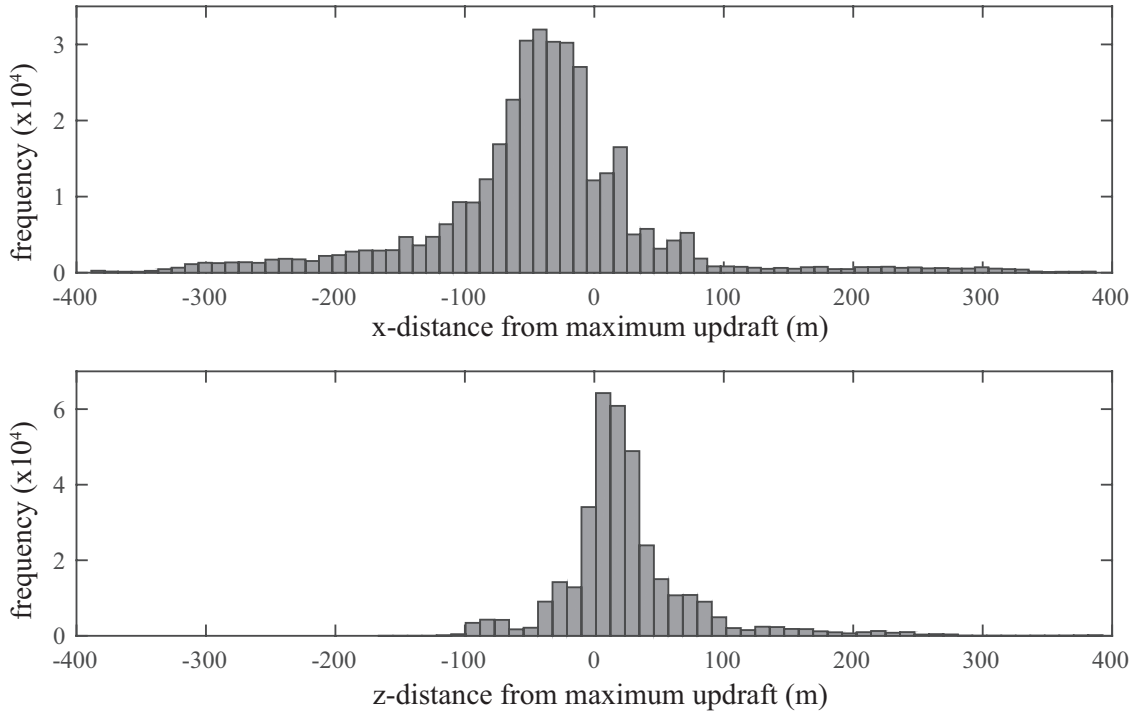


Figure 4.11: Histogram of the bird's distance from the point of maximum updraft on either the upper or lower ridge, depending on which is closer. (a) Perpendicular distance, (b) vertical distance. This was calculated from the flight data which was binned for each slice cutting through the ridge perpendicularly (as in Figure 4.7). For each slice, the point of maximum updraft on both the upper and lower ridges was identified.

4.4 Discussion

In this chapter we have illustrated how using CFD analysis is both a feasible and informative approach to analysing the soaring strategies of birds. Obviously the CFD model is an over simplification of the air flow and in reality there will be other factors for the bird to cope with such as thermal turbulence, wind gusts or a non-uniform inflow, but this analysis provides a good basis for understanding the underlying characteristics of the airflow.

In this particular case study, the results of predicted updraft patterns are per-

haps unsurprising; glider pilots have long followed the basic rule that for an ideal, semi-circular hill, we would expect the maximum updraft to extend in a plane perpendicular to the hill (Reichmann 1993). This is exactly what our results show and given the relatively smooth terrain and lack of substantial obstructions leading up the ridge, there are few patches of turbulence. Nevertheless, the difference between wind directions was unexpected and highlights the need for a suitable range of terrain to be included in the CFD domain.

However, the problem of determining suitable inflow conditions based on the wind measurements is a serious limitation that should be tackled in any future study on more complex flows, where changes in wind direction could have a more significant effect on the results. Preferably, measurements of the free stream wind velocity should be taken from a number of locations along the inlet boundary to the CFD model. Ideally the wind data would also be coupled with a full set of airspeed data from on board the bird, which will provide local samples of the atmosphere for comparison.

Results indicated that the bird does predominantly fly in the region of strongest updraft along the ridge, and that he explores different regions of space when slope soaring and thermalling. This was shown by the performance analysis of GPS track position and the qualitative comparison between updraft strength and position of the bird on the ridge. Although in such terrain (where the flow is fairly uniform and smooth) this may be unsurprising it nevertheless has not been quantified before and is a proof of principle.

This analysis leads to questions about the bird's motivation and flight strategy. Whilst slope soaring, our bird was not maximising his potential energy. Maximum total energy can be achieved at the highest altitudes; however, to achieve these altitudes in the first place the bird must work hard. Whether the greater total energy is worth the effort depends on what the bird's flight objective is. In the case of our steppe eagle there is little motivation to soar at very high altitudes as he is not attempting to travel long distances, but rather might desire to keep the falconer

(and the food) in sight. Migrating birds on the other hand are likely to climb higher in anticipation for when they leave the ridge line and the sources of lift become unreliable.

We also found no significant correlation between where the bird flew and the measurements of wind velocity for different flight days. Although we cannot eliminate the possibility of a constant airspeed, constant altitude strategy (i.e. the bird flies at same airspeed every day whilst altitude is constant for a specific flight but changes with day), this suggests that the bird does not soar at a constant airspeed but adjusts airspeed either based on the perceived updraft strength as an in-built optimisation mechanism, or to actively maintain a constant altitude relative to the ridge (regardless of wind strength). Alternatively of course he may not aim to optimise any parameter at all, but instead is aimlessly wandering up and down the ridge, and possibly enjoying the freedom. We explore the hypothesis that the bird is adjusting his airspeed according to the wind components in Chapter 6.

For future CFD studies, the next step will be to look at more interesting, complex geometries such as terrain with sharp gradient changes, valleys and spurs, or urban terrain—examining individual buildings or entire cities. This will allow researchers to explore how well birds perform in these more adverse and unpredictable environments, determine the flight objectives of wild species, and to test theories such as whether flightpaths change in different conditions. In addition, this could inform the developement of a set of governing rules for algorithms, which will allow UAV's to fly and soar in unmapped environments autonomously.

Chapter 5

Theory of gliding flight

5.1 Introduction

The glide polar is a convenient tool for characterising the gliding performance of any bird, or other complete airframe. The polar curve describes the relationship between a bird's airspeed, relative to the atmosphere, and its corresponding rate of altitude loss (sink rate) when flying at equilibrium (Pennycuick 1998; Tucker 1987; Tucker 1988). Performance measures, including the minimum (stall) speed (V_{stall}), minimum sink speed (V_{min}) and best glide speed (V_*), can be easily extracted either directly from the graph itself or from the equation that defines the curve (Ákos et al. 2008; Reichmann 1993). These parameters form the foundation of speed-to-fly calculations for efficient flight, the most famous of which is the McCready theory (McCready 1954; Reichmann 1993). Glide polars can be derived theoretically from the fundamentals of aerodynamics, but extracting a glide polar experimentally from a free-flying bird has long presented a challenge. By definition, the polar describes flight in nil wind conditions and accurately measuring the movement of the atmosphere at a bird's precise location is notoriously difficult (Pennycuick 1989a), even if the movement of the bird relative to the ground is somehow known. Consequently

the polar has been determined experimentally for relatively few species of bird (see Chapter 6) and often with insufficient accuracy for more subtle calculations of aerodynamic performance (Tucker and Parrott 1970).

Due to sparse and often noisy data obtained from these experiments, researchers tend to rely on the theoretical derivation of the polar for studying flight performance—which often bears little resemblance to the experimental data (Pennycuick 1971b). As shown in this chapter, the accuracy of the theoretical polar is highly dependent on the model and coefficients chosen, which have a substantial effect on the shape of the curve. Although they may be derived from rigorous aerodynamic theories, current coefficient estimates are little more than an educated guess, in the sense that the flight morphology of the bird is more complicated than such models can capture and varies continuously in flight. In addition, although the glide polar may be a valuable tool for fixed-wing aircraft, for birds which have multiple control surfaces and rarely fly in steady wind conditions, the polar may not be the best approach for understanding their flight. This will be dicussed further in Chapter 6.

5.2 The glide polar model

Whilst a bird is gliding, in still air, at a steady airspeed (V), it is considered to be at equilibrium and the net forces acting on the bird must be zero (Figure 5.1). The total aerodynamic force (F) can be resolved into a lift (L) component perpendicular to the airflow and a drag (D) component parallel to the airflow. Given that there is no thrust generated in a glide, the weight of the bird (mg) must be balanced by the total aerodynamic force ($F = mg = \sqrt{(L^2 + D^2)}$), where m is the bird's mass and g is gravitational acceleration. The bird inherently loses altitude at a rate V_s (sink speed) which, for a given airspeed, results in a glide angle α where $\sin(\alpha) = V_s/V$. It is also clear from Figure 5.1 that $\tan(\alpha) = D/L$, therefore the ratio of horizontal to vertical velocity corresponds to the ratio of lift to drag. The small angle approximation can be applied for glide angles of $\alpha < 10°$, such that

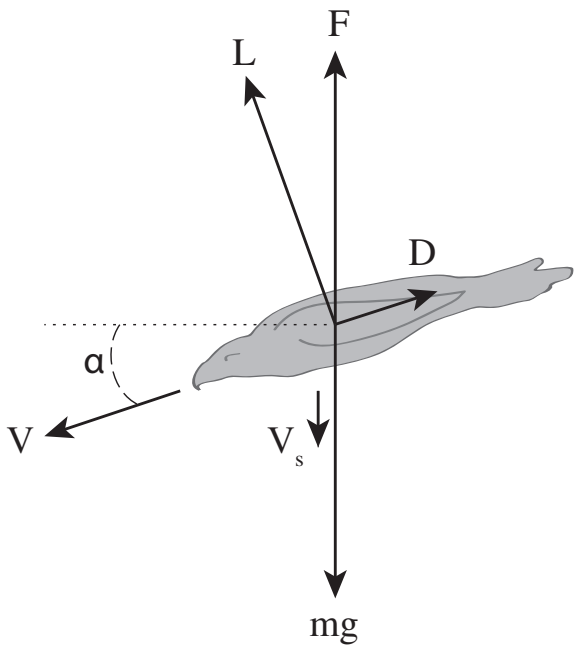


Figure 5.1: Forces acting on a bird whilst gliding at equilibrium at airspeed V and angle α. Total aerodynamic force ($F = mg$) is comprised of a lift force component (L) acting perpendicular to the oncoming airflow and a drag force component (D), acting parallel.

$\sin(\alpha) = \tan(\alpha) = \alpha$. Consequently for the majority of airspeeds at which birds fly, the lift force is assumed to approximately equal the weight of the bird ($L \approx mg$) and the relationship between V and V_s that describes the glide polar is dependent on the total drag generated:

$$V_s = \frac{VD}{mg} \tag{5.1}$$

Note that all airspeeds referred to in this chapter are equivalent airspeed standardised to sea level atmospheric conditions. The standard equation for drag force is:

$$D = \frac{1}{2}\rho V^2 S C_D \tag{5.2}$$

where ρ is air density at sea level (assumed to be 1.225kgm^{-3}), S is wing area and C_D is the drag coefficient. Total drag can be calculated by separating it into its additive components: induced (D_i), parasite (D_{par}) and profile (D_{pro}) drag. Estimates of the corresponding drag coefficients can therefore be used to generate the theoretical glide polar for a given bird or aircraft. This method is described in many aerodynamic

text books, see also (Pennycuick 1989a; Pennycuick 2008; Taylor and Thomas 2014; Tucker 1987).

5.2.1 Induced drag coefficient

Classical aerodynamics calculates the lift induced drag coefficient ($C_{D,i}$) from lifting line theory as (Pennycuick 1989a; Taylor and Thomas 2014):

$$C_{D,i} = \frac{k{C_L}^2}{\pi \text{Æ}} \tag{5.3}$$

where C_L is the lift coefficient and Æ is the aspect ratio of the bird calculated from wingspan (b) and wing area (S) as $\text{Æ} = b^2/S$. k is a dimensionless induced drag factor which represents the ratio of the induced drag predicted from theory to that obtained in practice, the difference is due to deviation from an ideal elliptical lift distribution in real wings. For gliders, k is expected to be about 1.1 and the same value has been frequently applied to bird flight (Pennycuick 1989a) though some studies have suggested that for birds this should be lower, and possibly even less than 1 for certain species (Pennycuick 1971b; Pennycuick et al. 2013; Raspet 1960). It is speculated that k will also change with any adjustment to wingspan that results in a non-elliptical lift distribution, but as yet any such effect has not been quantified (Tucker 1987) and given the relatively small impact k has on the shape of the polar (see Figure 5.6c) the accuracy of this constant is not critical.

From the assumption $L = mg$ during equilibrium gliding, C_L can be predicted from the standard lift equation as:

$$C_L = \frac{2mg}{\rho V^2 S} \tag{5.4}$$

Substituting this into Equation 5.3, the induced drag coefficient can therefore be rewritten:

$$C_{D,i} = \frac{4km^2g^2}{\pi\rho^2 V^4 S b^2} \tag{5.5}$$

5.2.2 Parasite drag coefficient

Parasite drag (also referred to as body drag) is due to both form and friction drag generated by the bird's body, which includes the head, tail and feet (Hedenström and Liechti 2001; Tucker 1987). As a bird's body is streamlined, the drag generated by its body frontal cross sectional area is less than the drag generated by a flat plate with the same area; this difference is accounted for by the parasite drag coefficient, $C_{D,par}$ (Pennycuick 1989a).

In most cases, $C_{D,par}$ is quoted proportional to the body cross sectional frontal area (S_b) rather than wing area (Hedenström and Liechti 2001; Tucker 1987). Based on the assumption that body shape is the same in all birds, S_b has been empirically derived proportional to the bird's mass as (Pennycuick 1989a):

$$S_b = 8.13 \times 10^{-3} m^{2/3} \tag{5.6}$$

Alternatively, on the pragmatic grounds that body frontal areas have not been measured for many species, Taylor and Thomas (2014) recently proposed that $C_{D,par}$ be approximated based on a correlation with wingspan, whilst Tucker (1987; 1990) previously advocated an approach common in aeronautics, where the estimated body frontal area and the drag coefficient are combined as one constant of equivalent flat plate area (S_{fp}). This he also empirically related to the bird's mass:

$$S_{fp} = S_b C_{D,par} = 3.34 \times 10^{-3} m^{2/3} \tag{5.7}$$

Effectively Equation 5.7 results in $C_{D,par} = 0.407$, independent of speed or size of bird, if S_b is calculated as in Equation 5.6. Fundamentally the choice of reference area has no impact on the polar itself, provided that $C_{D,par}$ is modified accordingly, but can be a source of confusion between studies. In this chapter we stick to the convention of quoting all values of $C_{D,par}$ relative to S_b, using the above equations to convert values where necessary.

Multiple attempts to measure $C_{D,par}$ for a range of species have resulted in values ranging between 0.14 and 0.77 (Hedenström and Liechti 2001; Henningsson and Hedenström 2011; Pennycuick et al. 1988; Pennycuick et al. 2013; Tucker 1990). The majority of measurements have been made using force balances or wake rakes in wind tunnels, on dead and often frozen bird bodies which have had the wings removed. However, these methods are often believed to result in overestimates of $C_{D,par}$ as interference drag is generated by the support (Pennycuick et al. 1988; Tucker 1990) and bodies have greater drag alone than their contribution when the wings are still attached (Tucker and Heine 1990).

Hedenström and Liechti's (2001) field measurements of body drag in passerines also reported a wide range of results but suggested a value of 0.4 for $C_{D,par}$ was suitable; this is fairly similar to Tucker's estimate from Equation 5.7. However these measurements assumed the atmosphere had no systematic effect on the results—e.g. vertical winds could have caused overestimates of drag. Based on the same study, Taylor and Thomas (2014) proposed that for larger soaring species which have more streamlined bodies, 0.37 is more appropriate.

The most commonly used value of $C_{D,par}$ is in fact 0.1 which was recommended by Pennycuick (1996) for birds with streamlined bodies based on a study of wingbeat frequency measurements. Although Pennycuick suggests that real flight results in lower $C_{D,par}$ than the values recorded in wind tunnel studies, 0.1 is still considerably lower than has ever been recorded. This is the value used in Pennycuick's (1989b) *Flight* program for estimating glide polars.

Although 0.1 is now generally used as the default value, it fails to take account of any effects of Reynolds number (Re) or airspeed on the parasite drag and the same value is used regardless of the species. Some researchers have suggested that there is evidence $C_{D,par}$ varies with both speed and size of bird (Pennycuick 1989a; Prior 1984). Pennycuick's earlier version of *Flight* did attempt to correct for bird size. Based on wind tunnel studies he approximated that birds with $Re < 50,000$ (calculated relative to body diameter) should use $C_{D,par} = 0.4$ whilst larger birds

with $Re > 200,000$ have $C_{D,par}$= 0.25, with a linear relationship for the intermediate values (Pennycuick et al. 1988). For a steppe eagle, this predicts $C_{D,par} \approx 0.29$ which is similar to the measurements recorded for a bald eagle (Pennycuick et al. 1988). It seems sensible that there should be some distinction between large soaring birds and small passerines, given their different morphologies.

Although in reality $C_{D,par}$ will increase at lower airspeeds (Pennycuick et al. 2013), it is universally assumed to be constant over the range of airspeeds used by birds, as the change in parasite drag is considered insignificant when compared to the variation seen in the induced and profile drags (Pennycuick 1989a; Taylor and Thomas 2014; Tucker 1987), see Figure 5.10.

Clearly there is considerable discrepancy in the literature over the appropriate value for $C_{D,par}$, and its dependency on a bird's size and shape is not well understood. The accuracy of the $C_{D,par}$ measurements depend considerably on the accuracy of the S_b calculation. Moreover, we do not know what the effect of changing wingspan will be; it is unlikely the body will have the same drag when wings are fully outstretched as when they are entirely folded, as might happen during a steep dive. During real flight, additional parasite drag will be generated when the bird spreads or lowers its tail, extends its feet or is yawed relative to the wind resulting in a side-slip angle (Pennycuick et al. 1988; Rosén and Hedenström 2001). These transient and unpredictable changes to $C_{D,par}$ could introduce significant error and noise in an experimentally generated glide polar. Consequently the chosen $C_{D,par}$ is never more than a best guess yet has a considerable impact on the shape of the polar curve.

5.2.3 Profile drag coefficient

Profile drag is caused by form and friction drag on the wings. This parameter is extremely difficult to measure. Many indirect estimates of $C_{D,pro}$ have been made by subtraction of the estimated induced and parasite drag components from measured total drag (Henningsson and Hedenström 2011; Pennycuick 1968; Tucker and Heine 1990; Tucker and Parrott 1970) but the accuracy of this method is highly sensitive

to the chosen value of $C_{D,par}$, which we have already shown is unreliable. It was also suggested that profile drag could be estimated as a proportion of the minimum combined parasite and lift induced drags (Pennycuick 1989a; Tucker 1973).

Direct measurements of profile drag on a Harris's hawk were attempted by Pennycuick (1992) using wake sampling in a wind tunnel. The default choice of 0.014 for $C_{D,pro}$ in Pennycuick's *Flight* program was based on this study (Pennycuick 1989b; Pennycuick 2008), though Tucker and Heine's (1990) estimate using the subtractive method for $C_{D,pro}$ on the same Harris's hawk individual resulted in a much higher mean of 0.026.

It is often assumed that $C_{D,pro}$ is constant, which is approximately true over the medium to high airspeed range, but at low airspeeds (and Reynolds numbers) $C_{D,pro}$ is highly influenced by the lift coefficient as the boundary layer becomes more likely to separate (Pennycuick 1989a; Pennycuick et al. 1992); $C_{D,pro}$ should therefore increase as Re decreases. As such, Taylor and Thomas (2014) propose that $C_{D,pro}$ can be estimated according to the classical laminar boundary layer solution for a flat plate (Tucker 1987; Van Dyke 1975):

$$C_{D,pro} = 2\Big(\frac{1.328}{\sqrt{Re}}\Big) \tag{5.8}$$

$$Re = \frac{\rho V S}{\mu b} \tag{5.9}$$

where μ is the dynamic viscosity of air (assumed to be 1.983×10^{-5} kgm^{-1}s^{-1} at sea level in the standard atmosphere). If we calculate $C_{D,pro}$ from Equation 5.8 for our steppe eagle, using the dimensions in Table 5.1, we find that over his normal airspeed range (approx. 10 to 25ms^{-1}, see Figure 6.3), $C_{D,pro}$ is on average just $0.0049 \pm 6.8 \times 10^{-4}$. This is considerably smaller than the default 0.014, though as the wings are not ideal flat plates it is expected to be an underestimate.

$C_{D,pro}$ is also influenced by the shape and smoothness of the wing surface, as well as the unknown effects of the bird's tail which generates aerodynamic force depending on its orientation (Hedenström and Liechti 2001; Thomas 1993). Any

twist along the wings will have an effect, and it seems likely that birds will actively move their wings to locally adjust $C_{D,pro}$ at specific chord locations (Pennycuick et al. 1992). These non-systematic effects will add noise to the experimental data. However, changing wingspan may have a systematic effect on the minimum $C_{D,pro}$ achievable at each airspeed. As with $C_{D,par}$, there is clearly huge variation in the literature over the correct method for estimating $C_{D,pro}$, though again no variation between species with entirely different wing morphologies is accounted for.

5.2.4 Fixed-wingspan polar model

By substituting the three drag components into Equation 5.1, we get the following relationship between sink rate and airspeed that defines the glide polar:

$$V_s = \frac{2kmg}{\pi\rho b^2 V} + \frac{\rho V^3 (SC_{D,pro} + S_b C_{D,par})}{2mg} \tag{5.10}$$

Conventionally V_s, which is positive as the bird loses altitude, is plotted along the vertical axis increasing downwards. If both $C_{D,pro}$ and $C_{D,par}$ are taken to be constant in Equation 5.10, we get the general form of the glide polar that has long been used for birds:

$$V_s = \frac{c_1}{V} + c_2 V^3 \tag{5.11}$$

where c_1 and c_2 are constants. This is the classic fixed wingspan model which can be applied to any aircraft.

5.2.5 Variable-wingspan polar model

The glide polar describes the minimum sink rate a bird can achieve for a given air speed in still air, at a set wingspan. However, the bird is not constrained to fly only along this single performance curve (Tucker 1987; Tucker 1988) and indeed the selection of flight speed can be influenced by a multitude of factors. For example, the bird may not aim to optimise glide angle or distance travelled but might purposefully

dive in order to land, capture prey, escape gusts or predators (Bruderer and Boldt 2001). Instead of a single curve, there is therefore a 'performance area' (a term coined by Tucker in 1987) in which the bird can fly by adjusting its wing morphology, or by extending its feet to increase drag (Tucker 1987), Figure 5.11.

The effect of changing wingspan can be incorporated into Equation 5.10 by including a span coefficient (β) which is the ratio of wingspan to the maximum possible span ($\beta = b/b_{max}$). β is equal to 1 when the wings are fully spread (Pennycuick 1989a). It has been observed to a first approximation that the relationship between span and wing area is linear with a slope that does not differ significantly from unity (Hedenström and Liechti 2001; Pennycuick 1989a). This implies that the mean chord does not change notably with a reduction in span. The same span coefficient can therefore be used to adjust for the corresponding changes in wing area. Equation 5.10 then becomes:

$$V_s = \frac{2kmg}{\pi\rho\beta^2 {b_{max}}^2 V} + \frac{\rho V^3(\beta S_{max} C_{D,pro} + S_b C_{D,par})}{2mg} \tag{5.12}$$

However, there is substantial evidence that this approximation is not valid for all species (Rosén and Hedenström 2001), with Tucker (1987) proposing a more formal calculation of the relationship between span and area which we do not cover here.

There is very little experimental data available on how wing morphology changes at different flight speeds. Hedenström and Rosén (2001) used wind tunnel tests of three species (jackdaw (Rosén and Hedenström 2001), Harris's hawk (Tucker and Heine 1990) and laggar falcon (Tucker and Parrott 1970)) to study the relationship between wingspan and airspeed. They found that the correlation was approximately linear for each species over the range of airspeeds tested, and that the slope of the relationship was dependent on the bird's stall speed, V_{stall}. An empirical formula to predict wingspan coefficient (β_e) was derived as:

$$\beta_e = \frac{5}{4} - \frac{V}{4V_{stall}} \tag{5.13}$$

This assumes that wingspan and area are both maximal at the stall speed. V_{stall} is calculated from the lift equation for the maximum lift coefficient $C_{L,max}$:

$$V_{stall} = \sqrt{\frac{2mg}{\rho S C_{L,max}}} \tag{5.14}$$

If no data are available on the maximum lift coefficient, it is assumed $C_{L,max} = 1.8$ (Pennycuick 2008; Rosén and Hedenström 2001). This model is plausible, however we might expect it to break down at higher airspeeds where it would otherwise result in negative wingspan. Hedenström limits the minimum value of β_e to 1/3, though again this is likely to change for birds with different morphologies.

If we take the assumption from Equation 5.13 that β_e is linearly proportional to V, β can be replaced by $\beta_e = \gamma + \eta V$ in Equation 5.12 (where $\gamma = 1 - \eta V_{stall}$). The polar model, accounting for linearly varying wingspan, then becomes:

$$V_s = \frac{2kmg}{\pi\rho(\gamma + \eta V)^2 {b_{max}}^2 V} + \frac{\rho V^3(\gamma + \eta V) S_{max} C_{D,pro}}{2mg} + \frac{\rho V^3 S_b C_{D,par}}{2mg} \tag{5.15}$$

Reducing the wingspan increases the induced drag, particularly at the lower airspeeds, but can cause a reduction in profile drag. Profile drag tends to decrease with wingspan until a critical point, beyond which it starts to increase again (Pennycuick 1989a), see also Figure 5.10. There is therefore an optimum point where the decrease in profile drag is larger than the increase in induced drag which allows the bird to achieve better sink rates (see Figure 5.10). The result is that reducing wingspan can in fact improve the glide ratio at higher speeds, resulting in lower sink rates. The set of best possible glide ratios that the bird can achieve by optimising its wingspan for each airspeed is known as the 'superpolar'. However, there is no evidence that birds actually use the superpolar (Pennycuick 2008).

Although the linearly varying wingspan model sees improvement in sink rate over the fixed-span model, it does not generate the optimum superpolar, as was demonstrated originally by Tucker (1987). Tucker derived an iterative method based on minimising the total drag in order to calculate the optimum wingspan coefficient

(β_{opt}) at each airspeed. This was later simplified by Pennycuick (1989a), who assumed the effect of changing wingspan on profile drag was negligible and that the same β could be used for span and area, resulting in:

$$\beta_{opt} = \left(\frac{8km^2g^2}{\pi\rho^2 b_{max}^2 S C_{D,pro} V^4} \right)^{\frac{1}{3}} \tag{5.16}$$

β_{opt} is derived from Equation 5.12 by solving $\frac{dV_s}{d\beta} = 0$. At the lower end of the airspeed range, Equation 5.16 results in $\beta_{opt} > 1$, which is anatomically impossible. It is therefore constrained to a maximum value of one. This means that at low airspeeds, whilst $\beta_{opt} = 1$, the superpolar will match the fixed wing polar model.

5.2.6 Performance area

The superpolar described by the optimum-wingspan model forms the upper limit of the performance area—which is the range of airspeeds and sink rates possible for the bird to glide at in still air, see Figure 5.2 (Tucker 1987).

The lower bound of the performance area (between points B and C) is described by the line $V = V_s$, where the weight of the bird is equal to the total drag ($D = mg$), in other words the bird is moving vertically downwards. We note that although theoretically possible, in real flight this is almost never observed, except perhaps during a stoop. Point C is the speed at which the bird descends fastest as it has reached its terminal velocity. This occurs when the bird's wings are fully closed and the only drag acting on the bird is parasite drag (Tucker 1987). Point C is therefore calculated as:

$$V = V_s = \sqrt{\frac{2mg}{\rho S_b C_{D,par}}} \tag{5.17}$$

Point B, the bird's slowest vertical descent rate, occurs when the bird is essentially parachuting down with wings fully outstretched and acting as flat plates perpendicular to the airflow. In this configuration, the profile drag is equal to 1 and there is no parasite or lift induced drag generated (Tucker 1987). The airspeed at point B

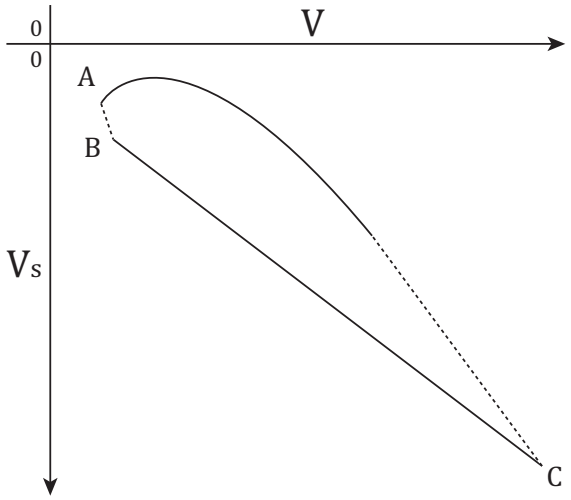


Figure 5.2: Schematic of the theoretical performance area for a gliding bird which encompasses the family of polar curves along which the bird can fly by changing its morphology. The upper boundary is defined by the bird's superpolar and the lower boundary is defined by $V = V_s$. Point A: minimum stall speed V_{stall}. Point B: minimum vertical descent rate. Point C: maximum vertical descent rate at terminal velocity.

is therefore simply:

$$V = V_s = \sqrt{\frac{2mg}{\rho S}} \tag{5.18}$$

Finally, point A represents the minimum airspeed the bird can achieve before stalling at $C_{L,max}$.

5.3 Theoretical glide polar for the steppe eagle

Using the theoretical models described above, the polar curves can be generated for any bird provided wingspan, wing area and body mass are known. But how much variation do the different forms of the model and choice of drag coefficients have on the shape of the polar and which should be used? We can examine this using the case study of our steppe eagle, whose morphological measurements have been well characterised and are shown in Table 5.1. For all theoretical polars presented here, $\rho = 1.225\text{kgm}^{-3}$ and $g = 9.81\text{ms}^{-2}$. We account for the weight of the onboard equipment ($\approx$0.07kg) by adding it to the bird's body mass, resulting in m=2.42kg.

In the absence of detailed knowledge about the spanwise loading distribution, we will assume ideal induced drag with $k = 1$, noting that the exact value of this coefficient has a comparatively small effect on the form of the polar.

parameter	value	units
m_b	2.35	kg
S	0.54	m^2
S_b	0.015	m^2
b	1.9	m

Table 5.1: Morphological measurements of the steppe eagle used in this study. Mean body mass (m_b) was calculated from daily measurements, not including mass of equipment. Wing area (S) and wingspan (b) are calculated from a photo silhouette of the bird with wings fully outstretched (Figure 2.1). Body frontal area (S_b) was calculated from Equation 5.6.

Figure 5.3 presents four polars calculated from the fixed-wingspan polar model in Equation 5.11, using the prominent combinations of parasite and profile drag coefficients proposed in the literature (Pennycuick 1989a; Pennycuick et al. 1988; Taylor and Thomas 2014; Tucker 1987). We see increasing differences between the four polars as speed increases; predictably the greater the sum of the two drag coefficients, the worse the performance. Given the range of coefficients used, the different curves are not unexpected but highlight the importance for appropriate selection of coefficients. Interestingly, the effect of the difference between $C_{D,par}$ for *polars 1* and *3* is partly cancelled out by the corresponding values of $C_{D,pro}$, resulting in a closer match between the curves than might have been expected.

5.3.1 Sensitivity of fixed-wingspan model to drag coefficients

Using *Polar 1* in Figure 5.3 as a reference with the default constants $k = 1$, $C_{D,pro} = 0.014$ and $C_{D,par} = 0.1$ referenced to body frontal area, the effect of changing the values of $C_{D,par}$, $C_{D,pro}$ and k are shown in Figures 5.4, 5.5 & 5.6 respectively. As well as parametrically varying the coefficients, the different values proposed in the

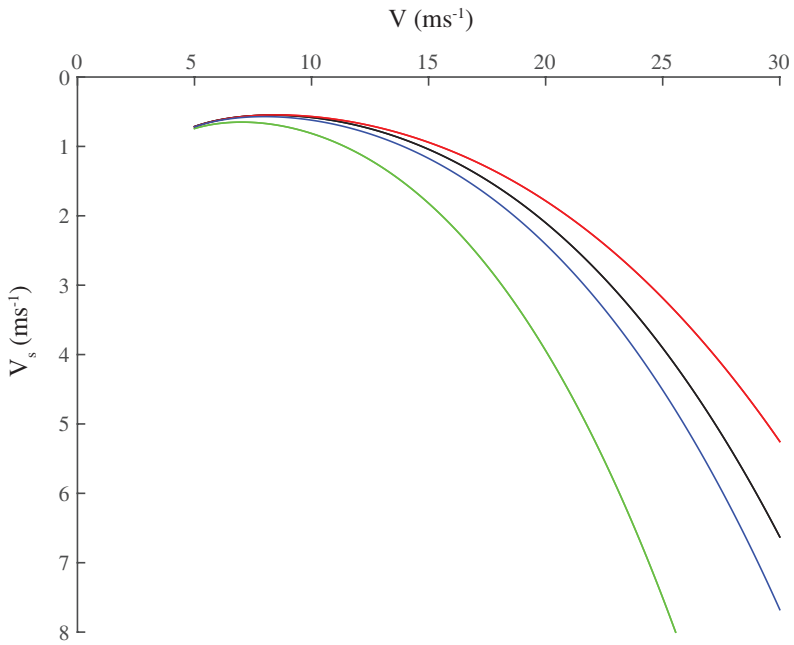


Figure 5.3: Theoretical glide polars for our steppe eagle calculated from Equation 5.11, showing the wide variation in the curves generated from the different drag coefficients frequently proposed in the literature. *Polar 1* (black) is currently the most widely used model, proposed by Pennycuick (1989b; 2008), with $C_{D,par} = 0.1$ and $C_{D,pro} = 0.0146$ (this is used as the reference polar). *Polar 2* (blue) is Pennycuick's (1989a) earlier iteration with $C_{D,par} = 0.28$ based on Re and $C_{D,pro} = 0.0125$, estimated from the minimum induced and parasite drag. *Polar 3* (red) is calculated from Taylor & Thomas (2014) with $C_{D,par} = 0.37$ and $C_{D,pro} = 0.0049$ which is the average value from Equation 5.8. *Polar 4* (green) uses $C_{D,par} = 0.41$ and $C_{D,pro} = 0.0228$ from Tucker's (1987; 1990) equations based on effective flat plate area and Re respectively. Sink rate increases (performance decreases) at higher airspeeds as the sum of the two drag coefficients increase.

literature are plotted.

As predicted from Equation 5.10, using a larger $C_{D,par}$ results in higher sink rates (Figure 5.4) and this effect increases with airspeed. For example, at 16ms^{-1}, approximately the mean airspeed recorded for our steppe eagle during gliding (see Chapter 6), a $C_{D,par}$ of 0.1 would predict $V_s = 1.19$ms^{-1} whilst with $C_{D,par} = 0.41$, $V_s = 1.67$ms^{-1}; a considerable difference of almost 0.5ms^{-1} (a 40% increase in sink rate).

$C_{D,pro}$ has an even greater impact on the polar, as shown in Figure 5.5 where the various estimates generate a much wider variety of polars as the wings contribute considerably more drag than the body. Also plotted in Figure 5.5 is the polar

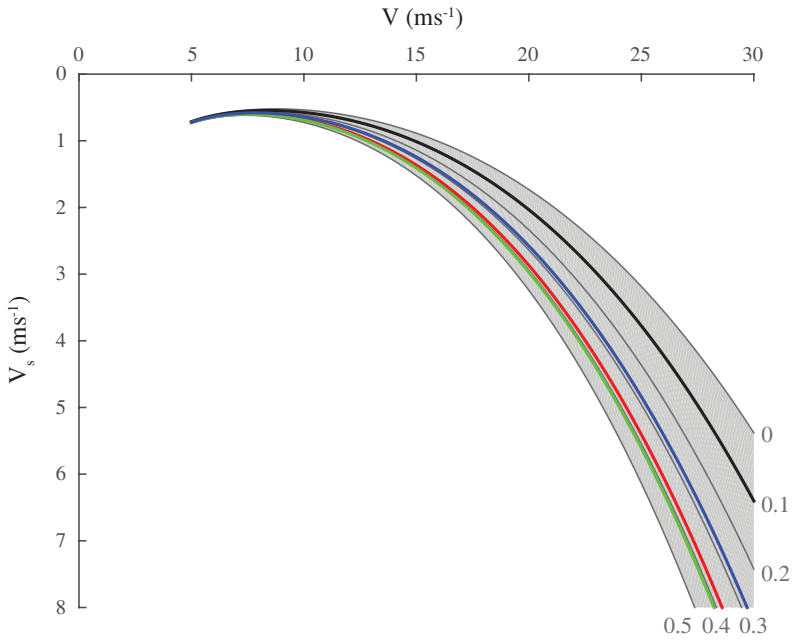


Figure 5.4: Theoretical fixed-wingspan glide polars for our steppe eagle showing the variation from different values of $C_{D,par}$ with default $C_{D,pro} = 0.014$ and k=1. Grey-lines: parametric effect of changing $C_{D,par}$ between 0 and 0.5. Black: $C_{D,par} = 0.1$. Blue: $C_{D,par} = 0.28$. Red: $C_{D,par} = 0.37$. Green: $C_{D,par} = 0.41$. As $C_{D,par}$ increases, sink rate increases and the difference becomes more pronounced at higher airspeeds.

generated using the varying, Reynolds number dependent value of $C_{D,pro}$, calculated from Equation 5.8. We see that the difference between this curve and the polar using the mean $C_{D,pro}$ from the same equation is extremely small over the range of airspeeds at which the bird usually flies (approx 10–25ms^{-1})—i.e. varying $C_{D,pro}$ with airspeed has a minimal effect. We can conclude that a constant value of $C_{D,pro}$ is therefore a valid simplification

As discussed previously, altering the values of k has little impact on the shape of the polar in comparison with the effects of the drag coefficients, and any change is only seen at the very low airspeeds. This is illustrated in Figure 5.6.

5.3.2 Effect of variable wingspan

To demonstrate how the different wingspan models change our bird's performance, we have computed each polar, arbitrarily using the current default drag coefficients

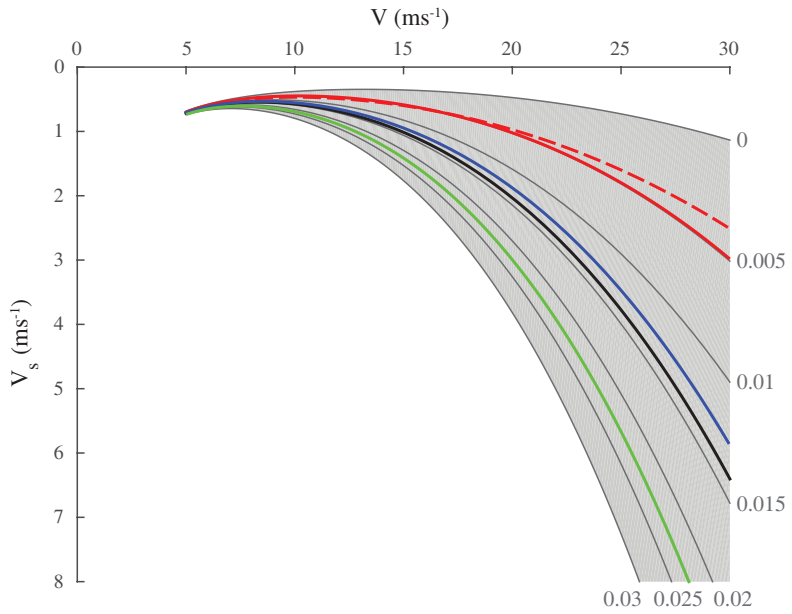


Figure 5.5: Theoretical fixed-wingspan glide polars for our steppe eagle showing the effect of changing $C_{D,pro}$ with default $C_{D,par}$ = 0.1 and k=1. Grey-lines: parametric effect of changing $C_{D,pro}$ between 0 and 0.03. Black: $C_{D,pro}$ = 0.0146. Blue: $C_{D,pro}$ = 0.0125. Red-dashed: $C_{D,pro}$ calculated from Equation 5.8, varies with airspeed. Red: mean $C_{D,pro}$ from Equation 5.8 = 0.0045. Green: $C_{D,pro}$ = 0.023. As $C_{D,pro}$ increases, sink rate increases. The range of $C_{D,pro}$ values in the literature has a much greater influence on the shape of the polar than the $C_{D,par}$ values.

($C_{D,par} = 0.1, C_{D,pro} = 0.0146$ (Pennycuick 2008)) given the uncertainty associated with the values. The resulting curves would therefore change considerably if different values were used as previously demonstrated, though the trends would be the same. Indeed, the effect of selecting different drag coefficients could have a larger effect on the shape of the polar than changing wingspan does.

Figure 5.9b compares the fixed, linear and optimal wingspan models for our steppe eagle and Figure 5.10 shows how the three drag force components change with airspeed for each model. For the optimum-wingspan model which results in the superpolar, β_{opt} was calculated from Equation 5.16 and predicted that up to speeds of 13.7ms^{-1} minimum drag is achieved at maximum wingspan ($\beta_{opt} = 1$, see Figure 5.9a); in this region the fixed-span and superpolar curves are the same. At higher airspeeds the β_{opt} starts to decrease and the superpolar achieves better sink rates.

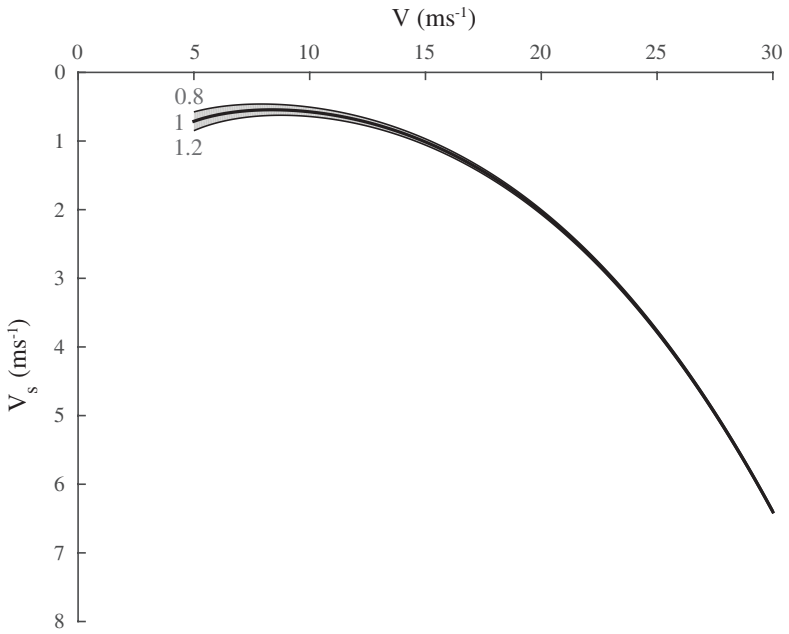


Figure 5.6: Theoretical fixed-wingspan glide polars for our steppe eagle showing the variation caused by the induced drag factor k, with default $C_{D,par} = 0.1$ and $C_{D,pro} = 0.014$. Grey-lines: parametric effect of changing k between 0.8 and 1.2. As k increases, sink rate increases at the low airspeeds.

β_e for the linear model was originally calculated using Equation 5.13, where $\eta = -0.0396$ for our bird, assuming $C_{L,max} = 1.8$. However, for our bird this model starts to breakdown at an airspeed of just 23ms^{-1} as this point corresponds with $\beta_e = 1/3$ which is the cut-off defined by Hedenström and Rosén (2001) for minimum wingspan. Not only is it highly unlikely that the bird maintains a constant wingspan when flying at the higher airspeeds, but from video footage, rarely do we see wingspans as small as 0.63m. Given that our bird is much larger and generally flies at higher airspeeds than the species used by Hedenström and Rosén to derive Equation 5.13, it is not unreasonable to assume our steppe eagle's change in wingspan is governed by different values of η and minimum β_e.

It was not possible to accurately model the relationship between wingspan and airspeed for our bird from the available video footage, but from scaling of images based on known dimensions (e.g. max wingspan, body length, etc.), we found that wings spans of <1m were rarely observed during steady flight, see Figure 5.7. There-

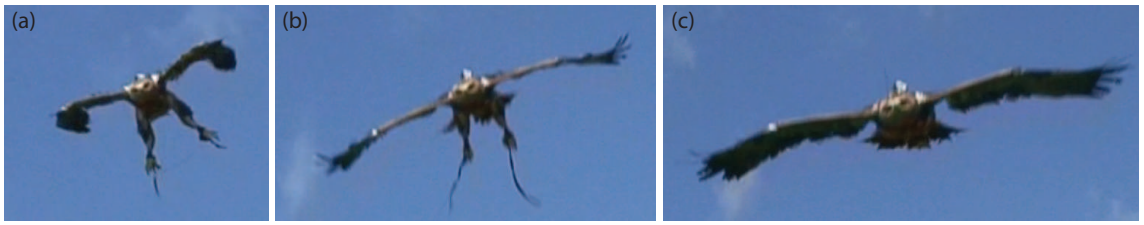


Figure 5.7: Video sequence illustrating the rapid change in wing configuration as wingspan changes between approximately 1.04m (frame (a)) to 1.8m which is slightly less than maximum wingspan (frame (c)) in just 0.2s. It also highlights how the legs can contribute dramatically to the parasite drag component generated by the body, and the changes in the tail configuration

fore perhaps a more appropriate minimum β_e is 0.5 for the range of gliding airspeeds we observed.

Figure 5.8 demonstrates the effect of η on the shape of the polar. As η initially increases from 0 (fixed-wingspan), the performance of the polar improves for higher airspeeds (>16.5ms^{-1}) until around η = -0.03, beyond which performance at all airspeeds starts to rapidly diminish. We also found the same optimal value of $\eta \approx -0.03$ for the three bird species used in Hedenström and Rosén's (2001) original wingspan study, based on the data provided in their paper and using the same drag coefficients as in Figure 5.8. It is likely however that optimum η will vary with the choice of drag coefficients. Of course below $\approx$ 16.5ms^{-1}, maximum wingspan is still optimal as was shown by the superpolar calculation, though the greatest difference in the polar sink rates in this range is just 0.07ms^{-1}.

If we use $\beta_e \approx 0.5$ for the highest airspeeds recorded for our bird when gliding ($\approx$ 25ms^{-1}), Figure 5.8a suggests that a suitable choice for η is between -0.02 and -0.03; in this range the polar is comparatively insensitive to the exact value of η (Figure 5.8b).

The linear-wingspan polar for η = -0.03 is compared with the other models in Figure 5.9b. As predicted, it performs better than the fixed-span polar at higher airspeeds but not as well at lower speeds. The optimum wingspan configuration is, by definition, predicted by the superpolar. However, the linear-wingspan polar is surprisingly similar given the extreme differences in β shown in Figure 5.9a up to

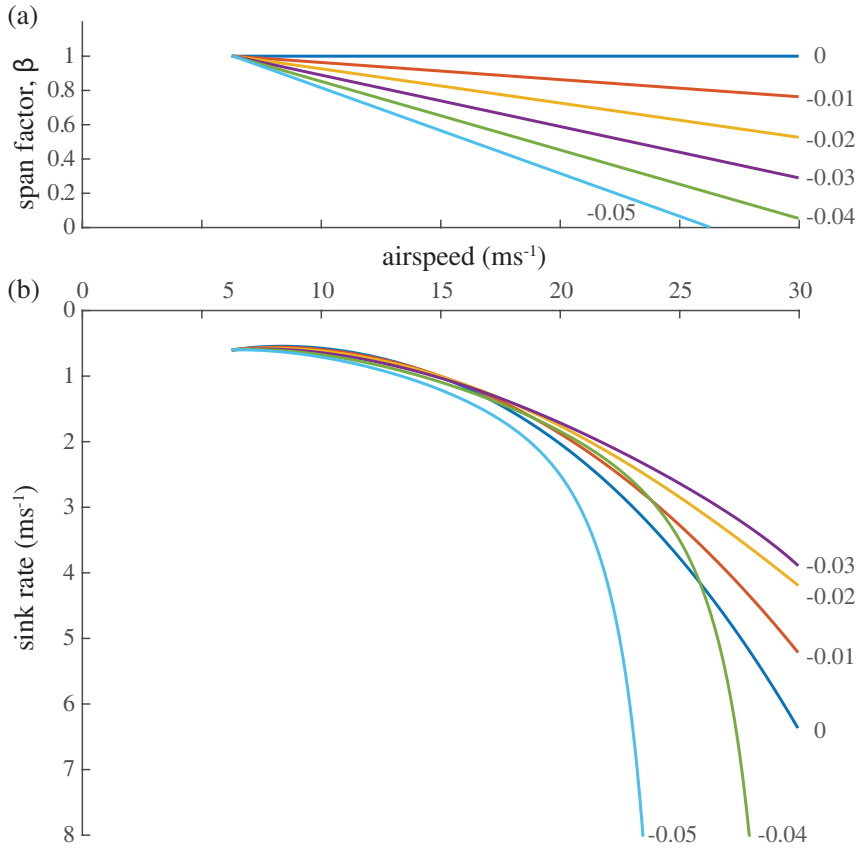


Figure 5.8: Effect of changing the slope (η) of the relationship between wingspan and airspeed from 0 to -0.05 in the linear-wingspan model of the glide polar. We have used $C_{D,pro} = 0.0146$, $C_{D,par} = 0.1$ and $k = 1$. (a) Change in span factor β_e for different η. (b) Glide polars calculated for different η. Line colours correspond to the value of η, as labelled. For airspeeds $> 16.5\text{ms}^{-1}$, glide performance improves from $\eta = 0$ up to $\eta \approx -0.03$, beyond which sink rates rapidly start to increase again. For the lower airspeeds, the fixed-wingspan model ($\eta = 0$) is optimal.

speeds of about 18ms^{-1}. This suggests that it matters little which variable-wingspan model the bird uses; the experimental data however supports a linearly varying wingspan which is likely easier to implement than the optimal model. Furthermore, given the number of additional factors that influence the bird's performance, the small difference between optimum and linear models is likely to be overwhelmed by factors such as wind effect and changes in tail and leg position (see Figure 5.7).

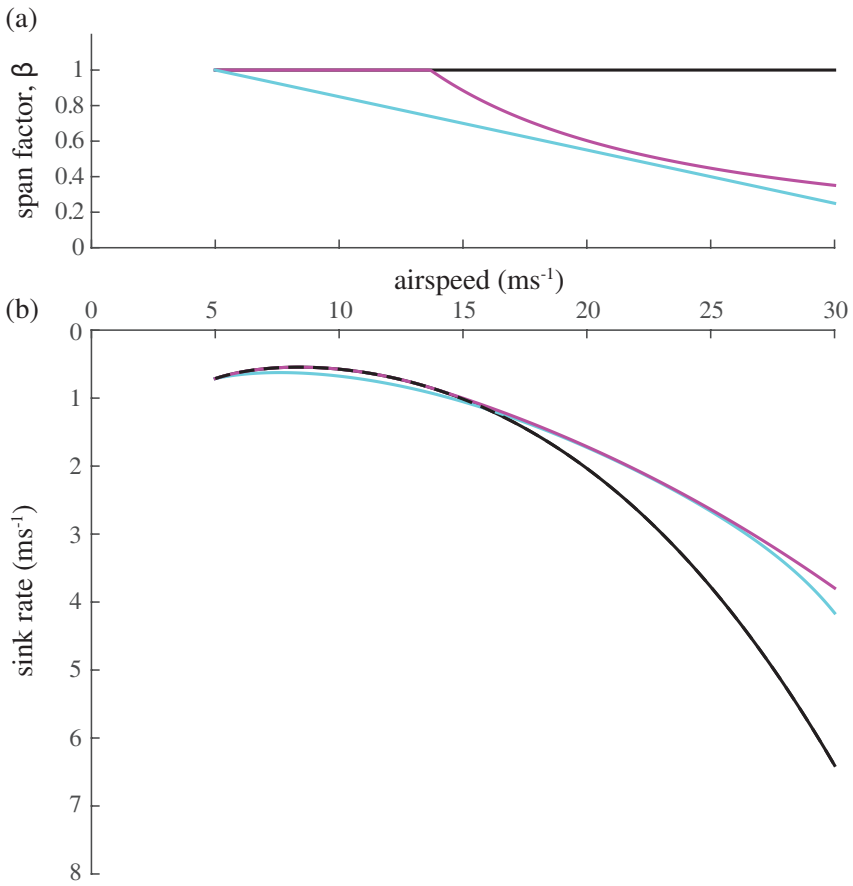


Figure 5.9: Comparison of fixed and variable-wingspan polars. (a) Change in predicted span factor β with airspeed. Black: fixed-wingspan, $\beta = 1$. Blue: linear-wingspan β_e, with $\eta = -0.03$ as estimated from video footage of steppe eagle. Purple: optimal-wingspan (superpolar) β_{opt} calculated from Equation 5.16. (b) Effect of changing wingspan with airspeed on the theoretical glide polar with $C_{D,par} = 0.1, C_{D,pro} = 0.0146, k = 1$. Black: fixed-wingspan model, Equation 5.10. Blue: linear-wingspan model, Equation 5.15. Purple: optimal-wingspan model, Equations 5.12 & 5.16. The linear and optimum variable-wingspan polars are extremely similar despite the difference in β at the lower airspeeds.

5.3.3 Estimated performance area

Based on the above estimate of our bird's superpolar, the performance area (Figure 5.11) can be described using the guidelines provided by Tucker (1987). Theoretically, any experimental glide data from our steppe eagle should fall within this area, assuming nil wind conditions. It is possible for the bird to achieve sink rates at airspeeds which fall outside of this performance area, but they would not constitute gliding flight and are only achievable through mechanisms such as flapping, exploitation of atmospheric updrafts and other manoeuvres.

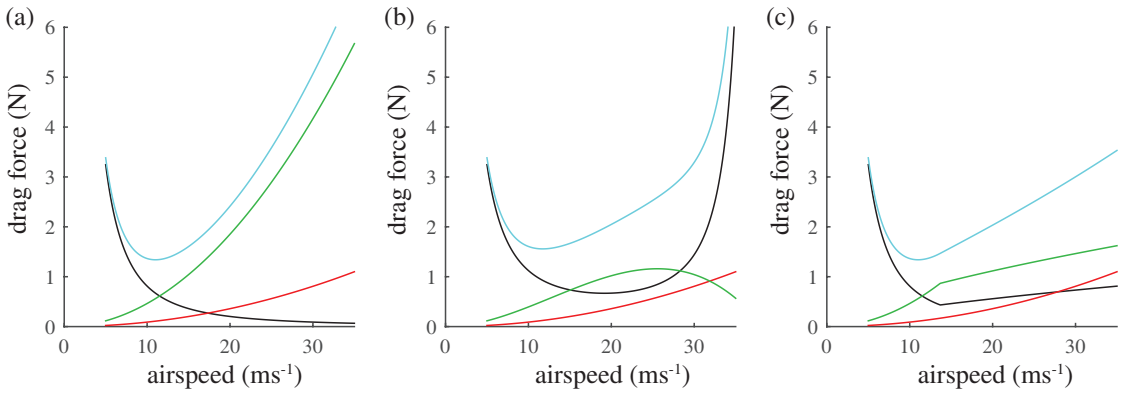


Figure 5.10: Changes in the drag components for (a) fixed-wingspan model, (b) linear-wingspan model and (c) optimal-wingspan model. Blue: total drag. Black: induced drag. Green: profile drag. Red: parasite drag. There is no effect between models of the parasite drag as this is unaffected by the changing wingspan, it simply increases with airspeed. Induced drag decreases as airspeed increases for all models initially, but as we start to see reductions in wingspan at the higher airspeeds, the induced drag starts to increase again—almost exponentially in the case of the linear-wingspan model (b)—as a high lift coefficient is required to generate sufficient lift to support the weight of the bird. Finally we see the greatest difference between the models in the profile drag. For fixed-wingspan, profile drag rapidly increases with airspeed and is by far the most dominant contribution to total drag. However the decrease in wingspan in frame (b) & (c) causes a massive reduction in the profile drag which, with the exception of the very highest airspeeds in the linear-wingspan model, outweighs any effect from increasing airspeed on the induced drag component and consequently results in significantly lower total drag.

5.4 Discussion

The different theoretical models have shown the extent to which the choice of coefficients and assumptions can affect the shape of the curve. Accurately determining these parameters, either theoretically or experimentally, has provided a challenge to researchers for over 40 years. However, in practice, how do the model uncertainties affect its uses?

Primarily the polar is a tool for comparing flight performance. This can essentially be quantified by extracting the lowest rate of altitude loss and the maximum glide ratio from the polar. The minimum sink speed, V_{min}, is the airspeed which corresponds to the lowest rate of altitude loss, $V_{s,min}$—this is the maximum point on the polar curve (see Figure 5.12). Flying at this minimum sink speed maximises the time a bird can glide for but does not maximise the distance covered during that time. Instead, this is achieved by flying at the maximum glide ratio. For any

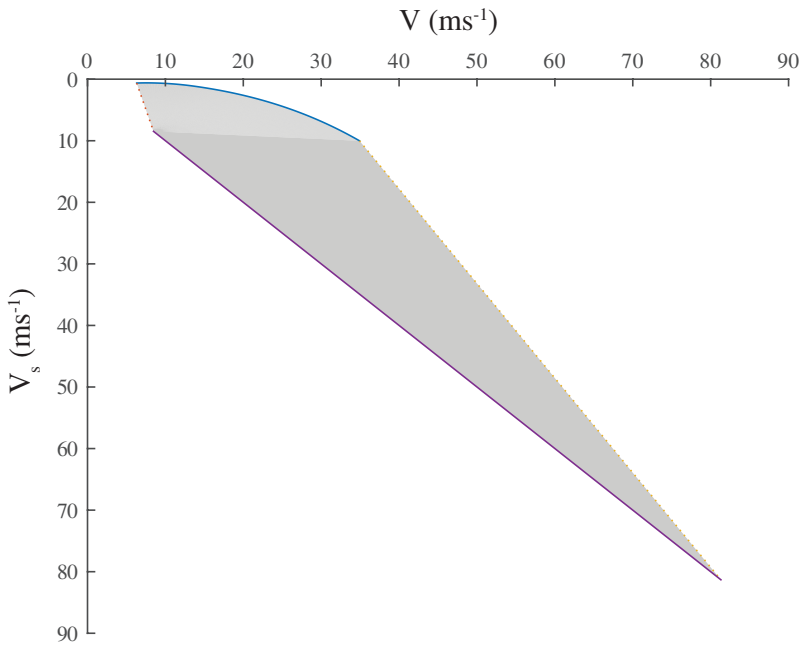


Figure 5.11: Performance area calculated for our steppe eagle. The upper boundary of the area is defined by the superpolar (blue), calculated with default coefficients $C_{D,par} = 0.1$, $C_{D,pro} = 0.0146$ and $k = 1$ for airspeeds from $V_{stall} = 6.31\text{ms}^{-1}$ (assuming $C_{L,max} = 1.8$) to 30ms^{-1}. The minimum performance curve along the lower boundary (purple) is defined by $V = V_s$. The minimum and maximum rates of vertical descent were calculated from Equations 5.18 and 5.17 respectively. The maximum sink rate is highly influenced by $C_{D,par}$; for this figure we used the higher estimate of $C_{D,par} = 0.4$, as with wings fully closed we would expect the drag on the body to be higher, and closer to the values of $C_{D,par}$ measured experimentally.

point on the polar curve, the glide ratio (V/V_s) can be found from the slope of a line drawn from the origin to the curve. The point on the curve at which this line forms a tangent with the polar is where the maximum glide ratio occurs (minimum glide angle). The airspeed at this point is known as the best glide speed, V_* (Figure 5.12), which maximises the distance covered for a given loss of altitude.

Minimum airspeed (V_{stall}, the lowest speed at which the bird can generate sufficient lift to support its weight before stalling (Pennycuick 2008)) is also a useful parameter, though for birds this is hard to define as they can increase their maximum lift coefficient well beyond what is possible for a fixed-wing glider with similar dimensions, consequently reducing the stall speed.

The glide polar remains valid with respect to the air mass at all times (Reichmann

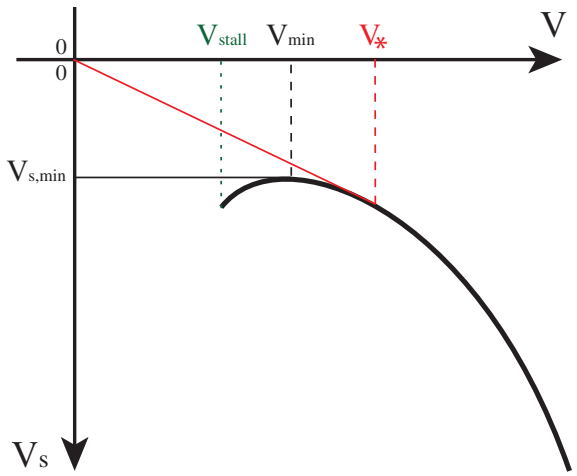


Figure 5.12: Theoretical glide polar (black) graphically illustrating how performance measures V_{stall}, V_{min} and V_* can be extracted from the polar data. The red line is a tangent from the curve to the origin.

1993), however the performance measures will change depending on the movement of the air mass relative to the bird. In zones of lift or sink, clearly the vertical speed of the air must be added to the sink rate of the polar, in effect shifting the polar up and down the y-axis. $V_{s,min}$ is therefore the minimum sink rate in still air plus the air's vertical velocity, though note that the minimum airspeed will not change. For calculation of the best glide speed, the tangent to the curve is drawn from the air's vertical velocity instead of from the origin, see Figure 5.13a. This implies that a bird should fly faster in sinking air and slower in lift. On the other hand, the effect of flying in a tail or head wind is equivalent to shifting the polar left or right respectively. As is illustrated in Figure 5.13b, this results in a slower V_* when flying in a tail wind, and a faster V_* in headwinds (Reichmann 1993).

Mathematically, these parameters can be calculated from the equation of the polar. V_{min} is calculated by finding V for when $\frac{dV_s}{dV} = 0$ whilst V_* is found by finding the airspeed at the point where the gradient of the curve is equal to the gradient of the line drawn from the curve to the origin (Hedenström 1993). If the effects of the wind are included, the polar is shifted. This can be expressed as:

$$\frac{dV_s(V)}{dV} = \frac{V_d}{V_g} = \frac{V_s(V) + W_z}{V + W_{xy}} \tag{5.19}$$

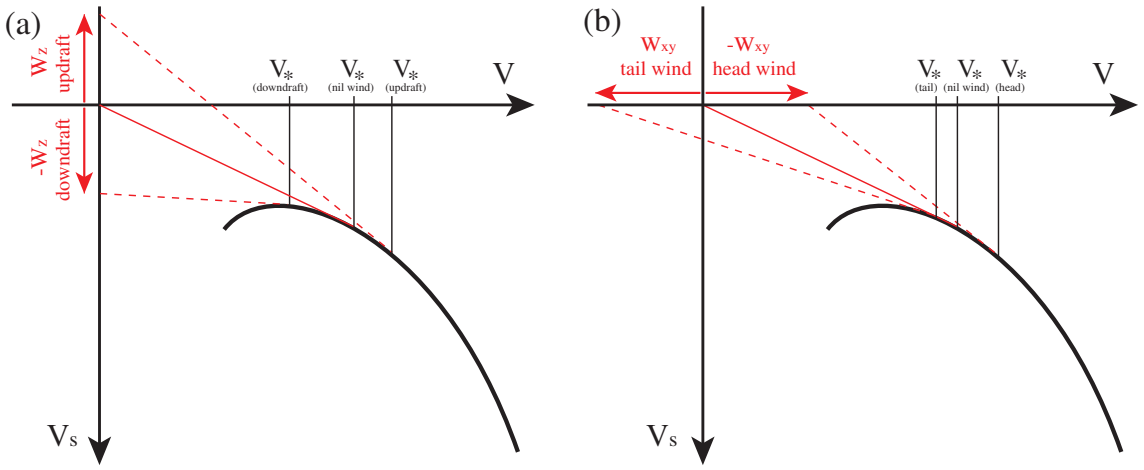


Figure 5.13: Graphical representation of the effect of (a) vertical, W_z, and (b) horizontal, W_{xy}, wind components on the calculation of optimal airspeed, V_*. In vertical winds, the polar is effectively shifted up and down the y-axis whilst horizontal winds move it along the x-axis.

where $\frac{dV_s(V)}{dV}$ is the gradient of the polar, V_d is the downward velocity of the bird which is the sum of the bird's inherent sink rate (V_s) and the vertical wind velocity component, W_z, and V_g is the ground speed of the bird which is the combined effect of airspeed (V) and the horizontal wind velocity, W_{xy}. We can therefore predict the expected relationship between V_* and either a vertical or horizontal wind component, using the form of the glide polar $V_s(V) = c_1/V + c_2V^3$, where c_1 and c_2 are constants. If $W_{xy} = 0$, then solving Equation 5.19 for V we get V_*:

$$\frac{dV_s(V)}{dV} = \frac{V_s(V) + W_z}{V}$$

$$-\frac{c_1}{V_*^2} + 3c_2V_*^2 = \frac{c_1}{V_*^2} + c_2V_*^2 + \frac{W_z}{V_*}$$

$$W_z = \frac{c_2V_*^4(3W_{xy} + 2V_*) - c_1(W_{xy} + 2V_*)}{V_*^2} \tag{5.20}$$

Similarly in horizontal winds, if $W_z = 0$:

$$\frac{dV_s(V)}{dV} = \frac{V_s(V)}{V + W_{xy}}$$

$$-\frac{c_1}{V_*^2} + 3c_2V_*^2 = \frac{c_1/V_* + c_2V_*^3}{V_* + W_{xy}}$$

$$W_{xy} = \frac{-2c_1V_* + 2c_2V_*^5 - W_zV_*^2}{c_1 - 3c_2V_*^4} \tag{5.21}$$

For the default fixed-wingspan polar of our steppe eagle, $c_1 = 3.418$ and $c_2 = 2.41 \times 10^{-4}$. It is therefore possible to numerically model the relationship between V_* and components of wind velocity, as is shown in Figure 5.14.

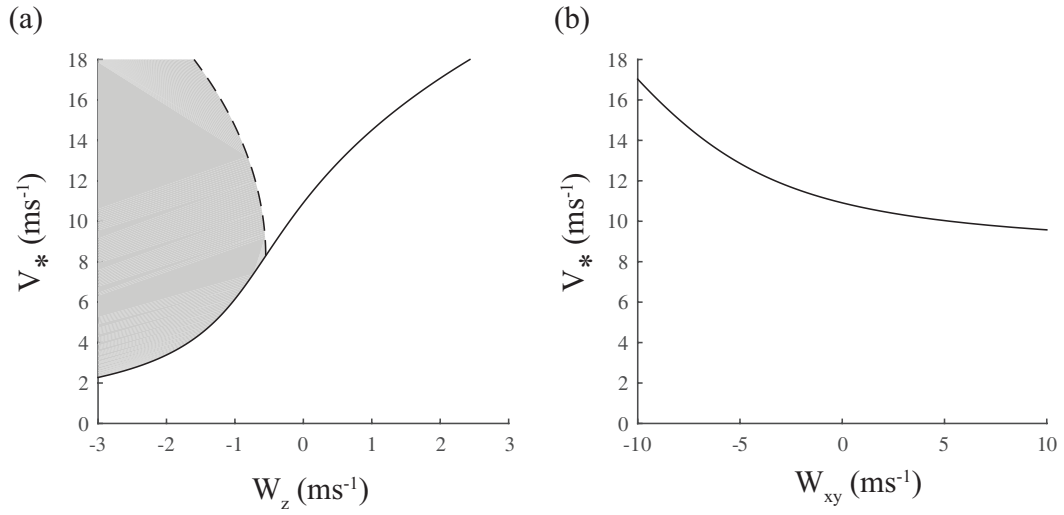


Figure 5.14: (a) Effect of vertical wind component (W_z) on the optimal airspeed (V_*), W_z is positive for updrafts. Solid-line: V_* calculated from Equation 5.19, increases in downdrafts. Dashed-line: airspeeds which result in zero altitude change (infinite glide). Shaded-grey area: indicates airspeeds which result in the bird gaining altitude. (b) Effect of horizontal wind component (W_{xy}) on V_*, W_{xy} positive for tailwind. V_* increases in headwinds, and the change in V_* is greater than in tailwinds.

From Figure 5.14a, in sinking air ($W_z < 0\text{ms}^{-1}$) V_* increases, and decreases in an updraft. However, above an updraft strength equal to $V_{s,min}$ ($\approx 0.585\text{ms}^{-1}$), the best glide ratio can instead be achieved by flying at an airspeed which corresponds

to $V_s = 0\text{ms}^{-1}$ relative to the air (dashed-line). In other words as the strength of the updraft increases, the bird can fly faster within the rising air whilst gliding indefinitely with zero altitude loss. If the bird chooses to fly at a lower airspeed, it will not travel as far but will gain energy as it increases altitude (this is represented by the grey-region in Figure 5.14). In the case of horizontal wind, Figure 5.14b, V_* increases in a headwind and decreases in a tailwind. The change in V_* is much smaller for a tailwind and generally the effect of W_{xy} is far smaller than W_z.

Estimations of V_{min} and V_* allow glider pilots to optimise their flight strategies by selecting the appropriate speed to fly, depending on their flight objective. For example, a pilot might aim to maximise their flight duration, in which case a strategy which minimised energy loss would be appropriate. This would require flying at V_{min}. Alternatively if they were aiming to maximise the distance travelled, it would instead be optimal to maximise the glide ratio, and therefore fly at V_*. Finally a slightly more involved objective would be to maximise cross-country speed which must also take into account the expected lift potential. This is the foundation of the MaCready speed to fly rule (Reichmann 1993).

The glide polar can also be used to explore flight optimisation strategies (Ákos et al. 2008; Hedenström 1993). Given birds are expected to have similar flight objectives to glider pilots, either when migrating, loitering for prey or hunting, it is reasonable to hypothesise that they will also adjust their behaviour according to the above speed-to-fly theories. Alternatively of course, a bird might not try to optimise anything at all. Although in wild birds this seems unlikely due to the energetic cost of flight, it is a particularly important consideration when looking at the behaviours of captive birds which are restricted to flying within a small area dictated by the falconer. Instead their objective might be to loiter within sight of the falconer and wait for food.

The different polar assumptions and coefficients clearly change the shape of the polar and consequently the performance measures we extract from it. For example, from the different theoretical curves generated for our steppe eagle based on com-

monly used coefficients in Figure 5.3, V_{min} ranges between 7.0ms^{-1} and 8.5ms^{-1} with corresponding $V_{s,min}$ 0.645ms^{-1} and 0.547ms^{-1}, whilst V_* ranges between 9.1ms^{-1} and 11.4ms^{-1}. However, although the absolute values of V_{min} and V_* may change between models and drag coefficients, provided the chosen model is consistent, results will remain the same for performance comparisons between species.

In this chapter, the traditional theory of gliding flight and glide polar models for both fixed and variable wingspan were presented. We explored the wide range of different drag coefficient estimates used throughout the literature and discussed their limitations and the assumptions on which they are based. A sensitivity analysis found that these assumed drag coefficients have a large impact on the polar curve and the perceived performance of a bird, though even the most current estimates are rough approximations derived from a relatively small sample of individuals and species.

Interestingly we found that there is an optimal slope (η) for any linear relationship between wingspan and airspeed, which generates a polar curve almost indistinguishable from the theoretical superpolar. Optimum η appears to be insensitive to the bird species but will change with the drag coefficients. From video footage and observations of our steppe eagle, $-0.02 < \eta < -0.03$ seems plausible.

The theoretical polars derived in this chapter are compared with experimental data extracted from our steppe eagle in Chapter 6 where we also explore the effect of wind on the glide data in more depth.

Chapter 6

Glide polar: experimental data and optimisation

6.1 Introduction

The need for better experimental glide data to determine a more accurate set of drag coefficients for computing theoretical glide polars was highlighted in Chapter 5. Achieving this is complicated by the nature of the bird's flexible air frame, the time intensive methods and the near impossibility of recording the movement of the atmosphere at the bird's location when flying freely.

Original attempts to ascertain the glide polar of birds used the glide comparison method which entailed following birds in a glider equipped with a tracker, such as the ornithodolite designed by Pennycuick (1982). As the polar curve of the glider was known from the manufacturers data, the bird's polar was found by simply comparing the vertical and forward speeds of the bird with those of the glider. This approach was first employed by Raspet (1950) for the American black vulture (*Coragyps atratu*) and later by Pennycuick (1971a) for the African white backed

vulture (*Gyps africanus*). Other studies have relied on ground based techniques with the obvious associated difficulties in assigning accurate local airspeed values to the measured bird. These include fulmar petrels (*Fulmarus glacialis*) (Pennycuick 1960) and white backed vultures (Tucker 1988) which were both tracked by ornithodolite, and also radar tracking of steppe eagles (*Aquila nipalensis*) during migration (Spaar and Bruderer 1996).

Wind tunnel experiments allow accurate control of the airflow, and the glide angle can be changed by tilting the tunnel. This has proved to be an effective method for extracting the glide polar of a range of species; pigeon (*Columba livia*) (Pennycuick 1968), lagger falcon (*Falco jugger*) (Tucker and Parrott 1970), black vulture (*Coragyps atratu*) (Parrott 1970), Harris' hawk (*Parabuteo unicinctus*) (Tucker and Heine 1990), jackdaw (*Corvus monedula*) (Rosén and Hedenström 2001) and common swifts *Apus apus* (Henningsson and Hedenström 2011). There have also been a number of studies on the wings of dead birds such as swifts (Lentink et al. 2007). Although wind tunnels provide a controlled environment, training birds to fly in laboratory conditions is not always feasible, particularly for the larger soaring species. Nor does it allow researchers to explore how a bird chooses to use the available range of speeds and polars in response to natural conditions.

In this chapter, periods of gliding flight are extracted from our steppe eagle free-flight data. This experimental data is then compared with the theoretical polar estimates derived in Chapter 5. Finally we explore the bird's flight strategy in different wind conditions and discuss the problem of determining suitable drag coefficients from the data.

6.2 Methods

6.2.1 Data collection

The same experimental set up as described in Chapter 2 was used to collect glide polar data of airspeed and sink rate for our steppe eagle. The polar curve describes

performance in still air, however unlike in a controlled wind tunnel environment, not only are completely nil wind conditions exceptionally rare in the field, but encouraging the bird to repeatedly glide long distances without flapping was infeasible. Instead gliding data were extracted from 36 flights where the bird was flown for extended periods of time in a range of atmospheric conditions—9 of the 45 flights originally recorded were not included in this analysis either due to incomplete data preventing use of suitable glide selection criteria, or in the case of one flight, because recorded airspeeds were exceptionally low and were considered unreliable. This method allowed us to obtain a much larger volume of data than has previously been used in similar studies, albeit from a single individual.

Observations of flights with and without onboard instrumentation indicate that the bird adapted effortlessly to the additional loading, which made no noticeable difference to flight behaviour. Although the equipment is likely to have had some small effect on the bird's sink rate by increasing body drag and mass. As the additional weight is within the limits of the bird's naturally changing body mass, the systematic error from this is assumed to be small. However, the effect of the equipment on the profile drag coefficient might be more significant.

6.2.2 Glide identification

Equivalent airspeed and sink rate were calculated from the raw onboard sensor data during post processing (Chapter 2). Samples which corresponded to equilibrium gliding flight were then extracted from the data. Equilibrium flight is defined as zero acceleration—in other words, when the bird is gliding straight at a constant airspeed.

To extract the gliding data, initially individual data points were selected that corresponded to straight flight. Provided the bird's recorded airspeed was greater than 5ms^{-1} and its ground speed greater than 1ms^{-1}, the bird was considered to be flying. This eliminated data where the bird was sat stationary or carried by the falconer. Straight flight was then identified using the bank angle calculated from

IMU data and the AHRS algorithm. Based on the small angle approximation, a bank angle threshold of 5° was used: we also experimented with a threshold of 10°, but found the more stringent criterion ensured no turning flight was included. In addition to these criteria, samples that coincided with flapping flight were excluded. Instances of flapping were identified using the flap template generated in Chapter 3. Airspeed and sink rate data were additionally smoothed over 1s (10 samples) to remove any high frequency noise components.

A large set of polar data was extracted using the above criteria as shown in Figure 6.1a, where each point represents a single sample. A further refinement was to only include samples where the above criteria were met consistently for a specified period of flight: either 3s or 5s. For example to identify glides which lasted at least 3s, if for each sample the preceding and following 15 recorded data points all met the flight and bank criteria, and no flap occurred, the 3s of flight was considered to be at equilibrium and the mean airspeed and mean sink rate of the 30 points were recorded. In this way we extracted data for 3s and 5s of gliding flight for bank angles <5°: no glides identified in this way occurred when the bird was obviously turning or in non-equilibrium conditions.

As a final check, the load factor (N_t) for each glide data point was examined. By trimming glides where mean load factor did not fall within ±10% of equilibrium (i.e. $0.9 < N_t < 1.1$), we ensured only equilibrium flight was selected.

6.3 Experimental results and analysis

Glide data extracted from the 36 steppe eagle flights using the bank angle, glide length and load factor selection criteria are shown in Figure 6.1. For the rest of this chapter we have used the data extracted for glides of 3s based on a maximum bank of 5° (Figure 6.1b) as this appears to give us the greatest range of airspeeds whilst still ensuring the bird is in a continuous glide at equilibrium.

The chosen set of glide data represents 1.3% (21 minutes) of the birds total

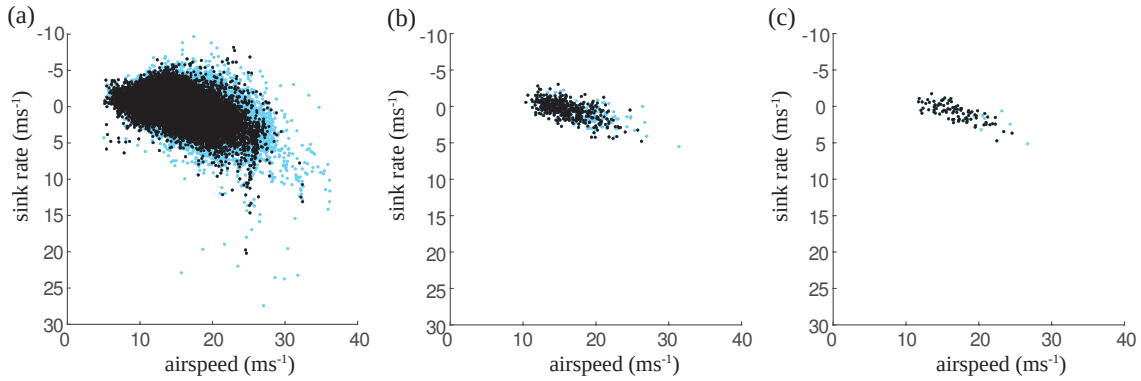


Figure 6.1: Comparison of the glide selection criteria. Glide data (airspeed vs sink rate) were extracted from 36 flights using the criteria of bank angle $< 5°$ and (a) sample period = 0.1s (1 sample point), (b) sample period = 3s, (c) sample period = 5s. Black-points: trimmed data after load factor criterion ($0.9 < N_t < 1.1$) was applied. Blue-points: before load factor criterion applied. The different criteria do not change the underlying characteristics of the glide data and there are examples of glides with negative sink rates (i.e. the bird is climbing) in each plot. The data in (a) are extremely noisy as, although these individual sample points might momentarily satisfy the gliding flight conditions, they do not necessarily correspond with a sustained glide. For the longer glide lengths, the range of airspeed and sink speed is significantly reduced and in fact for 5 second glides in (c), the data becomes very sparse and it appears we start to lose information.

recorded flight time. By plotting the position of each glide on the recorded GPS flight tracks, we found that the majority of glides occurred either at approximately 90° to the prevailing wind as the bird flew along the ridge line, or directly into a head wind during a glide following a climb up the ridge within a thermal. Recorded airspeeds were between 10.38ms^{-1} and 26.26ms^{-1} with a mean of 16.04±2.85ms^{-1}; on average slightly higher than the mean airspeed over all the recorded flights which was 14.2ms^{-1} which is unsurprising given that this includes periods of slow soaring flight, for example in thermals. This is consistent with Spaar & Bruderer's (1996) findings for free-flying steppe eagles in the wild, who recorded a mean gliding speed of 15.6ms^{-1} and mean cross country speed of 12.4ms^{-1} based on observations of multiple individuals. Sink rates range between 4.79ms^{-1} and -3.04ms^{-1} with an average of 0.46±1.22ms^{-1} which is lower than Spaar & Bruderer recorded (1.27±0.54ms^{-1}), perhaps due to the difference in glide lengths used between the two studies; 3s and 10s respectively. Figure 6.2 compares the experimental data sets for these two studies, which overlap.

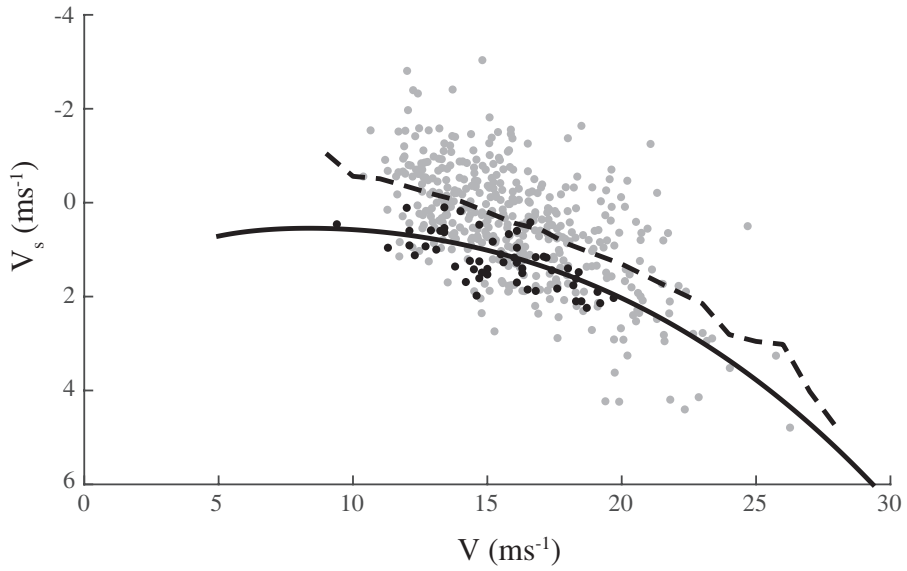


Figure 6.2: Comparison of experimental glide data for steppe eagles. Grey-points: data extracted from onboard instrumentation unit for the current study with mean sink rate for binned airspeed data shown by the black-dashed line. Black-points: data manually extracted from Spaar & Bruderer's (1996) study of free-flying steppe eagles tracked by radar. Black-line: theoretical fixed-wingspan glide polar calculated from Pennycuick's default drag coefficients $C_{D,par} = 0.1$ & $C_{D,pro} = 0.0146$ (Pennycuick 1989a). The two sets of experimental data fall within the same area. Although Spaar & Bruderer's data are sparse, they cover a much smaller range of airspeeds and sink rates than our measurements and lie closer to the theoretical fixed-span glide polar, despite recording from multiple individuals which will naturally introduce noise.

The minimum recorded airspeed of 10.38ms^{-1} corresponds with a lift coefficient of approximately 0.86. This is much lower than it is thought birds can achieve (up to approximately 1.8) and suggests that our steppe eagle can attain lower airspeeds but that these were not recorded during gliding flight; i.e. we are not seeing the full range of the polar during free-flight.

At lower airspeeds, on average the bird was found to be climbing (see Figure 6.3), implying that it was in fact straight line soaring in updrafts rather than gliding at these points. Indeed, as the bird was specifically flown at locations with substantial updraft potential, almost all of the recorded flight is expected to have occurred in ridge lift. It is not possible however to distinguish these soaring sections from flight in still air without knowledge of the bird's polar in the first place.

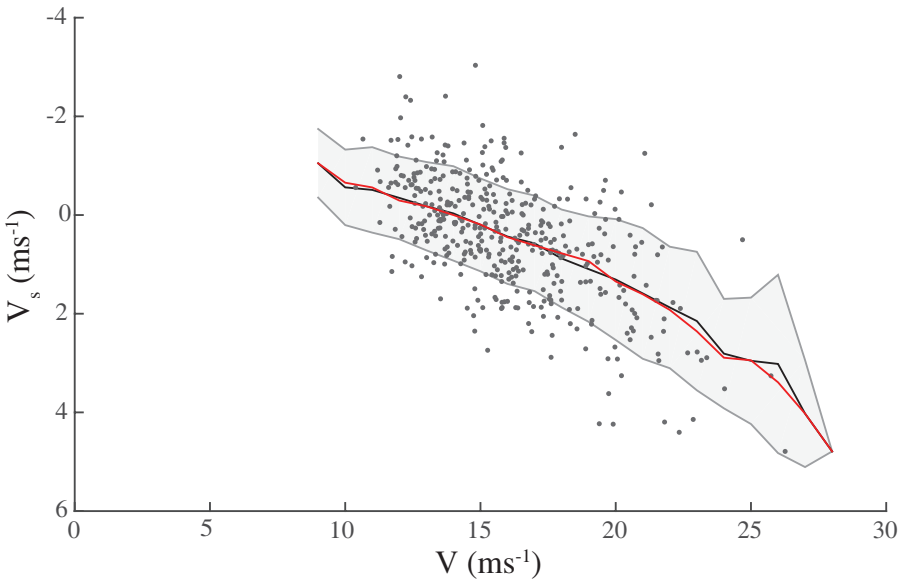


Figure 6.3: Experimental glide points with mean (red) and median (black) sink rates for binned airspeed data. The shaded area indicates the standard deviation of the sink rate about the mean. Given the mean and median are not dissimilar over the range of airspeeds, the data show no evidence of any skew in the recorded sink rate. We do not see the expected curvature characteristic of a glide polar over the recorded airspeed range and in fact the bird is on average climbing for airspeeds less than $\approx$14.5ms^{-1}.

6.3.1 Comparison of experimental and theoretical performance area

Ideally if the bird were flying in nil wind conditions, our experimental glide data would represent the theoretical performance area—or rather the bird's normal operating range within the performance area. Each glide would lie on one of a family of polars described by the bird's wing morphology. Extracting the underlying theoretical form of the glide polar from the experimental data would therefore be hindered by the changes in wing morphology which are unknown and may or may not be correlated with airspeed. In the majority of previous studies, it has been assumed that the bird is flying along a single polar curve at the minimum sink rate for each airspeed (either the fixed or variable wingspan model) and that any noise in the data is due to non-systematic atmospheric effects or measurement error. This is perhaps a fair assumption for wind tunnel studies where the bird's wing morphology in the controlled environment can be monitored, but is unrealistic for free-flight tests and

can miss interesting details in the data about the bird's performance or strategy.

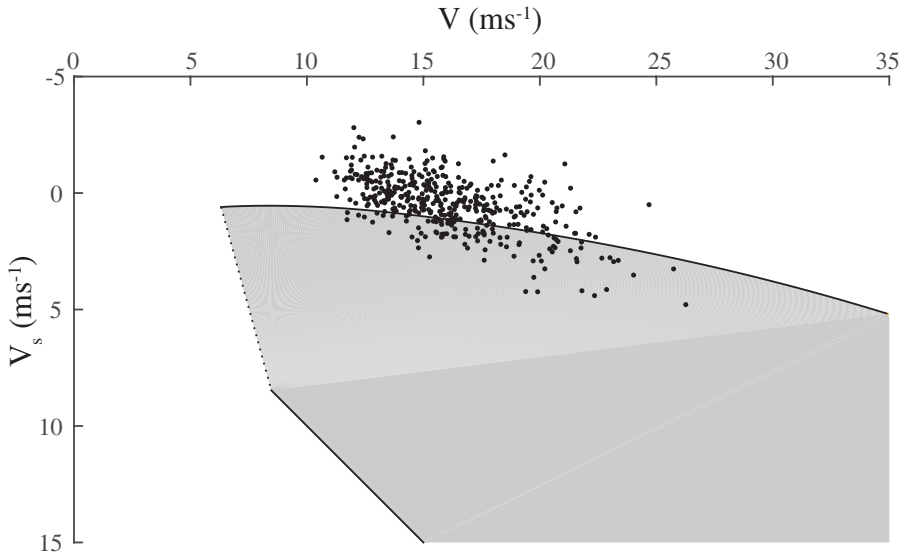


Figure 6.4: Comparison of experimental glide data (black) with theoretical performance area (grey) as calculated for Figure 5.11 in Chapter 5. The majority of glides recorded lower sink rates than are theoretically possible in nil wind conditions, which indicates that the bird is extracting energy from the atmosphere for the majority of the time he is gliding straight at equilibrium.

Comparing our set of experimental data with the predicted performance area for our steppe eagle (calculated in Chapter 5), we see in Figure 6.4 that the majority of the glide data lie outside of the theoretical performance area. Even accounting for the significant uncertainties in both the model and the coefficients used for calculating the superpolar (upper boundary), a single polar curve cannot explain the observed distribution of glide points, in particular the glides where the bird gains altitude. Other than instrumentation error, the only possible cause for the consistently low sink rates is external effects from the atmosphere and specifically the bird encountering updrafts which decrease the measured sink rate. There are 2 possible hypotheses; either the bird takes no account of the wind vector and each glide is simply shifted vertically on the polar plot by the magnitude of the updraft, or the bird actively adjusts its airspeed according to the sensed estimate of the wind vector. This may be a simple in-built mechanism which might, for example, cause the bird

to automatically fly faster in down drafts, or a more complex optimisation strategy where the bird chooses what parameter to optimise and subsequently adjusts for vertical and/or horizontal wind components.

6.3.2 Wind effect

To initially confirm that the glide data are influenced by the wind encountered by the bird, two simple tests were carried out correlating the bird's airspeed with estimated horizontal and vertical wind components respectively.

Horizontal wind component

The instantaneous horizontal component of the wind vector in the inertial frame was calculated from the onboard instrumentation data as described in Chapter 2. The tailwind component in the body-frame was then calculated from basic trigonometry based on GPS heading. Tailwinds were set as positive.

It has been shown already in previous studies (Spaar and Bruderer 1996) that a soaring bird's airspeed changes depending on the magnitude of the tailwind and we see the same relationship with our data in Figure 6.5. Both airspeed and ground-speed are significantly correlated with tailwind. Airspeed was reduced in tailwinds and increased in headwinds (linear regression: $V_a = -0.33W_{xy} + 14.21$, $n = 543$, $p < 0.0001$, $R^2 = 0.18$). On the other hand, ground velocity (V_g) increased with increasing tailwind (linear regression: $V_g = 0.53W_{xy} + 14.37$, $n = 543$, $p < 0.0001$, $R^2 = 0.33$). This is extremely similar to the correlation previously found for free-flying steppe eagles in 10s glides (airspeed: $V = -0.29W_{xy} + 15.71$, $n = 52$, $p < 0.005$, $R^2 = 0.15$, ground speed: $V_g = 0.59W_{xy} + 14.99$, $n = 52$, $p < 0.0001$, $R^2 = 0.36$ (Spaar and Bruderer 1996)). This similarity between the studies is perhaps surprising considering that Spaar and Brunderer recorded multiple individuals during migration which had a clear flight objective, whilst our individual steppe eagle had no motivation to fly at an optimal airspeed when simply loitering on a single ridge.

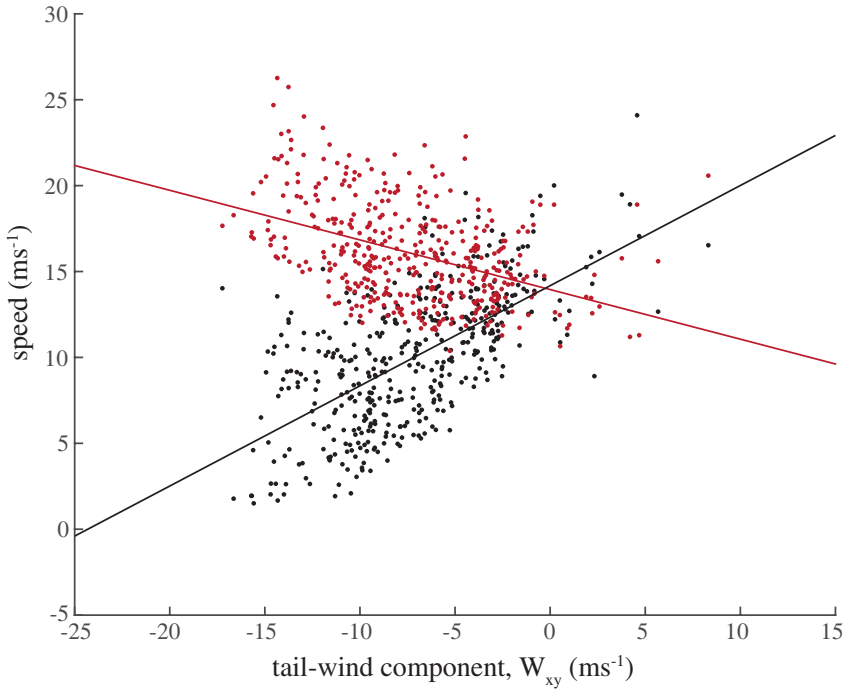


Figure 6.5: Airspeed, V_a (red) and ground speed, V_g (black) during gliding versus the tailwind component which is the estimated wind speed component in the direction of the glide. Corresponding linear regressions are for airspeed: $V_a = -0.33W_{xy} + 14.21$, N=543, p< 0.0001, R^2=0.18 (red-line) and for ground speed: $V_g = 0.53W_{xy} + 14.37$, N=543, p< 0.0001, R^2=0.33 (black-line). We see that the data are significantly correlated and that as the tailwind increases, ground velocity also increases whilst the airspeed is reduced. This matches the theory presented in Chapter 5.

The results of this analysis strongly suggest that adjusting airspeed according to the horizontal wind component is an in-built mechanism and that the bird is capable of estimating its speed. Whether it is sampling airspeed or ground speed however, we cannot tell.

We did not record many glides where the bird was flying in a tailwind. This is likely because the bird primarily soared along ridges with the prevailing wind perpendicular to the ridge line. To glide in tailwinds would mean flying directly towards the ridge line which the bird has little incentive to do.

Vertical wind component

There is a strong correlation between tailwind and airspeed, however a similar comparison for updrafts is not possible as we have no direct measure of the vertical wind

component. Instead, we can use predictions of the vertical wind velocity obtained from the Hay Bluff CFD analysis in Chapter 4 on a subsection of the glide data.

The CFD analysis provides a scalar estimate of the updraft strength for each glide based on the bird's position. In reality this updraft value will be scaled by the wind speed on the day, therefore we would expect to see different offsets of the sink rate glide data for each flight day. We fitted a linear model (ANOVA, type I) to the sink rate glide data as a function of flight number, predicted updraft strength and the interaction between flight number and predicted updraft. The model was significant overall ($F_{10,659} = 10.8$, $p < 0.0005$, $R^2 = 0.14$), as were the individual parameters; flight ($F_{5,659} = 4.47$, $p = 0.001$), predicted updraft ($F_{1,659} = 17.22$, $p < 0.0005$) and the interaction between flight and predicted updraft ($F_{4,659} = 17.11$, $p < 0.0005$).

We therefore conclude that a significant amount of the variation in sink rate for our glide data can be explained by the estimated updraft strength and the flight number, where flight number accounts for the difference in wind speeds between days. The results match the theoretical prediction that a bird should fly slower in updrafts and faster in downdrafts.

6.3.3 Soaring optimisation

We have shown that the experimental glide data recorded are influenced by both vertical and horizontal wind components. Interpreting the data purely in terms of the traditional glide polar loses these important features which affect the bird's gliding strategy. An alternative way of exploring the glide data is to unpack the glide polar and think in terms of optimisation. In this way we can build predictions of the bird's expected glide performance in given wind conditions based on the optimisation criteria presented previously. The bird's expected performance under this optimization is shown in Figure 6.6.

The original glide polar in Figure 6.6a plots airspeed against the bird's movement relative to the atmosphere; V_s. This polar curve can be expanded by instead plotting

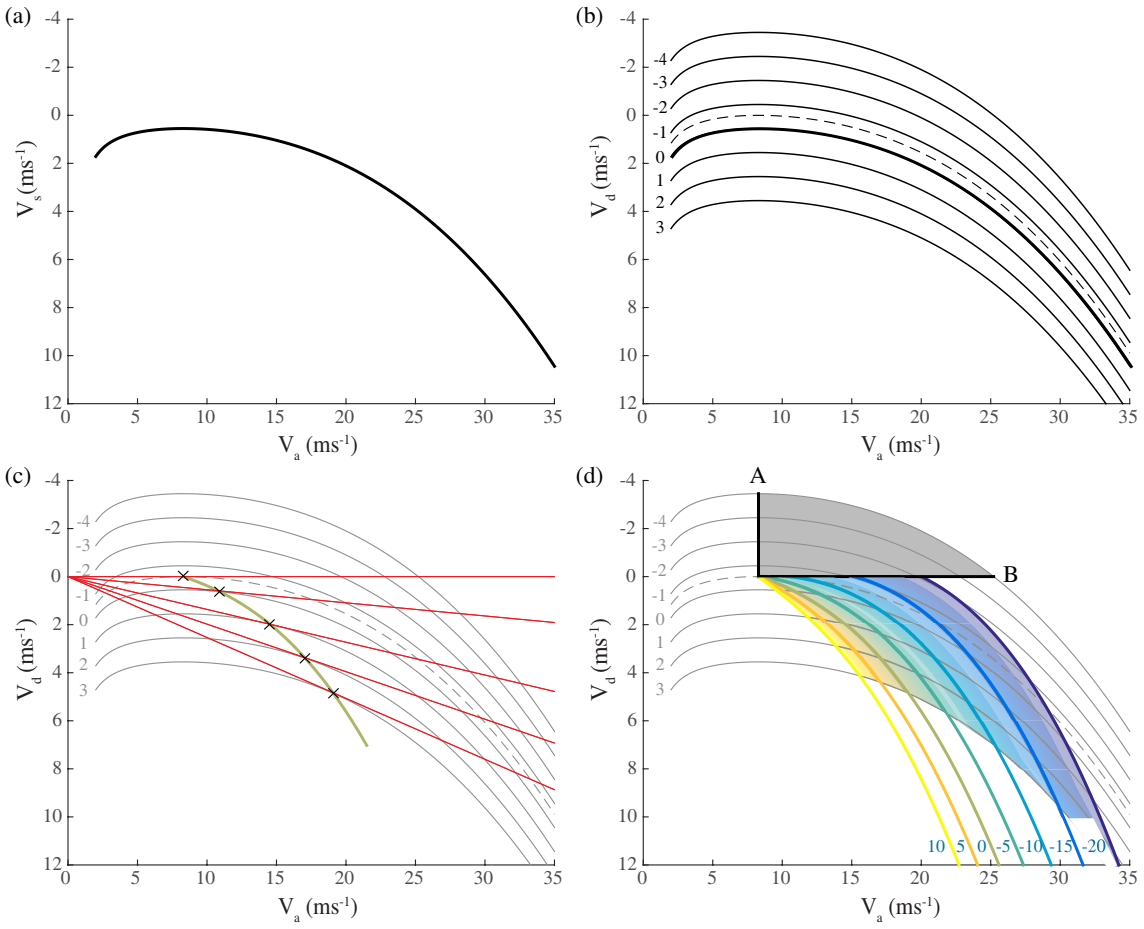


Figure 6.6: Building the glide polar 'optimisation chart'. (a) Traditional glide polar of airspeed (V_a) versus sink rate (V_s) relative to the atmosphere, calculated from fixed-wingspan model with default drag coefficients. (b) The glide polar is 'unpacked' to show effect of vertical wind on the bird's vertical velocity relative to the ground (V_d). Curves are labelled by the vertical wind velocity, down-drafts are positive. Black-dotted line represents the bird's vertical velocity and corresponding airspeed in a 0.54ms^{-1} updraft which is equal to the minimum sink rate of the traditional glide polar in nil wind (bold line), therefore if the bird were to fly at V_{min}, V_d would be 0ms^{-1}. (c) Graphical representation of the optimum airspeed (V_*) calculation, which minimises glide angle for each vertical wind velocity condition. Red-lines: tangents from each vertical wind shifted polar to the origin. V_* for each case is marked by black crosses. Green-line: isoline for zero tailwind condition ($W_{xy} = 0$ms^{-1}) connecting V_* for each wind shifted polar. (d) Isolines of V_* for tailwinds ranging from -20ms^{-1} to 10ms^{-1}, coloured by magnitude of tailwind and overlaid on the vertical-wind shifted polars. Line A is at V_{min} and indicates the lower limit of expected airspeeds, below which there is no motivation for the bird to fly. Line B describes the point at which the bird's vertical velocity is 0ms^{-1} as the inherent sink rate is perfectly balanced by the vertical wind component. Above this limit, there is no longer any benefit of flying at V_*. The grey region of the chart represents a Pareto optimisation area where the bird can optimise both distance travelled for a minimum loss of altitude (by flying along line B) and/or potential energy gained (line A). Where the bird choses to fly in this area will depend on the weighting given to both of these criteria.

the vertical velocity of the bird relative to the ground (V_d) which takes into account the vertical movement of the air (W_z), given that $V_d = V_s + W_z$. This is shown in Figure 6.6b for a range of vertical wind speeds from -4 to 3ms^{-1}. The bird can only fly along the polar defined by the vertical wind speed encountered, but can choose where it sits on the polar by adjusting its trim. The polar for a vertical wind speed of -0.54ms^{-1} is also shown (dashed-line) as in an updraft of this strength, the bird can glide indefinitely at V_{min} without losing altitude because $V_{s,min}$ is balanced by W_z.

As described previously, if the bird is attempting to optimise its flight by flying as far as possible with the existing altitude (Reichmann 1993) i.e. minimising glide angle or $\frac{dV_d}{dV}$, it should fly at V_* which is found by drawing a tangent from the polar to the origin. However, V_* will change depending on the magnitude of W_z as demonstrated in Figure 6.6c for each vertically wind-shifted polar curve (where V_* is indicated by a black-cross). If the V_* for each W_z are connected, an isoline of the best speed to fly at each vertical wind speed is formed, assuming the tailwind component is zero. This isoline is shown in green in Figure 6.6c. If the tailwind is not zero however, a different set of V_* are identified as, essentially, the curve tangents are no longer drawn from the origin but from the magnitude of the tailwind on the x-axis (see Figure 5.13 in Chapter 5). For a given W_{xy}, V_* can be calculated for any W_z. Mathematically these isolines can be derived by solving Equation 5.19 for W_z and substituting this back into $V_d = V_s + W_z$. This results in:

$$V_d = -\frac{2kmg(V_a + W_{xy})}{\pi\rho b^2 V_a^2} + \frac{3\rho V_a^2(V_a + W_{xy})(C_{D,pro}S + C_{D,par}S_b)}{2mg} \tag{6.1}$$

Equation 6.1 generates the isoline of V_d vs. V_a for a given W_{xy}. The set of isolines for the measured range of tailwinds in our data (-20 to 10ms^{-1}, see Figure 6.5) are plotted in Figure 6.6d, and are coloured by the magnitude of W_{xy}. From this chart, if W_{xy} and W_z are known, it is possible to determine the optimum airspeed and corresponding sink rate the bird should fly at in order to minimise glide angle.

Calculation of V_* in this way is only meaningful however if $V_d > 0$ms^{-1}. When

the updraft strength is greater than $V_{s,min}$, the airspeed found from the tangent is no longer the solution for minimising glide angle $\frac{dV_d}{dV}$, as this would result in the bird climbing and gaining potential rather than kinetic energy. If the bird's aim is to maintain altitude whilst flying as fast as possible, the bird should fly at $V_d = 0\text{ms}^{-1}$ along line B (Figure 6.6d). If instead the aim is to maximise gain in potential energy, the bird should fly at V_{min}, illustrated by line A. These strategies are also used by glider pilots who switch between flying on line A or line B but rarely in between when cross-country soaring. The grey region between lines A and B is a Pareto optimal zone where the bird can fly optimising one or both criteria (Taylor and Thomas 2014). However the relative weighting of the two criteria are unknown so we cannot predict where we would expect the bird to be flying within this zone. It is also likely that with different aims, the weightings will change. There is no reason for the bird to fly in the range of airspeeds below V_{min} (line A) given that both criteria (potential energy gain and distance travelled) are reduced as the bird moves away from V_{min}.

Comparing the optimisation with glide data

If the bird is optimising flight according to the theoretical predictions, for the measured range of W_{xy} and W_z conditions, we would therefore expect all glide measurements to fall within the shaded regions of Figure 6.6d. This comparison with our experimental data is shown in Figure 6.7 which is built from Pennycuick's classic fixed-wingspan model with coefficients $C_{D,pro} = 0.0146$, $C_{D,par} = 0.1$ and $k = 1$.

All but one of the experimental glide points fall within the predicted area on the optimisation chart, though we note that although the range of W_{xy} isolines is based on measurements from our instrumentation, the values for W_z were chosen to encompass the data as we have no direct measurement of the updrafts encountered. Although $-4\text{ms}^{-1} < W_z < 3\text{ms}^{-1}$ seems a reasonable estimate, the CFD analysis of Hay Bluff suggests a smaller range of vertical movement of the air would be more realistic.

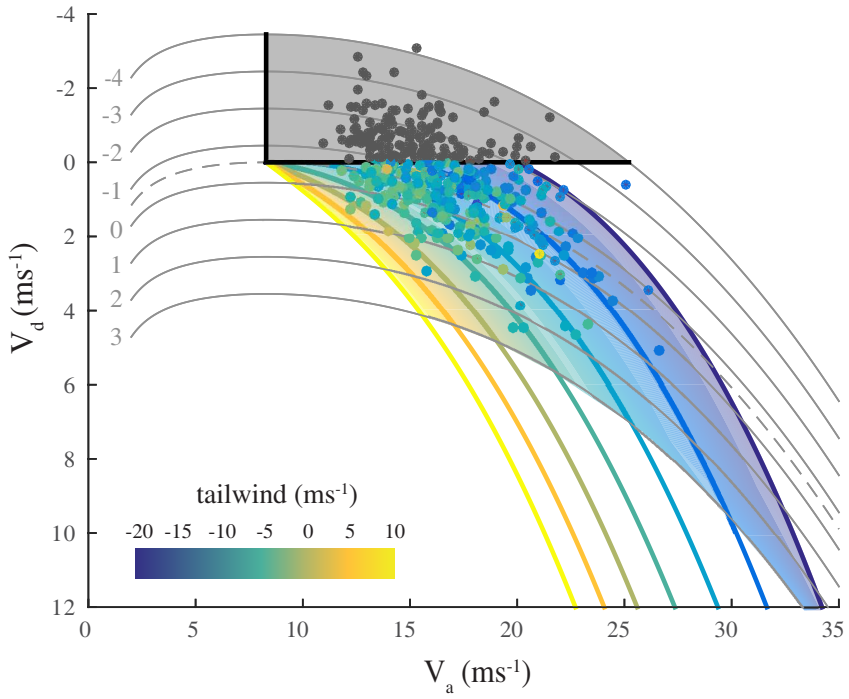


Figure 6.7: Theoretical glide optimisation area compared with our experimental glide data. Glide data where $V_d > 0\text{ms}^{-1}$ is coloured by the measured tailwind component. In the Pareto optimal region above $V_d = 0\text{ms}^{-1}$, glides are plotted in grey as we can make no predictions about tailwind in this area. The underlying polar is fixed-wingspan with coefficients $C_{D,pro} = 0.0146$, $C_{D,par} = 0.1$ and $k = 1$. All but one glide fall within the predicted zone when the range of measured tailwind components was used to generate the isolines of V_*.

We can assess the accuracy of this optimisation chart by comparing the measured W_{xy} for each glide with the predicted $\hat{W}_{xy}$ from the chart based on the position of the glide point. This is demonstrated qualitatively in Figure 6.7 where the glide data in the region $V_d > 0\text{ms}^{-1}$ has been coloured by measured W_{xy}. There is some correlation, though the data are noisy. Glides where the bird was climbing ($V_d < 0\text{ms}^{-1}$) are plotted in grey as we have no expectation of where they should fall in the Pareto optimal region without knowing the relative weighting of the two optimisation criteria. As with any glide analysis, the definition of these zones is highly sensitive to the form of the underlying polar. We therefore recomputed Figure 6.7 for the fixed and linear variable-wingspan polar models with the different drag coefficient estimates discussed earlier in this chapter. For the variable-wingspan

model, Equation 6.1 for the calculation of the W_{xy} isolines becomes:

$$V_d = \frac{(V_a + W_{xy})(-\frac{4km^2g^2(\gamma+3V_a\eta)}{\pi b^2(\gamma+V_a\eta)^3} + \rho^2 V_a^4(3C_{D,par}S_b + C_{D,pro}S(3\gamma + 4V_a\eta)))}{2\rho mgV_a^2} \tag{6.2}$$

where $\eta = -0.03$ was used for the calculation of β, based on the qualitative video analysis in Chapter 5. The coefficients and models used for each underlying polar in Figure 6.8 are summarised in Table 6.1. The coefficients for polars *a-c* and *e-g* are the values commonly quoted in the literature.

The same range of W_z and W_{xy} have been used for each polar in Figure 6.8. Other than for polar a, where a number of glides lie outside the measured range of W_{xy} isolines, all glides but one in each polar fall within the predicted regions of the chart if we were to extend the updraft component to $\approx 5\text{ms}^{-1}$.

polar	model	$C_{D,pro}$	$C_{D,par}$	k	η	r	p-value	MSE
a	fixed-span	0.0228	0.407	1	-	0.487	< 0.0001	62.8
b	fixed-span	0.0146	0.100	1	-	0.429	< 0.0001	38.4
c	fixed-span	0.0049	0.370	1	-	0.409	< 0.0001	35.4
e	linear variable-span	0.0228	0.407	1	-0.03	0.454	< 0.0001	49.9
f	linear variable-span	0.0146	0.100	1	-0.03	0.303	< 0.0001	35.4
g	linear variable-span	0.0049	0.370	1	-0.03	0.395	< 0.0001	34.4
d	fixed-span	0.0046	0.342	1	-	0.399	< 0.0001	34.9
h	linear variable-span	0.0054	0.325	1	-0.03	0.381	< 0.0001	33.8

Table 6.1: Models and coefficients used to generate polars in Figure 6.8 and the corresponding correlation coefficients (r), p-values and MSE for the comparison between model predicted and measured tailwind component. The coefficients for polars d & h are optimised to minimise MSE.

The expected $\hat{W}_{xy}$ can be calculated for each glide point by rearranging Equation 6.1 for the fixed-wingspan polars, where V_a and V_d are known. For the variable-wingspan polars, there is no analytical solution for W_{xy} from Equation 6.2. Instead

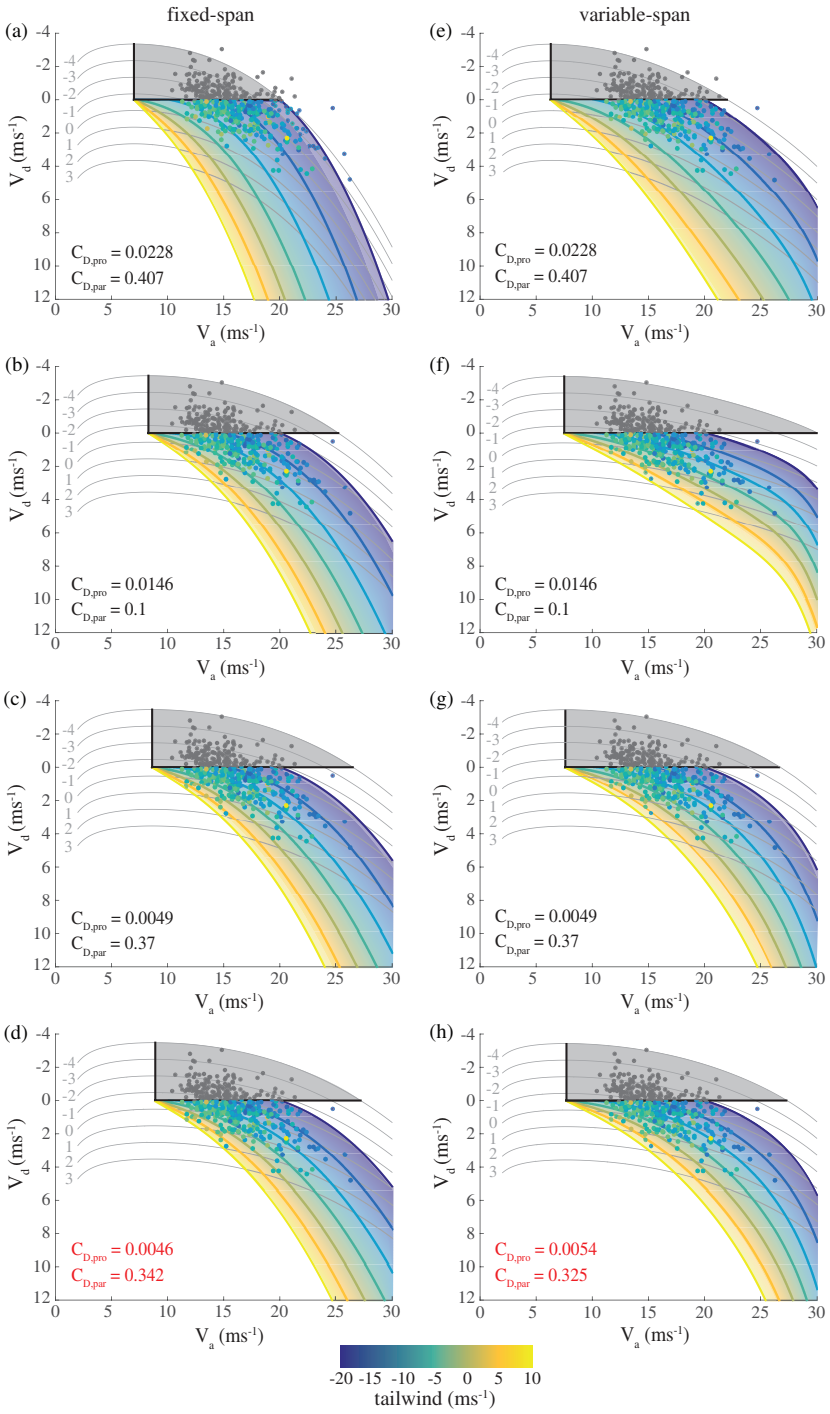


Figure 6.8: Experimental data compared with different glide optimisation areas derived from the fixed (*a-d*) and variable (*e-h*) wingspan models of the glide polar with a set of drag coefficients commonly used in the literature. Polars *d* and *h* shown the results of optimising the drag coefficients such that the error between the measured and model predicted tailwinds was minimised. V_* isolines are coloured by the magnitude of the tailwind component.

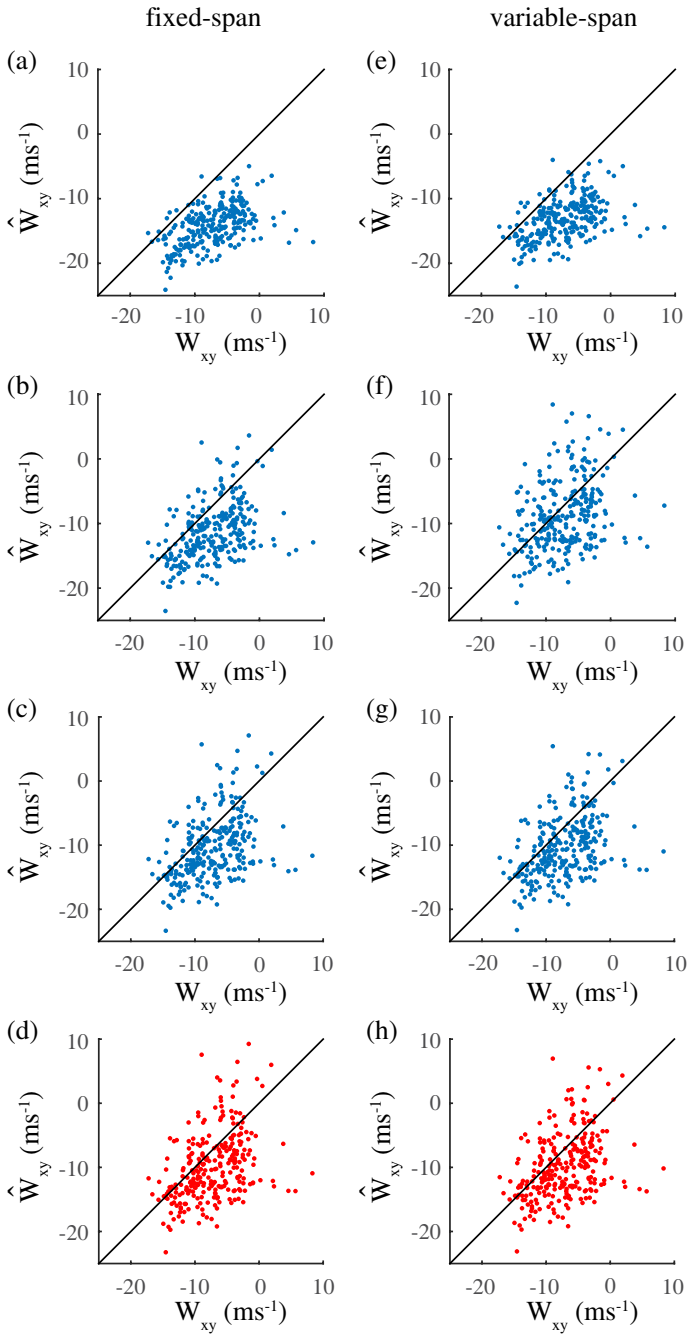


Figure 6.9: Tailwind correlation between the measured (W_{xy}) and model predicted ($\hat{W}_{xy}$) values for fixed and variable wingspan polars with drag coefficients described in Table 6.1. Black-lines: $W_{xy} = \hat{W}_{xy}$. As correlation decreases between the models, MSE increases. All models tested show a significant correlation. (d) & (h) show the correlation for the optimised drag coefficients which minimise the difference between predicted and modelled tailwinds in the fixed and variable-wingspan polar models respectively. These results also show that the bird systematically flies faster than the theory predicts.

a reference table of V_d values was created for each combination of W_{xy} and V_a. For each glide, the nearest value of V_d was found and the corresponding W_{xy} read off the table.

For glide points where $V_d > 0\text{ms}^{-1}$, the correlation coefficient (r) was calculated between the measured tailwind (W_{xy}) and the model estimated $\hat{W}_{xy}$ for each form of the polar. Results are shown in Table 6.1 with the corresponding p-values and illustrated in Figure 6.9. Although the correlations are not strong, they are significant for each form of the polar. The mean squared error (MSE) was then calculated to test the accuracy of the model predictions. The black lines in Figure 6.9 indicate the line of equality ($W_{xy} = \hat{W}_{xy}$). We see that despite the stronger correlations in polars *a* & *e* (calculated with drag coefficients proposed by Tucker) the MSE is largest for these models, whilst the opposite is true for polars *c* & *g* (with coefficients proposed by Taylor and Thomas (2014)). Therefore although the data are noisy, we conclude that the Taylor and Thomas coefficients provide the best match for our experimental data. Furthermore, the variable-wingspan polars are consistently less biased than their fixed-wingspan equivalents.

It is interesting to note the different shape of the curves, specifically Figure 6.8f where there is a clear effect of a small $C_{D,par}$ which, as the wingspan decreases at higher airspeeds, causes a pronounced reduction of V_d and results in a much flatter curve than for example Figure 6.8g which has a much smaller $C_{D,pro}$.

Optimal drag coefficients

Finally it is possible to find the optimum set of drag coefficients that minimise MSE for each model. This is illustrated in Figure 6.10 for the fixed-wingspan polar ($V_s = c_1V^{-1} + c_2V^3$) where constant c_2 generates a minimum MSE at approximately 1.93×10^{-4} (marked by red *). Also shown are the equivalent c_2 constants for polars *a*, *b* & *c*, where polar *c* is extremely similar to the optimum. The actual optimal values of $C_{D,pro}$ and $C_{D,par}$ were found using the MATLAB *lsqnonlin* function where $W_{xy} - \hat{W}_{xy}$ was minimised and resulted in $C_{D,pro} = 0.0046$ and $C_{D,par} = 0.342$ which

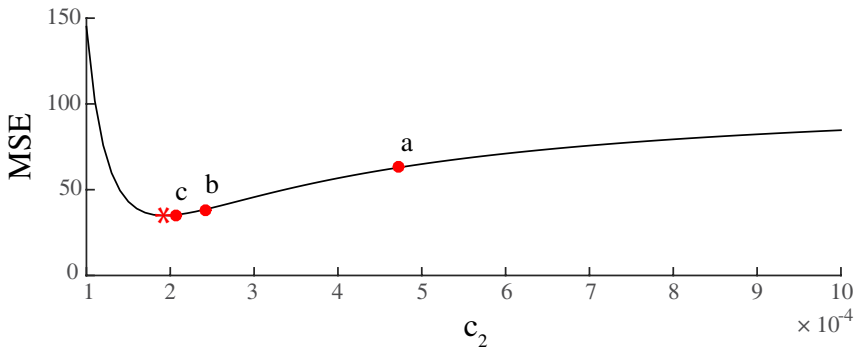


Figure 6.10: Modelling the effect of changing constant c_2 in the fixed-wingspan polar model $V_s = c_1 V^{-1} + c_2 V^3$ on the mean squared error (MSE) of the correlation between measured W_{xy} and model estimated $\hat{W}_{xy}$. Points a, b and c correspond to the c_2 values used in fixed-span polars a, b and c in Figure 6.8 and Table 6.1. (*) is the optimal value of k_c ($\approx 1.9 \times 10^{-4}$) which is extremely similar to point c—the model proposed by Taylor & Thomas (2014).

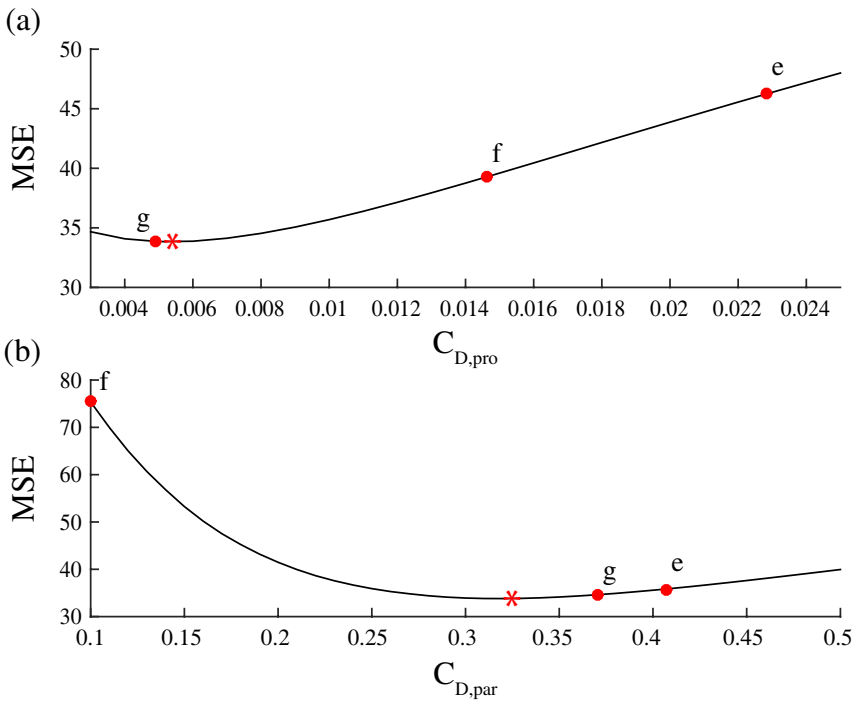


Figure 6.11: Mean squared error (MSE) of the correlation between measured W_{xy} and model estimated $\hat{W}_{xy}$ for the variable-wingspan polar model when the drag coefficients are changed. (a) $C_{D,pro}$ (b) $C_{D,par}$. Points e, f and g correspond to the coefficients used in the variable-span polars e, f and g in Figure 6.8 and Table 6.1. (*) is the estimated optimal drag coefficients ($C_{D,pro} = 0.0054$ and $C_{D,par} = 0.324$, assuming $\eta = -0.03$), both of which are again most similar to the model proposed by Taylor& Thomas (2014)—point g.

are similar values to polar c with coefficients from Taylor and Thomas (2014)—see Table 6.1. A similar optimisation was also done for c_1 to find the induced drag factor (k). However, this resulted in $k = 0.49$ which is far smaller than realistically possible. This is likely due to the lack of data in the low airspeed region which is most influenced by the value of k.

Optimal drag coefficients for the variable-wingspan model were found by parametrically varying $C_{D,pro}$ and $C_{D,par}$ individually and recording the MSE. This was an iterative process where the optimisation for each coefficient was performed with the most up to date optimum value for the other coefficient in the model; this was repeated until the optimal values no longer changed, see Figure 6.11. Again the resulting estimates of $C_{D,pro} = 0.0054$ and $C_{D,par} = 0.325$ are very similar to those proposed by Taylor & Thomas (polar g).

Although these results suggest that it is plausible the bird is optimising airspeed to fly as far as possible with minimum loss of altitude, the data are noisy and it appears that for most glides the bird is flying systematically faster than theory predicts (Figure 6.9). This is consistent with Spaar's findings but could easily be due to instrumentation error, particularly from the pitot tube measurements.

6.4 Discussion

We have demonstrated the feasibility of extracting experimental glide data for our steppe eagle from an onboard instrumentation unit. Like many other free-flight studies, our data contains considerable noise but the characteristics are consistent with similar steppe eagle glides recorded from ground based radar techniques (Spaar and Bruderer 1996). Sources of noise include unknown changes to control surfaces, the effect of the onboard equipment on the profile drag coefficient, tatty feathers and drag generated from the position of the bird's feet (particularly in steep dives to the right of the polar). We found however that the data could not be explained purely by the traditional polar models—even accounting for error in the model

estimates—and clearly fitting a single polar curve is an over simplification of the data. More research into accurate drag coefficient estimates and wing morphing models is perhaps required, but it is evident that for free-flying birds the effect of atmospheric conditions on the polar and their flight strategies plays an equal, if not a more important role in their performance; perfect nil-wind conditions are extremely rare and birds must constantly account for the changing winds.

Exploring the effect of wind, we found that airspeed was significantly correlated to both vertical and horizontal wind components, increasing in both downdrafts and headwinds as predicted by theory. This response to different wind conditions suggests that, to an extent, the bird is able to estimate the movement of the surrounding airflow and adjust its flight behaviour accordingly, improving glide performance. This may be a simple in-built mechanism saying for example, fly faster if a headwind or downdraft is detected, regardless of what the bird is trying to achieve. Given our bird has no motivation to fly at V_* when simply loitering on a ridge waiting for the falconer, an in-built mechanism is plausible.

To incorporate the effect of wind into the glide polar data, we generated the soaring optimisation chart which predicts, for known wind conditions, how we would expect the bird to fly if trying to either maximise distance travelled for a minimal loss of altitude and/or maximise potential energy gained. Comparing this with experimental data allows the researcher to study the optimisation strategies a bird might be using, specifically if the bird has a clear flight objective such as migration. This is an alternative way of looking at the glide polar in terms of energy optimisation.

There are 2 distinct regions on the chart. The first, when the bird is losing altitude ($V_d > 0\text{ms}^{-1}$), is comprised of isolines which predict, based on the optimal glide angle, a specific optimal airspeed for the bird to fly at given a set of wind conditions. The second, when the bird is climbing, represents a bifurcation with 2 possible parameters to optimise. The predictions in this region are unclear though the closer the bird flies to V_{min} the more potential energy it is trying to extract from the atmosphere, whilst the closer to $V_d = 0\text{ms}^{-1}$, the the further it can travel

without losing altitude.

Finally by testing our tailwind glide data against the estimated tailwind from the position of our glides on the optimisation chart for common forms of the glide polar, we found that the data were significantly correlated and could be best explained by the variable-wingspan model with coefficients $C_{D,pro} = 0.0054$ and $C_{D,par} = 0.325$, which are exceedingly similar to those proposed by Taylor and Thomas (2014), based on the classic laminar boundary layer solution for a flat plate and Hedenström and Liechti's (2001) field measurements respectively.

We note that although our set of data does lend itself to drag coefficients similar to those proposed by Taylor and Thomas, this esimate is specific to our bird, which is well adapted for soaring flight. It would be interesting to compare these results with data from other species and see if we reach the same conclusions.

Chapter 7

Thermalling characteristics

7.1 Introduction

In this thesis we have looked at various phases of flight in our steppe eagle, including flapping, gliding, and straight line soaring in ridge lift. Finally, in this chapter we focus on circling soaring periods, which are generally associated with the bird exploiting the energy available in thermals to climb.

Thermals are convection currents in the atmosphere, driven by a temperature contrast between the ground and the air from solar heating (Angevine 2006). The ground conducts heat to the nearby air causing it to expand and its density to decrease. However, the air can only start to rise as a thermal once it is sufficiently buoyant to overcome the viscous forces. The height of the thermal is dependent on the atmospheric stability and the temperature profile. Rising air in thermals may be only a degree or so warmer than the ambient temperature (Hunter 1984), with a vertical velocity in the range of 1-10ms^{-1} (Ákos et al. 2010). Land thermals can be up to a few kilometres in diameter (Bohrer et al. 2012) and have a life span of about twenty minutes (Bower et al. 2010).

The optimum turn radius, circling period and other performance characteristics for exploiting thermals are highly dependent on both the structure and strength of the individual thermal and the glide performance of the bird or glider. There are two commonly accepted models of thermal structure; air in a thermal can either rise as a continuous column which is replenished by warm air from the ground, or as a bubble of warm air which separates from the ground (Andersson et al. 2009). In reality, thermals are far more complicated with fluctuating, turbulent internal flows which can be comprised of both horizontal and vertical vortex rings—similar to the complex flows visualised in a smoke plume from a factory. The structure will also be influenced by the wind. However, general features include a region of sink surrounding a thermal, as air is drawn down to replace the rising warm air (Reichmann 1993), whilst the core of a thermal is stronger and more structured than the turbulent edges or base where the air is sucked in over the rough landscape (Angevine 2006). Most thermalling strategies focus on finding and staying in the core, though there is a trade-off between proximity to the core and a small turn radius which results in a higher sink rate. The classic summary of thermalling flight optimisation and of the various strategies for identifying and staying in the core of a thermal is found in Reichmann (1993).

Previous studies looking at the different behaviours of birds whilst circling have primarily been founded on ground based measurements or GPS tracks to get estimates of climb rates, turn radius, thermal location, airspeeds, etc. These characteristics are then often compared between species and to parameters such as topography, meteorological conditions or migratory behaviour (Cone 1962; Pennycuick 1971b; Pennycuick 1972; Shamoun-Baranes et al. 2003; Spaar and Bruderer 1996; Spaar and Bruderer 1997). Quantifying the benefit of thermalling in terms of cross-country speeds or energy minimisation (Duerr et al. 2012; Hedenström and Alerstam 1998) has led to the development of theories for optimal strategies, for example selecting suitable inter-thermal glide speeds according to climb rate in thermals (Ákos et al. 2008; Ákos et al. 2010; Pennycuick 1998). The foundation of many of these strategies are the methods and rules of thumb used by human glider pilots (Reich-

mann 1993).

In this chapter I present a descriptive analysis of the thermalling flight of our steppe eagle. Our onboard instrumentation provides high resolution data that allows us to examine the bird's typical circling characteristics. We also start to explore more subtle patterns in the data that cannot be detected from traditional measurements but may indicate what cues the bird uses to find the best lift. The analyses reported in this chapter are necessarily preliminary due to the extraordinary depth of detail that is present in this sort of data, and the novelty of the data sources. The chapter concludes by suggesting a number of hypotheses that deserve further testing and the possible analyses that can be used.

7.2 Methods

Many of the key parameters for characterising thermalling flight, such as bank angle, climb rate, airspeed and total energy gain were derived in Chapter 2. Further processing of the data is presented here to extract the sections of thermalling flight, remove the wind drift component and calculate additional parameters of turn radius and circling period.

7.2.1 Thermal identification

Thermal flight is easily identified from periods of circling as the bird, attempts to fly within the thermal column. To automatically extract these thermalling sections from our recorded data, we therefore use selection criteria in respect of yaw rate ($\dot{\psi}$) and the rate of change in total energy ($\dot{E}_t$) to determine when the bird is both circling and successfully extracting energy from the thermal.

The calibrated z-axis gyro data was used as the measurement of yaw rate; unlike the GPS heading measurement, this is unaffected by the wind vector. Although the gyro measurements contain considerable noise, we are only interested in the

general trend to identify circling, therefore significant filtering to eliminate the high frequency fluctuations was applied by smoothing the data over 10s using a moving average. In addition, as yaw rate was measured at the higher sampling rate of 50Hz it was then down sampled to 10Hz to match the sampling rate of the other measurements. A yaw rate threshold of $\dot{\psi} > 7.5°\text{s}^{-1}$ was chosen to capture all circling flight.

A strict threshold of $\dot{E}_t > 0\text{Js}^{-1}$ was applied to ensure the bird was simultaneously extracting energy (soaring) whilst circling. We note that due to its inherent sink rate, the bird continuously loses energy ($\dot{E}_d$, the rate of change in energy due to dissipation) therefore it is actually possible for the bird to gain energy from the atmosphere whenever $\dot{E}_t > \dot{E}_d$.

Many of the selected samples that met these two instantaneous thermalling criteria did not relate to continuous circling. The points were therefore filtered to remove sections that corresponded to less than 30 seconds of continuous thermalling (the equivalent of approximately two to three full turns, depending on turn rate). Finally, given that the bird may drop out of a thermal momentarily or perhaps fly straight in order to shift the centre of its circling, even changing direction, we allowed a gap of up to six seconds (60 points) within the thermal data where the instantaneous criteria were not met. Any larger gap and the bird was considered to have started a new period of thermalling flight.

These thermal identification criteria were set through trial and error by manually examining the data to ensure the maximum number of thermals were located with minimum false positives. Nevertheless, from 189 'thermals' found automatically across all 45 flights, a number of false sections of ridge soaring with high yaw rates were identified, and occasionally one continuous thermal was split into separate parts. To correct for this, the thermal data were manually trimmed to remove non-thermals and combine split ones. In this way we identified 146 thermals. An example of the thermals found for one flight is shown in Figure 7.1.

Inspecting each flight, we see a number of circling sections which resemble ther-

malling but were not identified as such in this analysis. In some cases, this occurred at the beginning or end of a thermal. This is likely due to our strict energy rate threshold of $>0 \text{Js}^{-1}$; a thermal tends to be weaker at the top and bottom and in these parts the updraft may not be strong enough to entirely overcome the bird's natural sink rate. To understand a thermalling strategy, it may be useful to also examine the periods of flight immediately before and after the formally identified 'thermalling' sections. In addition to identifying strictly thermalling flight, we therefore used the same method to also find purely circling flight by removing the energy gain criteria.

7.2.2 Drift elimination

Instead of a column of air rising vertically, thermals are often pushed across the terrain by the prevailing wind conditions. This makes finding and staying in the core of a thermal all the more challenging as the bird must keep up as it drifts; this is demonstrated in Figure 7.1. Thermal drift occurs in approximately the same direction as the prevailing wind, though both speed and direction can be affected by obstructions (such as the ridge). Nor is the drift necessarily constant throughout the thermal as wind increases with altitude, the thermal can be hit by sporadic gusts, or pass through a shear layer which abruptly changes the drift direction. For the bird, flying through the air, the main effect of these combined sources of drift is that visual cues related to the ground can be of little use for centering in the thermal or for maintaining airspeed or orientation.

To study the bird's movement relative to the atmosphere, rather than to the ground, it is desirable to remove the effect of this wind drift from the GPS track, which allows us to visualise how the bird is performing within the thermal. This also simplifies the calculation of turn radius and circling period (Ákos et al. 2008). We tried various methods for eliminating the wind drift component, including:

1. Removing the low frequency components of the horizontal velocity data using a Fourier analysis. For each thermal, the optimum cut-off frequency was selected

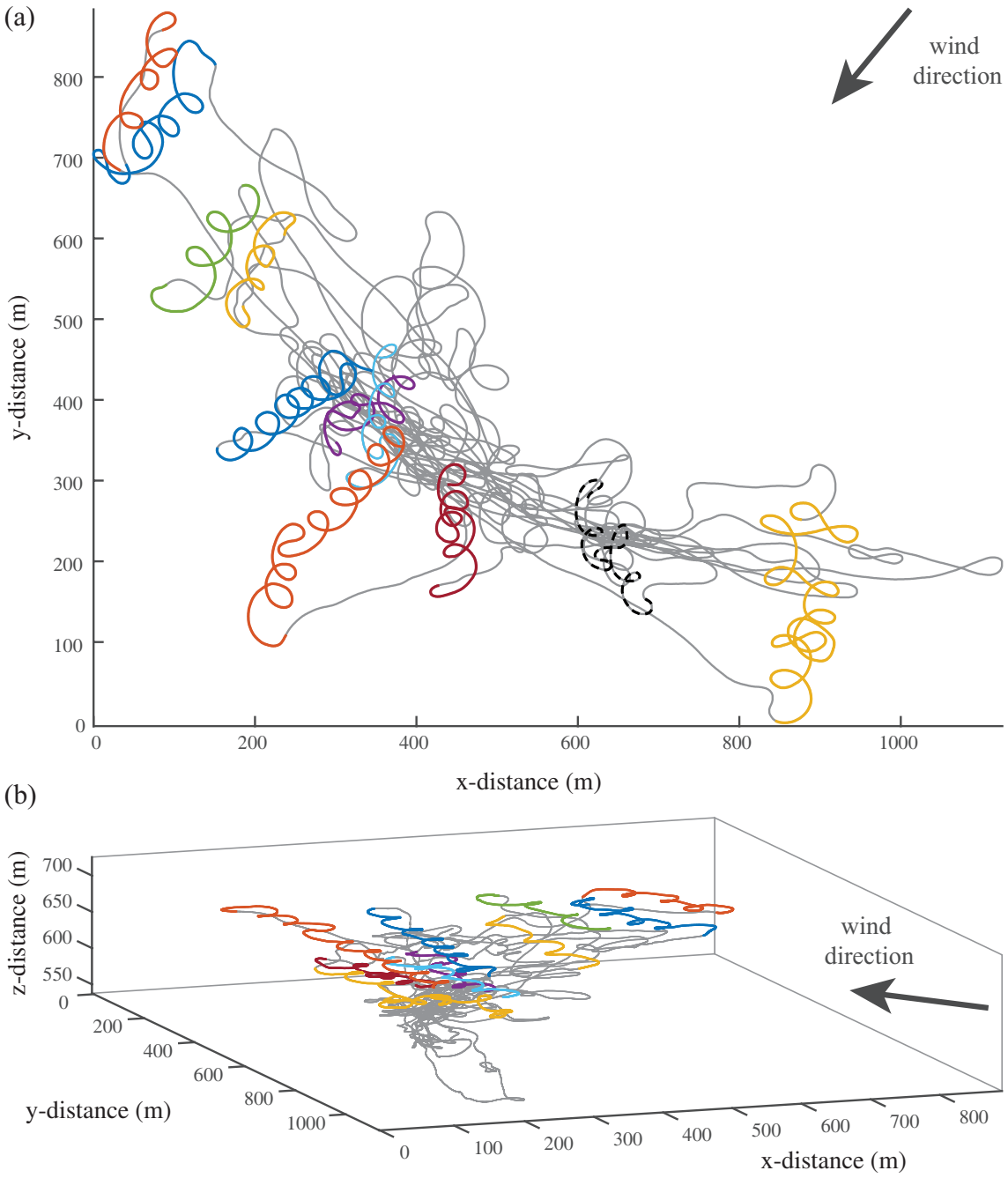


Figure 7.1: An example flight track showing the results of the thermal identification algorithm. (a) 2D view from above, (b) 3D view. Thermalling flight was found based on change in total energy and yaw rate criteria. The ten continuous sections of thermalling are highlighted in colour. The prevailing wind direction is also shown, illustrating the effect of wind drift as the thermals are pushed up the ridge. For each thermal section, the climb started top right and ended bottom left. Black-dashed: A section of circling flight not identified as thermalling as the $\dot{E}_t < 0 \text{Js}^{-1}$ criteria was not met.

by maximising the correlation between gyro angular rate data and the resulting rate of change of the track angle. Unfortunately, this was not robust for all thermals as it frequently removed actual features of the bird's flight.

2. A modified version of the drift elimination first described in a study by Akos et al. (2008), again based on removing the trend of the velocity data from both latitude and longitude position, see Figure 7.2a&b. This method was designed to account for variation in the magnitude of the thermal drift with altitude by fitting a spline interpolation to the maximum and minimum points of the velocity data and calculating the mean between them. The mean was then subtracted and position recomputed. However, this relies on the assumption that the bird's airspeed remains approximately constant during a turn, which has proved to be invalid (see Discussion). Although this method worked reasonably well for the majority of thermals, results were sporadic and it was often unclear what correction had been applied.

3. Finding and removing the optimum linear slope of the horizontal position data that maximises the correlation between the estimated yaw angle and the resulting track heading angle. Again this had variable success.

4. De-trending both the latitude and longitude position components by subtracting the linear regression slope of the data with time, see Figure 7.2c&d.

It is difficult to effectively validate the different wind drift methods and test their reliability as we cannot distinguish whether thermals that result in non-perfect circling are because the method is inaccurate, or because the bird is in fact actively circling irregularly, making adjustments during the thermal. Qualitatively comparing the different methods, the last (and simplest) method seems to produces the most consistent results. Although the more sophisticated approaches theoretically allow for variation in the magnitude of the wind drift during the thermal whilst remaining robust to irregularities such as changes in circling direction, they are almost too sensitive and might correct for movements that are in fact deliberate.

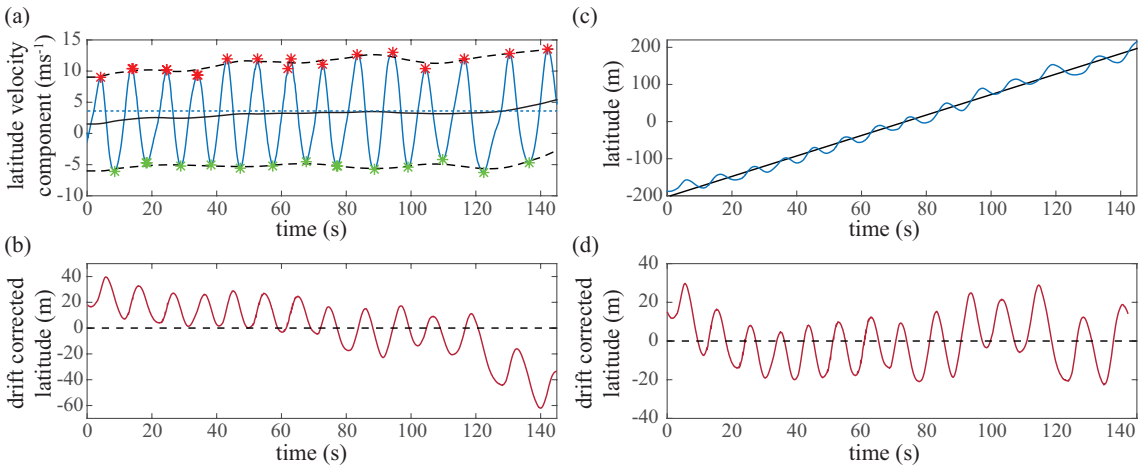


Figure 7.2: Illustration of drift elimination *methods II* & *IV* for the thermal in Figure 7.3a. (a) *Method II*: removing the velocity trend from the data (Ákos et al. 2008). Maximum (red) and minimum (green) points of the latitude velocity component (blue) of the thermal were found and spline interpolations fitted to each (black-dashed). Points that lay less than one standard deviation, or more than two standard deviations from the mean (blue-dashed) were not included to allow for irregular circling. Finally the mean (black) of the two splines was calculated and subtracted from the velocity data before position was recomputed. (b) Recomputed latitude position data from the analysis in (a). Not all drift has been eliminated. (c) *Method IV*: removing the linear slope (black) from the position data (blue). (d) Latitude position after wind drift removal from (c). Although *Method II* is designed to take account of changes in the wind drift within the thermal, *Method IV* appears to perform better, likely because the assumption that the bird's airspeed speed is constant whilst thermalling is not valid.

Method IV simply assumes that the wind drift is constant over the course of the thermal, and removes the linear component of the position data (by eliminating the linear regression component of both the latitude and longitude recordings). This is not necessarily a bad assumption as the majority of our identified incidences of thermalling are relatively short (mean number of turns per thermal = 5.9±5 turns) and it is unlikely that the change in wind drift within this period will be dramatic. The advantage of this method is that it is clear what correction has been applied, see Figure 7.3 for a selection of drift corrected thermals. The limitations of this method should be remembered when using the drift corrected data and we note that future studies may benefit from a more rigorous analysis of the wind drift (e.g. developing *Method II* to include airspeed).

One way to validate the wind drift elimination is to compare the estimated

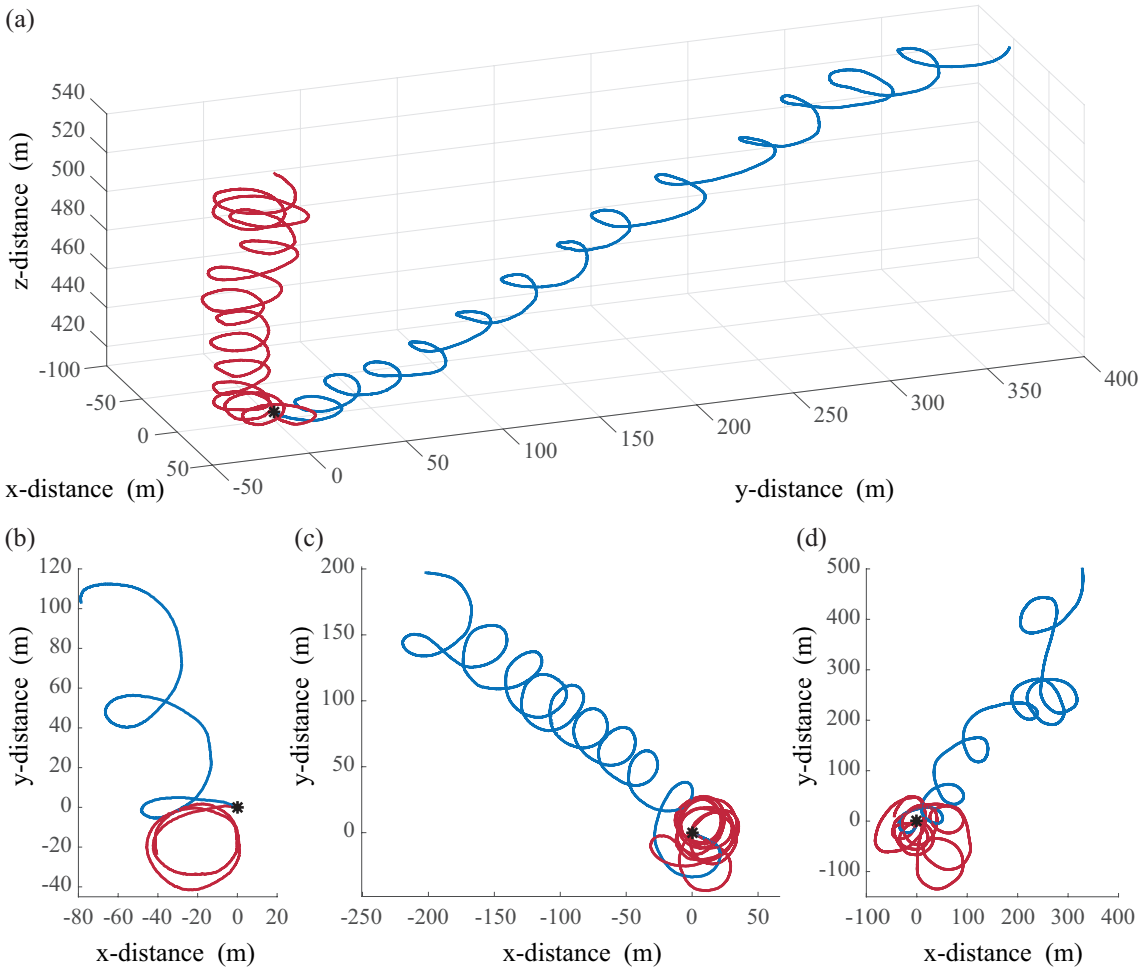


Figure 7.3: Four thermal examples of the wind drift removal method used in this study based on the removal of the linear slope from position data. Blue: original GPS track. Red: track after wind drift removed. Black-point: start position. (a) 3D view, estimated wind drift for this thermal is 2.8ms^{-1}. Thermals (a) to (c) appear to show accurate wind drift removal, resulting in a near circular flight path. Thermal (d) would seem to be less successful as the bird's circling flight is more irregular, but this might be an accurate representation of the bird shifting his circling position.

drift with recorded wind velocity on the day from both MIDAS and anemometer measurements. We find that both are significantly correlated (MIDAS regression: $n = 146$, $R^2 = 0.15$ $p < 0.0001$, whilst for the anemometer: $n = 146$, $R^2 = 0.06$ $p < 0.001$). As the wind estimates are averaged over the whole flight, the poor variance is not unexpected, especially given the large and variable distance of the weather station from the different flight sites (this error will also change with wind direction). The MIDAS and anemometer data tend to under and over predict the

drift magnitude respectively, perhaps because of the difference in altitude of the measurements; the anemometer is positioned at the top of the ridge where the flow is accelerated.

Turn radius and circling period

Here we present three ways to calculate the turn radius (r) of the bird during thermalling from our set of data, and one estimate for circling period (i.e. the time for the bird to complete a 360° turn in the thermal).

Method 1: The most basic approximation (similar to that used by Pennycuick (1983)), is to identify the maximum and minimum points of the track for each circle, and calculate the distance between them. In this way, we get an estimate for turn radius every 180°, for both of the latitude and longitude readings (four per 360°). This was done for the GPS thermal tracks after the wind drift was eliminated, as illustrated in Figure 7.4. The maximum and minimum points were automatically found by differentiating the latitude and longitude data.

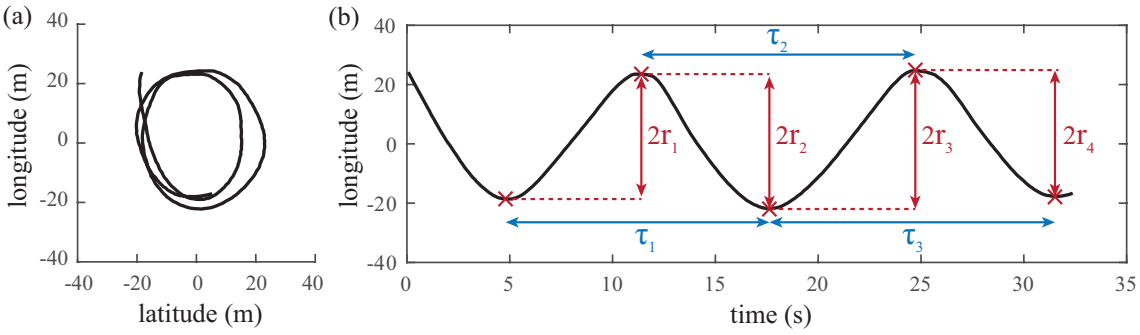


Figure 7.4: (a) Thermal track after wind drift elimination, for the thermal in Figure 7.3b. (b) Example of **method 1** turn radius (r) estimates from the drift corrected longitude (for the same thermal). r is calculated every 180° as half the distance between the maximum and minimum latitudes (red-crosses), which were found automatically by differentiating the data. The calculation of the circling period (τ) is also illustrated in blue, as the time between maximum or minimum points. For this thermal, $\bar{r} \approx 20.5$m and $\bar{\tau} \approx 13.9$s.

Based on the same analysis, we can also obtain estimates of the bird's circling

period (τ) as the time between each maximum or minimum of both latitude and longitude position data (Figure 7.4)—again providing four measurements every turn (Ákos et al. 2008; Pennycuick 1983).

Method 2: Alternatively we can obtain an instantaneous measure of r from two velocity vectors along the flight path, again calculated from the wind drift corrected GPS data after conversion to meters.

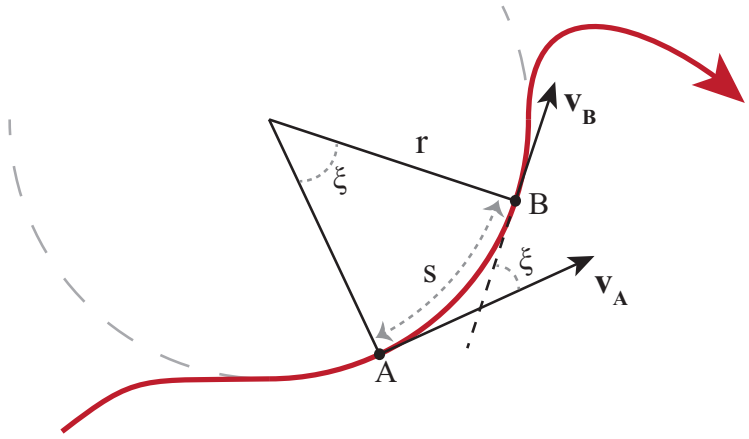


Figure 7.5: Diagram of the instantaneous turn radius calculation in **method 2** ($r = s/\xi$), assuming points A and B lie on a circle (grey-dashed). Red: flight path of bird. ξ is the angle between velocity vectors at A and B ($\mathbf{v_A}$, $\mathbf{v_B}$), which is also equal to the angle made by the arc at the centre of the circle. s is the length of the arc.

Assuming that two points (A and B) on the bird's path, lie on the circumference of a perfect circle—given that the time interval (t) is short—the length of the circular arc (s) between them is calculated by $s = r\xi$. Here ξ is the angle made by the arc at the centre of the circle, in radians (see Figure 7.5).

The bird's total velocity vector ($\mathbf{v}$) at each point along the path is calculated by finite differencing the latitude and longitude position data over time. s can then be simply estimated as the mean velocity for each sample point between A and B ($\bar{v}_{A-B}$), multiplied by the time interval ($s = t\bar{v}_{A-B}$). Finally, the angle ξ is found from simple trigonometry as it is equal to the angle between the velocity vectors at

points A and B (which are perpendicular to the flight path). From the dot product rule, this angle is:

$$\xi = \cos^{-1}\left(\frac{\mathbf{v_A} \cdot \mathbf{v_B}}{|\mathbf{v_A}||\mathbf{v_B}|}\right) \tag{7.1}$$

Once we know s and ξ, we can estimate r. The accuracy of r is influenced by the choice of the time interval between the two points, and the optimum value will vary depending on the curvature of the path. We chose $t = 3$s (30 points) from trial and error. This method often results in instances where the radius is calculated to be close to infinite due to short sections of straight flight, or when the bird changes its circling direction. This will skew estimates of mean circling radius for a given thermal, so for average radius statistics we therefore use the mode, (see Figure 7.6).

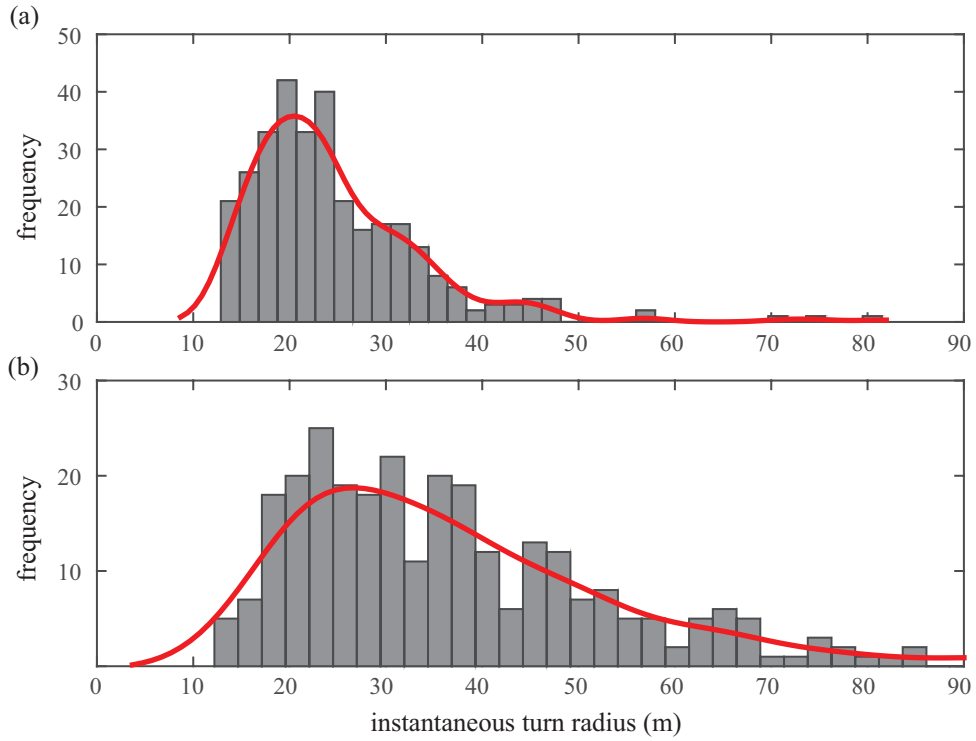


Figure 7.6: Histograms of the turn radius for the example thermal in Figure 7.4 calculated from (a) *method 2* where the modal radius of 20.5m was found by fitting a nonparametric, kernel-smoothing distribution (red), and (b) *method 3* with a much larger modal radius of 26.8m. The results from the bank angle estimation are noisier with a wider variation. The skew of the data is illustrated in both cases.

Method 3: The final approach is to use the relationship between turn radius, bank angle (ϕ) and airspeed (V) which is based on the assumption of a steady turn:

$$r = \frac{V^2}{g \tan \phi} \tag{7.2}$$

where g is gravitational acceleration (Pennycuick 1983; Taylor and Thomas 2014; Vinh 1993). This estimate is independent from the GPS track data and so is unaffected by the accuracy of our wind drift elimination method, but is highly sensitive to the accuracy of the bank angle data derived from the AHRS in Chapter 2. The instantaneous turn radii we get from this calculation are therefore extremely noisy, made worse by the noise in the airspeed data.

Methods 1 and 2 produce very similar results. Both are based on the drift corrected data, the accuracy therefore relies on the success of the drift removal. Comparing the instantaneous turn radius results from methods 2 and 3, we find that although the regression between them is significant, the variance is huge, likely due to the noise in both bank angle and airspeed data ($n = 84547$, $R^2 = 0.19$, $p < 0.001$). Figure 7.6 also demonstrates how the radii calculated from method 3 are systematically higher, this could be due to error in either the bank angle or airspeed data or it could be because the steady turning assumption is invalid. Indeed, watching steppe eagles (and many other birds) thermalling, they often appear to bank in a somewhat jerky manner though the GPS track can still look quite smooth as a result of the double integration between acceleration and position. Method 3 calculates turn radius from 10Hz instantaneous data, method 2 calculates it from 3 second samples, method 1 from samples taken twice per circle (about 7 seconds), it is therefore possible that the systematically larger radii of method 3 are not just due to noise, but actually reflect the unsteady nature of thermalling 'circles'. All three methods approximate the bird's turn performance, they are related to the turn radius, but each represents a distinct but valid approach.

7.3 Results

The automatic thermal identification method found 146 thermalling sections of flight of varying lengths (mean 81±71s) from the 45 flights. The results for each flight are shown in Appendix C. The bird was found in total to thermal for 17.2% of the time. This is lower than recorded by Spaar and Bruderer (1996) for steppe eagles flying in Israel (28%), which is unsurprising given the poorer thermal soaring conditions in Wales. Periods of circling flight indicate when the bird is attempting to thermal, irrespective of whether the updraft is sufficient to increase total energy. The total proportion of circling across all flights was 26.7%; the results for each test day are shown in Figure 7.7. We also calculated the proportion of each flight the bird spent flapping, based on the flap identification method described in Chapter 3. However, flapping occurred rarely (<1% for any flight) and was not correlated with the proportion of thermalling.

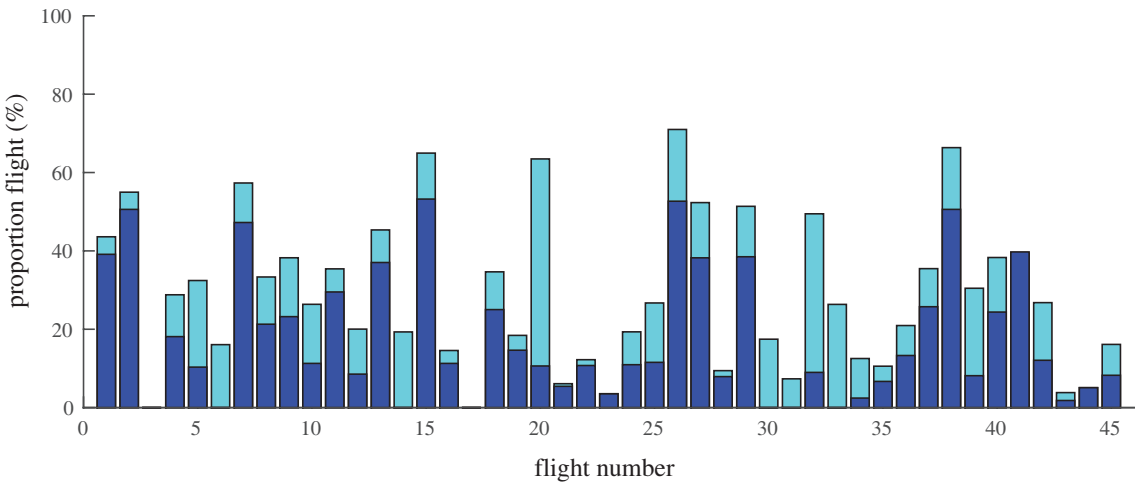


Figure 7.7: Proportion of thermalling (dark blue) and circling (light blue) flight for each test day (flight numbers correspond with the GPS tracks in Appendix C, ordered by date). Across all flights, the mean proportion of thermalling was 17.7±16.6%, whilst circling was 29.0±19.3%. This illustrates the wide variation in soaring strategy the bird used between flights and we note that there is no correlation with time.

As test days (and times) were selected based on their soaring potential, we

cannot draw any conclusions about diurnal or annual changes in the bird's soaring performance. Previous studies have investigated these effects and, as expected, found that birds thermal better in the middle of the day and the summer when thermal generation is at its maximum. We would expect to find similar results with our bird.

However, we can look at the different weather conditions between test days. Linearly regressing percentage of thermalling on measures of atmospheric conditions for each flight day, we find that thermalling is significantly negatively correlated with wind speed, regardless of whether ultrasonic anemometer, MIDAS or RASP data measurements are used (regressing the MIDAS wind velocity on % thermalling resulted in $n = 45$, $\mathrm{R}^2 = 0.17$, $p < 0.005$). Calmer wind conditions may allow thermals to develop before the warm air is blown away, and it may be easier to find, and stay, in thermals when wind speeds are low, but also on light wind days our eagle has to use thermals if he is to stay up as slope lift will be weak or absent. From our analysis in Chapter 3, this supports the hypothesis that wing tucks are not correlated with thermal turbulence (wing tucks are positively correlated with wind speed). We found no other significant relationships between the proportion of thermalling and other atmospheric parameters estimated from RASP such as surface temperature, MSL pressure or thermal height.

The typical characteristics of our steppe eagle's flight in thermals are summarised in Table 7.1 and presented as histograms in Figure 7.8.

During a banked turn, the bird's vertical component of lift force (L) is $L\cos\phi$. If the turn is steady, this must be balanced by the weight (mg), we therefore get:

$$L = \frac{mg}{\cos\phi} \tag{7.3}$$

The classic lift equation ($L = \frac{1}{2}\rho V^2 S C_L$) can then be rewritten for level turning flight by substituting L for Equation 7.3 and V^2 from Equation 7.2. Rearranging

measurement	thermalling average
turn radius	18.18 m
circling period	13.8±3.6 s
airspeed	12.7±1.8 ms^{-1}
climb rate	0.89±1.31 ms^{-1}
bank angle	23.7±13.2 °
load factor	1.13±0.20
lift coefficient	0.97
ground speed	10.13±3.43 ms^{-1}

Table 7.1: Summary of parameters characterising the thermalling flight of our steppe eagle. Means with standard deviations are presented from all 146 thermals identified. Note the turn radius quoted here is the mode, calculated using *method 2* with instantaneous velocity vectors. Bank angle is estimated from the AHRS results in Chapter 2 and the lift coefficient is calculated from Equation 7.5 using average values.

we get (Pennycuick 1971b; Vinh 1993):

$$r = \frac{mg}{S}\frac{2}{\rho g C_L \sin\phi} \tag{7.4}$$

or, in terms of the lift coefficient (C_L) as calculated for Table 7.1:

$$C_L = \frac{2m}{\rho S r \sin\phi} \tag{7.5}$$

where ρ is the density of air and S is the wing area which is assumed to be at its maximum ($0.54m^2$) when the bird is thermalling. Equation 7.4 predicts that if ϕ and C_L are constant, a bird's turn radius should be proportional to its wing loading ($mg/S = 42.7$ for our individual). The theoretical limiting value for a bird's turn radius is calculated for when C_L is a maximum (often 1.2) and $\phi = 90°$, though realistically a vertical bank angle is not achievable. For our bird, minimum turn radius is therefore approximately 5.9m, during steady turning. The lowest radius we estimated (from method 2 in Figure 7.6) was $\approx$ 4.5m; the bird can achieve this lower turn radius instantaneously, but not for prolonged turning.

The values calculated in Table 7.1 describe the average thermalling character-

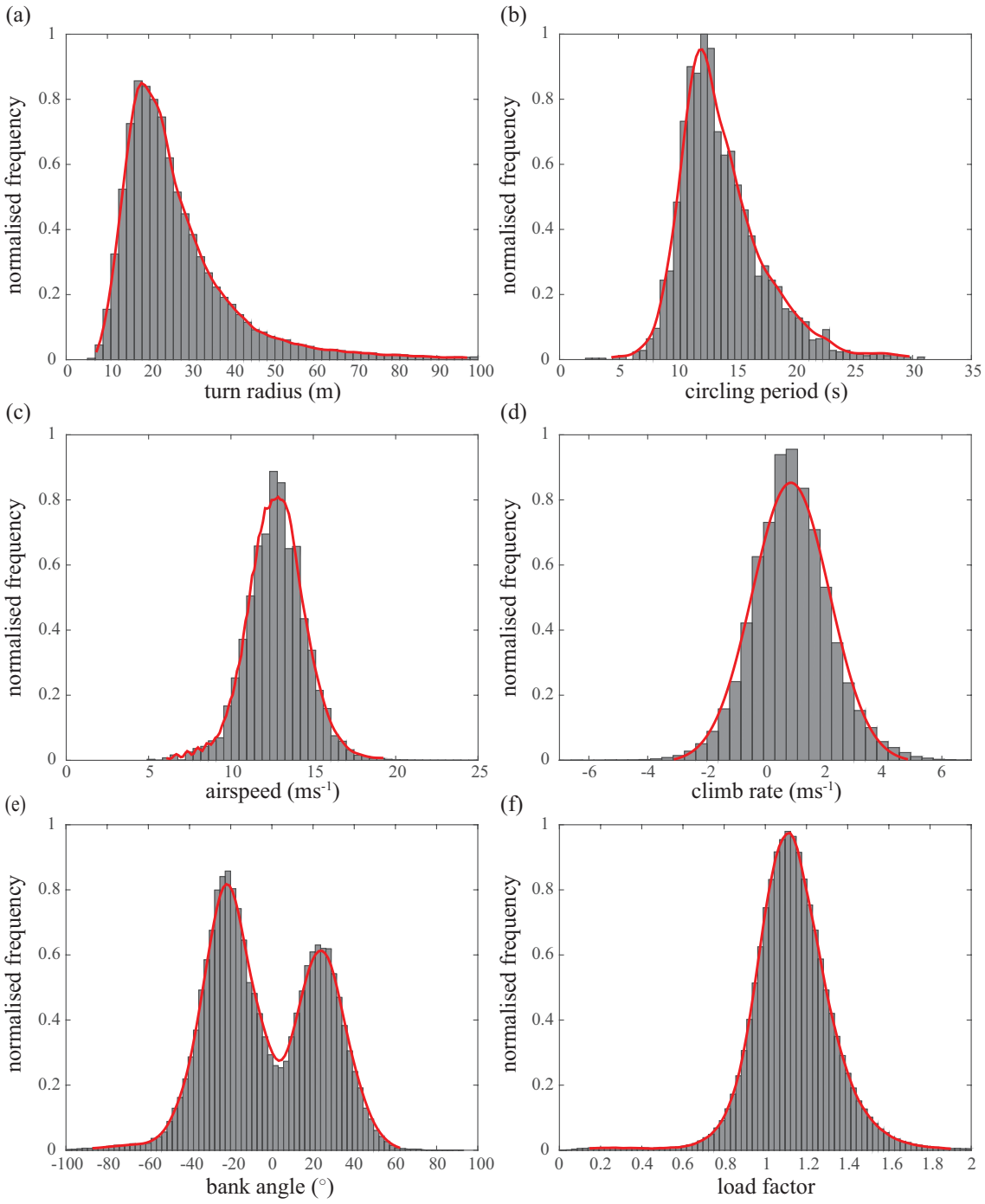


Figure 7.8: Histograms showing the normalised frequency density of instantaneous (a) turn radius, (b) circling period, (c) airspeed, (d) climb rate, (e) bank angle and (f) load factor for all data in the 146 sections of flight identified as thermalling. Red: Non-parametric kernel smoothing distributions.

istics of our bird. A similar set of parameters are quoted in other thermal studies (Ákos et al. 2008; Pennycuick 1983; Spaar and Bruderer 1996) but are often cal-

culated from the steady turning equations (see Equations 7.2–7.5), based only on flight path measurements. From these average variables, researchers have compared thermalling between species, and their adaptations to environmental conditions. For example, Pennycuick (1983) predicts that turn radius should be proportional to bird's wing loading. Although this might be the case for a given lift coefficient and bank angle, birds are not restricted to fly at these set conditions. Indeed, to optimise altitude gain in a thermal, theoretically they should adjust turn radius according to the thermal shape and structure. The variations in behaviour, both between and within thermals, is therefore of more interest for understanding soaring strategies. Here we discuss some preliminary analysis for exploring these patterns in our data, but first we note some general features of the bird's thermalling behaviour from Figure 7.8.

7.3.1 Thermal characteristics

Whilst the absolute bank angle was used to calculate the mean value quoted in Table 7.1, both positive and negative bank angles are plotted in Figure 7.8e. This is an indication of the bird's turn direction and implies that the bird turned left more often when thermalling. We found that for 96 thermals the bird circled continuously in one direction, in 46 he changed direction one or more times whilst for a few (four) the track was more irregular, almost a like searching pattern. We do not know what prompted the bird to change direction, though it was likely in order to shift his centre of circling closer to the thermal core.

In Figure 7.8f we have plotted the load factor (N_t). As we would predict in lift, the average load factor is greater than one. Given that (Vinh 1993):

$$\frac{L}{mg} = N_t = \frac{1}{\cos\phi} \tag{7.6}$$

the load factor can provide further validation of the bank angle data. If $N_t = 1.13$, then $\phi = 27.8°$. This is slightly higher than the bank angle recorded from the AHRS,

perhaps reflecting additional g-loads from unsteady turns and thermal turbulence, or perhaps just the different error sources in the two estimates (for example bank angle is estimated at 10Hz by combining data from multiple instruments, while the load factor just takes accelerometer data at 50Hz—gyros drift, accelerometers are noisy).

Climb rate is one of the most useful measures for judging performance in thermals as generally the objective is to gain altitude. The climb rate distribution in Figure 7.8d is dependent on the thermal identification method we have used. Therefore although our mean climb rate is higher than some other studies recorded, this does not necessarily mean our bird is performing better or that the soaring conditions are better. Indeed, our fairly low value for C_L actually suggests that the bird is not on average maximising his climb rate; if he were to fly at lower airspeeds closer to his minimum sink rate, his climb rate would improve. Of course there are difficulties associated with flying at speeds approaching stall which our bird might wish to avoid given he has little motivation to climb quickly. Climb rate is a more useful parameter when comparing individual thermals. The negative values are recorded when the bird loses lift momentarily or increases airspeed enough that sink rate is greater than the updraft strength.

Airspeeds are expected to be lower during thermalling than when gliding or slope soaring as the bird slows down to turn and maintain position in the thermal, decreasing sink rate and maximising energy gain. Field data confirm this expectation e.g. (Spaar and Bruderer 1996) and our results show the same trend (mean thermalling airspeed was 12.7ms^{-1}, compared to mean glide speed of 16.0ms^{-1}). Theoretical analysis suggests that, if we assume a parabolic polar, the speed for maximum glide ratio (which we might expect to be chosen as default gliding speed) should be $3^{1/4}$ times the minimum sink speed (which might be expected when maximising climb rate) (Irving 1999); 12.7 x $3^{1/4}$ = 16.7ms^{-1}. However, given the other parameters in Table 7.1, this airspeed is perhaps higher than expected. Substituting the average ϕ and r into Equation 7.2 predicts a mean airspeed of just 8.2ms^{-1}. Alternatively

if we assume airspeed is equal to the circumference of the bird's (drift removed) circling, divided by circling period ($2\pi r/\tau$), we get 8.8ms^{-1} (Pennycuick 1983). It is possible the disagreement in results is caused by error in the pitot tube measurements themselves; either from calibration error or the poor accuracy of the sensor at lower airspeeds. Although the pitot is perhaps the least reliable of our sensors, our previous analyses of airspeed have been consistent with other studies (Spaar and Bruderer 1996). More likely the difference is because the bird is not turning steadily (as we show in Figure 7.10) and consequently the equations are invalid. Furthermore, using mode radius in Equation 7.2, excludes the straighter flight sections where the bird is likely to fly faster, contributing to an increased average airspeed.

7.3.2 Thermal comparison

To investigate the variation in the parameters between individual thermals, we created the correlation matrix shown in Figure 7.9. Statistically significant correlations are highlighted in red.

From Figure 7.9, the longer the bird spent in a thermal, the higher above the ridge he climbed. He also reached higher altitudes when his average climb rate was larger (i.e. stronger thermal updraft). Predictably, turn radius and circling period were highly correlated as they are based on the same analysis of the GPS track. Moreover, both these variables were correlated with the start and end altitudes (relative to the ridge height). The bird tends to turn wider at higher altitudes, perhaps because the thermal becomes more structured and easier to exploit. Alternatively, this might be an artefact of the thermal time; on average there were more changes in direction and irregular circling in longer thermals, which increases average turn radius and circling period.

As is predicted by Equation 7.2, turn radius and bank angle were correlated, as were bank angle and airspeed (assuming the bird banks at constant C_L, its airspeed will accelerate from the imbalance between the vertical conponent of lift and the bird's weight, this will increase the load factor until the lift and weight balance),



Figure 7.9: Correlation matrix exploring the average variables for each identified thermal. Variable names are shown on the diagonal, in the top right frames are scatterplots of the data whilst the bottom left boxes enclose the corresponding Pearson's linear correlation coefficient (r-values). Red indicates the correlation is significant with p-value < 0.05; p-value's < 0.005 are highlighted with a star (*). n=146, except for the airspeed and bank angle parameters where n=121 due flights where airspeed did not record. The start and end altitude variables are quoted 'relative to ridge' (RTR); calculated from the barometric altitude minus the maximum height of the local ridge to eliminate effect of location. Turn radius was calculated from the mode of the non-parametric distribution for the individual thermal, all other variables represent the mean. The wind drift estimate (calculated from the drift elimination method) is used as the local measure of wind speed.

though we note the correlation between airspeed and turn radius was not significant. Instead we found that airspeed and circling period were negatively correlated as clearly when the bird flies faster, the time to complete a full turn decreases. This

was also consistent with the thermal time correlations with airspeed and circling period; the bird spent less time in a thermal when flying in faster circles. Though oddly we do not find the same correlation between airspeed and turn radius.

Finally comparing our wind velocity estimate which is based on the magnitude of the wind drift removed from the thermal, we see that it was negatively correlated with the time spent in the thermal and positively with the start altitude (wind speed increases with altitude), but not the end altitude. The windier it was, the less time was spent in a thermal which matches our earlier results. The bird was also recorded to climb faster in thermals when the wind drift was stronger. In windier conditions, to a point, the thermal may become more structured and easier to exploit, or the thermal might superimpose on the ridge lift.

7.3.3 Time series and spatial analysis of thermalling behaviour

In Figure 7.10 we have plotted the time series data for an example thermal. This illustrates how the bird is constantly adjusting his airspeed and bank angle which consequently affects turn radius and therefore his position within the thermal, which ultimately dictates the climb rate and energy gain he achieves. Clearly this is not steady turning. There is an abundance of information in this data, but extracting patterns from it is extremely difficult, especially given the individual nature of each thermal. For example, are there specific cues that the bird uses to locate the best updrafts, such as a surge in load factor? Or perhaps we expect to see climb rate increase at the beginning of a thermal as the bird finds the best lift, and then decrease again towards the end. Alternatively, climb rate might peak at the same point in each turn as the bird regularly dips in and out of the core.

Other than bank angle and turn radius, there appears to be little correlation between the parameters in Figure 7.10, and ground speed is the only one to show a distinctive periodicity that matches the bird's circling; he slows down when flying

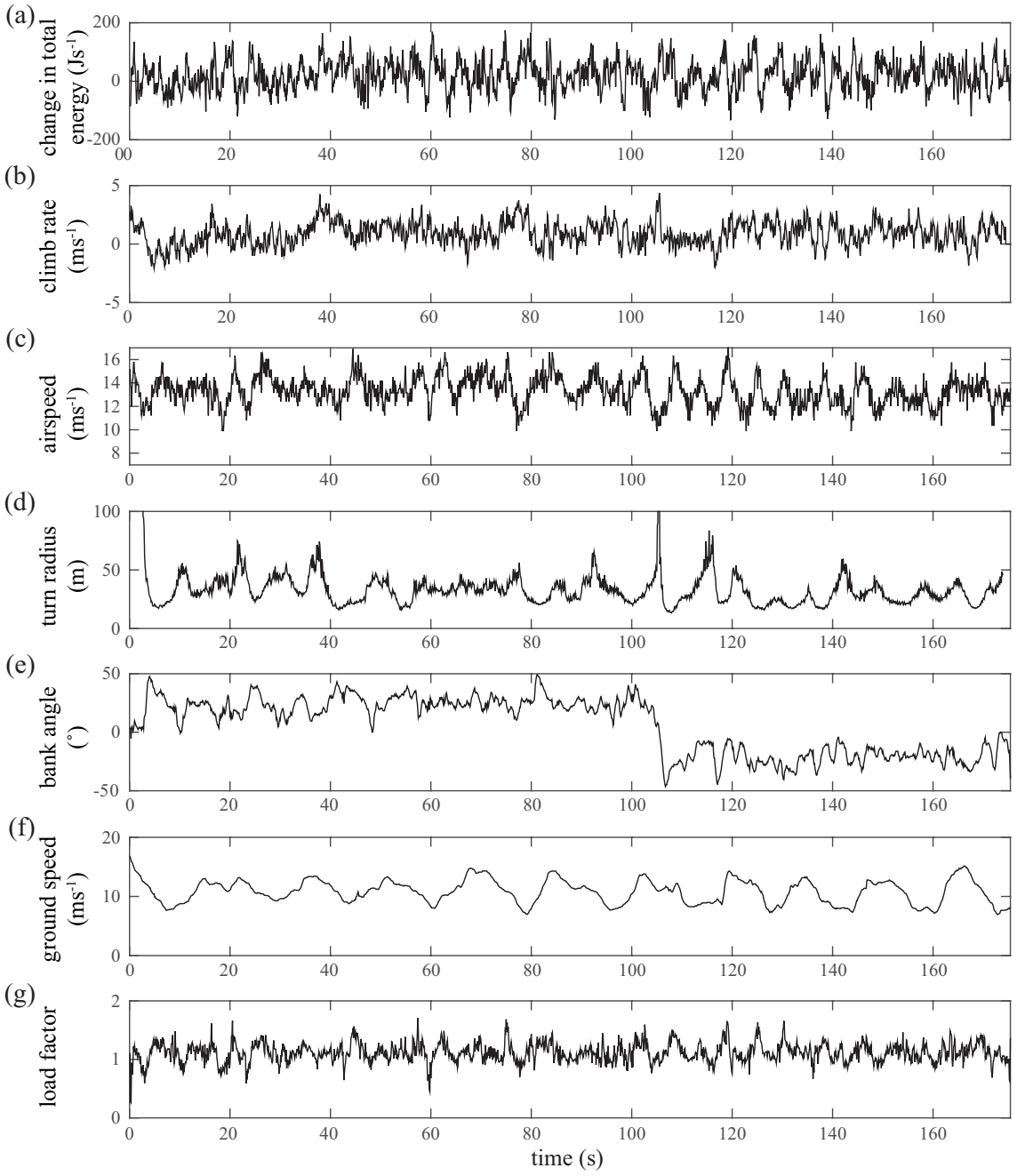


Figure 7.10: Example time series data for an individual thermal (a) rate of change of total energy (b) climb rate (c) airspeed (d) turn radius (e) bank angle (f) ground speed (g) load factor. See Figure 7.11 for GPS track of this thermal. Mean rate of change of total energy is 20.1Js^{-1}. Clearly the bird is not circling steadily as bank angle, turn radius and airspeed all continuously fluctuate. The ground speed is relatively predictable with the bird flying slower when turning into the wind. However, the periodicity of this pulsing does not match the fluctuations of the other variables. Bank angle and turn radius follow the same pattern (as bank angle decreases, radius increases), and both indicate the point where the bird changes direction at approximately 105s.

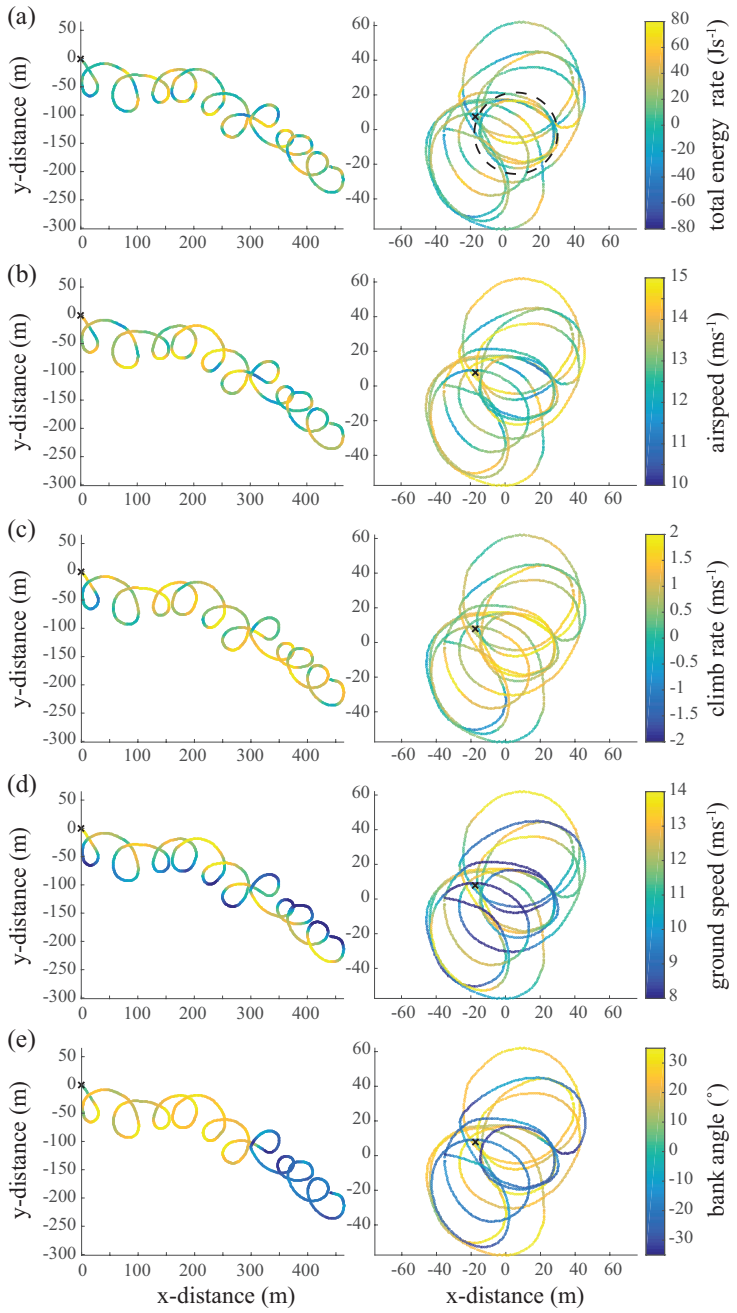


Figure 7.11: Spatial analysis of the variables during thermalling. (a) Rate of change of total energy, (b) airspeed, (c) climb rate, (d) ground speed, (e) bank angle. Frames on the left show the original GPS track which display no distinctive pattern, with the exception of ground speed. Bank angle highlights the change on circling direction. Frames on the right show the wind drift eliminated position, allowing us to explore the variables relative to the atmosphere. Although there is considerable noise in the data, it could be interpreted that the energy rate, and climb rate are consistently higher in the area marked by the black-dashed line, whilst the airspeed is slower. This perhaps indicates the location of the thermal core. The start of the thermal is marked by a cross.

into the wind. An alternative way to visualise the data is to plot the variables on the GPS track, which allows us to look for spatial patterns (Ákos et al. 2010; Allen 2005; Edwards and Silberberg 2010). This is shown for the same example thermal in Figure 7.11, both for the original GPS position data and the estimated position after the elimination of wind drift. From the original GPS track, for airspeed, bank angle, climb rate and total energy, there appears to be no spatial pattern in the pulsing. The drift eliminated position allows us to compare the variables relative to the atmosphere. It is possible that in the middle of the region in which the bird is circling, there is a higher density of peaks in both climb rate and energy rate, and correspondingly lower airspeeds. This could plausibly be interpreted as the thermal core where the updraft is stronger, though is quantitatively difficult to test. However, the data is extremely noisy and any interpretation of the wind drift tracks should be treated cautiously as the accuracy of the wind drift elimination will greatly influence the results.

Theoretically we might expect that in regular, structured thermals, the bird would be able to circle more smoothly, therefore we would record less variation in the parameters (i.e. a lower standard deviation). To test this we use mean climb rate and the wind magnitude (MIDAS measurements) as proxies for the thermal structure. Larger climbs might indicate a stronger and more structured updraft, however we found no significant correlation between mean climb rate and the standard deviation of airspeed, bank angle or total energy rate. On the other hand, wind speed was significantly positively correlated with the standard deviation of all four variables (std airspeed: $n = 121$, $R^2 = 0.07$, $p < 0.005$, std climb rate: $n = 146$, $R^2 = 0.06$, $p < 0.005$, std bank angle: $n = 146$, $R^2 = 0.04$, $p < 0.05$, std total energy rate: $n = 121$, $R^2 = 0.12$, $p < 0.001$). As wind speed increased, the variation in the parameters increased. Wind speed is positively associated with the generation of turbulence, therefore in strong winds, the bird must constantly compensate for the more unpredictable airflows within the thermal, resulting in higher standard deviations of our variables. However, we also found that average climb rate improved in windier conditions, so although the bird must work harder to combat the turbulent

flows, he is able to extract more energy from the thermal (regression of mean total energy rate and wind speed: $n = 146$, $R^2 = 0.06$, $p < 0.005$).

7.4 Discussion

This chapter was a preliminary study, exploring various techniques for the analysis of thermalling flight. Obviously more analysis of this data is required before we can hope to understand the subtleties of our bird's soaring strategy, but we have demonstrated the huge amount of information contained within our onboard data, and how we can start to interpret it.

Although to the casual observer, birds circling in thermals appear to soar gracefully and effortlessly, this analysis has emphasised that in reality (and any glider pilot would agree) the extremely unpredictable and unstable airflow in thermals means that the bird is not steady circling at all. He must continuously adjust his flight according to the changing airflow. This makes finding patterns in the data all the more challenging, particularly when the conditions were turbulent. Despite the fact that the bird thermalled less when there were strong wind conditions, we found that if he did thermal, he had to work harder to cope with the increased turbulence but was actually able to gain more energy.

Chapter 8

Discussion

This thesis has explored how a free-flying steppe eagle interacts with the atmosphere using a specialised onboard instrumentation unit. I have looked at the fundamental components that comprise the bird's soaring flight, from gliding and gust response to soaring both in slope lift and thermals, in order to study how the bird's morphology and decision strategies have evolved to exploit its aerial environment. The main conclusions from this work are summarised here and I discuss some directions for future research.

The greatest limitation of previous free-flight studies has been the lack of suitable equipment for recording the required data directly from the bird. The use of integrated sensors attached to the bird, recording at very high sampling rates has provided us with a wealth of information about the subtleties of the bird's flight, accurately describing its attitude and behaviour. Methods for fusing the measurements from these sensors and interpreting the data were discussed in Chapter 2.

The value of such data is immediately demonstrated by the first characteristic I studied in this thesis: the wing tuck. The wing tuck is a discrete but extremely rapid manoeuvre ($\approx$ 3Hz) which can only be detected by very high frequency sampling.

Originally this manoeuvre was investigated by Gillies (2010), but was entirely re-analysed in Chapter 3 using the new set of data I collected and resulting in a more complete understanding of its occurrence and mechanism. We proposed that the wing tuck is not a deliberate movement, but occurs as a result of an imbalanced musculoskeletal moment in the wings, caused by the drop in aerodynamic loading which is generated by a sudden gust. However, there is still some question over the actual benefit of the tuck movement, if any. The tension in the flight muscles which actually causes the wing tuck might serve to damp the atmospheric turbulence during normal soaring, but the tuck itself could simply be a result of when the system is pushed passed its limits. Further analysis, perhaps using dynamic modelling, is required to resolve this.

As the bird was always flown on slopes generating ridge lift, before exploring any soaring strategies the bird might be using it was important to understand the movement of the air flow. A CFD analysis of Hay Bluff was therefore used in Chapter 4 to model the ridge lift component. This highlighted the effect of the landscape on the flow direction. It is also the first study where the results of a CFD model of the atmosphere have been compared with real free-flight measurements of a bird to test the bird's ability, or preference, to fly in the strongest updraft regions. The analysis revealed that, on average, the bird flew in the strongest updrafts but did not attempt to maximise its altitude gain, nor appear to adjust its distance from the ridge according to the wind strength which might be expected in a constant altitude, constant airspeed strategy. This was the first hint that the bird might be adjusting its airspeed according to the updraft strength. Further studies comparing the results for more complex (for example, urban) terrain would help to complete our understanding of slope soaring strategies, including how well birds detect and avoid downdrafts. Ideally tests would also be done with wild birds that are likely to have different flight objectives to our eagle, and consequently may display different behaviours in the slope lift. However, if choice of airspeed is an in-built mechanism as we suspect, the results might be similar. Ultimately such research may also influence the design of algorithms for increasing the endurance of loitering UAVs.

The difference seen between the CFD predicted updraft strength and the measured climb rate was primarily due to the bird's inherent sink rate. This naturally led us to look at gliding flight and the glide polar—without knowing the bird's inherent sink rate, it is not possible to accurately estimate the magnitude of the updraft the bird is flying in. However, after reviewing the literature in Chapter 5, it became clear that an accurate theoretical derivation of the glide polar was not trivial as various contradictory estimates for parasite and profile drag coefficients were reported in different studies. The shape of the glide polar, and the performance parameters derived from it, proved to be highly sensitive to the choice of drag coefficients—much more so, perhaps, than the existing literature indicates or acknowledges. It is also clear that more experimental data is required on how birds actually change their wingspan with airspeed in natural conditions. In particular it would be worth testing whether the hypothesis that there is an optimum linear relationship between wingspan and airspeed is reflected in reality, and if so whether the slope of that relationship itself takes an optimum value—though these will both be highly sensitive to the drag coefficients.

To attempt to verify some form of the glide polar for our steppe eagle, I tried to extract the polar from experimental data which was automatically identified from sections of straight flight (Chapter 6). However, this resulted in a wide distribution of points which illustrated the severe effect of atmospheric conditions on the glide data, such that traditional polars were not able to explain the recorded variation. Interestingly both the horizontal (estimated from the airspeed and ground speed) and vertical (predicted from the CFD model) components of wind velocity were found to be correlated with the bird's gliding airspeed. This analysis suggests that the bird is able to estimate the movement of the atmosphere and adjusts its airspeed, as would be expected if the bird is trying to optimise its glide performance for maximum average cross-country speed. Again this points towards an in-built mechanism because our bird is not going anywhere, so there is no obvious incentive to optimise airspeed for cross-country flying.

This observation motivated the development of the soaring optimisation chart which was designed to incorporate the effect of wind in the glide polar. For a given flight objective and wind condition, the chart should predict the region in which the bird is expected to glide, based on the classic theory for glide speed optimisation. Comparing the chart with our steppe eagle data enabled me to determine the optimal drag coefficients for the theoretical polar of our bird. For both the fixed and variable wingspan polar models, these optimised drag coefficients (fixed-wingspan: $C_{D,pro} = 0.0046$ and $C_{D,par} = 0.34$, variable-wingspan: $C_{D,pro} = 0.0054$ and $C_{D,par} = 0.33$) were extremely similar to the values suggested by Taylor and Thomas (2014) ($C_{D,pro} = 0.0049$ and $C_{D,par} = 0.37$), where profile drag is based on the classic laminar boundary layer solution for a flat plate and parasite drag comes from Hedenström and Liechti's (2001) field measurements. It would be interesting to repeat this analysis with more individuals and species, perhaps using radar measurements of wind velocity, to test these hypotheses.

The thesis concludes with a preliminary study of thermalling flight (Chapter 7). Examining the thermalling data further highlighted the complexity of the atmosphere and the difficulty in detecting patterns from the onboard data. Clearly the bird does not circle steadily as all the recorded variables continuously fluctuate. These fluctuations were found to increase with wind speed suggesting that more turbulent conditions force the bird to work harder and continuously make adjustments in order to thermal successfully.

Evidently, considerably more research is required before the complex details of bird's thermalling strategies can be understood. For example, further analysis that can be done with this specific data set would be to use signal processing methods to detect trends or identify events preceding a specific behaviour (such as a change in direction). A good starting point is to compare the bird's flight with the various strategies currently used by human glider pilots (Ákos et al. 2008; Pennycuick 1972; Reichmann 1993) and in UAV simulations (Allen and Lin 2007; Andersson et al. 2010; Cowling et al. 2009) and if there are differences, to understand these.

A limitation of the experimental approach used in this thesis is that our bird has no definite motivation for optimising his flight—the nature of the field tests enforce the bird to take-off and land at the same location, meaning he does not need to optimise cross-country speed or maximise energy gain. Nevertheless, the various analyses presented hint towards an in-built mechanism that dictates the airspeed the bird flies at, depending on the atmospheric conditions detected by the bird. By the same reasoning, it also suggests that the bird is capable of estimating the wind velocity.

Another important limitation is how the bird's flight behaviour might be impacted by wearing the equipment. Although the instrumentation is small, more streamlined than previous iterations (Gillies 2010), and weighs less than 5% of the bird's mass, it will undoubtedly still have an effect. For example, it is likely to have increased the bird's body drag and consequently its sink rate which will alter the glide polar. Moreover, perhaps the bird is less willing to fly in more risky conditions when wearing the unit which might affect its stability, or cause it to turn in one direction more frequently than the other if not perfectly aligned. Despite no observable difference to the bird's performance when watching the bird fly with and without the unit, these factors are important—if unavoidable—considerations. As instrumentation units continue to be improved with increasingly small sensors and larger battery capacity, it will become possible to mount units with similar capabilities as the one used for this work on much smaller species and reduce the effect it may have on the bird's performance. With the exception of the thermometer, all sensors on the unit provided valuable data on our bird's flight characteristics.

This thesis contains several empirically-motivated theoretical models which represent conceptual advances in our understanding of the mechanisms involved in soaring flight. Together with the technological advances of our equipment, this work presents exciting developments in how we can approach the study of free-flying birds, providing an exceptional level of detail. Realistically it should now be possible to expand the scope of future research to other birds.

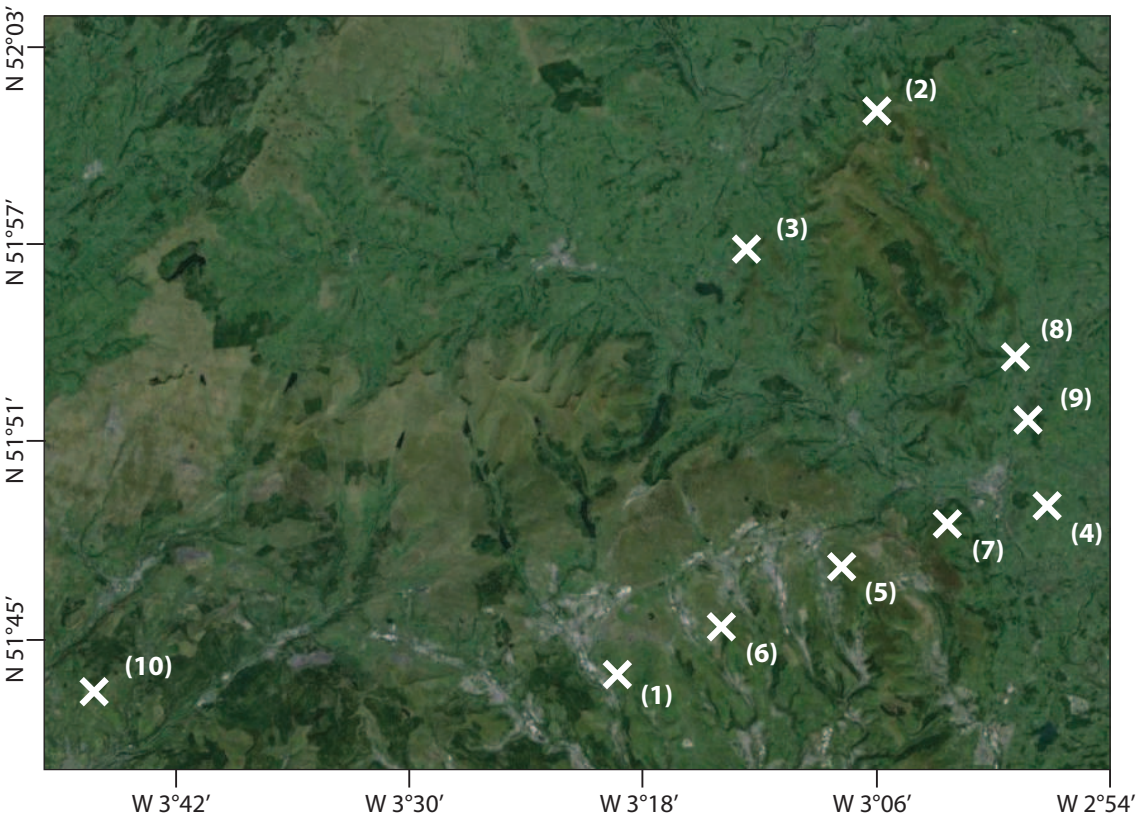
Appendix A

Flight sites

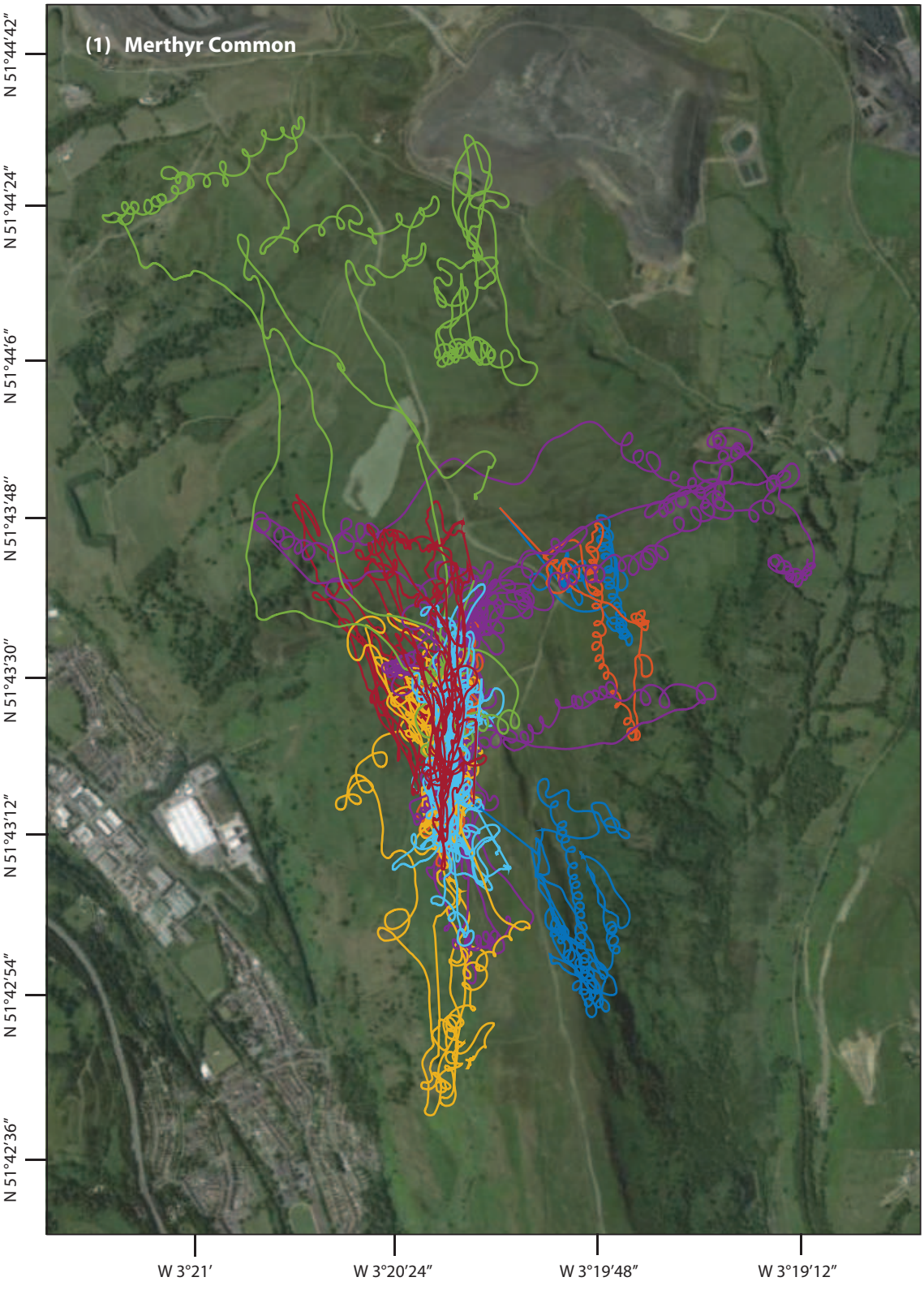
The 10 flight sites used for collecting data in this thesis are shown here with GPS tracks from the flights plotted on Google Earth. Each map is approximately on the same scale.

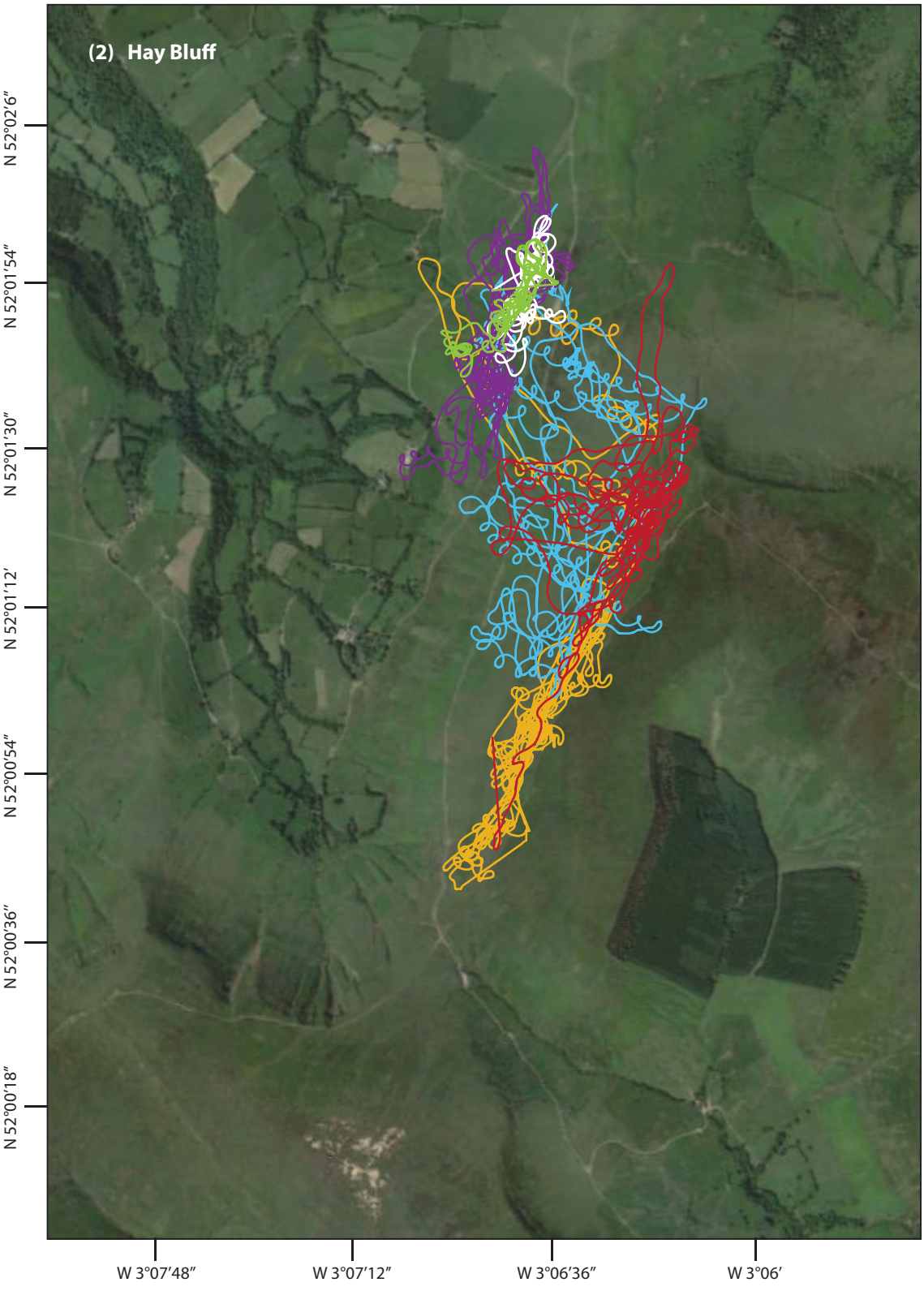
No.	site	coordinates (dd.dd)		No. flights
1	Merthyr Common	51.725977 N	-3.332133 W	14
2	Hay Bluff	52.020322 N	-3.107739 W	6
3	Llangorse	51.947011 N	-3.222856 W	3
4	Llanddewi Rhydderch	51.813242 N	-2.960578 W	10
5	Blaenavon	51.781715 N	-3.146225 W	2
6	Abertysswg	51.747380 N	-3.244051 W	2
7	Blorenge	51.803840 N	-3.061836 W	1
8	Great Llwgy Farm	51.946478 N	-3.222592 W	3
9	Skirrid	51.857886 N	-2.983035 W	1
10	Bryncaws	51.715363 N	-3.783703 W	2

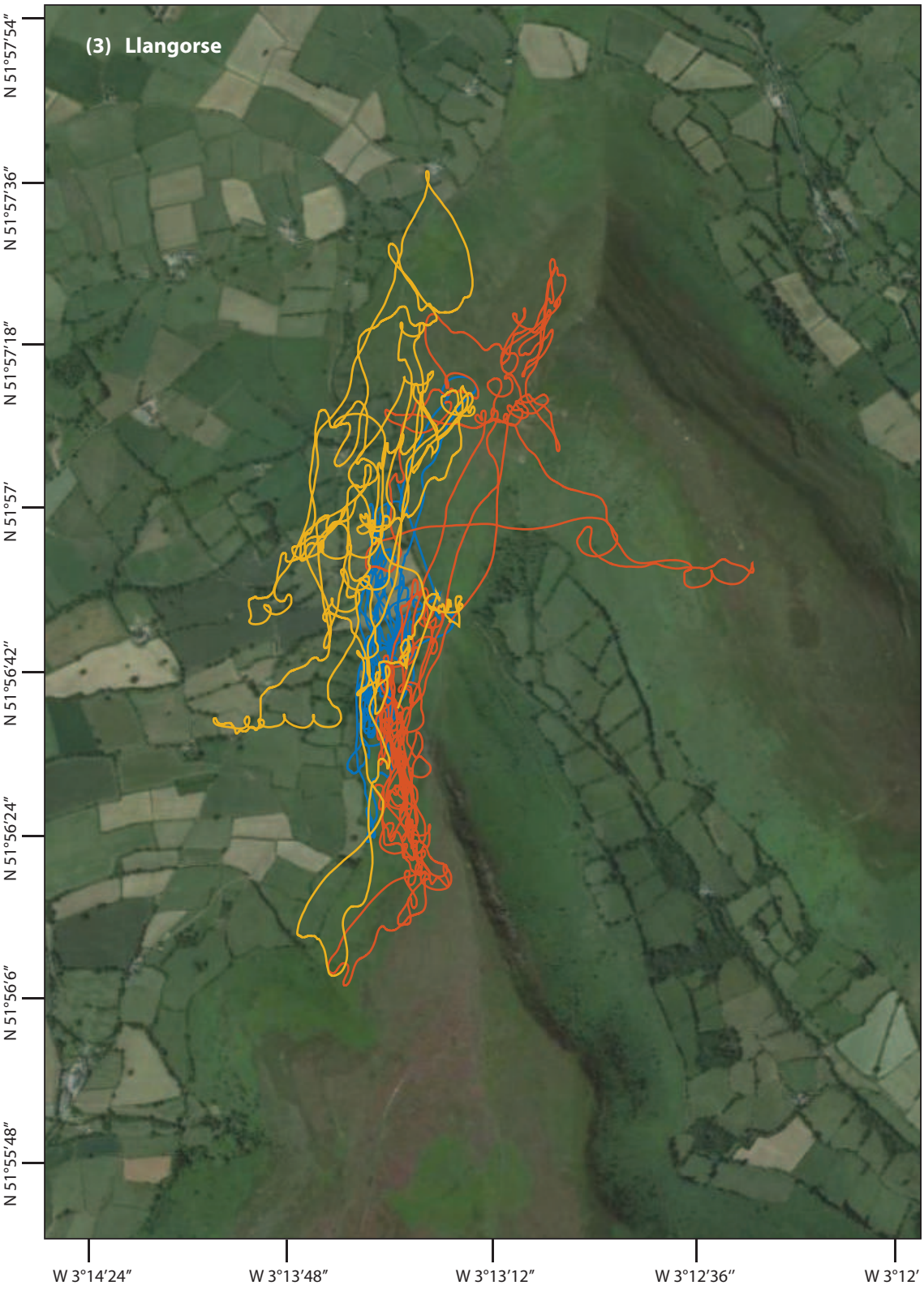
Site numbers, names, launch coordinates and number of flights recorded at the site.

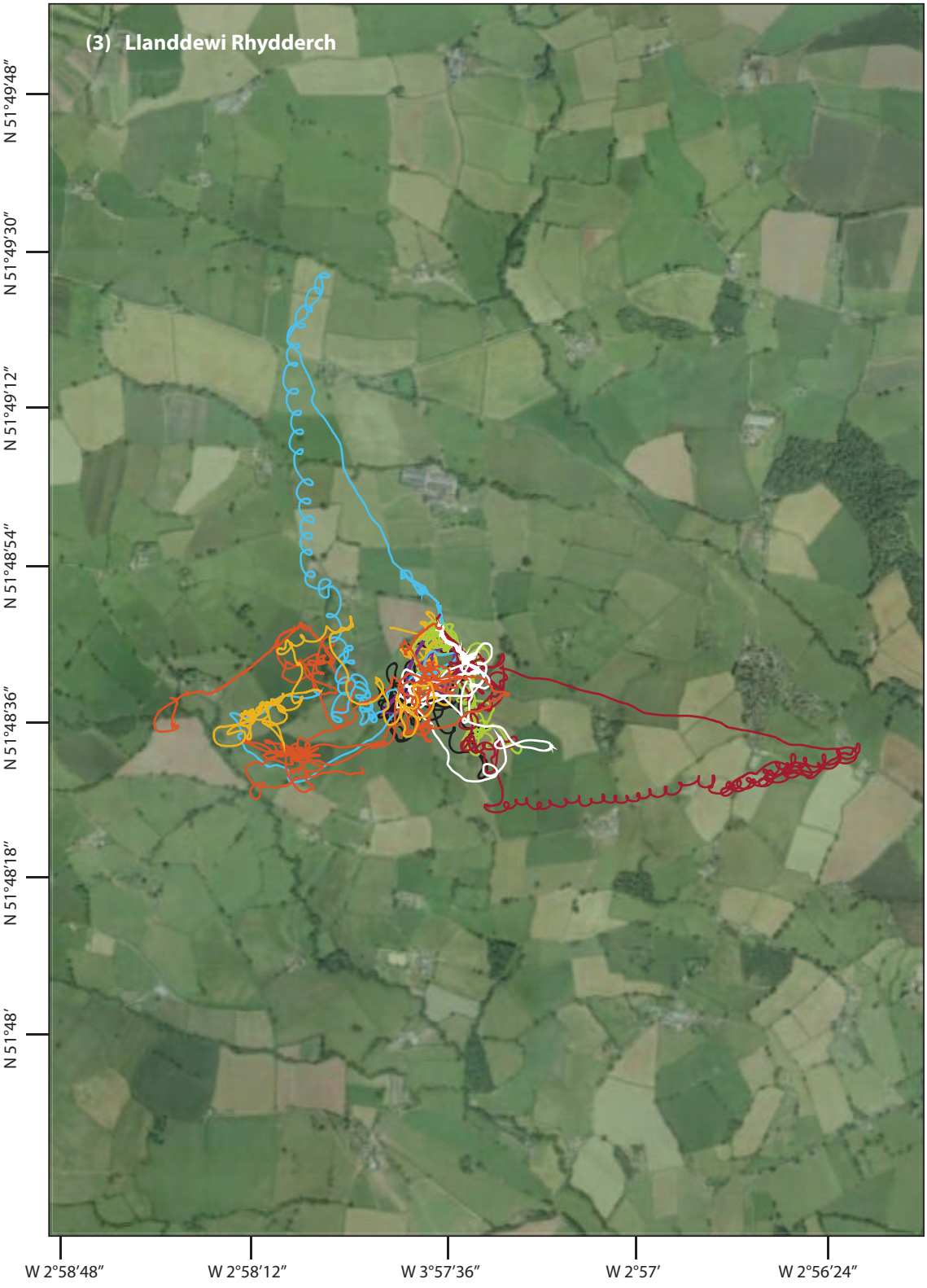


Location of all sites in the Black Mountains region of South Wales, UK. Labels match site numbers in the above table.

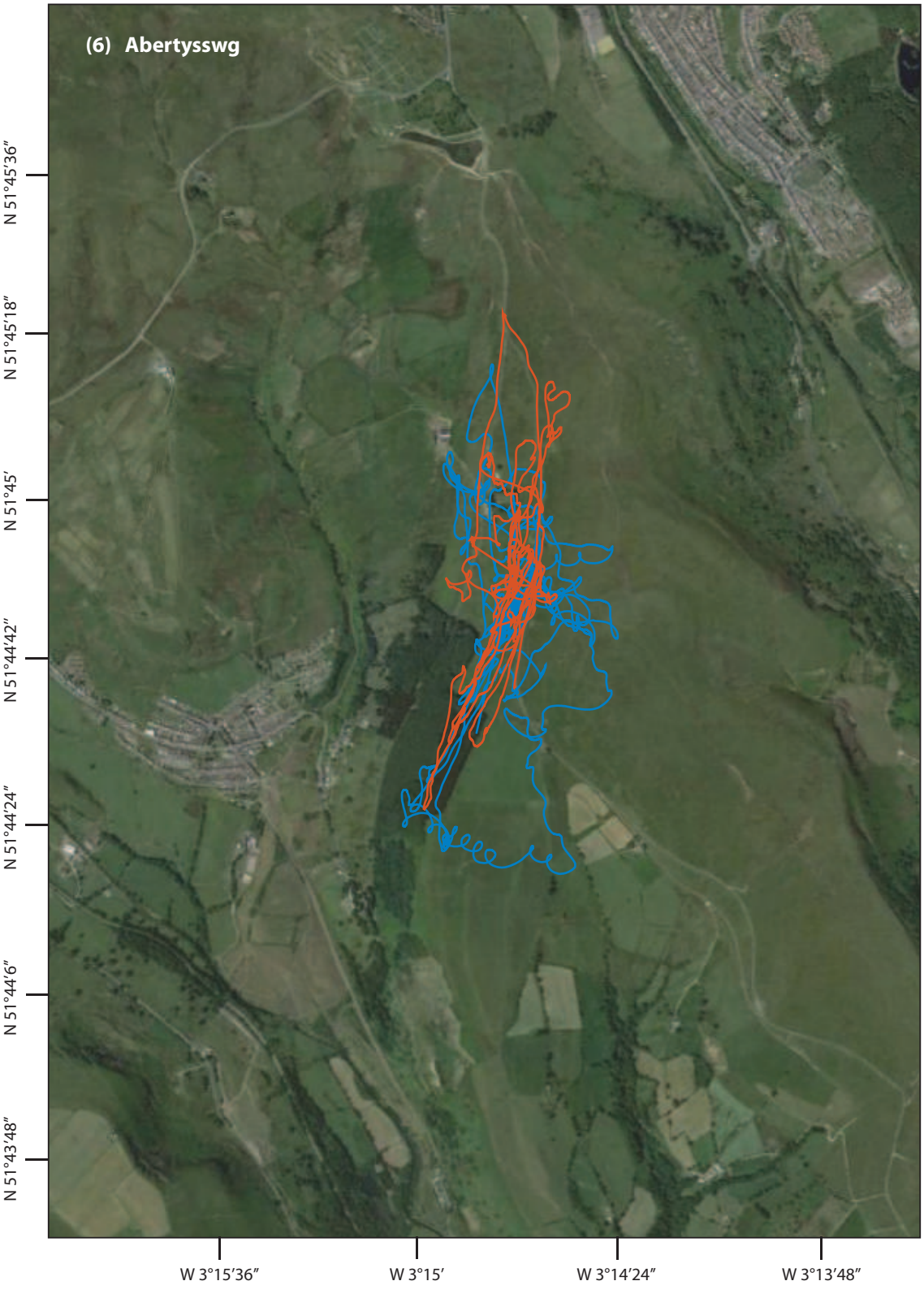

(1) Merthyr Common
N 51°44′42″
N 51°44′24″
N 51°44′6″
N 51°43′48″
N 51°43′30″
N 51°43′12″
N 51°42′54″
N 51°42′36″
W 3°21′
W 3°20′24″
W 3°19′48″
W 3°19′12″


(2) Hay Bluff
N 52°02′6″
N 52°01′54″
N 52°01′30″
N 52°01′12′
N 52°00′54″
N 52°00′36″
N 52°00′18″
W 3°07′48″
W 3°07′12″
W 3°06′36″
W 3°06′

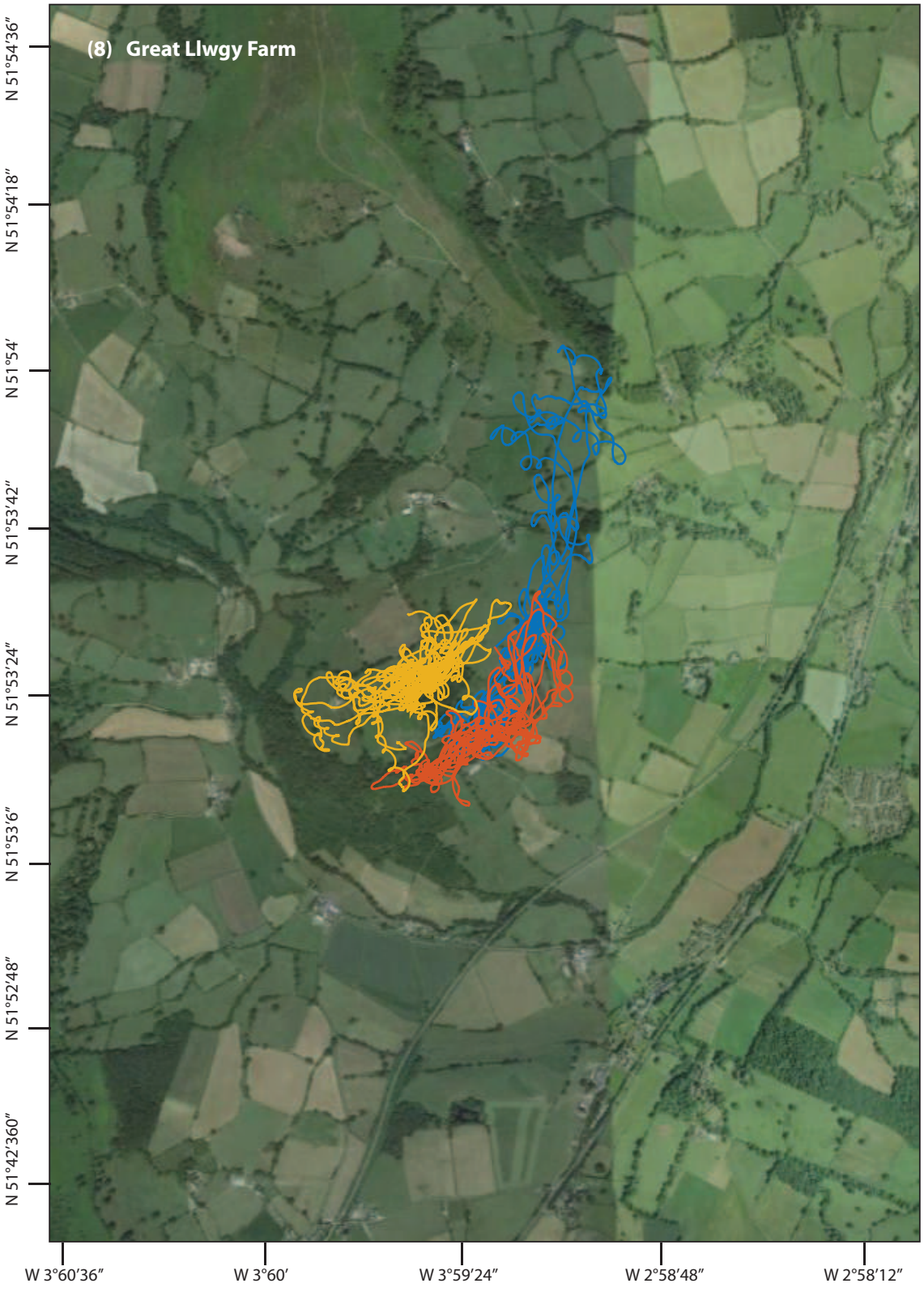

(3) Llangorse
N 51°57′54″
N 51°57′36″
N 51°57′18″
N 51°57′
N 51°56′42″
N 51°56′24″
N 51°56′6″
N 51°55′48″
W 3°14′24″
W 3°13′48″
W 3°13′12″
W 3°12′36″
W 3°12′


(3) Llanddewi Rhydderch
N 51°49′48″
N 51°49′30″
N 51°49′12″
N 51°48′54″
N 51°48′36″
N 51°48′18″
N 51°48′
W 2°58′48″
W 2°58′12″
W 3°57′36″
W 2°57′
W 2°56′24″

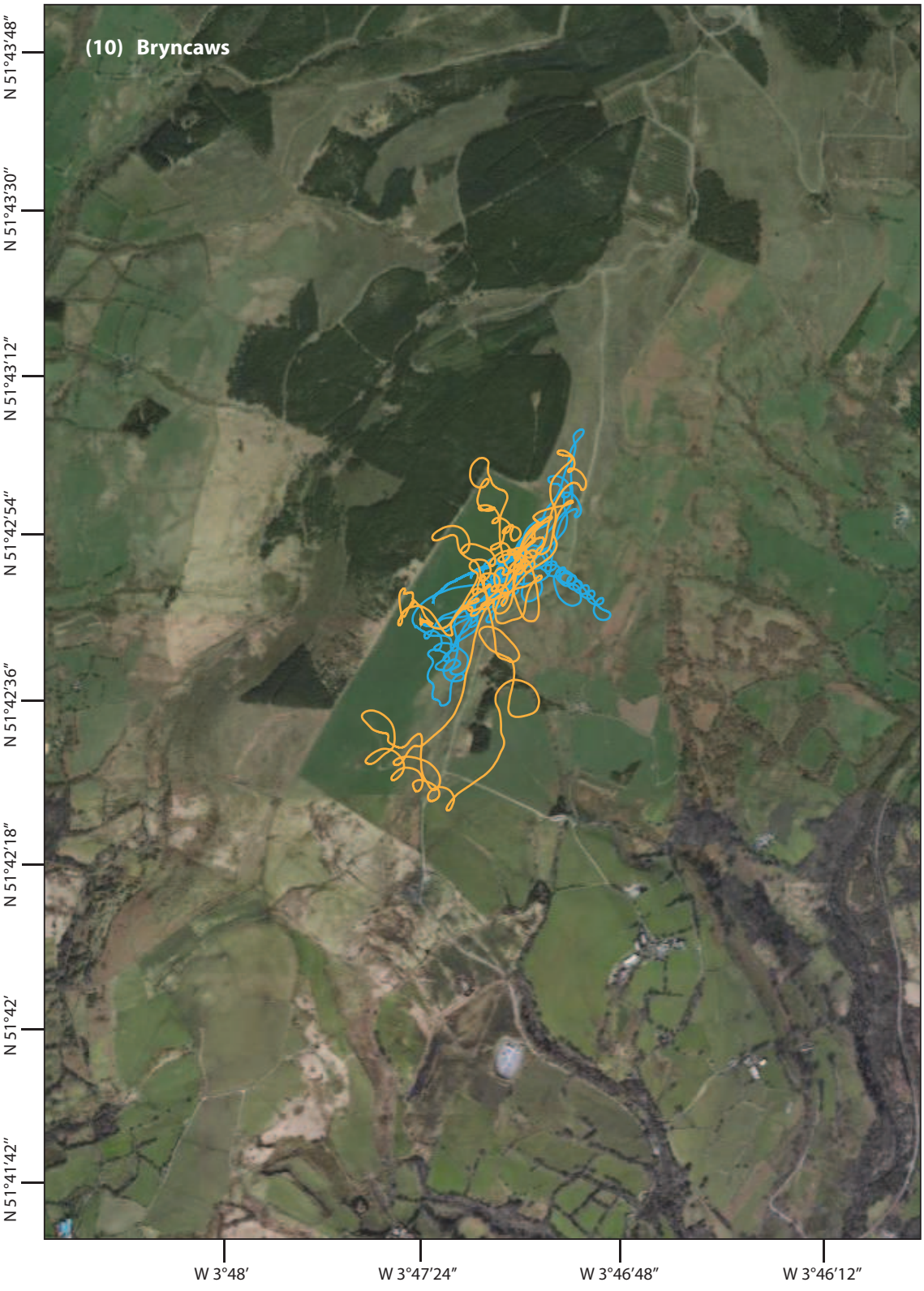

(1) Blaenavon
N 51°47′42″
N 51°47′24″
N 51°47′6″
N 51°46′48″
N 51°46′30″
N 51°46′12″
N 51°45′54″
W 3°09′36″
W 3°09′
W 3°08′24″
W 3°07′48″
W 3°07′12″


(6) Abertysswg
N 51°45′36″
N 51°45′18″
N 51°45′
N 51°44′42″
N 51°44′24″
N 51°44′6″
N 51°43′48″
W 3°15′36″
W 3°15′
W 3°14′24″
W 3°13′48″


(7) Blorenge
N 51°49′12″
N 51°48′54″
N 51°48′36″
N 51°48′18″
N 51°48′
N 51°47′42″
N 51°47′24″
N 51°47′6″
W 3°21′
W 3°20′24″
W 3°19′48″
W 3°19′24″


(8) Great Llwgy Farm
N 51°54'36"
N 51°54'18"
N 51°54'
N 51°53'42"
N 51°53'24"
N 51°53'6"
N 51°52'48"
N 51°42'360"
W 3°60'36"
W 3°60'
W 3°59'24"
W 2°58'48"
W 2°58'12"


(9) Skirrid
N 51°52′12″
N 51°51′54″
N 51°51′36″
N 51°51′18″
N 51°51′
N 51°50′42″
N 51°50′24″
W 3°21′
W 3°20′24″
W 3°20′24″
W 3°19′48″
W 3°19′24″


(10) Bryncaws
N 51°43′48″
N 51°43′30″
N 51°43′12″
N 51°42′54″
N 51°42′36″
N 51°42′18″
N 51°42′
N 51°41′42″
W 3°48′
W 3°47′24″
W 3°46′48″
W 3°46′12″

Appendix B

AHRS algorithm Theory and implementation

Theory

Three Euler angles (roll ϕ, pitch θ and yaw ψ) are typically used to describe an objects attitude as a series of rotations from the inertial frame to the body-fixed frame. For example the rotation matrix $[{}^{b}_{i}\mathbf{R}]$ in Equation B.1, which describes the transformation from the inertial to body coordinate frame, is formed from consecutive rotations about the z, y then x-axis by the angles ψ, θ and ϕ respectively, where each subsequent rotation is performed on the new axis system:

$$
\begin{aligned}
{}^{\mathbf{b}}_{\mathbf{i}}\mathbf{R} &= \mathbf{R}_\phi \mathbf{R}_\theta \mathbf{R}_\psi \\
&= \begin{bmatrix} 1 & 0 & 0 \\ 0 & \cos\phi & -\sin\phi \\ 0 & \sin\phi & \cos\phi \end{bmatrix} \begin{bmatrix} \cos\theta & 0 & \sin\theta \\ 0 & 1 & 0 \\ -\sin\theta & 0 & \cos\theta \end{bmatrix} \begin{bmatrix} \cos\psi & -\sin\psi & 0 \\ \sin\psi & \cos\psi & 0 \\ 0 & 0 & 1 \end{bmatrix} \\
&= \begin{bmatrix} \cos\theta\cos\psi & -\cos\theta\sin\psi & \sin\theta \\ \cos\psi\sin\phi\sin\theta + \cos\phi\sin\psi & \cos\phi\cos\psi - \sin\phi\sin\theta\sin\psi & -\cos\theta\sin\phi \\ -\cos\phi\cos\psi\sin\theta + \sin\phi\sin\psi & \cos\psi\sin\phi + \cos\phi\sin\theta\sin\psi & \cos\phi\cos\theta \end{bmatrix}
\end{aligned}
\tag{B.1}
$$

Different estimates of Euler angles can be computed from combinations of gyro, accelerometer and magnetometer data, though each method is limited by the inherent inaccuracies and different characteristics of the sensors. The following equations of motion form the foundation of the attitude and heading reference system (AHRS).

Body angular rates measured from the 3-axis gyro $[\omega_x, \omega_y, \omega_z]$ can be converted to Euler angular rates $[\dot{\phi}, \dot{\theta}, \dot{\psi}]$ in the inertial reference frame, if the initial attitude is known, as in Equation B.2. Estimates of the Euler angles can be obtained by simply integrating these Euler rates (Barton 2012a). This gyro based calculation provides high frequency attitude estimates, but the results tend to drift due to the accumulation of error from gyro bias.

$$
\begin{bmatrix} \dot{\phi} \\ \dot{\theta} \\ \dot{\psi} \end{bmatrix} = \begin{bmatrix} 1 & \sin\phi\tan\theta & \cos\phi\tan\theta \\ 0 & \cos\theta & -\sin\phi \\ 0 & \sin\phi\sec\theta & \cos\phi\sec\theta \end{bmatrix} \begin{bmatrix} \omega_x \\ \omega_y \\ \omega_z \end{bmatrix} \tag{B.2}
$$

Roll and pitch angles can also be computed using accelerometer measurements of specific force $[\alpha_x, \alpha_y, \alpha_z]$. This approach assumes steady state (unaccelerated flight) (Barton 2012a; Beard and McLain 2012) where the translational acceleration

component is essentially zero and only centripetal and gravitational (g) components of acceleration are considered. The measured accelerations can therefore be modelled in terms of gyro body rate $[\omega_x, \omega_y, \omega_z]$, inertial velocity in body coordinates $[V_{g,x}, V_{g,y}, V_{g,z}]$ and the gravity vector which is expressed in the body reference frame using roll and pitch angles. Solving Equation B.3 for roll and pitch angles provides lower frequency estimates than from gyro data alone, which suffer from large accelerometer noise.

$$\begin{bmatrix} \alpha_x \\ \alpha_y \\ \alpha_z \end{bmatrix} = \begin{bmatrix} \omega_x \\ \omega_y \\ \omega_z \end{bmatrix} \times \begin{bmatrix} V_x \\ V_y \\ V_z \end{bmatrix} - g \begin{bmatrix} -\sin\theta \\ \sin\phi\cos\theta \\ \cos\phi\cos\theta \end{bmatrix} \tag{B.3}$$

Finally, the yaw angle can be estimated from the 3D magnetometer unit vector of magnetic north in body coordinates $[\beta_x, \beta_y, \beta_z]$. A correction must be applied for both the difference between true and magnetic north (declination angle, δ), and the difference between the horizontal plane and the magnetic field vector (inclination angle, ξ). Both the declination and inclination angles are extremely location dependant and approximate local values can be found from online datasheets (CGS network 2011). For our flight sites $\delta \approx 2.33°$ and $\xi \approx 66°$. The transformation of the unit magnetic field vector from the inertial system to body coordinates can therefore be achieved by rotating the unit vector through $-\delta°$ about the z-axis then through $-\xi°$ about the y-axis and finally through the Euler angles using ${}^{\mathbf{b}}_{\mathbf{i}}\mathbf{R}$, as shown in Equation B.4:

$$\begin{bmatrix} \beta_x \\ \beta_y \\ \beta_z \end{bmatrix} = {}^{\mathbf{i}}_{\mathbf{b}}\mathbf{R} \begin{bmatrix} \cos\xi\cos\delta & \cos\xi\sin(-\delta) & \sin(-\delta) \\ -\sin(-\delta) & \cos\delta & 0 \\ -\sin(-\xi)\cos\delta & -\sin(-\xi)\sin(-\delta) & \cos\xi \end{bmatrix} \begin{bmatrix} 1 \\ 0 \\ 0 \end{bmatrix} \tag{B.4}$$

An estimate of the body yaw angle from true north can then be obtained by solving B.4 for ψ.

The accuracy and reliability of these attitude estimates can be improved using

sensor fusion techniques. Numerous methods for implementing such AHRS algorithms which compute the optimum attitude solution from multiple sensors have been successfully developed but by far the most common approach in navigation applications is to use an extended Kalman filter (EKF) which, unlike a standard Kalman filter, allows for non-linear models and measurements by linearising about the state estimates (Barton 2012a; Beard and McLain 2012; Brown and Hwang 1993).

Fundamentally the EKF is an iterative process that predicts the desired state variables based on their values from the previous time step which are then updated with current observations, weighted by the Kalman gain.

For this study we chose to implement an open source, EKF based state estimation algorithm which was originally designed for use on small UAV's (Barton 2012a) and consequently makes use of similar sensors and dynamic models as our bird mounted instrumentation unit. The SUAS algorithm written by Barton, provides a basic 7-state estimation of vehicle attitude and gyro biases. We customised the code for our data set and included a correction for magnetic inclination. A possible future development of the code would be to include additional states such as wind velocity or altitude. Here we briefly describe the underlying theory of the AHRS and outline its implementation. For more detail refer to Barton (Barton 2012a) or the original SUAS code (Barton 2012b).

AHRS Implementation

The algorithm is implemented using quaternions which are an alternative way of representing attitude. They have the benefit of considerably lower computational requirements than the equivalent direction cosine matrix (DCM) implementation and avoid singularity problems as pitch nears 90° (Barton 2012a). Four quaternions are required to fully describe a body's attitude: q_1, q_2 and q_3 define the quaternion 'vector' whilst q_0 is the scalar that defines the magnitude of the rotation about the specified vector (*Understanding Quaternions*). The relationship between Euler

angles and quaternions is:

$$\phi = \tan^{-1}\left(\frac{2(q_0q_1 + q_2q_3)}{q_0^2 - q_1^2 - q_2^2 + q_3^2}\right) \tag{B.5}$$

$$\theta = -\sin^{-1}(2(q_1q_3 - q_0q_2)) \tag{B.6}$$

$$\psi = \tan^{-1}\left(\frac{2(q_0q_3 + q_1q_2)}{q_0^2 + q_1^2 - q_2^2 - q_3^2}\right) \tag{B.7}$$

In the general case, the EKF attempts to estimate time evolving states ($\hat{\mathbf{x}}$) based on multiple measurements ($\mathbf{z}$) of those states. Both the nonlinear dynamics of the true state vector ($\mathbf{x}$) and the measurements ($\mathbf{z}$) must therefore be modelled mathematically. The propagation of $\mathbf{x}$ is defined by its time derivative ($\mathbf{x} = \mathbf{x}+\dot{\mathbf{x}}\mathbf{dt}$), therefore the non-linear continuous time model of our system has the general form:

$$\dot{\mathbf{x}} = f(x), w(t) \tag{B.8}$$

$$\hat{\mathbf{z}} = h(x), r(t) \tag{B.9}$$

where $f(x)$ and $h(x)$ are the update functions representing the nonlinear state dynamics and measurement model respectively. It is assumed that the noise functions w and r are zero mean Gaussian with corresponding covariance's $\mathbf{Q}$ and $\mathbf{G}$. For implementation of these models in the EKF, the characteristics of w and r must be quantified. The $\mathbf{G}$ matrix is essentially the estimate of the measurement noise whilst $\mathbf{Q}$ is the estimated process noise matrix which is how much we expect reality to vary from our modelled equations of motion. The non-linear dynamic and measurement functions $f(x)$ and $h(x)$ must be linearised before they can be used in the Kalman filter. It is assumed that the functions are linear about the states, the linearised models can therefore be determined from the Jacobians $\mathbf{F}=\frac{d(\dot{x})}{dx}$ and $\mathbf{H}=\frac{d(\hat{z})}{dx}$ based on a Taylor series expansion (Beard and McLain 2012). They are then subsequently converted to the discrete time domain ($\mathbf{F}(\mathbf{k}), \mathbf{H}(\mathbf{k}), \mathbf{Q}(\mathbf{k}), \mathbf{G}(\mathbf{k})$) using the VanLoan

Method (Barton 2012b).

The state variables for our system are the 4 quaternions that define the board attitude and the 3 biases associated with each gyro axis ($\mathbf{x} = [q_0, q_1, q_2, q_3, b_{\omega_x}, b_{\omega_y}, b_{\omega_z}]^T$), whilst the measurement vector is comprised of the 3-axis accelerometer and magnetometer data ($\mathbf{z} = [\alpha_x, \alpha_y, \alpha_z, \beta_x, \beta_y, \beta_z]^T$).

The initial state estimate ($\hat{\mathbf{x}}_\mathbf{0}$) is calculated using the 3D magnetometer data to estimate initial yaw angle as in equationB.4, whilst all other states (roll, pitch and the gyro biases) are assumed to be zero. The Euler angles are then converted to quaternions and these initial values are fed into the EKF.

$$\dot{\mathbf{x}}_{\mathbf{k+1}} = \begin{bmatrix} \dot{q_0} \\ \dot{q_1} \\ \dot{q_2} \\ \dot{q_3} \\ \dot{b_{\omega_x}} \\ \dot{b_{\omega_y}} \\ \dot{b_{\omega_z}} \end{bmatrix} = \begin{bmatrix} \mathbf{C} \begin{bmatrix} \omega_x - b_{\omega_x} \\ \omega_y - b_{\omega_y} \\ \omega_z - b_{\omega_z} \end{bmatrix} \\ 0 \\ 0 \\ 0 \end{bmatrix} \tag{B.10}$$

$$\mathbf{C} = \frac{\mathbf{1}}{\mathbf{2}} \begin{bmatrix} -q_1 & -q_2 & -q_3 \\ q_0 & -q_3 & q_2 \\ q_3 & q_0 & -q_1 \\ -q_2 & q_1 & q_0 \end{bmatrix} \tag{B.11}$$

The EKF uses the system model of $\dot{\mathbf{x}}$ to predict the states for the next time step from the current state; the state model for our system is shown in Equation B.10 where the quaternions rates are calculated from the current state gyro biases and gyro measurements of body attitude rates using the current state quaternion conversion matrix ($\mathbf{C}$). This is the same conversion from the body to inertial reference frame as was described in Equation B.2 but in quaternion format rather than Euler angles.

The EKF also propagates and outputs the state covariance matrix $\mathbf{P}$ at each time step. $\mathbf{P}$ is an estimate of the accuracy of $\hat{\mathbf{x}}_\mathbf{t}$ and is initially calculated from $\mathbf{F}(\mathbf{k})$ and $\mathbf{Q}(\mathbf{k})$ before being updated using information from the current state measurement vector ($\mathbf{z_t}$) (Barton 2012b; Beard and McLain 2012). The $\mathbf{P}$ matrix is used in the EKF to propagate the Kalman gain ($\mathbf{K}$).

The Kalman gain essentially weights the state estimate uncertainties ($\mathbf{P}(\mathbf{k})$) with the measurement uncertainty ($\mathbf{G}(\mathbf{k})$) and dictates how much the measurement will affect the state estimate (Barton 2012b). The optimum value of $\mathbf{K}$ is chosen to minimise the mean square estimation error (Brown and Hwang 1993).

Based on Equations B.3 and B.4, predictions of acceleration and magnetic field strength measurements $\hat{\mathbf{z}}$ are calculated from the current states estimates $\hat{\mathbf{x}}$ and the gyro measurements (Equation B.12). ${}^{\mathbf{i}}_{\mathbf{b}}\mathbf{R}$ is the DCM calculated from the current state quaternions that describes the transformation required to convert, either the gravitational vector (g) or the unit magnetic field vector, from inertial to body coordinates. $\mathbf{R}_\delta$ is the DCM that rotates about the vertical z-axis to correct for the declination angle whilst $\mathbf{R}_\xi$ corrects the inclination angle by rotating around the y-axis.

Finally, the residual error between these estimates and the actual sensor observations ($\mathbf{z}-\hat{\mathbf{z}}$) is used with the Kalman gain to update the state estimates as shown in Equation B.13.

$$\hat{\mathbf{z}} = \begin{bmatrix} \hat{a_x} \\ \hat{a_y} \\ \hat{a_z} \\ \hat{\beta_x} \\ \hat{\beta_y} \\ \hat{\beta_z} \end{bmatrix} = \begin{bmatrix} \begin{bmatrix} \omega_x - b_{\omega_x} \\ \omega_y - b_{\omega_y} \\ \omega_z - b_{\omega_z} \end{bmatrix} \times \begin{bmatrix} V_{g,x} \\ V_{g,y} \\ V_{g,z} \end{bmatrix} - {}^{\mathbf{i}}_{\mathbf{b}}\mathbf{R} \begin{bmatrix} 0 \\ 0 \\ g \end{bmatrix} \\ {}^{\mathbf{i}}_{\mathbf{b}}\mathbf{R}\mathbf{R}_\xi\mathbf{R}_\delta \begin{bmatrix} 1 \\ 0 \\ 0 \end{bmatrix} \end{bmatrix} \tag{B.12}$$

$$\hat{\mathbf{x}}_{\mathbf{t}} = \hat{\mathbf{x}}_{(\mathbf{t}|\mathbf{t-1})} + \mathbf{K}_{\mathbf{t}}(\mathbf{z}_{\mathbf{t}} - \hat{\mathbf{z}}_{\mathbf{t}}) \tag{B.13}$$

The AHRS code was implemented in MATLAB using variables after the calibrations and centre of mass correction described earlier in the chapter had been applied. It was tuned by adjusting the error covariance matrix of the sensors to achieve optimum results. This was quantified by looking at the standard deviation of the residual error of between the estimated and measured accelerometer and magnetometer data and from inspection of the error covariance matrix $\mathbf{P}$, which converged over the course of a flight. The pseudo code for the implementation of the AHRS is described in Algorithm 1.

A final correction for the misalignment between the bird and board axis systems was required. This was achieved by assuming that during the course of a flight the bird's roll and pitch angle were on average zero, excluding periods of circling flight in thermals (see Chapter 7 for thermal identification analysis). The mean offset of the roll and pitch angles could then be subtracted from the data for each flight. For the yaw angle bias correction, it was assumed that on average the side slip angle was zero. Side slip was calculated as the difference between the yaw angle and the track angle from the GPS position data. The resulting offset was then subtracted. This was generally sucessful though in the case of 5 flights, on examination of the roll data, it appears as though the board may have moved during the flight causing an offset in our estimated attitude data.

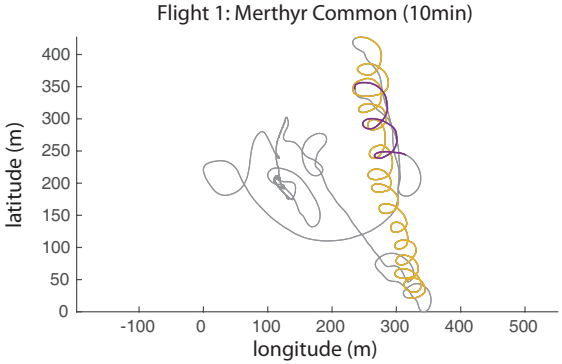
Algorithm 1 Pseudo code for AHRS implementation

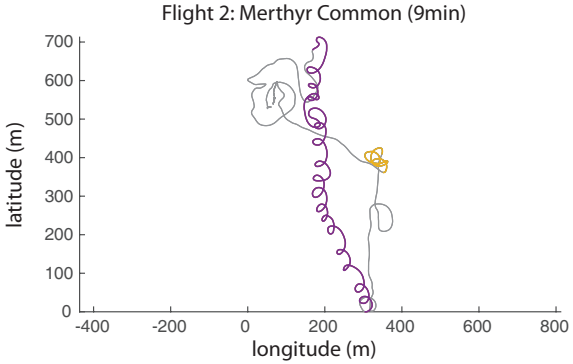
Calibrate gyro, accelerometer and magnetometer data
Correct accelerations for centre of mass of bird $[\alpha_x, \alpha_y, \alpha_z]$
Use magnetometers to find initial yaw estimate ($\hat{\psi}_0$) and set $\hat{\phi}_0 = \hat{\theta}_0 = 0$
Convert initial Euler estimates $[\hat{\phi}_0, \hat{\theta}_0, \hat{\psi}_0]$ to quarternions $[q_0, q_1, q_2, q_3]$
Assume initial gyro biases $[b_{w,x0}, b_{w,y0}, b_{w,z0}] = 0^\circ s^{-1}$
Initialise covariance matrix $\mathbf{P}_{[\mathbf{7x7}]}$
Initialise: $\hat{\mathbf{x}} = \mathbf{x_0}$
Use EKF to propagate $\hat{\mathbf{x}}$ and $\mathbf{P}$ by stepping through each sample time T_k
for $k = 1$ to *lengthdata* **do** EKF
    Compute $\dot{\mathbf{x}}$ and $\mathbf{F}$:
    $\rightarrow \dot{\mathbf{x}} = [\dot{q_0}, \dot{q_1}, \dot{q_2}, \dot{q_3}, 0, 0, 0]$
    $\rightarrow \mathbf{F} = \mathbf{d}(\dot{\mathbf{x}})/\mathbf{dx}$
    Predict state estimate: $\hat{\mathbf{x}} = \hat{\mathbf{x}} + \dot{\mathbf{x}}\mathbf{dt}$
    Compute $\hat{\mathbf{z}}$ and $\mathbf{H}$:
    $\rightarrow \mathbf{H} = \mathbf{d}(\hat{\mathbf{z}})/\mathbf{dx}$
    $\rightarrow \hat{\mathbf{z}} = [\hat{\alpha_x}, \hat{\alpha_y}, \hat{\alpha_z}, \hat{\beta}_x, \hat{\beta}_y, \hat{\beta}_z]$
    Convert $\mathbf{F}, \mathbf{H}, \mathbf{Q}$& $\mathbf{G}$ from linearized continuous-domain to discrete time domain using the VanLoan method.
    Predict state covariance matrix ($\mathbf{P} = \mathbf{PHI_k} * \mathbf{P_k} * \mathbf{PHI'_k} + \mathbf{Q_k}$)
    Compute kalman gain matrix ($\mathbf{K} = \mathbf{PH'}[\mathbf{HPH'} + \mathbf{R}] - \mathbf{1}$)
    Calculate measurement residuals ($\mathbf{z} - \hat{\mathbf{z}}$)
    Use measurement residuals and $\mathbf{K}$ to update state estimates $\hat{\mathbf{x}}$ and $\mathbf{P}$
    $\rightarrow \hat{\mathbf{x}} = \hat{\mathbf{x}} + \mathbf{K}(\mathbf{z} - \hat{\mathbf{z}})$
    $\rightarrow \mathbf{P} = [\mathbf{I} - \mathbf{KH}]\mathbf{P}$
end for
Re-compute Euler angles from new state estimate quaternions
Correct for instrumentation and bird axis system misalignment

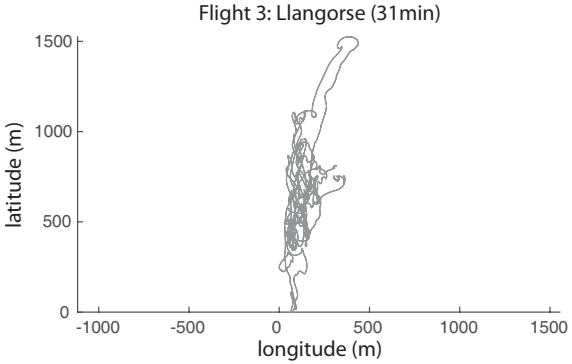
Appendix C

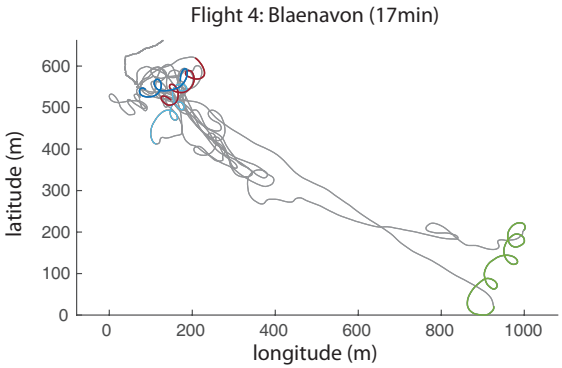
Thermal identification

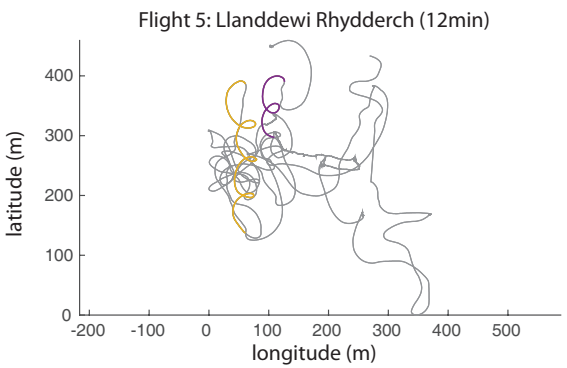
The following figures show the 45 individual GPS flight tracks recorded for our steppe eagle with the sections of thermalling flight automatically identified, highlighted in colour.

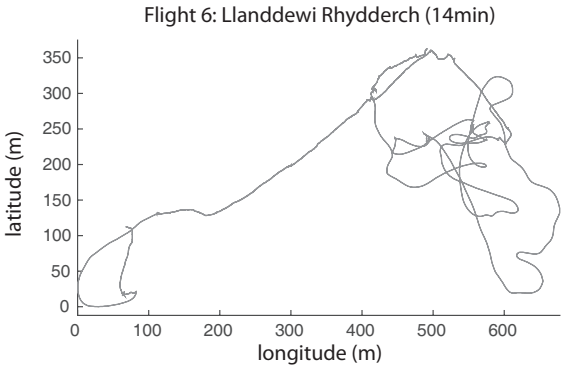

Flight 1: Merthyr Common (10min)
latitude (m)
longitude (m)

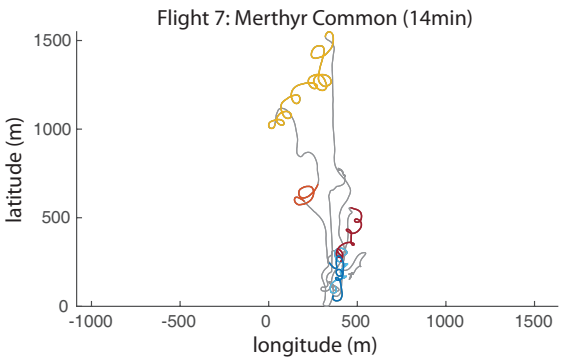

Flight 2: Merthyr Common (9min)
latitude (m)
longitude (m)

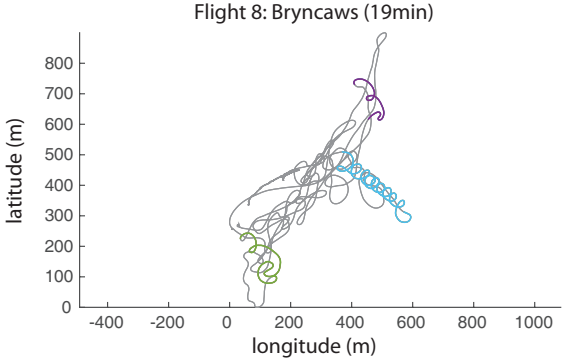

Flight 3: Llangorse (31min)
latitude (m)
longitude (m)

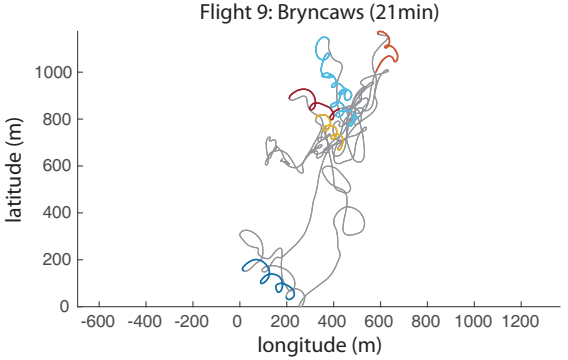

Flight 4: Blaenavon (17min)
latitude (m)
longitude (m)

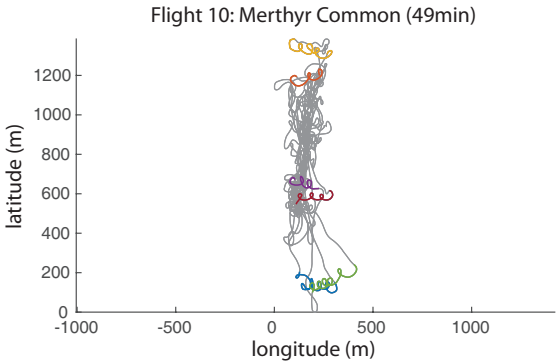

Flight 5: Llanddewi Rhydderch (12min)
latitude (m)
longitude (m)

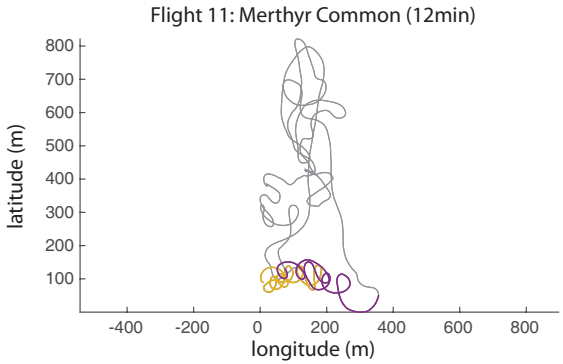

Flight 6: Llanddewi Rhydderch (14min)
latitude (m)
longitude (m)

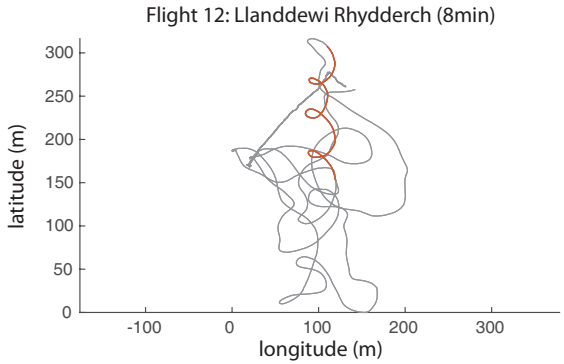

Flight 7: Merthyr Common (14min)
latitude (m)
longitude (m)

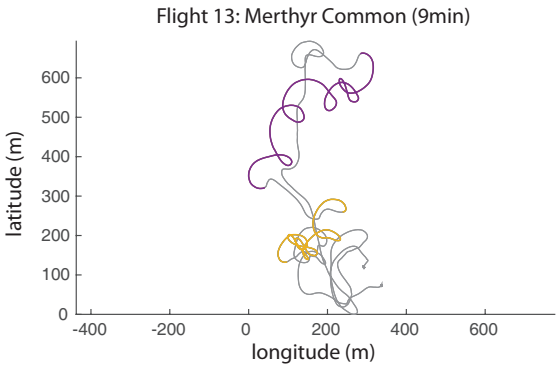

Flight 8: Bryncaws (19min)
latitude (m)
longitude (m)

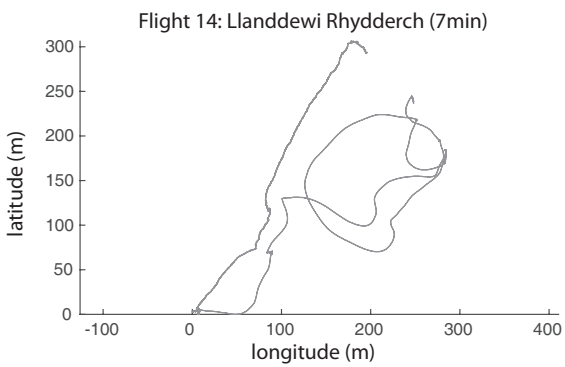

Flight 9: Bryncaws (21min)
latitude (m)
longitude (m)

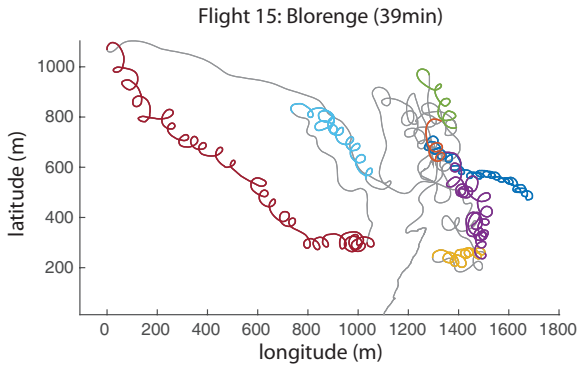

Flight 10: Merthyr Common (49min)
latitude (m)
longitude (m)

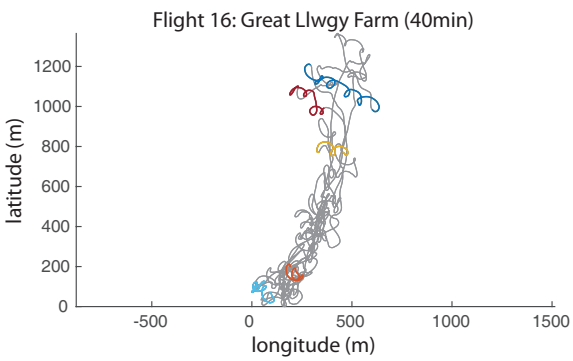

Flight 11: Merthyr Common (12min)
latitude (m)
longitude (m)

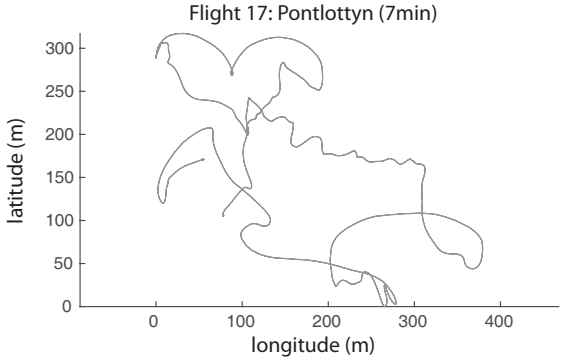

Flight 12: Llanddewi Rhydderch (8min)
latitude (m)
longitude (m)

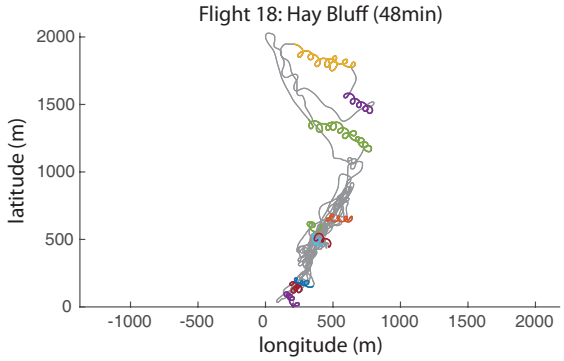

Flight 13: Merthyr Common (9min)
latitude (m)
longitude (m)

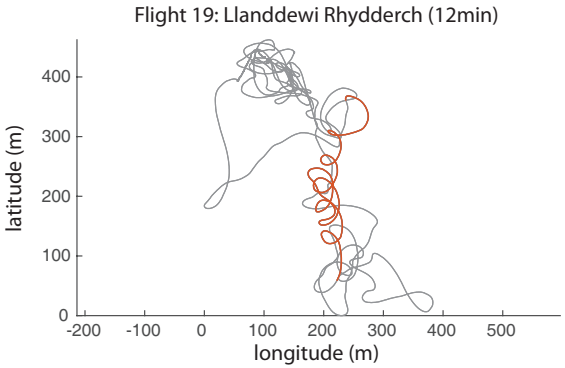

Flight 14: Llanddewi Rhydderch (7min)
latitude (m)
longitude (m)

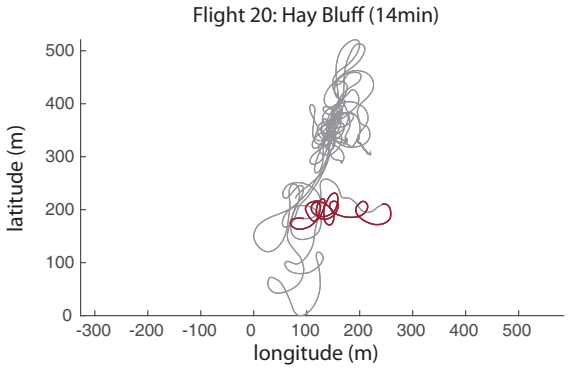

Flight 15: Blorenge (39min)
latitude (m)
longitude (m)

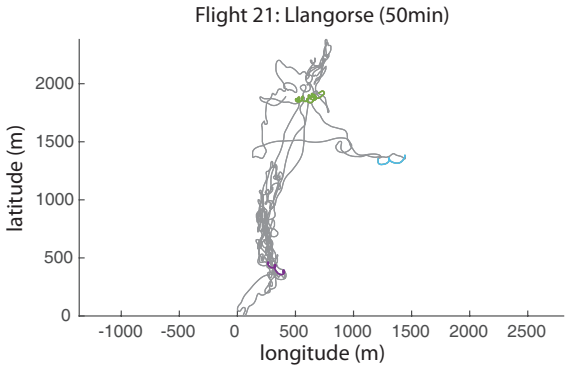

Flight 16: Great Llwgy Farm (40min)
latitude (m)
longitude (m)

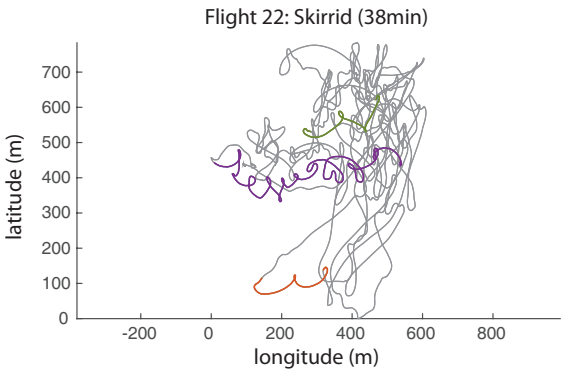

Flight 17: Pontlottyn (7min)
latitude (m)
longitude (m)

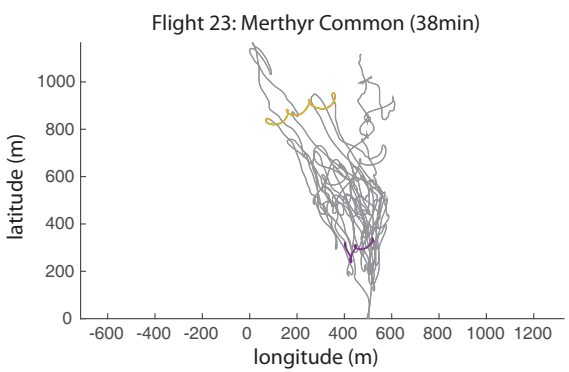

Flight 18: Hay Bluff (48min)
latitude (m)
longitude (m)

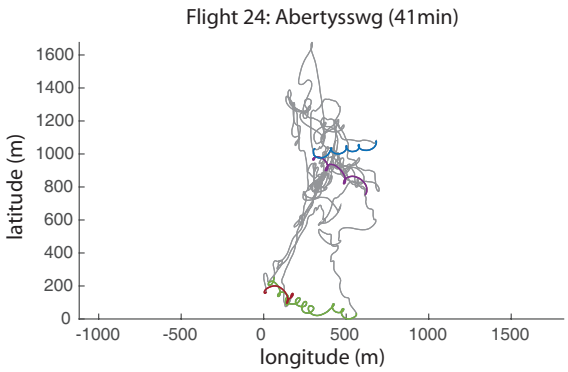

Flight 19: Llanddewi Rhydderch (12min)
latitude (m)
longitude (m)

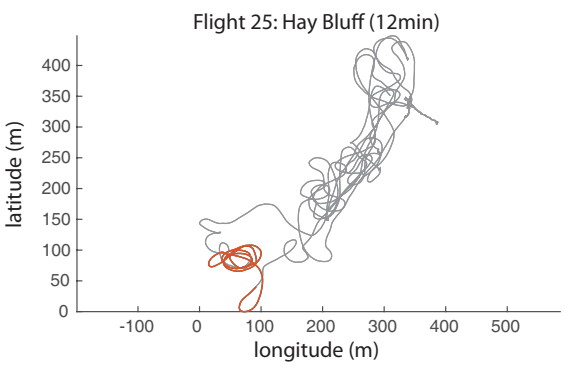

Flight 20: Hay Bluff (14min)
latitude (m)
longitude (m)

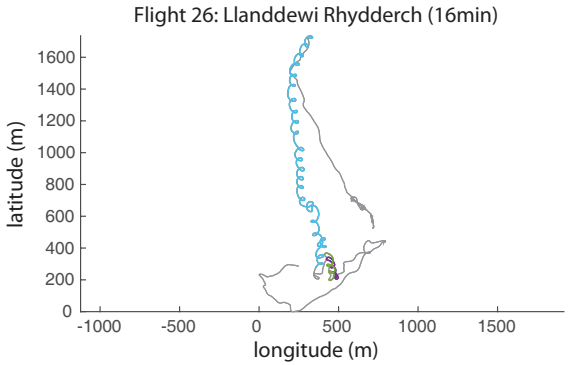

Flight 21: Llangorse (50min)
latitude (m)
longitude (m)

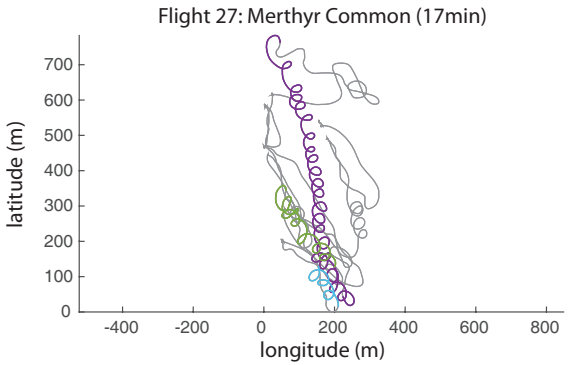

Flight 22: Skirrid (38min)
latitude (m)
longitude (m)

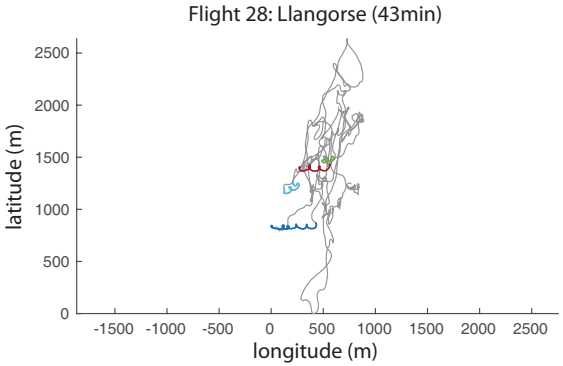

Flight 23: Merthyr Common (38min)
latitude (m)
longitude (m)

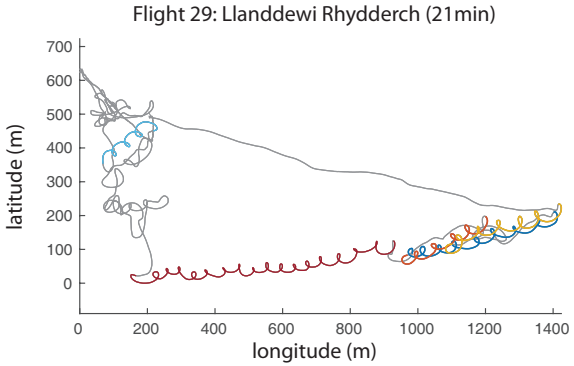

Flight 24: Abertysswg (41min)
latitude (m)
longitude (m)

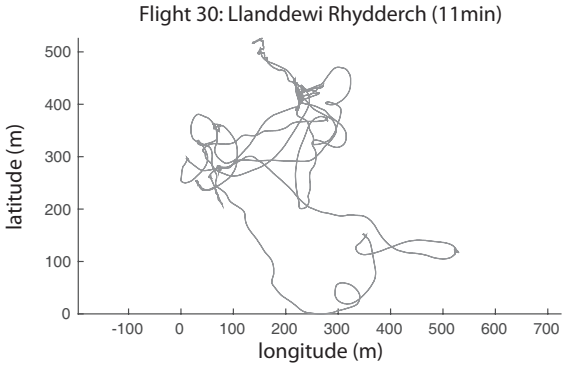

Flight 25: Hay Bluff (12min)
latitude (m)
longitude (m)

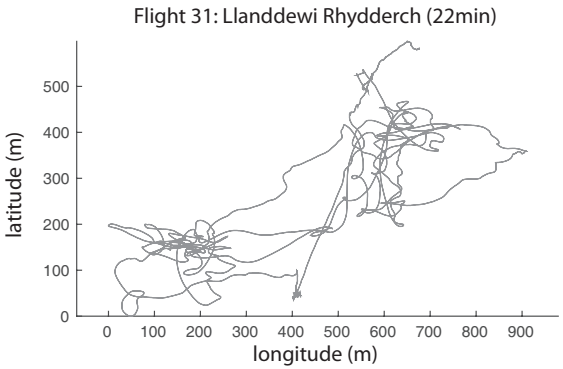

Flight 26: Llanddewi Rhydderch (16min)
latitude (m)
longitude (m)

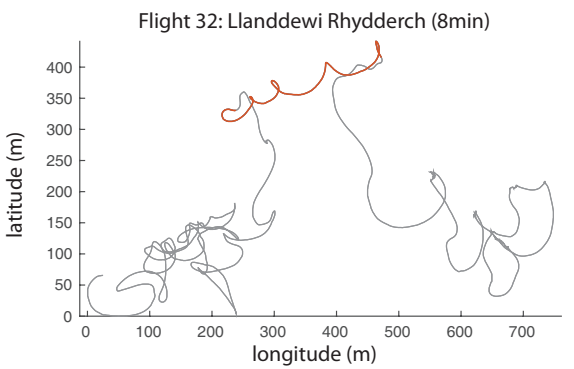

Flight 27: Merthyr Common (17min)
latitude (m)
longitude (m)

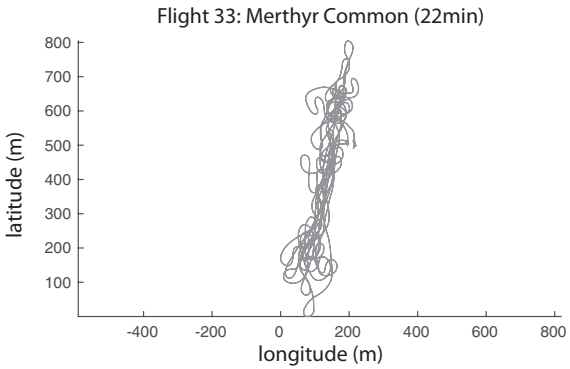

Flight 28: Llangorse (43min)
latitude (m)
longitude (m)

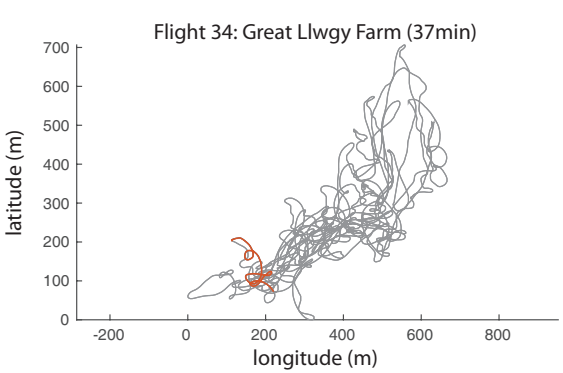

Flight 29: Llanddewi Rhydderch (21min)
latitude (m)
longitude (m)

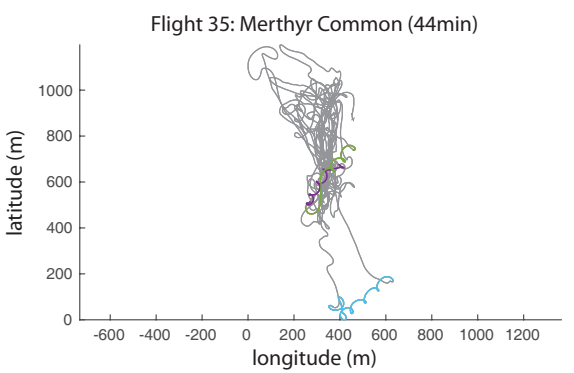

Flight 30: Llanddewi Rhydderch (11min)
latitude (m)
longitude (m)

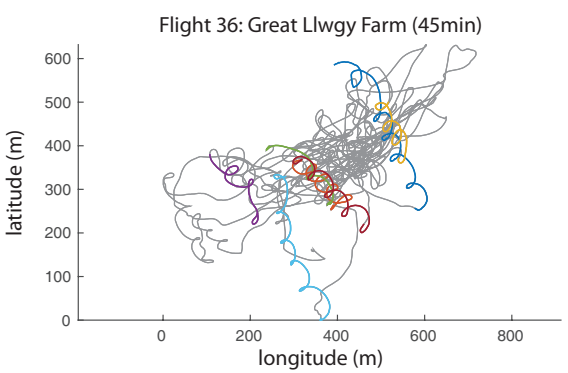

Flight 31: Llanddewi Rhydderch (22min)
latitude (m)
longitude (m)

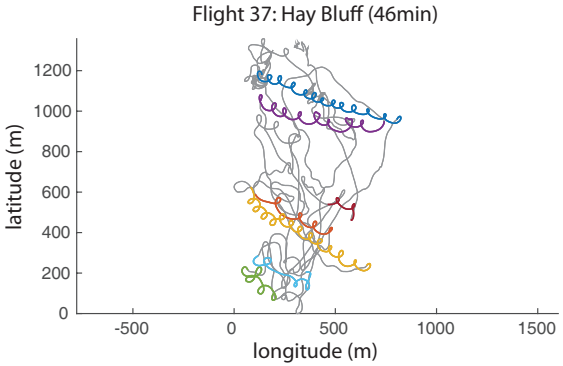

Flight 32: Llanddewi Rhydderch (8min)
latitude (m)
longitude (m)

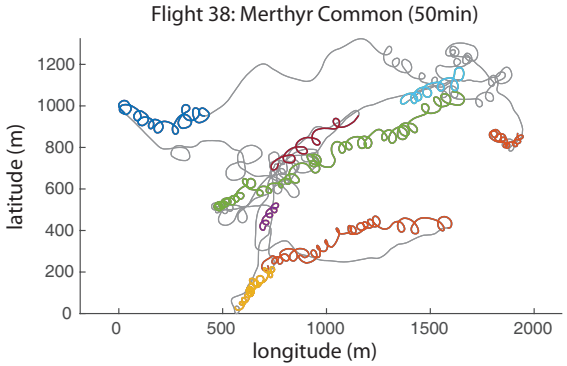

Flight 33: Merthyr Common (22min)
latitude (m)
longitude (m)

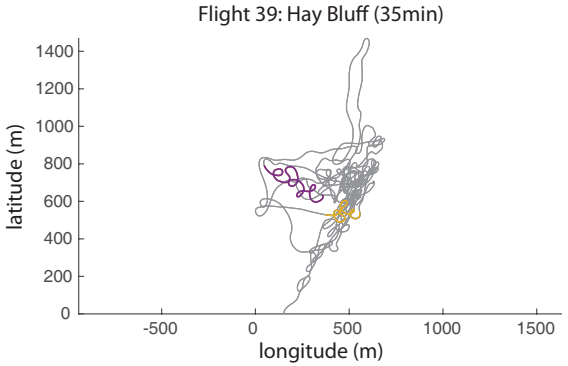

Flight 34: Great Llwgy Farm (37min)
latitude (m)
longitude (m)

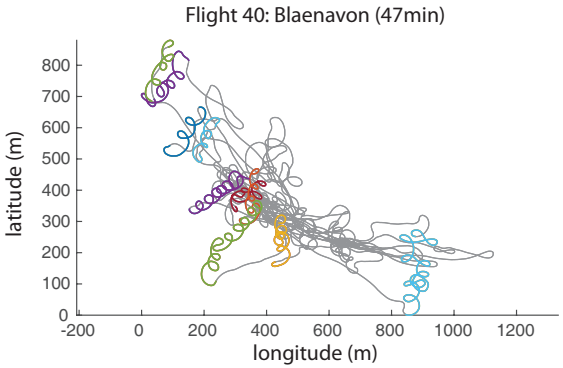

Flight 35: Merthyr Common (44min)
latitude (m)
longitude (m)

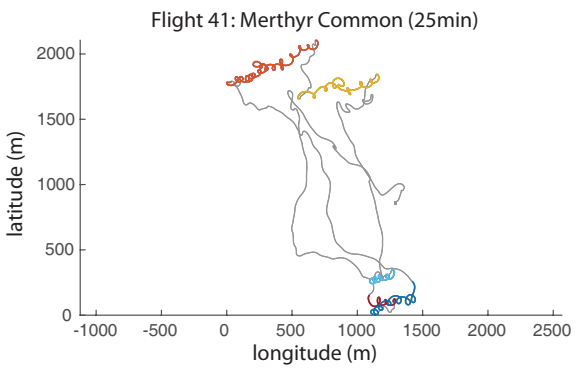

Flight 36: Great Llwgy Farm (45min)
latitude (m)
longitude (m)

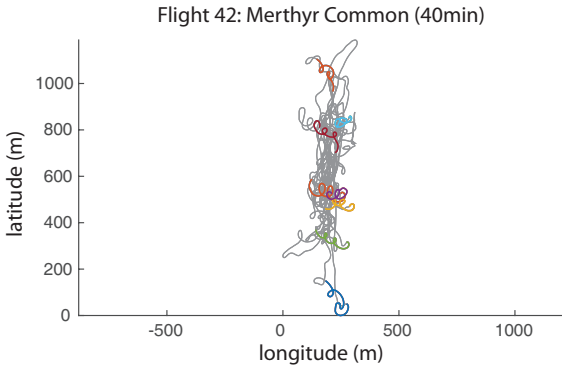

Flight 37: Hay Bluff (46min)
latitude (m)
longitude (m)

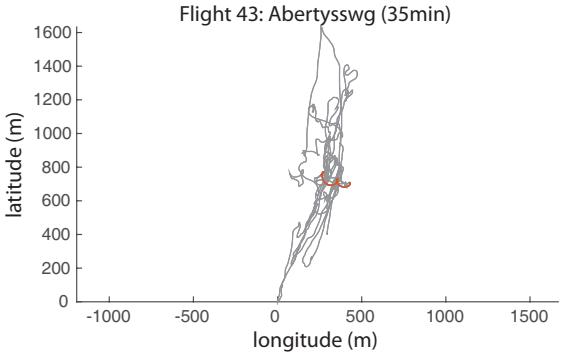

Flight 38: Merthyr Common (50min)
latitude (m)
longitude (m)

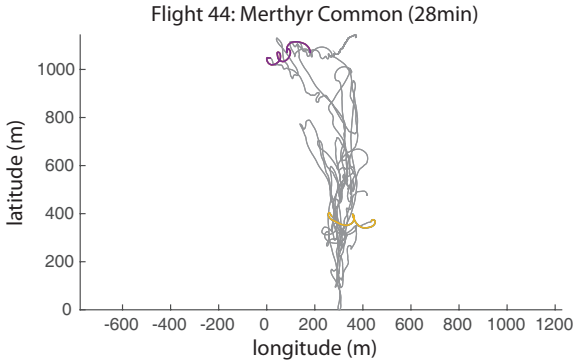

Flight 39: Hay Bluff (35min)
latitude (m)
longitude (m)

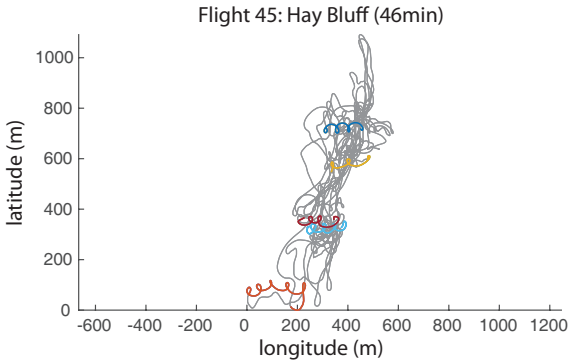

Flight 40: Blaenavon (47min)
latitude (m)
longitude (m)


Flight 41: Merthyr Common (25min)
latitude (m)
longitude (m)


Flight 42: Merthyr Common (40min)
latitude (m)
longitude (m)


Flight 43: Abertysswg (35min)
latitude (m)
longitude (m)


Flight 44: Merthyr Common (28min)
latitude (m)
longitude (m)


Flight 45: Hay Bluff (46min)
latitude (m)
longitude (m)

Bibliography

3D Robotics (2012). *Mission Planner*. Available from: `http://planner.ardupilot.com/` [Accessed 15 February 2012].

Ákos, Z., Nagy, M., and Vicsek, T. (2008). "Comparing bird and human soaring strategies". In: *PNAS* 105 (11), pp. 4139–4143.

Ákos, Z., Nagy, M., Leven, S., and Vicsek, T. (2010). "Thermal soaring flight of birds and unmanned aerial vehicles". In: *Bioinspir. Biomim.* 5 (4), pp. 4139–4143.

Allen, M. (2005). "Autonomous soaring for improved endurance of a small uninhabitated air vehicle". In: *43rd AIAA Aerospace Sciences Meeting and Exhibit*. doi:10.2514/6.2005-1025.

Allen, M. and Lin, V. (2007). "Guidance and control of an autonomous soaring vehicle with flight test results". In: *45th AIAA Aerospace Sciences Meeting and Exhibit*. Aerospace Sciences Meetings. doi:10.2514/6.2007-867. American Institute of Aeronautics and Astronautics.

Andersson, K., Kaminer, I., Jones, K. D., Dobrokhodov, V., and Lee, D. (2009). "Cooperating UAVs using thermal lift to extend endurance". In: *AIAA Unmanned Unlimited Conference, Seattle, WA*.

Andersson, K., Kaminer, I., and Jones, K. (2010). "Autonomous soaring; flight test results of a thermal centering controller". In: *AIAA Guidance, Navigation, and Control Conference*. doi:10.2514/6.2010-8034.

Angevine, W. M. (2006). "Thermal Structure and Behavior". In: *RC Soaring*. Available from: `http://www.rcsoaring.com/docs/thermals_2006.pdf`.

Baier, D. B., Gatesy, S. M., and Jenkins, F. A. (2007). "A critical ligamentous mechanism in the evolution of avian flight". In: *Nature* 445 (7125). doi:10.1038/nature05435, pp. 307–310.

Barton, J. D. (2012a). "Fundamentals of small unmanned aircraft flight". In: *Johns Hopkins APL technical digest* 31 (2), pp. 132–149.

— (2012b). *SUAS code: Small fixed-wing UAS state estimation examples*. Available from: `http://www.jhuapl.edu/ott/Technologies/Copyright/SuasCode.asp` [Accessed 26 November 2014].

Beard, R. W. and McLain, T. W. (2012). *Small unmanned aircraft: Theory and practice*. Princeton University Press.

Biro, D., Meade, J., and Guilford, T. (2004). "Familiar route loyalty implies visual pilotage in the homing pigeon". In: *PNAS* 101 (50), pp. 17440–17443.

Bohrer, G., Brandes, D., Mandel, J. T., Bildstein, K. L., Miller, T. A., Lanzone, M., Katzner, T., Maisonneuve, C., and Tremblay, J. A. (2012). "Estimating updraft

velocity components over large spatial scales: contrasting migration strategies of golden eagles and turkey vultures". In: *Ecol. Lett.* 15 (2), pp. 96–103.

Boisserie, B. (2012). "Modelling the updrafts at Hay Bluff (Black Mountains)". Unpublished M.Sc. Thesis. Cranfield University.

Bouten, W., Baaij, E. W., Shamoun-Baranes, J., and Camphuysen, K. C. J. (2013). "A flexible GPS tracking system for studying bird behaviour at multiple scales". In: *J. Ornithol.* 154 (2), pp. 571–580.

Bower, G. C., Flanzer, T. C., Naiman, A. D., and Saripalli, S. (2010). "Dynamic environment mapping for autonomous thermal soaring". In: *AIAA Guidance, Navigation and Control Conference, Toronto*. Vol. 8031.

Brown, R. G. and Hwang, P. Y. C. (1993). *Introduction to random signals and applied Kalman filtering: with MATLAB exercises and solutions*. 3rd ed. John Wiley & Sons.

Bruderer, B. and Boldt, A. (2001). "Flight characteristics of birds". In: *Ibis* 143 (2), pp. 178–204.

Burnham, K. P. and Anderson, D. R. (2002). *Model selection and multimodel inference: a practical information-theoretic approach*. 2nd ed. New York: Springer Verlag.

Careau, V., Therrien, J. F., Porras, P., Thomas, D., and Bildstein, K. (2006). "Soaring and gliding flight of migrating broad-winged hawks: behavior in the Nearctic and Neotropics compared". In: *J. Ornithol.* 118 (4), pp. 471–477.

Carruthers, A. C., Walker, S. M., Thomas, A. L. R., and Taylor, G. K. (2010). "Aerodynamics of aerofoil sections measured on a free-flying bird". In: *Proc. Inst. Mech. Eng. G J. Aerosp. Eng.* 224 (8), pp. 855–864.

CGS network (2011). *Length Of A Degree Of Latitude And Longitude Calculator*. Available from: `http://www.csgnetwork.com/degreelenllavcalc.html` [Accessed 12 March 2014].

Chakrabarty, A. and Langelaan, J. W. (2011). "Energy-based long-range path planning for soaring-capable unmanned aerial vehicles". In: *J. Guid. Control. Dynam.* 34 (4).

CHRobotics. *Understanding Quaternions*. Available from: `http://www.chrobotics.com/library/understanding-quaternions` [Accessed 5 November 2014].

Cone, C. D. (1962). "Thermal soaring of birds". In: *Am. Sci.* Pp. 180–209.

Cowling, I. D., Willcox, S., Patel, Y., Smith, P., and Roberts, M. (2009). "Increasing persistence of UAVs and MAVs through thermal soaring". In: *Aeronaut. J.* 113 (1145), pp. 479–489.

DoD Positioning, Navigation, and Timing Executive Committe (2008). *Global positioning system standard positioning service performance standard*. 4th ed. Washington: Department of Defense.

Duerr, A. E., Miller, T. A., Lanzone, M., Brandes, D., Cooper, J., O'Malley, K., Maisonneuve, C., Tremblay, J., and Katzner, T. (2012). "Testing an emerging paradigm in migration ecology shows surprising differences in efficiency between flight modes". In: *PLoS One* 7 (4), p. 35548.

Edwards, D. J. and Silberberg, L. M. (2010). "Autonomous soaring: The Montague cross-country challenge". In: *J. Aircraft* 47 (5), pp. 1763–1769.

Etkin, B. and Reid, L. D. (1996). *Dynamics of flight: stability and control*. 3rd ed. New York: Wiley.

Forest encyclopedia (2008). *Mechanical and thermal turbulence*. Available from: http://www.forestencyclopedia.net/p/p418 /view [Accessed 10 March 2013].

Gebre-Egziabher, D., Elkaim, G. H., Powell, D. J., and Parkinson, B. W. (2001). "A non-linear, two-step estimation algorithm for calibrating solid-state strapdown magnetometers". In: *8th International St. Petersburg Conference on Navigation Systems (IEEE/AIAA)*.

Gillies, J. A. (2010). "Soaring flight in the steppe eagle (*Aquila nipalensis*)". Unpublished D.Phil Thesis. Oxford University, UK.

Gillies, J. A., Bacic, M., Yuan, F. G., Thomas, A. L. R., and Taylor, G. K. (2008). "Modeling and identification of steppe eagle (Aquila nipalensis) dynamics". In: *Proc. AIAA Modeling and Simulation Technologies Conf.*

Gillies, J. A., Thomas, A. L. R., and Taylor, G. K. (2011). "Soaring and manoeuvring flight of a steppe eagle Aquila nipalensis". In: *J. Avian Biol.* 42 (5), pp. 377–386. DOI: doi:10.1111/j.1600-048X.2011.05105.x.

Gray, S. J. (1968). *Animal Locomotion*. London: Weidenfeld & Nicolson.

Grünewälder, S., Broekhuis, F., Macdonald, D. W., Wilson, A. M., McNutt, J. W., Shawe-Taylor, J., and Hailes, S. (2012). "Movement activity based classification of animal behaviour with an application to data from cheetah (Acinonyx jubatus)". In: *PLoS ONE* 7 (11). doi:10.1371/journal.pone.0049120.

Guilford, T., Meade, J., Willis, J., Phillips, R. A, Boyle, D., Roberts, S., Collett, M., Freeman, R., and Perrins, C. M. (2009). "Migration and stopover in a small pelagic seabird, the Manx shearwater Puffinus puffinus: insights from machine learning". In: *Proc. R. Soc. B*. doi:DOI: 10.1098/rspb.2008.1577.

Hankin, E. H. (1913). *Animal flight: a record of observation*. London: Iliffe & Sons.

Hedenström, A. (1993). "Migration by soaring or flapping flight in birds: the relative importance of energy cost and speed". In: *Philos. Trans. R. Soc. Lond. B* 342 (1302), pp. 353–361.

Hedenström, A. and Alerstam, T. (1998). "How fast can birds migrate?" In: *J. Avian Biol.* Pp. 424–432.

Hedenström, A. and Liechti, F. (2001). "Field estimates of body drag coefficient on the basis of dives in passerine birds". In: *J. Exp. Biol.* 204 (6), pp. 1167–1175.

Henningsson, P. and Hedenström, A. (2011). "Aerodynamics of gliding flight in common swifts". In: *J. Exp. Biol.* 214 (3), pp. 382–393.

Hunter, L. (1984). "The art and physics of soaring". In: *Phys. Today* 37 (4), pp. 34–41.

InvenSense (2011). *MPU-6000 and MPU-6050 Product Specification*. PS-MPU-6000A-00. Rev. 3.2.

Irving, F. (1999). *The paths of soaring flight*. Imperial College Press.

Jacobson, M. Z. (2005). *Fundamentals of atmospheric modeling*. 2nd ed. New York: Cambridge University Press.

Kahveci, N. E., Ioannou, P. A., and Mirmirani, M. D. (2007). "A heuristic search algorithm for maneuvering of UAVs across dense thermal areas". In: *AIAA Guidance, Navigation and Control Conference and Exhibit*, p. 6652.

Kuroda, N. (1961). "A note on the pectoral muscles of birds". In: *The Auk*, pp. 261–263.

Langelaan, J. W. (2007). "Long distance/duration trajectory optimization for small uavs". In: *AIAA Guidance, Navigation and Control Conference*.

Lentink, D., Müller, U. K., Stamhuis, E. J., De Kat, R., van Gestel, W., Veldhuis, L. L. M., Henningsson, P., Hedenström, A., Videler, J. J., and van Leeuwen, J. L. (2007). "How swifts control their glide performance with morphing wings". In: *Nature* 446 (7139), pp. 1082–1085.

Leshem, Y. and Yom-Tov, Y. (1998). "Routes of migrating soaring birds". In: *Ibis* 140 (1), pp. 41–52.

Lind, A. J. (2010). *Soaring Steppe Eagle*. [Online]. [Accessed 14 June 2014]. Available from: http://www.youtube.com/watch?v=83FN7CuvjZE.

— (2011). *Soaring Steppe Eagles*. [Online]. [Accessed 14 June 2014]. Available from: http://www.youtube.com/watch?v=3tlM96-HVl0.

Looney, M. (2010). "A simple calibration for MEMS gyroscopes". In: *EDN* 55 (9), p. 21.

Mandel, J. T., Bildstein, K. L., Bohrer, G., and Winkler, D. W. (2008). "Movement ecology of migration in turkey vultures". In: *PNAS* 105 (49), pp. 19102–19107.

Mandel, J. T., Bohrer, G., Winkler, D. W., Barber, D. R., Houston, C. S., and Bildstein, K. L. (2011). "Migration path annotation: cross-continental study of migration-flight response to environmental conditions". In: *Ecol. Appl.* 21 (6), pp. 2258–2268.

McCready, P. (1954). "An optimal airspeed selector". In: *Soaring*.

McGowan, A. R., Cox, D. E., Lazos, B. S., Waszak, M. R., Raney, D. L., Siochi, E. J., and Pao, S. P. (2003). "Biologically inspired technologies in NASA's morphing project". In: *Proc. SPIE 5051, Smart Structures and Materials 2003: Electroactive Polymer Actuators and Devices (EAPAD)*. doi:10.1117/12.484714. International Society for Optics and Photonics, pp. 1–13.

McLaren, J. D., Shamoun-Baranes, J., and Bouten, W. (2012). "Wind selectivity and partial compensation for wind drift among nocturnally migrating passerines". In: *Behav. Ecol.* 23 (5), pp. 1089–1101.

Mellone, U., Limiñana, R., Mallia, E., and Urios, V. (2011). "Extremely detoured migration in an inexperienced bird: interplay of transport costs and social interactions". In: *J. Avian Biol.* 42 (5), pp. 468–472.

MetOffice (2012). *Met Office Integrated Data Archive System (MIDAS) Land and Marine Surface Stations Data (1853-current), NCAS British Atmospheric Data Centre*. Available from: `http://badc.nerc.ac.uk/view/badc.nerc.ac.uk_ATOM_dataent_ukmo-midas`.

Meyburg, B., Meyburg, C., and Paillat, P. (2012). "Steppe eagle migration strategies: Revealed by satellite telemetry". In: *Brit. Birds* 105 (9), p. 506.

Meyers, R. A. (1993). "Gliding flight in the american kestrel (Falco sparverius): an electromyographic study". In: *J. Morphol.* 215 (3), pp. 213–224.

Meyers, R. A. and Stakebake, E. F. (2005). "Anatomy and histochemistry of spread-wing posture in birds. 3. Immunohistochemistry of flight muscles and the shoulder lock in albatrosses". In: *J. Morphol.* 263 (1), pp. 12–29.

Mohamed, A, Carrese, R, Fletcher, DF, and Watkins, S (2015). "Scale-resolving simulation to predict the updraught regions over buildings for MAV orographic lift soaring". In: *J. Wind. Eng. Ind. Aerod.* 140, pp. 34–48.

Nathan, R., Spiegel, O., Fortmann-Roe, S., Harel, R., Wikelski, M., and Getz, W. M. (2012). "Using tri-axial acceleration data to identify behavioral modes of free-ranging animals: general concepts and tools illustrated for griffon vultures". In: *J. Exp. Biol.* 215 (6), pp. 986–996.

Parrott, G. C. (1970). "Aerodynamics of gliding flight of a black vulture Coragyps atratus". In: *J. Exp. Biol.* 53 (2), pp. 363–374.

Pennycuick, C. J. (1960). "Gliding flight of the fulmar petrel". In: *J. Exp. Biol.* 37 (2), pp. 330–338.

— (1968). "A wind-tunnel study of gliding flight in the pigeon Columba livia". In: *J. Exp. Biol.* 49 (3), pp. 509–526.

— (1971a). "Control of gliding angle in rüppell's griffon vulture Gyps rüppellii". In: *J. Exp. Biol.* 55 (1), pp. 39–46.

— (1971b). "Gliding flight of the white-backed vulture Gyps africanus". In: *J. Exp. Biol.* 55 (1), pp. 13–38.

— (1972). "Soaring behaviour and performance of some east african birds, observed from a motor glider". In: *Ibis* 114 (2), pp. 178–218.

— (1982). "The flight of petrels and albatrosses (Procellariiformes), observed in South Georgia and its vicinity". In: *Philos. Trans. R. Soc. Lond. B* 300 (1098), pp. 75–106.

— (1983). "Thermal soaring compared in three dissimilar tropical bird species, Fregata magnificens, Pelecanus occidentals and Coragyps atratus". In: *J. Exp. Biol.* 102 (1), pp. 307–325.

— (1989a). "Bird flight performance: A practical calculation manual". In:

— (1989b). *Flight program*. Available from: `http://www.bristol.ac.uk/biology/people/colin-j-pennycuick/index.html`.

— (1996). "Wingbeat frequency of birds in steady cruising flight: new data and improved predictions". In: *J. Exp. Biol.* 199 (7), pp. 1613–1618.

— (1998). "Field observations of thermals and thermal streets, and the theory of cross-country soaring flight". In: *J. Avian. Biol.* Pp. 33–43.

— (2001). "Speeds and wingbeat frequencies of migrating birds compared with calculated benchmarks". In: *J. Exp. Biol.* 204 (19), pp. 3283–3294.

— (2002). "Gust soaring as a basis for the flight of petrels and albatrosses (Procellariiformes)". In: *Avian Science* 2 (1), pp. 1–12.

— (2008). *Modelling the flying bird*. Elsevier.

Pennycuick, C. J., Obrecht, H. H., and Fuller, M. R. (1988). "Empirical estimates of body drag of large waterfowl and raptors". In: *J. Exp. Biol.* 135 (1), pp. 253–264.

Pennycuick, C. J., Heine, C. E., Kirkpatrick, S. J., and Fuller, M. R. (1992). "The profile drag of a hawk's wing, measured by wake sampling in a wind tunnel". In: *J. Exp. Biol.* 165 (1), pp. 1–19.

Pennycuick, C. J., Åkesson, S., and Hedenström, A. (2013). "Air speeds of migrating birds observed by ornithodolite and compared with predictions from flight theory". In: *J. R. Soc. Interface* 10 (86), p. 20130419.

Peters, S. E. and Dobbins, C. S. (2012). "A comparative study of the mechanics of the pectoralis muscle of the red-tailed hawk and the barred owl". In: *J. Morphol.* 273 (3), pp. 312–323.

Portugal, S. J., Hubel, T. Y., Fritz, J., Heese, S., Trobe, D., Voelkl, B., Hailes, S., Wilson, A. M., and Usherwood, J. R. (2014). "Upwash exploitation and downwash avoidance by flap phasing in ibis formation flight". In: *Nature* 505 (7483), pp. 399–402.

Prior, N. C. (1984). "Flight energetics and migration performance of swans". PhD thesis. University of Bristol.

Quan, W., Li, J., Gong, X., and Fang, J. (2015). *INS/CNS/GNSS Integrated Navigation Technology*. Springer, p. 78.

Raspet, A. (1950). "Performance measurements of a soaring bird". In: *Aeronautical Engineering Review* 9 (12), pp. 14–17.

— (1960). "Biophysics of bird flight." In: *Science (New York, NY)* 132 (3421), p. 191.

Rayner, J. M. V. (1982). "Avian flight energetics". In: *Annual review of physiology* 44 (1), pp. 109–119.

Reichmann, H. (1993). *Cross-country soaring*. Soaring Society of Amer.

Renaudin, V., Afzal, M. H., and Lachapelle, G. (2010). "Complete triaxis magnetometer calibration in the magnetic domain". In: *Journal of Sensors* 2010.

Reynolds, K. V., Thomas, A. L. R., and Taylor, G. K. (2014a). "Wing tucks are a response to atmospheric turbulence in the soaring flight of the steppe eagle Aquila nipalensis". In: *J. R. Soc. Interface* 11 (101). DOI: 10.1098/rsif.2014.0645.

— (2014b). *Wing tucks are a response to atmospheric turbulence in the soaring flight of the steppe eagle Aquila nipalensis: Data supplement*. Available from: http://rsif.royalsocietypublishing.org/content/11/101/20140645.figures-only.

Rohli, R. and Vega, A. J. (2011). *Climatology*. 2nd ed. Sudbury, MA: Jones & Bartlett.

Ropert-Coudert, Y. and Wilson, R. P. (2005). "Trends and perspectives in animal-attached remote sensing". In: *Front. Ecol. Environ.* 3 (8), pp. 437–444.

Ropert-Coudert, Y., Beaulieu, M., Hanuise, N., and Kato, A. (2009). "Diving into the world of biologging". In: *Endanger. Species Res.* 10, pp. 21–27.

Rosén, M. and Hedenström, A. (2001). "Gliding flight in a jackdaw: a wind tunnel study". In: *J. Exp. Biol.* 204 (6), pp. 1153–1166.

Sachs, G. (2005a). "Aerodynamic yawing moment characteristics of bird wings". In: *J. Theor. Biol.* 234 (4), pp. 471–478.

— (2005b). "Yaw stability in gliding birds". In: *J. Ornithol.* 146 (3), pp. 191–199.

Sachs, G. (2007). "Tail effects on yaw stability in birds". In: *J. Theor. Biol.* 249 (3), pp. 464–472.

— (2009). "Speed stability in birds". In: *Math. Biosci.* 219, pp. 1–6.

— (2015). "New model of flap-gliding flight". In: *J. Theor. Biol.* 377, pp. 110–116.

Sachs, G. and Moelyadi, M. A. (2010). "CFD based determination of aerodynamic effects on birds with extremely large dihedral". In: *J. Bionic. Eng.* 7 (1), pp. 95–101.

Sachs, G., Traugott, J., Nesterova, A. P., Dell'Omo, G., Kuemmeth, F., Heidrich, W., Vyssotski, A. L., and Bonadonna, F. (2012). "Flying at no mechanical energy cost: Disclosing the secret of wandering albatrosses". In: *PloS One* 7 (9).

Sachs, G., Traugott, J., Nesterova, A. P., and Bonadonna, F. (2013). "Experimental verification of dynamic soaring in albatrosses". In: *J. Exp. Biol.* 216 (22), pp. 4222–4232.

Sapir, N., Wikelski, M., McCue, M. D., Pinshow, B., and Nathan, R. (2010). "Flight modes in migrating European bee-eaters: heart rate may indicate low metabolic rate during soaring and gliding." In: *PLoS One* 5 (11), e13956–e13956.

Scorer, P. (2012). *Regional atmospheric soaring prediction (RASP); Blipmap forecasts*. Available from: `http://rasp.inn.leedsmet.ac.uk/` [Accessed 4 September 2012].

Shamoun-Baranes, J., Leshem, Y., Yom-Tov, Y., and Liechti, O. (2003). "Differential use of thermal convection by soaring birds over central Israel". In: *The Condor* 105 (2), pp. 208–218.

Shamoun-Baranes, J., Bom, R., van Loon, E. E., Ens, B. J., Oosterbeek, K., and Bouten, W. (2012). "From sensor data to animal behaviour: an oystercatcher example". In: *PloS One* 7 (5), e37997.

Shepard, E. L. C., Wilson, R. P., Quintana, F., Laich, A. G., Liebsch, N., Albareda, D. A., Halsey, L. G., Gleiss, A., Morgan, D. T., and Myers, A. E. (2008). "Identification of animal movement patterns using tri-axial accelerometry". In: *Endanger. Species Res.* 10 (2.1).

Sibley, D. A. (2003). *The sibley field guide to birds of western north america*. London: Christopher Helm.

Sokal, R. R. and Rohlf, F. J. (1994). *Biometry: the principles and practice of statistics in biological research*. 3rd ed. San Francisco: Freeman & Co.

Spaar, R. (1997). "Flight strategies of migrating raptors; a comparative study of interspecific variation in flight characteristics". In: *Ibis* 139 (3), pp. 523–535.

Spaar, R. and Bruderer, B. (1996). "Soaring migration of steppe eagles Aquila nipalensis in southern Israel: flight behaviour under various wind and thermal conditions". In: *J. Avian Biol.* Pp. 289–301.

— (1997). "Optimal flight behavior of soaring migrants: a case study of migrating steppe buzzards, Buteo buteo vulpinus". In: *Behav. Ecol.* 8 (3), pp. 288–297.

Sparr, R., Liechti, O., and Bruderer, B. (2000). "Forecasting flight altitudes and soaring performance of migrating raptors by the altitudinal profile of atmospheric conditions". In: *Technical Soaring* 24 (2), pp. 49–55.

Stengel, R. F. (2004). *Flight dynamics*. Princeton University Press.

Stombaugh, T., Shearer, S. A., Fulton, J., and Ehsani, M. R. (2002). "Elements of a dynamic GPS test standard". In: *ASAE Meeting Paper*. 021150.

Taylor, G. K. and Thomas, A. L. R. (2002). "Animal flight dynamics II. Longitudinal stability in flapping flight". In: *J. Theor. Biol.* 214 (3), pp. 351–370.

— (2014). *Evolutionary biomechanics: selection, phylogeny, and constraint*. Oxford: Oxford University Press.

Taylor, G. K., Bacic, M., Bomphrey, R. J., Carruthers, A. C., Gillies, J., Walker, S. M., and Thomas, A. L. R. (2008). "New experimental approaches to the biology of flight control systems". In: *J. Exp. Biol.* 211 (2), pp. 258–266.

Thomas, A. L. R. (1993). "On the aerodynamics of birds' tails". In: *Philos. Trans. R. Soc. Lond. B* 340 (1294), pp. 361–380.

Thomas, A. L. R. and Taylor, G. K. (2001). "Animal flight dynamics I. Stability in gliding flight". In: *J. Theor. Biol.* 212 (3), pp. 399–424.

Tucker, V. A. (1973). "Bird metabolism during flight: evaluation of a theory". In: *J. Exp. Biol.* 58 (3), pp. 689–709.

— (1987). "Gliding birds: the effect of variable wing span". In: *J. Exp. Biol.* 133 (1), pp. 33–58.

— (1988). "Gliding birds: descending flight of the whitebacked vulture, Gyps africanus". In: *J. Exp. Biol.* 140 (1), pp. 325–344.

— (1990). "Body drag, feather drag and interference drag of the mounting strut in a peregrine falcon, Falco peregrinus". In: *J. Exp. Biol.* 149 (1), pp. 449–468.

Tucker, V. A. and Heine, C. (1990). "Aerodynamics of gliding flight in a harris' hawk, Parabuteo unicinctus". In: *J. Exp. Biol.* 149 (1), pp. 469–489.

Tucker, V. A. and Parrott, G. C. (1970). "Aerodynamics of gliding flight in a falcon and other birds". In: *J. Exp. Biol.* 52 (2), pp. 345–367.

Van Dyke, M. (1975). *Perturbation methods in fluid mechanics*. Applied Mathematics and Mechanics. Stanford: Parabolic Press.

Videler, J. J. (2005). *Avian flight*. Oxford Ornithology Series. Oxford: Oxford University Press.

Vinh, N. X. (1993). *Flight mechanics of high-performance aircraft*. Vol. 4. Cambridge University Press.

Wahdan, A., Georgy, J., Abdelfatah, W., and Noureldin, A. (2013). "A technique for fast magnetometer calibration with little space coverage". In: *Proceedings of the 26th International Technical Meeting of The Satellite Division of the Institute of Navigation*, pp. 1098–1104.

Watanabe, S., Izawa, M., Kato, A., Ropert-Coudert, Y., and Naito, Y. (2005). "A new technique for monitoring the detailed behaviour of terrestrial animals: a case study with the domestic cat". In: *Appl. Anim. Behav. Sci.* 94 (1), pp. 117–131.

Wharington, J. and Herszberg, I. (1998). "Control of a high endurance unmanned air vehicle". In: *Proceedings of the 21st ICAS Congress.*

White, C., Lim, E. W., Watkins, S., Mohamed, A., and Thompson, M. (2012). "A feasibility study of micro air vehicles soaring tall buildings". In: *J. Wind Eng. Ind. Aerodyn.* 103, pp. 41–49.

Wilson, A. M., Lowe, J. C., Roskilly, K., Hudson, P. E., Golabek, K. A., and McNutt, J. W. (2013). "Locomotion dynamics of hunting in wild cheetahs". In: *Nature* 498 (7453), pp. 185–189.

Wright, W. (1900). *Wilbur Wright Notebook: September-October 1900. Box 1, Wilbur Wright and Orville Wright Papers.* Washington, D.C. Manuscript Division, Library of Congress.

Yoda, K., Sato, K., Niizuma, Y., Kurita, M., Bost, C., Le Maho, Y., and Naito, Y. (1999). "Precise monitoring of porpoising behaviour of Adélie penguins determined using acceleration data loggers". In: *J. Exp. Biol.* 202 (22), pp. 3121–3126.